A CONTRIBUTION TO THE MODELING OF METAL PLASTICITY AND FRACTURE:
FROM CONTINUUM TO DISCRETE DESCRIPTIONS

A Dissertation

by

SHYAM MOHAN KERALAVARMA

Submitted to the Office of Graduate Studies of
Texas A&M University
in partial fulfillment of the requirements for the degree of

DOCTOR OF PHILOSOPHY

December 2011

Major Subject: Aerospace Engineering

A CONTRIBUTION TO THE MODELING OF METAL PLASTICITY AND FRACTURE:
FROM CONTINUUM TO DISCRETE DESCRIPTIONS

A Dissertation

by

SHYAM MOHAN KERALAVARMA

Submitted to the Office of Graduate Studies of
Texas A&M University
in partial fulfillment of the requirements for the degree of

DOCTOR OF PHILOSOPHY

Approved by:

Chair of Committee,	Amine Benzerga
Committee Members,	Tom Arsenlis
	Tahir Cagin
	Dimitris Lagoudas
	Theofanis Strouboulis
	John Whitcomb
Head of Department,	Dimitris Lagoudas

December 2011

Major Subject: Aerospace Engineering

ABSTRACT

A Contribution to the Modeling of Metal Plasticity and Fracture:
From Continuum to Discrete Descriptions. (December 2011)
Shyam Mohan Keralavarma, B.Tech., University of Kerala;
M.S., Texas A&M University
Chair of Advisory Committee: Dr. A. Amine Benzerga

The objective of this dissertation is to further the understanding of inelastic behavior in metallic materials. Despite the increasing use of polymeric composites in aircraft structures, high specific strength metals continue to be used in key components such as airframe, fuselage, wings, landing gear and hot engine parts. Design of metallic structures subjected to thermomechanical extremes in aerospace, automotive and nuclear applications requires consideration of the plasticity, creep and fracture behavior of these materials. Consideration of inelasticity and damage processes is also important in the design of metallic components used in functional applications such as thin films, flexible electronics and micro electro mechanical systems.

Fracture mechanics has been largely successful in modeling damage and failure phenomena in a host of engineering materials. In the context of ductile metals, the Gurson void growth model remains one of the most successful and widely used models. However, some well documented limitations of the model in quantitative prediction of the fracture strains and failure modes at low triaxialities may be traceable to the limited representation of the damage microstructure in the model. In the first part of this dissertation, we develop an extended continuum model of void growth that takes into account details of the material microstructure such as the texture of the plastically deforming matrix and the evolution of the void shape. The need for such

an extension is motivated by a detailed investigation of the effects of the two types of anisotropy on the materials' effective response using finite element analysis. The model is derived using the Hill–Mandel homogenization theory and an approximate limit analysis of a porous representative volume element. Comparisons with several numerical studies are presented towards a partial validation of the analytical model.

Inelastic phenomena such as plasticity and creep result from the collective behavior of a large number of nano and micro scale defects such as dislocations, vacancies and grain boundaries. Continuum models relate macroscopically observable quantities such as stress and strain by coarse graining the discrete defect microstructure. While continuum models provide a good approximation for the effective behavior of bulk materials, several deviations have been observed in experiments at small scales such as an intrinsic size dependence of the material strength. Discrete dislocation dynamics (DD) is a mesoscale method for obtaining the mechanical response of a material by direct simulation of the motion and interactions of dislocations. The model incorporates an intrinsic length scale in the dislocation Burgers vector and potentially allows for size dependent mechanical behavior to emerge naturally from the dynamics of the dislocation ensemble. In the second part of this dissertation, a simplified two-dimensional DD model is employed to study several phenomena of practical interest such as strain hardening under homogeneous deformation, growth of microvoids in a crystalline matrix and creep of single crystals at elevated temperatures. These studies have been enabled by several recent enhancements to the existing two-dimensional DD framework described in Chapter V.

The main contributions from this research are: (i) development of a fully anisotropic continuum model of void growth for use in ductile fracture simulations and (ii) enhancing the capabilities of an existing two-dimensional DD framework for large scale simulations in complex domains and at elevated temperatures.

To my teachers, friends and family

ACKNOWLEDGMENTS

The work presented in this dissertation is the result of over five years of research under the guidance of Prof. Amine Benzerga. I would like to acknowledge contributions from several people with whom I have been associated during this time period. First and foremost, I would like to thank my advisor, Prof. Amine Benzerga, for his constant encouragement, guidance and financial support without which this work would not have been possible. He has for the most part allowed me the freedom to direct my research work according to my interests and tastes. During moments of self-doubt, his ability to look at problems from a broader perspective and to identify positives has helped me greatly in making progress.

I would like to thank the committee members for taking time out of their busy schedules to serve on my dissertation committee. I have had the opportunity for personal interactions with Dr. Strouboulis, Dr. Cagin and Dr. Lagoudas, all of whom have contributed to my academic development. Special thanks are also due to Dr. Tom Arsenlis for traveling all the way from California to attend my defense. Part of the work presented in this dissertation has been performed in collaboration with Prof. Javier Segurado and Prof. Javier LLorca from Universidad Politécnica de Madrid. I would like to sincerely thank them for graciously hosting me at UPM during the summer of 2009 and for their technical input towards improving my work. I would like to thank Prof. William Curtin and Dr. Srinath Chakravarthy for hosting me at Brown university in December 2008 and providing the source code for their fast multipole routines.

Financial support I received from the Department of Aerospace Engineering, the National Science Foundation and Lawrence Livermore National Lab, through my advisor, is gratefully acknowledged. Thanks are also due to the members of

the support staff in Aerospace Engineering, particularly Miriam Alderete and Karen Knabe, for their timely assistance. I would like to thank all my friends and well wishers in College Station for their support and encouragement. In particular, I would like to thank Jayashankar C., Suresh Rajendran, P.J. Guruprasad, Chandraveer Singh, Sujay Deshmukh, Madhu K., Xavier Poulain and Babak Kondori for making my stay in College Station a memorable experience. Thanks are also due to the members of SPICMACAY-TAMU for all those wonderful musical evenings. Last but not least, I wish to thank my family for their love, support and prayers. A special thank you to my wife Vidya for supporting me through a challenging period of my academic and personal life.

TABLE OF CONTENTS

CHAPTER Page

CHAPTER Page

CHAPTER Page

LIST OF TABLES

LIST OF FIGURES

FIGURE Page

FIGURE Page

FIGURE Page

FIGURE Page

FIGURE Page

FIGURE Page

FIGURE Page

FIGURE Page

FIGURE Page

FIGURE Page

FIGURE Page

FIGURE Page

FIGURE Page

CHAPTER I

INTRODUCTION

Technologically important materials used in aircraft and spacecraft structures include a host of metallic materials. Examples include Al alloys which are used in most structural components like airframe, fuselage and wings, steel for landing gears and alloys of Ti and Ni for hot engine parts. Since metallic components are being designed to withstand increasingly severe thermal and mechanical loads, while using less material to keep weight and cost down, specific strength is an important requirement for efficient design. Ensuring reliability and safety over the operational life of the aircraft requires a sound design approach that takes into account the plasticity, creep and fatigue characteristics of the materials. Such an approach is also relevant in other fields of engineering where materials are subjected to extreme environments, e.g. design of nuclear reactors against high thermal loads and radiation dosages that lead to high defect concentrations in the material, crashworthy automobile parts, naval vessels that are exposed to corrosive environments and in manufacturing processes like cutting and forming. Besides structural applications, consideration of plasticity and creep are also important for metallic materials used in functional components. Examples include thin films used in a variety of applications such as thermal barrier coatings, flexible electronics and other micro and nano electro-mechanical systems (MEMS/NEMS) [1]. Plasticity and creep are important reliability issues in MEMS devices [2, 3] and metallic components used in electronic applications such as interconnects and packaging [4].

Modeling of inelastic deformation and fracture processes in structural and func-

---

This dissertation follows the style of Philosophical Magazine.

tional materials is a long standing problem in solid mechanics. Most models are phenomenological and there is an increasing effort towards embedding more physics into these models. Some limitations of phenomenological modeling approaches have been exposed by the recent trend towards using novel nanostructured materials, and miniaturization of components. It has long been appreciated that mechanical properties such as strength and hardness depend on internal material length scales such as grain size. Empirical models such as the Hall-Petch relation are widely used to model the observed strengthening. On the other hand, there is mounting experimental evidence in recent literature that indicates that material strength and hardening rates also depend on structural length scales such as the specimen size [5–8]. Traditional continuum models, being size independent, can not naturally account for such effects observed in small scale experiments. The present trend towards micro and nano engineering and use of advanced materials with tailored microstructures in several engineering applications necessitates a new and more fundamental approach to the constitutive modeling of materials taking into account the multi scale nature of the failure processes that operate. Unlike in structural applications, such an approach may even be critical for the successful use of metallic materials in small scale functional components such as in MEMS devices [2].

Ductile materials such as metals are characterized by their ability to dissipate large amounts of mechanical energy before fracture. Material defects across different length scales play a central role in determining key material properties such as strength and toughness. At the nano scale, the nucleation and glide of crystal dislocations on well defined slip systems is a primary toughening mechanism that accounts for the macroscopic plastic flow and energy dissipation. The short range interaction of dislocations such as mutual cutting and pinning at grain boundaries, precipitates and other inhomogeneities leads to strain hardening. On the other hand, crack prop-

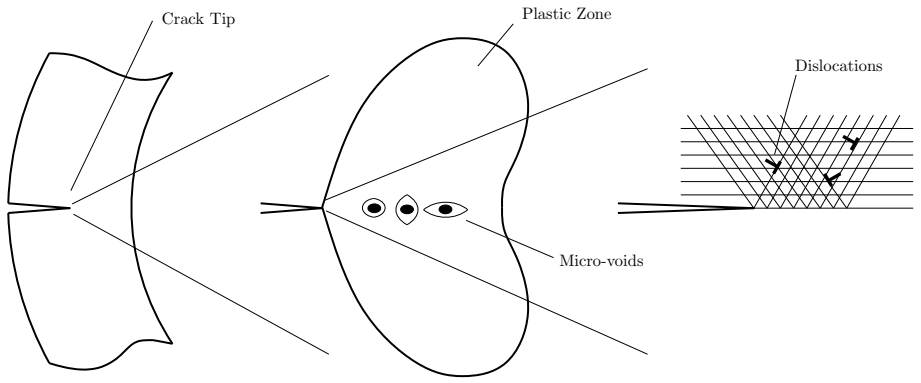

Fig. 1. Schematic diagram of a crack in a ductile material showing the interactions between defects at multiple scales that determine the overall toughness.

agation due to material separation occurs due to the influence of meso-scale defects such as voids which grow and coalesce due to the plastic deformation of the surrounding matrix aided by highly triaxial stress state in the fracture process zone. Hence, fracture in ductile materials is essentially a multi-scale phenomenon involving the generation and interaction of defects across several length scales (see Fig. 1).

Unlike the case of brittle fracture, conventional continuum models have been less successful in modeling fracture in ductile materials due to the fact that plastic dissipation occurs across a multiplicity of length scales during ductile failure as pointed out earlier. This is illustrated in Fig. 2, which shows the results from finite element investigations of Tvergaard and Hutchinson [9] for crack growth under mode I loading in an elastoplastic power law hardening solid. Material separation along the crack plane is modeled using a cohesive zone approach [10]. The figure shows the steady state fracture toughness, Γ_f, as a function of the maximum supportable interface traction, $\hat{\sigma}$. These quantities are normalized by the interface work of separation calculated from the cohesive zone model, Γ_0, and the yield stress of the material, σ_y, respectively. The different curves correspond to different values of the power law hardening exponent N. The results show that the toughness goes to

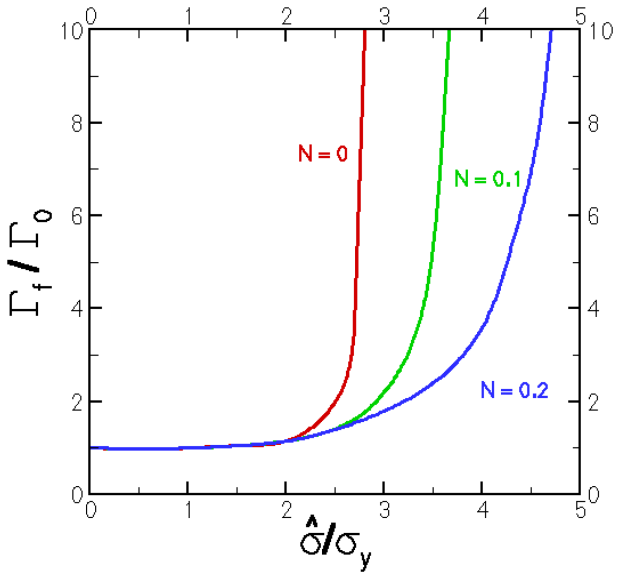

Fig. 2. Predictions from continuum finite element computations for the steady state fracture toughness, Γ_f, normalized by the interface work of separation, Γ_0, as a function of the maximum supportable interface traction, $\hat{\sigma}$, normalized by the material yield stress, σ_y. The material is assumed to be an isotropic elastoplastic power law hardening solid with a hardening exponent, N, and material separation is modeled using a cohesive zone model.

infinity asymptotically as $\hat{\sigma}$ approaches a value of $2.97\sigma_y$ for a non-hardening material ($N = 0$). I.e. crack propagation does not take place for values of $\hat{\sigma}$ larger than about three. Another observation is that increasing the hardening exponent has the effect of reducing the fracture toughness for a given $\hat{\sigma}$, which implies that the plasticity of the material ahead of the crack tip plays an important role in determining the materials' crack growth resistance. Nevertheless, the main message from these results is that, for realistic values of the hardening exponent, continuum plasticity coupled with a cohesive zone fracture model does not predict crack growth for $\hat{\sigma}/\sigma_y > 4$–5, while realistic values for $\hat{\sigma}$ are $10\sigma_y$ or larger. This result illustrates two important points that serve as the motivation for the research undertaken in this dissertation: (i) continuum approaches to fracture mechanics, such as the cohesive zone model, are inadequate to model ductile crack growth and (ii) fracture toughness is sensitive to the plasticity and hardening characteristics of the material. Consequently, there is a need to (i) improve existing ductile fracture models, for example, by incorporating more microstructure information and (ii) develop better approaches to modeling plastic deformation in confined volumes. These issues are addressed respectively in the first and second parts of this dissertation, as detailed below.

Traditional models of ductile fracture have followed a "top-down" approach where continuum mechanics based models containing internal damage variables are used to predict the evolution of damage, while experiments are used to calibrate the deformation characteristics of the material and the statistics of damage initiating sites. The void growth models of Rice and Tracey [11] and Gurson [12] and later extensions of the same fall into the above class of models. The Gurson model in particular [12] has been highly successful in modeling several experimentally observed aspects of ductile fracture such as the cup-cone fracture of a uniaxial tensile specimen [13] and the formation of shear bands under plane-strain conditions [14]. Despite these successes,

the Gurson model suffers from certain well known limitations that stem from the underlying assumptions in the model [15]. First, the model predicts unrealistically high fracture strains in general compared to experiments. Second, the model does not account for plastic strain localization within the elementary volume, which partially explains the high fracture strains due to the fact that coalescence can only take place by mutual impingement of the voids. Third, predictions for plastic flow localization preceding macroscopic crack growth using the Gurson model are inherently mesh dependent due to the lack of an internal length scale in the model [15, 16]. Finally, many of the commonly used models of void nucleation such as [17, 18] are empirically based. Micromechanics–based models of void nucleation such as [19] have not not been developed to the level of sophistication as the void growth models. Some of the above limitations stem from the assumption of isotropy in the Gurson model both in the plastic flow of the matrix and spherically symmetric void growth, which may be violated under low triaxiality loading conditions. At low stress triaxiality with no major shear component, void growth rates are predicted to be faster than obtained through direct micromechanical finite element calculation (which represents the 'exact' reference solution). Under shear dominated loadings, the Gurson model predicts no or little damage growth whereas materials apparently do fail in shear. In the first half of this dissertation, we seek to address the first of the above mentioned limitations by developing a micromechanics based model for void growth that takes into account the anisotropy of the material microstructure due to the texture of the plastically deforming matrix and the evolving shape and orientation of the voids. Large strain finite-element computations on micromechanical unit cells are presented in Chapter II to motivate the need for a fundamental coupling between the two types of material anisotropy, namely the void shape and material texture. In Chapter III, a homogenized constitutive model of anisotropic void growth is developed using non-

linear homogenization theory and limit analysis within a finite strain setting. The model is validated by comparisons with numerically derived upper-bound yield loci for anisotropic materials and with finite-element simulations in Chapter IV.

The other major ingredient required for modeling the mechanical response of ductile metals are theories of plastic deformation and hardening. Several experiments have demonstrated that material properties like flow strength and hardening become size dependent at micron scales and below [5, 6, 20–22]. These results have exposed one of the fundamental limitations of continuum crystal plasticity models, namely the absence of an internal length scale. While several extensions to classical continuum plasticity using constitutive formulations involving strain gradients and higher order stresses have been used to explain some of the observed size effects under imposed macroscopic strain gradients [23, 24], these can not provide adequate rationale for the size effects observed in the absence of specimen level strain gradients. Moreover, the internal length scale used in the gradient formulations remains a heuristic parameter that needs to be fitted with experiment for a given class of problems. On the other hand, the recent availability of powerful computer hardware have enabled the development of "bottom up" modeling frameworks for plasticity by direct simulation of the motion and interaction of discrete dislocations, which are the carriers of plastic deformation at the smallest scale. At the cost of added computational complexity, these dislocation dynamics (DD) frameworks enable the prediction of the material response from constitutive assumptions regarding the motion and interaction of dislocations. More significantly, DD models enable the modeling of size-dependent material response without the need for a heuristic length scale parameter, since the model embeds a physically meaningful length scale in the dislocation Burgers vector. In the second half of this dissertation, a two-dimensional DD model originally developed by Van der Giessen and Needleman [25] and extended by Benzerga et al. [26] is

reviewed. In this model, the long range interactions between the discrete dislocations and specimen boundaries are computed using small strain elasticity theory while their short range interactions are approximated using a set of constitutive rules. Several enhancements to this DD framework are developed in Chapter V that fall into two broad categories: (i) enhancements to the algorithms that allow for efficient treatment of very large dynamical systems, arbitrary multiply connected computational domains and periodic microstructures and (ii) incorporation of dislocation climb aided by bulk vacancy diffusion into the constitutive formulation that enables DD simulations at elevated homologous temperatures. The following applications are chosen to illustrate the above enhancements through the solution of a variety of boundary value problems:

1. Investigation of strain hardening in large dislocation systems with focus on the transition to bulk behavior (Chapter VI).

2. Investigation of void growth in a periodic single crystalline matrix with hardening (Chapter VII).

3. Creep of single crystalline Al specimens at high temperatures under plane strain tension (Chapter VIII).

CHAPTER II

VOID GROWTH AND COALESCENCE IN ANISOTROPIC PLASTIC SOLIDS*

A. Introduction

Ductile fracture in structural materials results from the nucleation, growth and coalescence of micro-voids that initiate from second phase particles and inclusions. Accurate modeling of void growth and coalescence under arbitrary imposed loading conditions is critical to the predictive modeling of ductile fracture. Gurson [12] derived an analytical model of void growth in an *isotropic* medium based on analysis of a spherical representative volume element (RVE) made of an ideal plastic von Mises material and containing a concentric spherical void. The somewhat idealized choice of the RVE geometry was dictated by the complexity of the analytical approach. Alternatively, finite element (FE) calculations of appropriately chosen unit cells subjected to a remote triaxial loading have been used to simulate periodic arrays of voids. Needleman [27] performed a two-dimensional plane-strain analysis of a periodic array of cylindrical voids in an isotropic matrix, while a transverse isotropic distribution of spherical voids in an isotropic matrix was analyzed by Tvergaard [28] and later by Koplik and Needleman [29]. The finite element results were used as benchmarks to calibrate the Gurson model and heuristic corrections were suggested to enhance the quantitative agreement between the model and the cell calculations [13, 28]. Subsequently, three-dimensional investigations of cubic patterns of spherical voids [30, 31] under triaxial loadings have evidenced good agreement with the axisymmetric calculations. In particular, these unit cell computations identified the porosity and the loading triaxiality

*Reprinted with permission from "Void growth and coalescence in anisotropic plastic solids" by Keralavarma, S. M., Hoelscher, S. and Benzerga, A. A., 2011. Int J Solids Struct 48, 1696–1710, Copyright [2011] Elsevier Ltd.

(the ratio of the mean to the von Mises effective stress) as key parameters affecting void growth and coalescence. More recent unit cell analyses of initially spherical voids have also shown some influence of the third invariant of the stress tensor, through the Lode parameter, on void growth and coalescence [32–36]. FE Cell model studies have *de facto* become a major tool in understanding material behavior at intermediate scales and were recently reviewed by Benzerga and Leblond [15], including aspects pertaining to the void nucleation stage.

In recent years, various extensions of the Gurson model have been proposed which account for initial or deformation-induced anisotropies [32, 37–41]. The commonality among these models is that they are based on micromechanical treatments, with homogenization and limit analysis being the theoretical foundation [15]. The performance of the model of Gologanu et al. [38] in predicting void shape effects has been assessed by Sovik and Thaulow [42], and more thoroughly by Pardoen and Hutchinson [43], who used the unit cell model considering initially spheroidal voids in an isotropic matrix. Similarly, Benzerga and Besson [32] carried out a series of unit cell calculations for initially spherical voids embedded in a transversely isotropic matrix. They have shown that their extension of the Gurson model to orthotropic matrices provided a good quantitative prediction of the voided cell results for sufficiently high stress triaxialities.

However, the more general models that combine effects of void shape and plastic anisotropy have not yet been assessed against the voided cell model. Keralavarma and Benzerga [41] presented some preliminary results to motivate their development of a new porous metal plasticity model. Also, their set of calculations focussed on pre-localization void growth. The objective in this chapter is to report on a large set of such calculations, probing the parameter space much beyond the report of Keralavarma and Benzerga [41]. While we offer new findings by means of the voided

cell model, the present results can also serve as reference to calibrate advanced models of ductile fracture. General conditions of transverse isotropy are discussed and used, thus enabling a two-dimensional axisymmetric analysis. Emphasis is laid on the combined effects of void shape and matrix anisotropy on void growth and micro-scale flow localization, the latter setting the stage for void coalescence.

B. Problem Formulation

The void distribution in the plane of transverse isotropy of the matrix is an approximation of a hexagonal arrangement. Such a microstructure may be constructed from an infinite repetition of the unit cell sketched in Fig. 3a. The hatched bands in the figure schematically represent the texture of the matrix. Fig. 3b shows a planar cross section of the unit cell in Fig. 3a. A cylindrical unit cell is taken to approximate this hexagonal arrangement and is sketched in Fig. 3c (front view) and Fig. 3d (top view). The boundaries of the unit cell are constrained to remain straight from considerations of periodicity, in the absence of shear loading, so that the RVE retains its cylindrical shape during the deformation. Exploiting the symmetry of the problem, one only needs to mesh the shaded region in Fig. 3b. Let $(\mathbf{e}_{\mathrm{L}}, \mathbf{e}_{\mathrm{T}}, \mathbf{e}_{\mathrm{S}})$ denote the triad associated with the orthotropy of the matrix. We also define a Cartesian coordinate system $(\mathbf{e}_1, \mathbf{e}_2, \mathbf{e}_3)$ as shown in Fig. 3d where $\mathbf{e}_3$ is aligned with the common axis of the voids. The latter is itself identified with the axis of transverse isotropy of the matrix, i.e. $\mathbf{e}_3 \equiv \mathbf{e}_{\mathrm{S}}$, so that the effective behavior of the unit cell is transversely isotropic, and one may perform axisymmetric calculations.

Our finite element implementation of the voided cell model follows that of Benzerga and Besson [32] using the object oriented code ZeBuLoN [44]. The weak form of the momentum balance for a body undergoing finite deformations in the absence

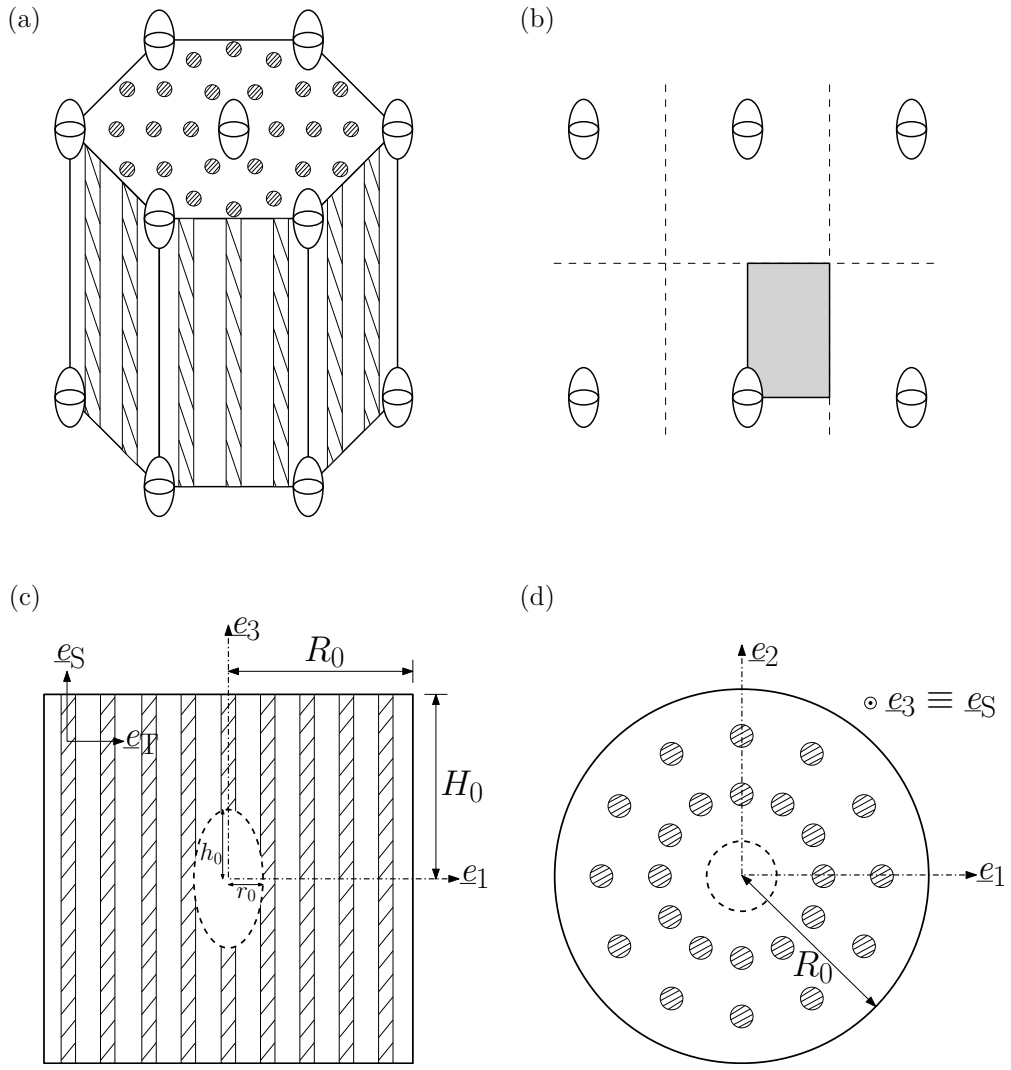

Fig. 3. Idealized representation of microstructure in the voided cell model: (a) hexagonal periodic unit and (b) cross-section in the plane of the paper. Cylindrical unit cell used in the axisymmetric calculations: (c) front view and (d) top view.

of body forces is generally written as

$$\int_V \mathbf{S} : \delta\mathbf{E} \, \mathrm{d}V = \int_S \mathbf{T} \cdot \delta\mathbf{u} \, \mathrm{d}S \tag{2.1}$$

with

$$\mathbf{S} = J\mathbf{F}^{-1} \cdot \boldsymbol{\sigma} \cdot \mathbf{F}^{-\mathrm{T}}, \qquad \mathbf{E} = \frac{1}{2}(\mathbf{F}^{\mathrm{T}} \cdot \mathbf{F} - \mathbf{I}) \tag{2.2}$$

where $\mathbf{S}$ is the symmetric second Piola-Kirchoff stress tensor, $\mathbf{E}$ is the Green-Lagrange strain, $\mathbf{F}$ is the deformation gradient, $J = \det(\mathbf{F})$, $\mathbf{I}$ is the second-order identity tensor, $\boldsymbol{\sigma}$ is the Cauchy stress, $\mathbf{T}$ is the surface traction in the reference configuration, $\mathbf{u}$ is the displacement vector and V and S are respectively the volume and surface of the body in the reference configuration. An updated Lagrangian formulation is used [45, 46] which employs objective space frames with the reference configuration being chosen at the end of the increment so that the stress measure $\mathbf{S}$ reduces to the Cauchy stress.

The material constitutive model is assumed to be that of a rate-independent elastically isotropic and plastically anisotropic solid. In the objective frame, the deformation rate tensor is written as the sum of an elastic part, $\mathbf{d}^{\mathrm{e}}$, and a plastic part, $\mathbf{d}^{\mathrm{p}}$. Assuming small elastic strains and isotropic elasticity, a hypo-elastic law is expressed in terms of the rotated stress $\mathbf{P}$

$$\mathbf{d}^{\mathrm{e}} = \mathbb{C}^{-1} : \dot{\mathbf{P}}, \qquad \mathbf{P} = J\mathbf{R}^{\mathrm{T}} \cdot \boldsymbol{\sigma} \cdot \mathbf{R} \tag{2.3}$$

where $\mathbb{C}$ is the rotated tensor of elastic modulii and $\mathbf{R}$ is the skew-symmetric tensor obtained from the polar decomposition of the deformation gradient, so that the Green-Naghdi rate of $\boldsymbol{\sigma}$ is used. The plastic part of the deformation rate $\mathbf{d}^{\mathrm{p}}$ is obtained by normality from an orthotropic yield function of the Hill type [47], $\mathcal{F}(\boldsymbol{\sigma})$.

$$\mathbf{d}^{\mathrm{p}} = \Lambda \frac{\partial \mathcal{F}}{\partial \boldsymbol{\sigma}}, \qquad \mathcal{F}(\boldsymbol{\sigma}) = \frac{3}{2}\boldsymbol{\sigma} : \mathbb{p} : \boldsymbol{\sigma} - \bar{\sigma} = \frac{3}{2}\boldsymbol{\sigma}' : \mathbb{h} : \boldsymbol{\sigma}' - \bar{\sigma} \tag{2.4}$$

where Λ is the plastic multiplier, $\boldsymbol{\sigma}' = \boldsymbol{\sigma} - \frac{1}{3}\mathrm{tr}(\boldsymbol{\sigma})\mathbf{I}$ is the stress deviator, $\mathbb{p}$ is the Hill anisotropy tensor [47], $\mathbb{h}$ is the anisotropy tensor in the space of deviatoric stresses (related to $\mathbb{p}$ through $\mathbb{p} = \mathbb{J} : \mathbb{h} : \mathbb{J}$ where $\mathbb{J} = \mathbb{I} - \frac{1}{3}\mathbf{I} \otimes \mathbf{I}$ is the deviatoric projector, $\mathbb{I}$ being the 4th order identity tensor; see [32]). Also, $\bar{\sigma}$ is the flow stress in an arbitrarily chosen reference direction. An isotropic power law hardening model is assumed, of the form

$$\bar{\sigma}(p) = \sigma_{\mathrm{S}} \left(\frac{p}{\epsilon_0} + 1 \right)^n, \qquad \epsilon_0 = \frac{\sigma_{\mathrm{S}}}{E} \tag{2.5}$$

where p is an effective measure of plastic strain defined to be work conjugate to $\bar{\sigma}$. p is obtained through $p = \int_0^t \dot{p}\, \mathrm{d}t$ with

$$\dot{p} = \sqrt{\frac{2}{3}\mathbf{d}^{\mathrm{p}} : \hat{\mathbb{p}} : \mathbf{d}^{\mathrm{p}}} \tag{2.6}$$

where $\hat{\mathbb{p}}$ is a formal inverse of Hill's tensor $\mathbb{p}$ defined through $\mathbb{p} : \hat{\mathbb{p}} = \hat{\mathbb{p}} : \mathbb{p} = \mathbb{J}$. In (2.5) σ_{S} is the initial matrix yield stress in the axial direction $\mathbf{e}_{\mathrm{S}}$, n is the hardening exponent and E is Young's modulus. A fully implicit time integration procedure was used, based on an iterative Newton-Raphson method, and the consistent tangent matrix was obtained following [48].

Traction-free boundary conditions are imposed on the surface of the void while symmetry conditions are imposed on the bottom and left boundaries of the cell quadrant (Fig. 3b). Special boundary conditions are formulated whereby the displacement of the top surface is incremented at a constant rate while the displacements of the lateral boundary are iteratively adjusted to maintain a constant stress triaxiality ratio at every step of the deformation. The principal components of the macroscopic stress tensor, $\boldsymbol{\Sigma}$, are obtained by integrating the surface tractions along the external cell boundary such that

$$\Sigma_{11} = \Sigma_{22} = \frac{R_0}{RH} \int_0^{H_0} [T_1]_{X_1^2 + X_2^2 = R_0}\, \mathrm{d}X_3, \qquad \Sigma_{33} = \frac{2}{R^2} \int_0^{R_0} [T_3]_{X_3 = H_0}\, X_1 \mathrm{d}X_1 \tag{2.7}$$

where X_i are the components of the position vector $\mathbf{X}$ in the initial configuration, R and H are respectively the radius and half the height of the unit cell in the current configuration and R_0 and H_0 are the corresponding quantities in the reference configuration (see Fig. 3c). The principal components of the macroscopic strain tensor, $\mathbf{E}$, for the unit cell are written as

$$E_{11} = E_{22} = \log \frac{R}{R_0}, \qquad E_{33} = \log \frac{H}{H_0} \tag{2.8}$$

We consider remote axisymmetric loadings of the type $\mathbf{\Sigma} = \Sigma_{11}(\mathbf{e}_1 \otimes \mathbf{e}_1 + \mathbf{e}_2 \otimes \mathbf{e}_2) + \Sigma_{33}\mathbf{e}_3 \otimes \mathbf{e}_3$. The stress triaxiality ratio, T, is related to the ratio of radial to axial stresses, θ, through

$$T \equiv \frac{\Sigma_{\mathrm{m}}}{\Sigma_{\mathrm{e}}} = \frac{1}{3}\frac{2\theta + 1}{|1 - \theta|}, \qquad \theta \equiv \frac{\Sigma_{11}}{\Sigma_{33}} \tag{2.9}$$

where Σ_{m} and Σ_{e} denote the mean and von Mises effective macroscopic stresses, respectively given by

$$\Sigma_{\mathrm{m}} = \frac{1}{3}\mathrm{tr}(\mathbf{\Sigma}) = \frac{2\Sigma_{11} + \Sigma_{33}}{3}, \qquad \Sigma_{\mathrm{e}} = \sqrt{\frac{3}{2}\mathbf{\Sigma}' : \mathbf{\Sigma}'} = |\Sigma_{33} - \Sigma_{11}| \tag{2.10}$$

Each value of T is generally associated with two distinct values of θ corresponding to a major axial stress ($\theta < 1$) and a major radial stress ($\theta > 1$). In this study we restrict our attention to cases of major axial stress ($\theta < 1$). Each calculation is carried out under conditions of a constant imposed triaxiality (proportional loading path). We investigate the material response under moderate ($T = 1$) to high ($T = 2, 3$) values of the stress triaxiality as are prevalent in notched bars or in the plastic zone ahead of a blunted crack tip. An effective strain measure work conjugate to Σ_{e} is given by

$$E_{\mathrm{e}} = \frac{2}{3}|E_{33} - E_{11}| \tag{2.11}$$

The effective stress and strain measures defined above are used to compare the stress–strain responses of the unit cells in all the results presented here.

In the frame of material orthotropy, the anisotropy tensor $\mathbb{h}$ in (2.4) is represented thanks to Voigt's reduction by a diagonal 6×6 matrix whose diagonal elements, designated $h_{\mathrm{L}}, h_{\mathrm{T}}, h_{\mathrm{S}}, h_{\mathrm{TS}}, h_{\mathrm{SL}}, h_{\mathrm{LT}}$, completely characterize the orthotropy of the matrix. An extensive tabulation of the available experimental data on the Hill coefficients of structural metals was provided in [49]. Here, we restrict our attention to transversely isotropic materials subjected to axisymmetric loading aligned with the axis of material symmetry, taken to be $\mathbf{e}_{\mathrm{S}}$. The requirement of transverse isotropy about $\mathbf{e}_{\mathrm{S}}$ further entails that $h_{\mathrm{L}} = h_{\mathrm{T}} = h_{\mathrm{LT}}$ and $h_{\mathrm{TS}} = h_{\mathrm{SL}}$ since the directions $\mathbf{e}_{\mathrm{L}}$ and $\mathbf{e}_{\mathrm{T}}$ are equivalent.

In this chapter we investigate five different material categories, including the isotropic case, Table I. The Hill coefficients in Table I are chosen to span the experimental ranges of values tabulated in [49] (see Annexe-A-V). Materials (ib) and (iib) are variants of material categories (i) and (ii) previously employed by [32] with lower values of the out-of-plane "shear" Hill coefficients $h_{\mathrm{TS}} = h_{\mathrm{SL}}$. Material categories (i) and (ii) have relatively high values of the shear Hill coefficients $h_{\mathrm{TS}}(= h_{\mathrm{SL}})$ compared to the isotropic case making them weaker under shear than under tensile loading in the principal directions. The opposite is true for material categories (iii) and (iv). In addition, materials (ib) and (iii) have equal yield strengths in tension (EYT) along the principal directions. This is not the case for the other materials, which are assumed to have the same yield stresses as the isotropic material along $\mathbf{e}_{\mathrm{L}}$ and $\mathbf{e}_{\mathrm{T}}$ while being softer (material (iib)) or harder (material (iv)) in tension along $\mathbf{e}_{\mathrm{S}}$. Material categories (ii) and (iv) are closer to realistic material parameters as tabulated in [49]. However, categories (i) and (iii) were chosen for ease of interpretation of the results, as will be shown below. In another set of calculations, the coefficient $h_{\mathrm{TS}}(= h_{\mathrm{SL}})$ is systematically varied in the case of material category (iii).

Besides the Hill anisotropy factors for the matrix, the microstructure in the cell

Table I. The five matrix material categories and corresponding anisotropy parameters used in the unit cell calculations. Coefficients h_i ($i = \mathrm{L, T, S, TS, SL, LT}$) represent the diagonal elements of the Voigt representation of anisotropy tensor $\mathbb{h}$, expressed in the frame of material orthotropy, and h is a scalar invariant of $\mathbb{h}$ defined in equation (2.14). Wider ranges of variation of h_{TS} were also reported.

Material	h_{L}	h_{T}	h_{S}	h_{TS}	h_{SL}	h_{LT}	Notes		h
Isotropic	1.000	1.000	1.000	1.000	1.000	1.000	reference	EYT	2.000
(ib)	1.000	1.000	1.000	2.333	2.333	1.000	weak in shear	EYT	1.757
(iib)	0.667	0.667	1.167	1.750	1.750	0.667	weak in shear	S-soft	2.028
(iii)	1.000	1.000	1.000	0.500	0.500	1.000	shear resistant	EYT	2.366
(iv)	2.333	2.333	0.333	1.000	1.000	2.333	shear resistant	S-hard	1.757

model is completely specified by three dimensionless parameters: the void volume fraction, f, the void aspect ratio, w, representing the average void shape and the cell aspect ratio, λ, representing the anisotropy in void distribution. These are defined by

$$f = \frac{2r^2 h}{3R^2 H}, \qquad w = \frac{h}{r}, \qquad \lambda = \frac{H}{R} \tag{2.12}$$

where r and h respectively denote the radial and axial semi-axes of the void in the current configuration (Fig. 3c). The ranges of all the parameters being explored in this study are tabulated in Table II. Unlike the Hill coefficients, the values of these microstructural variables evolve during deformation. A subscript 0 is used in the remainder of this chapter to indicate values in the undeformed configuration. The case $w_0 = 1/30$ corresponds to a penny-shaped crack and other values of 1/10 and 1/20 were used in probing limit behavior. The value of the strain hardening exponent n is taken to be 0.1 in all calculations.

Typical meshes employed in this study are shown in Fig. 4. Since the meshes

Table II. Ranges of initial microstructural and loading parameters considered in the unit cell calculations. * Requires special choice of porosity as discussed in Section 4.

Parameter	Values Used
f_0	0.0001, 0.001
w_0	1/30*, 1/6, 1/2, 1, 2, 6
λ_0	1
T	1, 2, 3

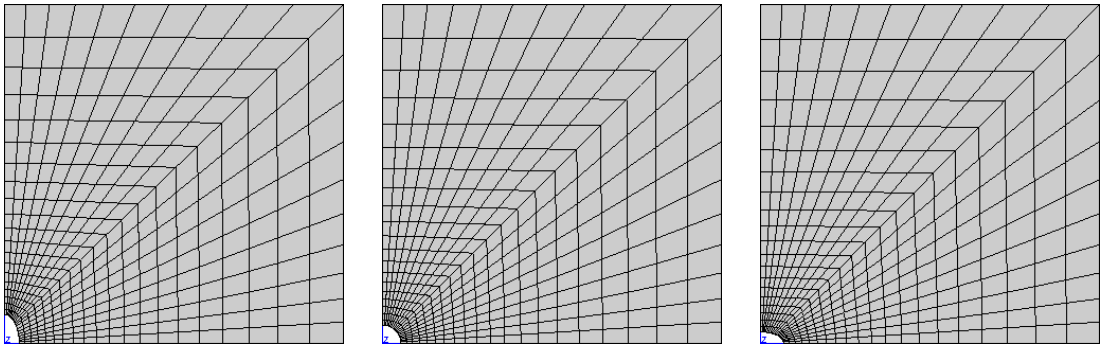

(a) (b) (c)

Fig. 4. FE meshes used in some calculations corresponding to $f_0 = 0.0001, \lambda_0 = 1$ and (a) $w_0 = 2$, (b) $w_0 = 1$, (c) $w_0 = 1/2$.

undergo significant elongation in the axial direction due to the influence of the major axial stress, initially flat elements are used in the expected necking zone (the ligament separating the voids in the radial direction) using appropriate grading of the edge nodes. In most calculations void coalescence took place by strain localization along the radial ligament, for which meshes of the type shown in Fig. 4 were used. However, certain types of material anisotropy were observed to promote strain localization away from the radial direction. For materials that exhibited this trend, we have used alternate (finer) meshes with a uniform element density throughout the domain so as to capture better the details of the localization band.

C. Results

1. Basic Phenomenology

The deformation of the unit cell under axisymmetric loading exhibits two distinct stages: (i) void growth aided by diffuse plastic deformation in the matrix and (ii) void growth through localization of plastic deformation in the inter-void ligament, leading to void coalescence. These stages are illustrated in Fig. 5. The transition between them, which is indicated with the $\times$ mark, is referred to as the *onset* of void coalescence. The latter is a continuous process occurring over a narrow strain window but rather large windows of stress and porosity. Fig. 5a shows the effective stress–strain response for a unit cell containing an initially spherical void in an isotropic matrix, subjected to a stress triaxiality ratio $T = 2$. Here, and in all subsequent stress–strain plots, the effective stress is normalized by $\sigma_{\rm S}$; see equation (2.5). The onset of coalescence is accompanied by a rapid drop in the stress carrying capacity of the unit cell. As discussed by Koplik and Needleman [29], the transition from the void growth to the coalescence stage may be discerned by a transition from a triaxial

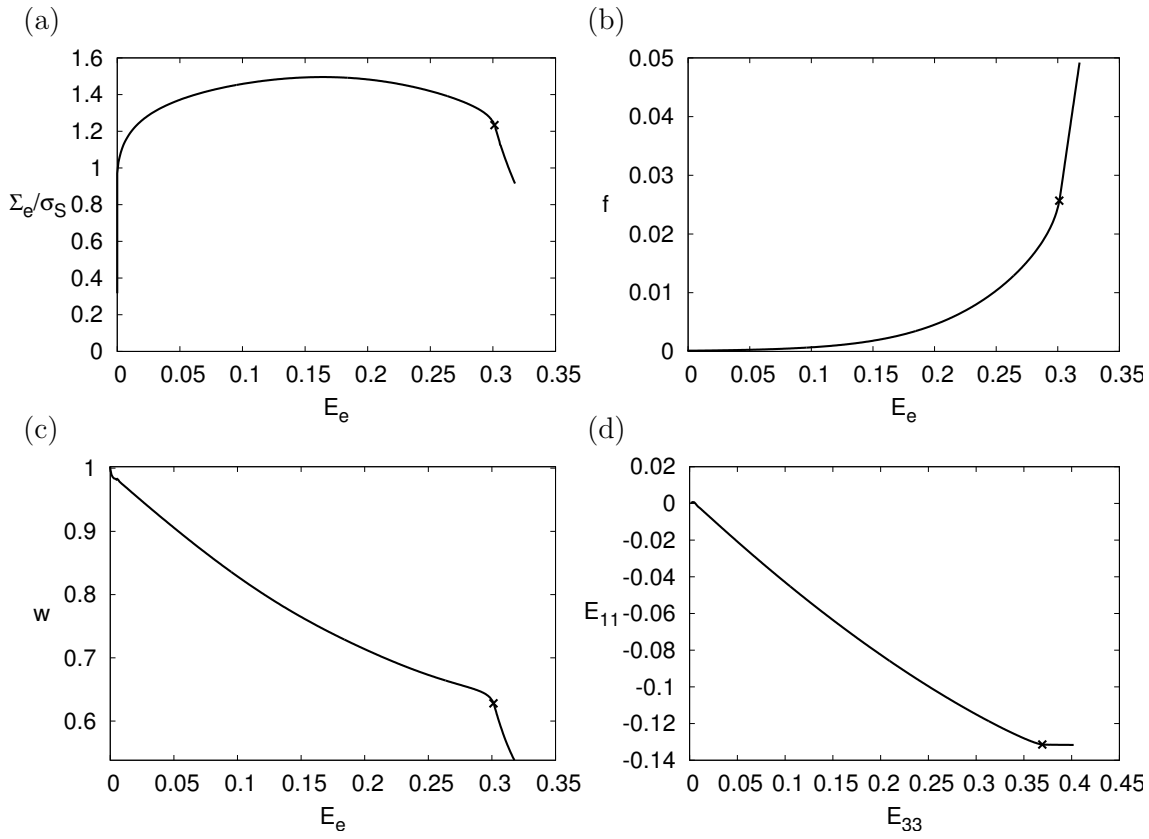

Fig. 5. A typical emergent behavior in a cell model calculation for an initially spherical void in an isotropic matrix using $f_0 = 0.0001$, $\lambda_0 = 1$ and $T = 2$. (a) Effective stress–strain response. (b) Evolution of porosity. (c) Evolution of void aspect ratio. (d) Radial strain E_{11} versus axial strain E_{33}. The $\times$ mark on each curve indicates the onset of coalescence.

to a uniaxial mode of deformation for the cell, i.e. the cell deforms uniaxially in the $\mathbf{e}_3$ direction while plasticity localizes to the intervoid ligament along the radial direction. This behavior is clearly seen in Fig. 5d. The stage of micro-scale localization (past the the $\times$ mark) is also accompanied by an accelerated growth of porosity (Fig. 5b) and a rapid drop in the void aspect ratio (Fig. 5c) due to the lateral void expansion during ligament necking. The void volume fraction (or porosity f) is accurately estimated from the overall volumetric expansion of the cell using the plastic incompressibility property of the matrix. However, the void aspect ratio w, as defined in (2.12) and shown in Fig. 5c and subsequent figures, describes the actual void shape only approximately. Under certain circumstances, such as in the post-localization stage, the void shape may substantially deviate from a spheroid so that w alone no longer characterizes the true void shape accurately.

In what follows, the effective strain to coalescence, $E^{(c)}$, and the void volume fraction at the onset of coalescence, $f^{(c)}$, are defined as the values taken by E_e and f at the onset of micro-scale localization. These measures will be used to compare the various cases as we explore the parameter space.

2. Regime of High Triaxiality

We first consider the high triaxiality case due to its importance in crack growth studies. The stress triaxiality prevailing in the crack tip plastic zones of thick specimens is typically in the range $2-3$. A highly triaxial stress state significantly enhances void growth since the rate of porosity growth has a well known exponential dependence on the mean normal stress prior to localization. Fig. 6 shows results for $T=2$ and three EYT matrix materials: isotropic, material (ib) and material (iii) from Table I. EYT materials have equal yield stresses in the three principal directions of orthotropy, and this leads to roughly similar values for the effective yield stresses (see Fig. 6a). This is

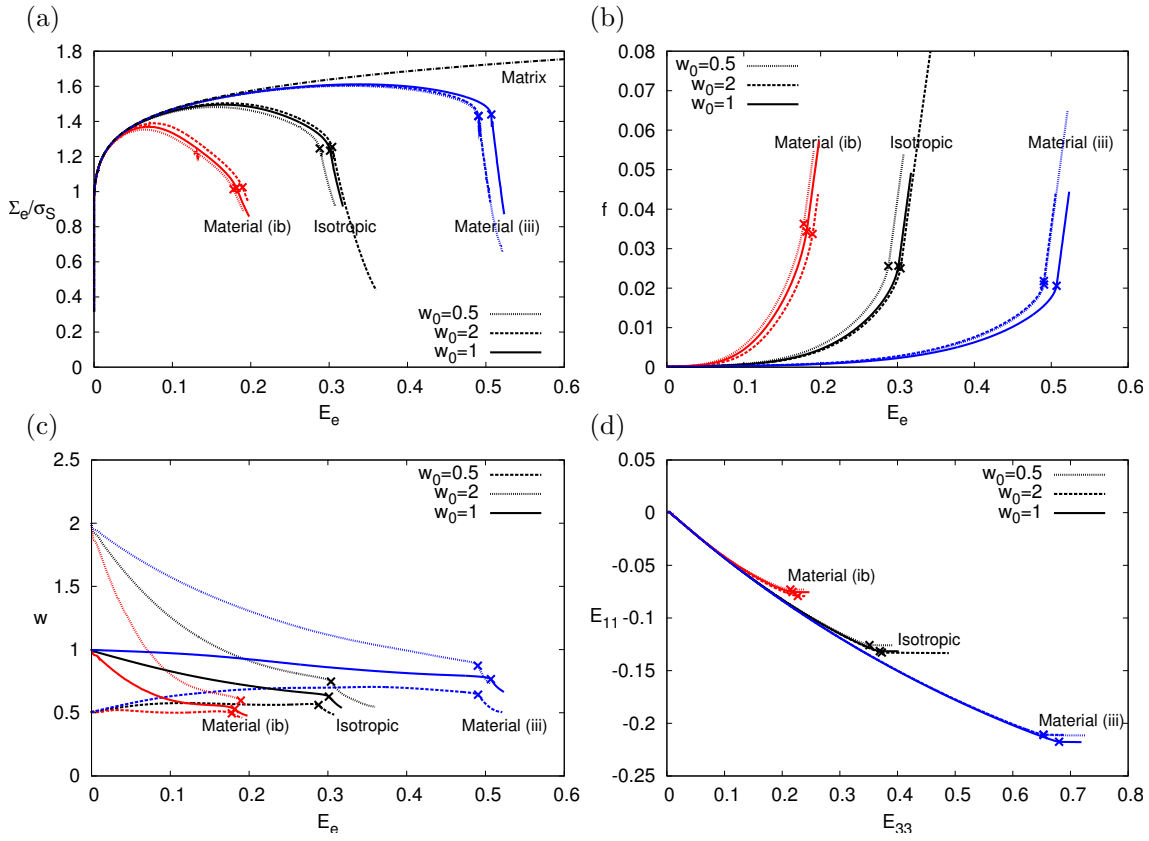

Fig. 6. Effect of matrix material anisotropy on the cell model response for $f_0 = 0.0001$, $\lambda_0 = 1$, $T = 2$ and three values of w_0. Case of EYT (equal yield in tension) materials (Table I). (a) Effective stress–strain response, (b) evolution of porosity, (c) evolution of the void aspect ratio and (d) radial strain E_{11} vs. axial strain E_{33}.

desirable in drawing comparisons, since the porosity rate has an exponential dependence on the mean stress. In particular, any differences in the porosity rates between the three materials (at least in the initial hardening regime) would result from differences in void shapes and Hill anisotropy parameters and not from the different stress levels. Materials (ib) and (iii) are differentiated only by the values of the "shear" Hill coefficients $h_{\mathrm{TS}} = h_{\mathrm{SL}}$ with material (ib) having a lower yield stress under shear in the T-S plane than the isotropic material and material (iii) having a higher shear yield stress than the isotropic material. For each material, three different initial void shapes, $w_0 = 2$ (prolate), $w_0 = 1$ (spherical) and $w_0 = 1/2$ (oblate) are compared. The stress–strain response of the dense matrix ($f \equiv 0$) is also shown as a reference. All calculations were continued beyond the onset of coalescence (Fig. 6d).

The results in Fig. 6 clearly indicate a strong effect of matrix material anisotropy on void growth and coalescence thus affecting the gradual loss of stress bearing capacity of the porous material. On the other hand, the initial void shape has a minor effect at the triaxiality level considered here. Further, unit cells made of material (ib) are seen to have the highest rates of void growth and lowest ductility (Fig. 6b) along with an accelerated void growth in the lateral direction (note the faster drop in w with increasing E_{e} in Fig. 6c) On the other hand, material (iii) exhibits the slowest rate of void growth and the highest ductility.

Similar trends are shown in Fig. 7 for a loading triaxiality $T = 3$ with the effect of void shape becoming even less noticeable, especially for materials (ib) and the isotropic matrix. Notice that the effective strain to coalescence is much lower at $T = 3$ as compared to $T = 2$ for each material, due to the accelerated void growth resulting from the higher mean normal stresses. Figs. 8a-c show the contours of the matrix effective plastic strain, p, for the three materials at the same unit cell effective strain. Material (ib) shows the maximum void enlargement, consistent with the results in

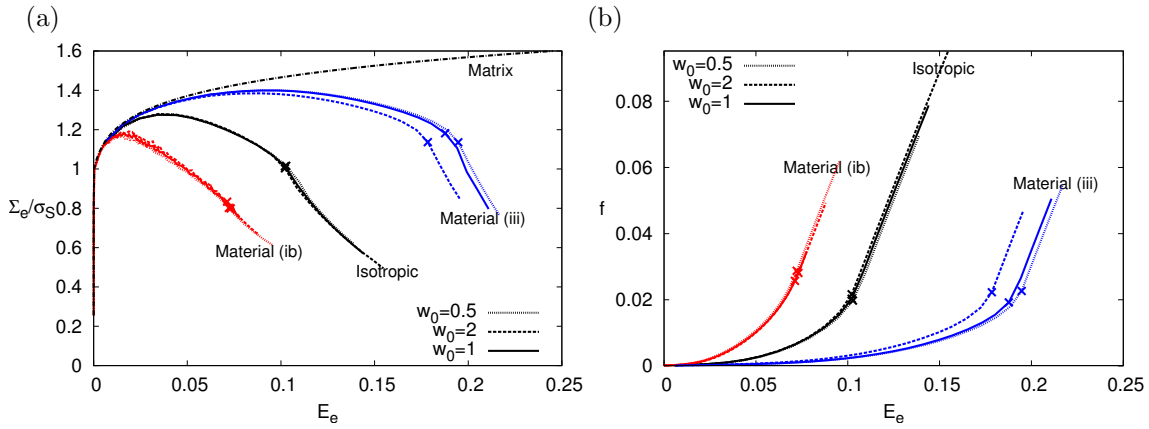

Fig. 7. Effect of matrix material anisotropy on the cell model response for $f_0 = 0.0001$, $\lambda_0 = 1$, $T = 3$ and three values of w_0. Case of EYT (equal yield in tension) materials (Table I). (a) Effective stress–strain response, (b) evolution of porosity.

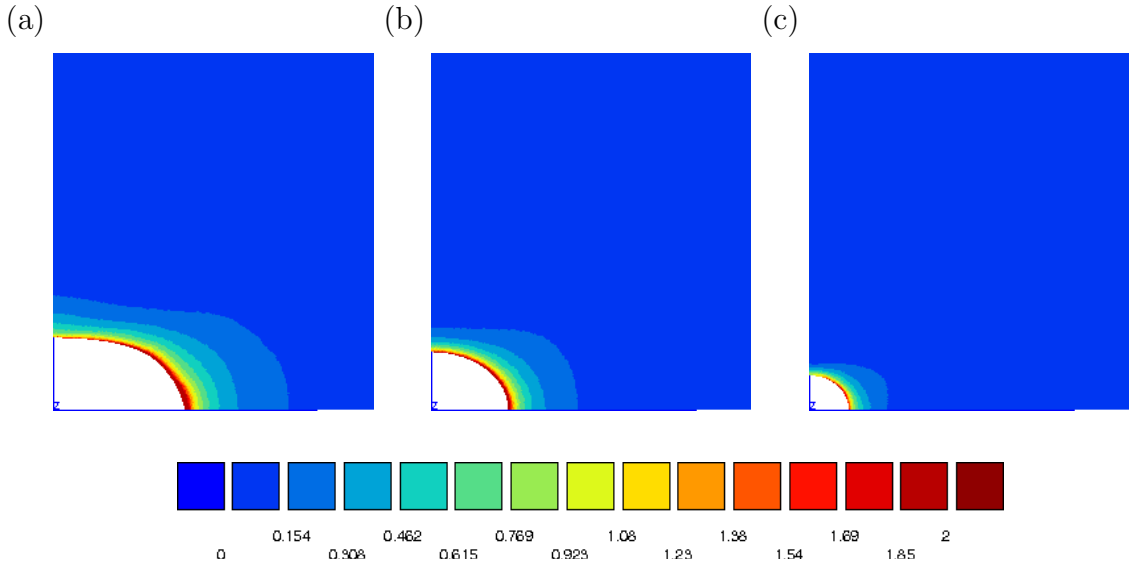

Fig. 8. Contours of effective plastic strain p in the current configuration at a unit cell effective strain $E_e = 0.07$ for initially spherical voids with $f_0 = 0.0001$, $\lambda_0 = 1$ and $T = 3$: (a) material (ib), (b) isotropic material and (c) material (iii).

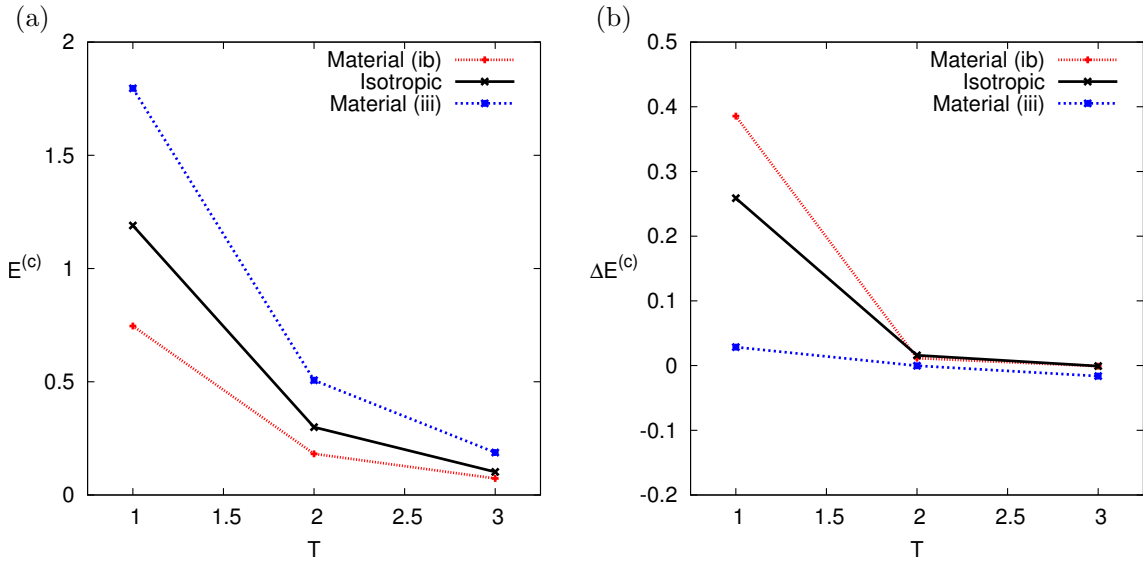

Fig. 9. Variation of (a) the effective strain to coalescence, $E^{(c)}$, for spherical voids and (b) the void shape sensitivity parameter $\Delta E^{(c)}$ as a function of triaxiality T.

Fig. 7b. Note that the voids develop into oblate shapes although the major load is axial. This typically nonlinear effect is visible for the isotropic material and is more clear for material (ib). In fact the void configuration in the case of material (ib) is very close to the critical configuration for the onset of coalescence while material (iii) shows the least void growth. Finally, we note that in all the calculations at high T ($T \geq 2$) coalescence occurred by necking of the inter-void ligament in the radial direction.

Fig. 9 summarizes our results for EYT materials in the range of triaxiality $T = 1$ to $T = 3$ and for an initial porosity $f_0 = 0.0001$. Fig. 9a shows the effective strain to coalescence, $E^{(c)}$, for initially spherical voids as a function of the loading triaxiality. Material (iii) systematically exhibits higher coalescence strains as compared to an isotropic material while material (ib) exhibits lower ductility than the isotropic material for all values of T considered. While there is an apparent reduction in the ductility difference between the three materials at higher triaxialities, the relative

differences are nevertheless significant, as already shown in Figs. 6 and 7.

To quantify the effect of the initial void shape for a given matrix material, we define an *ad hoc* void shape sensitivity parameter, $\Delta E^{(c)}$, by

$$\Delta E^{(c)} \equiv E^{(c)}_{w_0=2} - E^{(c)}_{w_0=1/2} \tag{2.13}$$

i.e. the difference in the void coalescence strains between the initially prolate and oblate voids with aspect ratios 2 and 1/2 respectively. Fig. 9b shows the variation of $\Delta E^{(c)}$ as a function of T for each EYT material considered. In all cases, $\Delta E^{(c)}$ approaches zero at $T \geq 2$ indicating a reduced sensitivity for the ductility to the initial void shape at high triaxialities. On the other hand, at $T = 1$, the isotropic material and material (ib) show a high sensitivity to the initial void shape while material (iii) shows a low void shape sensitivity.

One conclusion that already emerges from this work is that while the effect of void shape vanishes at high stress triaxiality, that of material anisotropy persists. Another emergent behavior is that certain forms of matrix material anisotropy (namely shear-resistant materials of category (iii)) seem to render the effect of void shape less relevant, even at moderate triaxiality. This indicates a strong coupling between void shape effects and material anisotropy. This issue is examined in greater detail in the following section.

3. Regime of Moderate Triaxiality

The effect of void shape on the unit cell response at $T = 1$ and in the case of an isotropic matrix is illustrated in Fig. 10. In this section, $\lambda_0 = 1$ as above and, unless otherwise noted, the initial porosity is $f_0 = 0.001$. Unlike at high triaxialities, the initial void shape has a clear effect on both the evolution of porosity and the strains to coalescence. This is in keeping with the trends seen in previous investigations focused

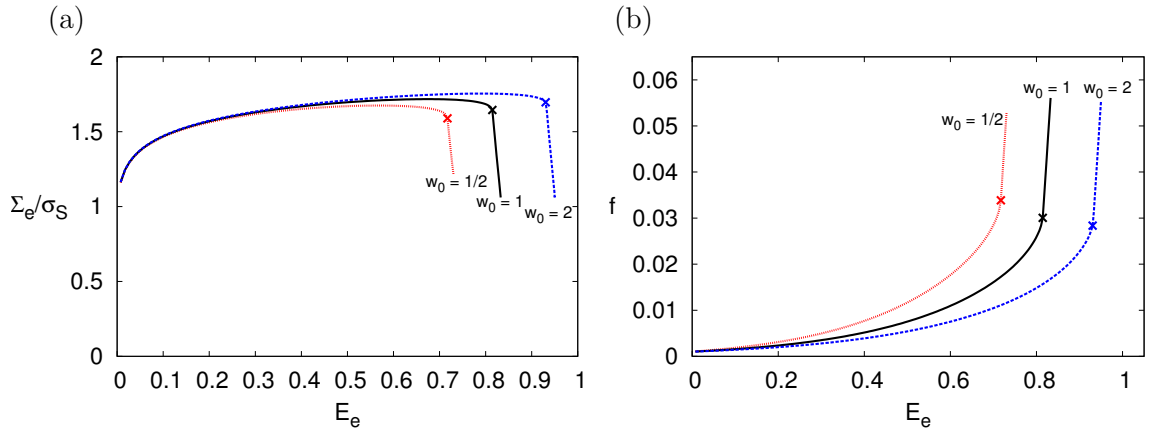

Fig. 10. Effect of initial void aspect ratio on the effective response of porous unit cells for an isotropic matrix, $f_0 = 0.001$, $\lambda_0 = 1$ and $T = 1$: (a) effective stress–strain response, (b) evolution of porosity.

on isotropic materials [43].

At the same moderate triaxiality ($T = 1$), the effect of matrix material anisotropy is illustrated in Fig. 11 for initially spherical voids. As above, focus is restricted to EYT materials, Table I. The conditions are identical to those previously analyzed by Benzerga and Besson [32] except that the present calculations were pursued beyond the onset of void coalescence. Just like at high triaxialities, material anisotropy significantly affects both the flow stress and the strains to coalescence. Comparison of the two sets of results above shows that, in an isotropic matrix, the effective strains to coalescence range from 0.7 to 0.9 for initially oblate and prolate voids, respectively, (Fig. 10) while the range is from 0.6 to 1.2 for the three anisotropic materials considered in Fig. 11. This indicates that at moderate triaxialities both void shape effects and material anisotropy can significantly influence the material response.

In the above analyses, either the initial void shape or the matrix was isotropic. Interestingly, analysis of the combined effect of void shape and material anisotropy

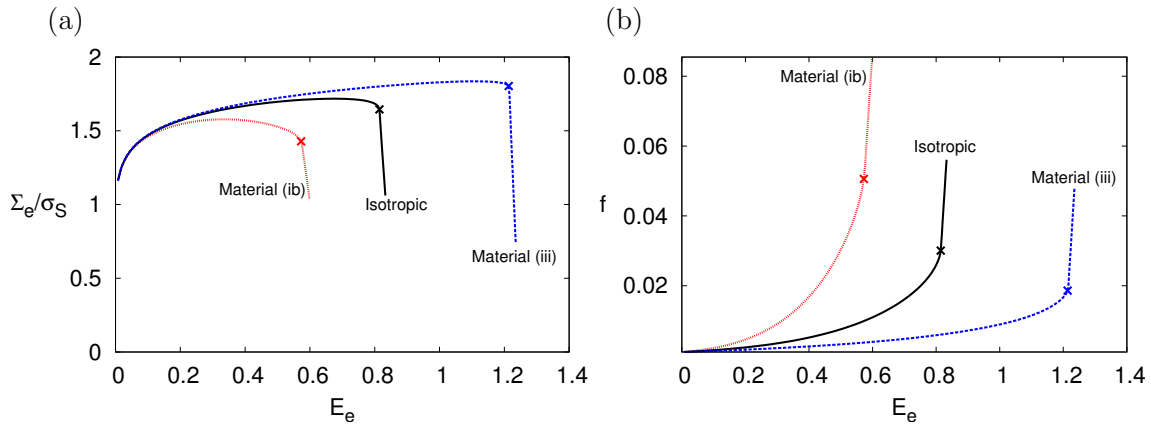

Fig. 11. Effect of matrix plastic anisotropy on the effective response of porous unit cells for EYT materials and spherical voids with $f_0 = 0.001$, $\lambda_0 = 1$ and $T = 1$: (a) effective stress–strain response, (b) evolution of porosity.

at $T = 1$ yields the results depicted in Fig. 12. Four sets of curves are shown which correspond to the cases of initially prolate ($w_0 = 2$) and oblate ($w_0 = 1/2$) voids in unit cells made of EYT materials (ib) and (iii). In the case of material (ib), material anisotropy appears to enhance the effect of initial void shape, while the effect of void shape is completely masked in the case of material (iii) (at least in the range of void shapes considered here). This result is not intuitive from inspection of the individual effects of void shape and material anisotropy in Figs. 10 and 11, respectively, and indicates a non-trivial coupling between the two. This effect is obviously not restricted to the particular conditions chosen here. A similar trend was reported in Fig. 9b for a much lower initial porosity $f_0 = 0.0001$.

In order to further illustrate the subtle coupling between void shape and plastic anisotropy, we examined contours of effective plastic strain in the matrix at a unit cell effective strain $E_e = 0.5$ for initially prolate voids ($w_0 = 2$) in all three EYT materials, Fig. 13. Conclusions from previous investigations of void shape effects [43] had indicated that materials with more elongated voids consistently show higher duc-

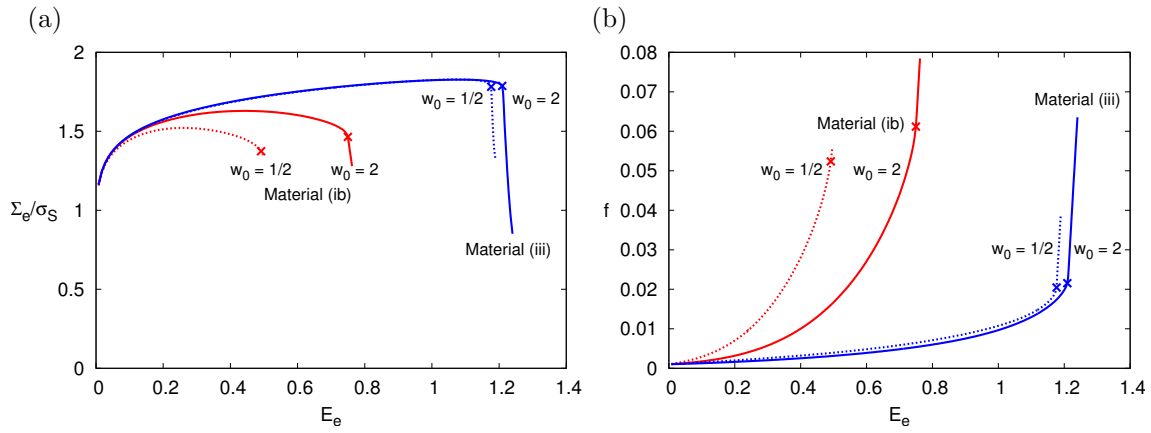

Fig. 12. Combined effect of void shape and matrix plastic anisotropy on the effective response of porous unit cells for EYT materials with $f_0 = 0.001$, $\lambda_0 = 1$, $T = 1$ and two values of the void aspect ratio: (a) effective stress–strain response, (b) evolution of porosity.

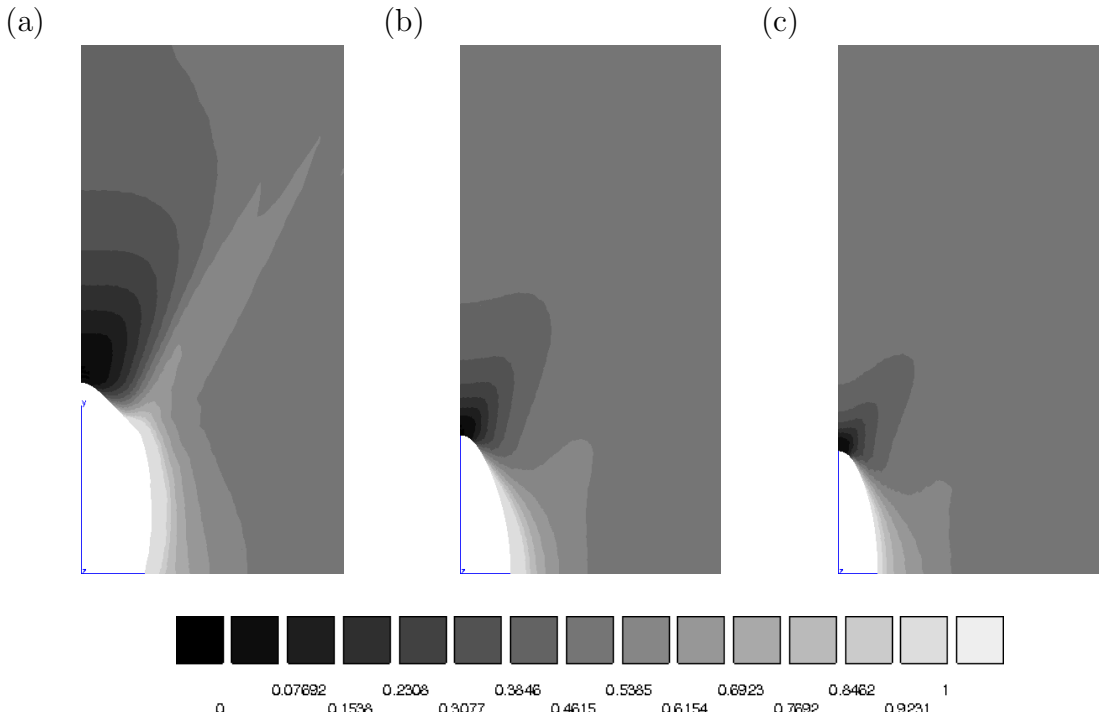

Fig. 13. Contours of effective plastic strain p at $E_e = 0.5$ for initially prolate voids with $f = 0.001$, $w_0 = 2$ and $T = 1$: (a) material (ib), (b) isotropic matrix and (c) material (iii).

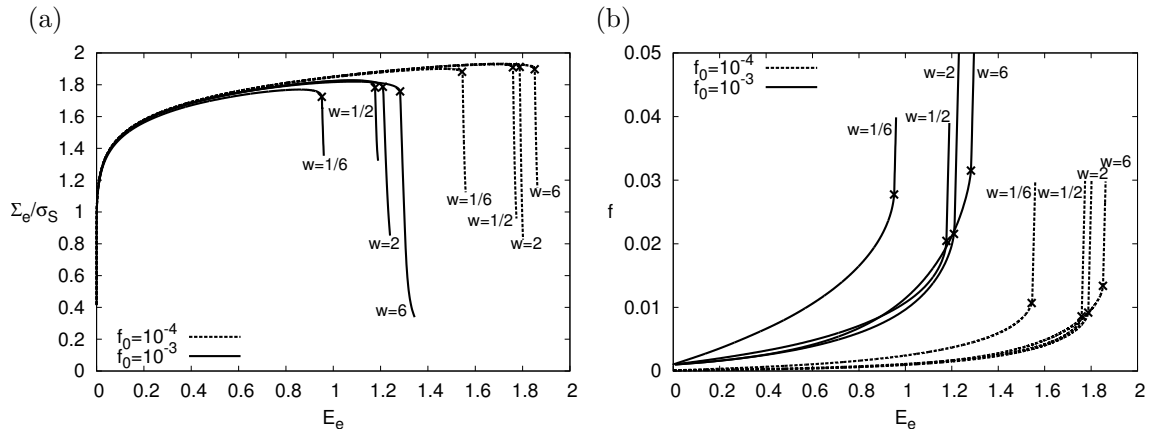

Fig. 14. An elaboration on the results of Fig. 12 for material (iii) over a wider window of initial void aspect ratio w_0 for two values of initial porosity, $\lambda_0 = 1$ and $T = 1$: (a) effective stress–strain response, (b) evolution of porosity.

tility (slower growth of porosity with effective strain). However, further investigation reveals that the evolution of the void aspect ratio for the three unit cells in Fig. 13 (not shown) is roughly similar up to $E_e = 0.5$, as can be seen from the void shapes in Fig. 13. Despite this fact, material (ib) shows greater void growth than the isotropic matrix while material (iii) shows the least void growth at equal macroscopic strain levels. Also, the distribution of plastic strains in the matrix is different for the three materials with material (ib) showing a greater tendency for shear localization along an inclined band, due to its lower yield stresses in shear compared to the other materials.

In materials with enhanced shear-resistance (category (iii)), the effect of initial void shape is found to be negligible within the range $w_0 = 1/2$ to 2 (see Fig. 12 above). We have conducted additional calculations to explore a broader range of void shapes from $w_0 = 1/6$ to 6. The corresponding results are shown in Fig. 14 for two values of the initial porosity. The results show that the strains to coalescence $E^{(c)}$ are not significantly changed for larger values of w_0 (> 2), while flatter voids ($w_0 = 1/6$) lead to a reduction in ductility, although not to the extent expected for isotropic

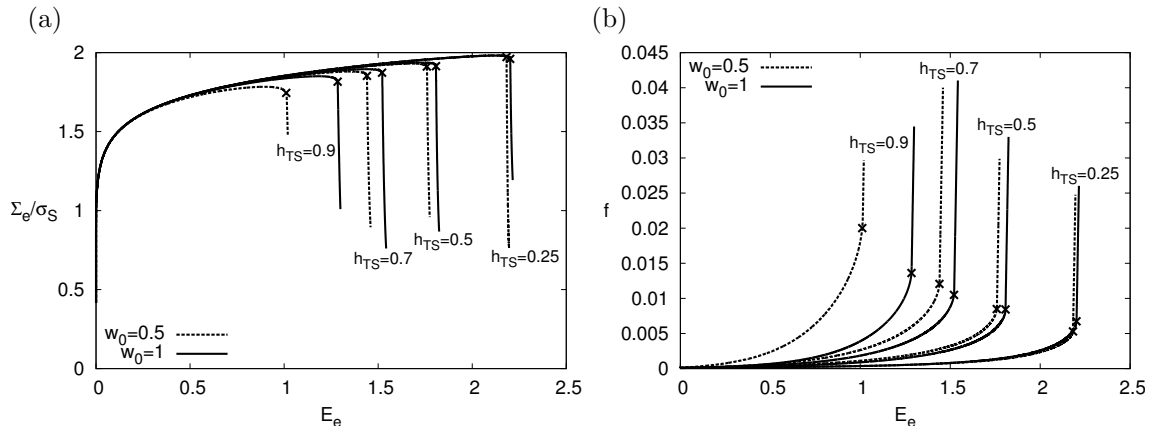

Fig. 15. Transition from a material (i) type behavior to a material (iii) type behavior. Effect of varying the out-of-plane "shear" Hill coefficient, $h_{\rm TS}$, on the effective response of porous unit cells with $f_0 = 0.001$, $\lambda_0 = 1$ and $T = 1$: (a) effective stress–strain response, (b) evolution of porosity.

materials.

Next, for the same category of materials (iii) with enhanced shear resistance, we examine the conditions on the anisotropy parameters that lead to the non-trivial coupling between void shape and matrix flow anisotropy. The difference between an isotropic matrix and material (iii) lies in the values of the shear Hill coefficients, with $h_{\rm TS} = h_{\rm SL} = 0.5$ for material (iii) as opposed to unity for the isotropic material (see Table I). In Fig. 15, we continuously vary the values of $h_{\rm TS}$ between 0.25 and 1 to observe the effect on the void shape sensitivity for the coalescence strains and the growth rate of porosity. Two values of initial void shapes, $w_0 = 1$ and $w_0 = 1/2$, are compared. One can see that a transition occurs approximately at $h_{\rm TS} = 0.5$ below which the difference between the curves corresponding to the two initial void shapes is negligible. Fig. 16 shows the variation of the void shape sensitivity parameter $\Delta E^{(\rm c)}$, defined in equation (2.13), as a function of the Hill coefficients $h_{\rm TS}$. The void shape sensitivity is seen to increase with increasing $h_{\rm TS}$ with an inflexion point around the isotropic value of $h_{\rm TS} = 1$. The void shape sensitivity approaches zero for $h_{\rm TS} < 0.5$

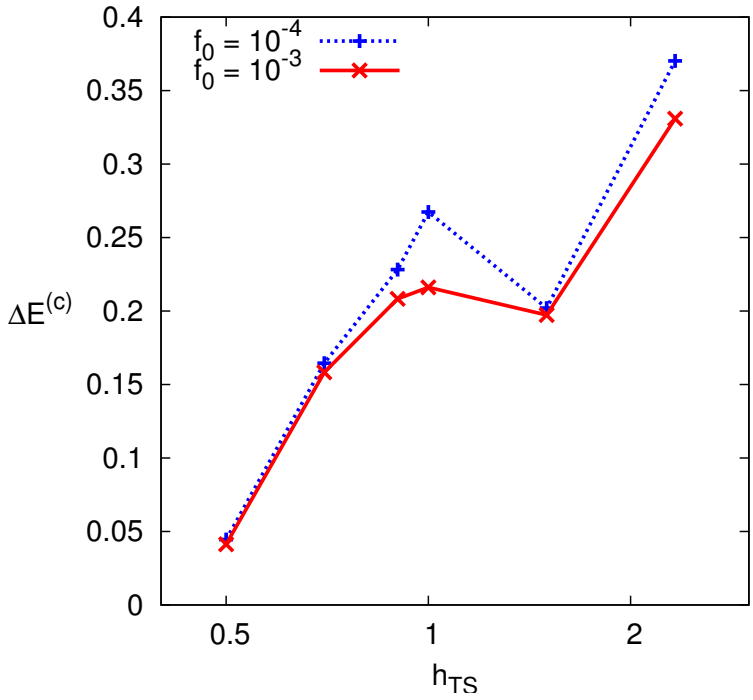

Fig. 16. Variation of the void shape sensitivity parameter $\Delta E^{(c)}$ for a wide range of EYT materials described by the out-of-plane shear Hill coefficient h_{TS}. Matrix materials with $h_{\mathrm{TS}} < 1$ are shear-resistance (type (iii)) and matrices with $h_{\mathrm{TS}} > 1$ are weak in shear (type (i)).

(materials of type (iii)) whereas the void shape sensitivity is seen to be high for $h_{\rm TS} > 2$ (materials of type (i)).

4. Case of Penny Shaped Cracks

The limiting case of highly oblate voids or penny shaped cracks is an important one in practice. Such cracks were observed to initiate in brittle phases in multi-phase materials [50, 51] or simply due to cracking of second phase particles; see the review by Benzerga and Leblond [15]. Lassance et al. [52] carried out a series of cell model studies of penny shaped voids embedded in an isotropic matrix. In this section, we explore amendments to their conclusions when matrix anisotropy is taken into account. Attention is restricted to the same EYT materials investigated above. One issue with using the cell model of Fig. 3 for particle–matrix systems is that it ignores the effect of particles. A useful result in this respect from Lassance et al.'s [52] investigation is that particle shielding is weak for particle volume fractions below 1% or so. We shall rely on this finding to justify the relevance of the voided cell model to particle–matrix material systems, in addition to multi-phase ones.

Three realizations of the penny-shaped crack were investigated using $w_0 = 1/30$, $w_0 = 1/20$ and $w_0 = 1/10$ keeping the same radial void size to void spacing ratio ($\chi_0 = 0.247$). Such initial configurations correspond to different values of the initial porosity but share the same value of the equivalent porosity $f_0^e = 0.01$. Here, f_0^e is defined as the volume fraction of a spherical void having a radius equal to that of the "crack". The actual porosity $f_0 = w_0 f_0^e$ is therefore much smaller. It was found that the response of the unit cell is weakly dependent upon the specific choice of w_0 in the range considered, irrespective of the type of material anisotropy. Thus, we will only present results for $w_0 = 1/20$ focussing on the effect of matrix anisotropy.

Fig. 17 shows the results obtained for a loading triaxiality of $T = 1$ (solid lines).

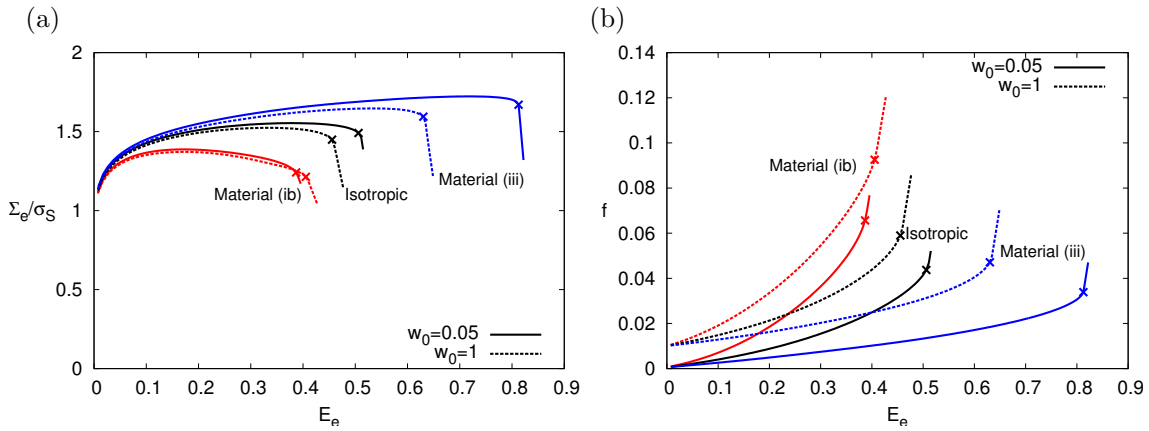

Fig. 17. Effect of matrix plastic anisotropy on the effective response of porous unit cells containing initially penny shaped cracks ($w_0 = 1/20$) with and effective porosity $f_0^e = 0.01$ (solid lines) and spherical voids with $f_0 = 0.01$ (dashed lines), under axisymmetric loading with $T = 1$: (a) effective stress–strain response, (b) evolution of porosity.

These results clearly indicate that the effect of matrix anisotropy is as significant in this limit case of penny shaped cracks as it is for other void shapes. For instance the effective strain to coalescence for material (iii) is about twice as much as for material (ib). This effect was qualitatively expected because the crack quickly blunts in the matrix and opens up into a void with a roughly equiaxed shape.

To interpret further these results, a set of reference calculations were carried out for the equivalent microstructure, i.e., for spherical voids with $f_0 = 0.01 = f_0^e$. The corresponding results are also included in Fig. 17 (dashed lines). An interesting finding in the case of material (iii) is that the response for penny shaped cracks is very different from that obtained for the equivalent spherical voids. This puts into question the very notion of "equivalence". On the other hand, it is noted that the responses for the equivalent and actual microstructures are indeed close to each other in the case of the isotropic matrix and material (ib). It is possible to explain why this equivalence works well for isotropic matrices. In fact, it results from the competing effects of

extremely oblate shape (negative for ductility) and low initial porosity (positive). When the two effects cancel out "equivalence" works. However, deviations from that behavior are conceivable in the presence of large deformation induced microstructure evolution. Such deviations are realized in materials of type (iii) as shown in Fig. 17.

5. Materials with Unequal Principal Yield Strengths

The material anisotropy parameters used in the set of results presented thus far were chosen such that the materials have the same nominal yield stresses in the three principal directions of orthotropy ($h_{\rm L} = h_{\rm T} = h_{\rm S} = 1$). As a consequence, for all such EYT materials the unit cell effective and mean normal stresses are initially equal. Since the evolution of porosity has an exponential dependence on the mean stress, the choice of EYT materials enabled us to apportion the effects of material anisotropy and void shape. However, the case of $h_{\rm L}, h_{\rm T}, h_{\rm S} \neq 1$ is more general and commonly observed experimentally [53]. In this section, we present a set of results for categories of materials with $h_{\rm L} = h_{\rm T} \neq 1$ and $h_{\rm S} \neq 1$.

Fig. 18a shows the comparison of stress–strain responses for unit cells made of an isotropic matrix, material (iib) and material (iv) from Table I. Material (iib) is similar to material (ib) from the previous set of calculations in the sense that they both have relatively high values of the shear Hill coefficients $h_{\rm TS} (= h_{\rm SL})$ compared to the isotropic case making them weaker under shear loading. On the other hand, material (iv) is weaker under tension along the principal directions similar to material (iii) used previously. Three different values of w_0 (= 1/2, 1 and 2) are compared and all the unit cells had $f_0 = 0.001$ and $\lambda_0 = 1$. Each of these materials has the same yield strengths $\sigma_{\rm L} = \sigma_{\rm T}$ in the radial direction but the axial yield strength $\sigma_{\rm S}$ varies for each material. For comparison purposes, the effective stresses in Fig. 18a are normalized by the initial yield stress, $\sigma^{\rm iso}$, of the isotropic matrix. This avoids normalization by

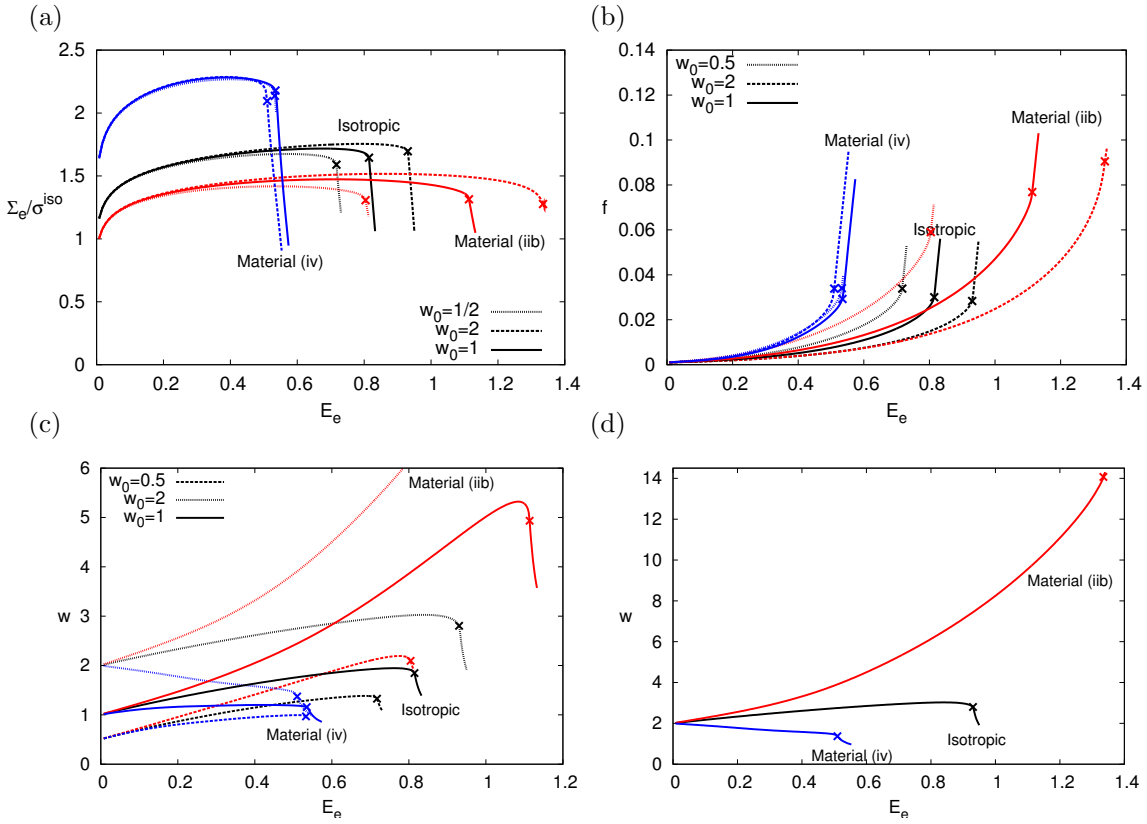

Fig. 18. Effect of matrix material anisotropy on the cell model response for $f_0 = 0.001$, $\lambda_0 = 1$, $T = 1$ and three values of w_0. Case of non EYT materials (Table I). (a) Effective stress–strain response, (b) evolution of porosity, (c) evolution of the void aspect ratio w; and (d) evolution of w for initially prolate cavities with $w_0 = 2$. The anisotropic materials being compared have different yield stresses in uniaxial tension along $\mathbf{e}_S$.

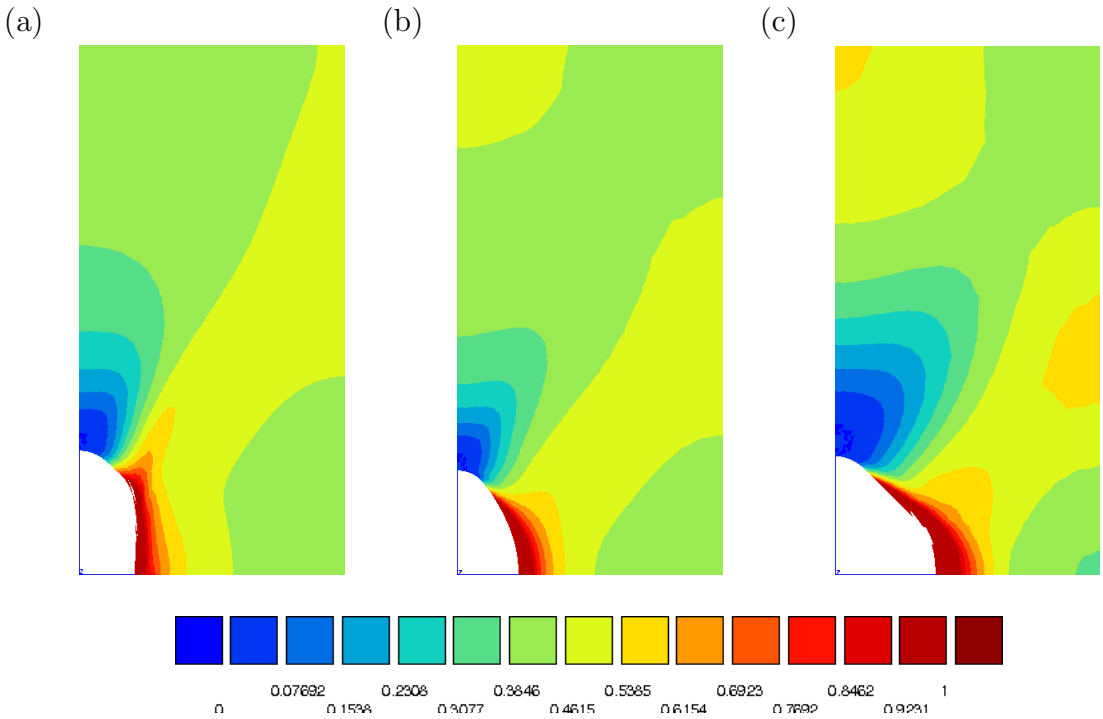

Fig. 19. Contours of effective plastic strain p at $E_e = 0.45$ for non EYT materials and initially spherical voids with $f = 0.001$ and $T = 1$: (a) material (iib), (b) isotropic matrix and (c) material (iv).

a variable quantity.

One can see from Fig. 18a that material (iv) has the highest effective strength while material (iib) has the lowest strength. Clearly, the effect of the overall stress level reflects in the evolution of the porosity shown in Fig. 18b, where material (iv) consistently shows faster void growth compared to material (iib). Nevertheless, some qualitative features of the effect of the shear Hill coefficients $h_{TS} = h_{SL}$ observed in the previous calculations are retained. For instance, the effect of the initial void shape is seen to be negligible for material (iv) while the effect is magnified for material (iib) (in comparison to the case of the isotropic matrix). These trends are identical to those observed for material (iii) and material (ib), respectively, in the previous sections. One common feature of these results is that orthotropic materials that are weaker

under shear in one of their principal planes compared to an isotropic material (i.e. $h_{\mathrm{TS}} = h_{\mathrm{SL}} > 1$ in the transverse isotropic case) appears to exhibit higher sensitivity to the initial void shape, while materials that have a high resistance to yielding under shear exhibit lower void shape sensitivity.

Fig. 18c shows the evolution of the void aspect ratio w and Fig. 18d shows the evolution of w in the $w_0 = 2$ case with an expanded range for the ordinate. The interesting observation from Fig. 18d is that the mode of coalescence in the case of material (iib) appears to be different from the case of the other materials. Although the cell exhibits a transition to the uniaxial straining mode, this is not accompanied by a corresponding drop in w associated with the rapid lateral expansion of the voids. In fact, examination of the contours of effective plastic strain in the deformed configuration of the unit cell (Fig. 19) reveals that significant plastic strain has accumulated along an inclined band in the case of material (iib). This eventually leads to significant deviations from a spheroidal shape for the cavity. As a result, coalescence takes place in a plane parallel to the equatorial plane, by necking of the smallest deformed ligament. A more through investigation of the conditions under which these alternate modes of coalescence are favored under axisymmetric loading will be provided in a forthcoming paper.

D. Discussion

The primary motivation for pursuing cell model studies of the type presented in this chapter is to analyze the influence of matrix material anisotropy on void growth and coalescence. Previous finite element cell studies have focussed on the separate effects of void shape [35, 42, 43] and plastic flow anisotropy in single crystals [54] or textured polycrystals [32]. Here, the aim has been to assess the relative importance

of void shape and plastic anisotropy effects on ductile fracture under a variety of triaxial proportional loading conditions. The results of the present study also provide benchmarks for calibrating continuum models of ductile fracture in anisotropic materials. These include extensions of the Gurson model to incorporate additional microstructural information, such as void shape and material texture [32, 38–41], as well as alternative porous metal plasticity models accounting for texture effects in polycrystalline materials [55]. Furthermore, once appropriately extended to account for plastic anisotropy, the void coalescence models that were independently developed by Gologanu et al. [56], Pardoen and Hutchinson [43] and Benzerga [57] can also be assessed using the present findings from cell model calculations.

The voided cell model is a powerful tool for investigating ductile failure mechanisms at intermediate scales. Three kinds of parameters enter the model, which relate to the applied loading, the microstructure (i.e., void population attributes) and the plastic flow in the matrix. When the present results are added to the rich literature on this subject [15], it becomes evident that the effect of matrix anisotropy is most important among all matrix related parameters, including strain hardening. To illustrate this, the $E^{(c)}$ measure of failure strain decreases by more than 0.7 when Hill coefficient h_{TS} varies between 0.5 and 2.33 for an initial porosity of $f_0 = 0.001$. For reference, the relative change in failure strain is about 0.7 for the same f_0 when the stress triaxiality ratio varies between 1 and 3. The effect of matrix anisotropy is thus comparable to the exponential effect of triaxiality.

To understand the effect of matrix anisotropy, consider the following combination of Hill's coefficients

$$h = 2\left[\frac{2}{5}\frac{h_L + h_T + h_S}{h_L h_T + h_T h_S + h_S h_L} + \frac{1}{5}\left(\frac{1}{h_{TS}} + \frac{1}{h_{SL}} + \frac{1}{h_{LT}}\right)\right]^{\frac{1}{2}} \tag{2.14}$$

For an isotropic material $h = 2$. This scalar is an invariant of the fourth order tensor

$\mathbb{h}$, expressed in axes pointing toward the principal directions of matrix orthotropy. It has emerged in all previous analytical treatments of the problem at hand, or variants thereof, by means of homogenization theory [32,39,41]. According to these theoretical models, the growth rate of porosity may be written as

$$\dot{f} \propto \sinh\left(\kappa \frac{\Sigma_h}{\bar{\sigma}}\right) \tag{2.15}$$

where Σ_h is a weighted mean of the normal stresses, $\bar{\sigma}$ is the matrix flow stress and κ is a factor that depends on both void shape and matrix anisotropy. Interestingly, κ has a $1/h$ dependence and is exactly $3/h$ for spherical voids. The essence of the effect of matrix anisotropy on void growth is rooted in the way invariant h changes from one material category to another. The values taken by h, as reported in Table I, correlate with the trends observed for all EYT materials investigated. In particular, the exponential dependence of void growth upon stress triaxiality (through Σ_h) and matrix anisotropy (through h) clarifies the comparable effects of T and anisotropy pointed out above. Yerra et al. [54] have also pointed out the usefulness of equation (2.14) as a rationale of their results on void growth in single crystals.

Our results show that the effect of matrix anisotropy is both persistent and subtle. The persistent effect, including at extreme stress triaxialities or void shapes, is essentially explained by an average resistance to void growth represented by invariant h. On the other hand, the effect can be subtle due to varying stress levels (such as in materials with unequal yield strengths) or to strong coupling with void shape effects. In fact, the factor κ in (4.10) may depend on other transversely isotropic invariants of tensor $\mathbb{h}$, as inferred from the theoretical analysis of Keralavarma and Benzerga [41]. Such subtleties may also explain some trends discussed by Yerra et al. [54].

We emphasize that the average resistance introduced through h arises irrespective of the major load direction. Evidently, some additional dependence upon load

direction will manifest in any anisotropic material. The analysis of any such dependence would require fully 3D calculations. The key finding is that any given material is characterized by a factor h, which sets its average resistance to void growth.

Among the obtained trends some findings merit further discussion. At high levels of remote load triaxiality ($T \geq 2$), the effect of material plastic anisotropy is a predominant factor affecting the overall ductility, unlike the effect of void shape (Figs. 6–8). A continuum model for plastically orthotropic porous materials has previously been developed by Benzerga and Besson [32] following a micromechanics based approach similar to that of Gurson [12]. It was demonstrated that this model captured the effect of material anisotropy on the effective response of the porous medium well, as evidenced by comparisons of the model with unit cell calculations of the type presented here using initially spherical voids. Since at high T, void shape evolution has a negligible effect for initially spherical cavities, the model of Benzerga and Besson [32] neglecting void shape effects is an adequate extension of the Gurson model to plastically anisotropic materials.

The behavior at moderate stress triaxialities ($2/3 \leq T \leq 1.5$) prevailing in notched bars can be quite different. As is now widely documented in the literature, void shape effects are important in this regime. This effect is best quantified using a void shape sensitivity parameter, $\Delta E^{(c)}$, defined as the difference between strains to coalescence for initially prolate and oblate voids[1]. At high triaxiality, $\Delta E^{(c)} \approx 0$ whereas at $T = 1$ the difference in ductilities is already above 0.25. This figure increases further upon decreasing the triaxiality down to $T > 1/3$. For $T = 1/3$, void coalescence does not take place for $f_0 \leq 0.001$, irrespective of the initial void

[1]The values chosen in the text for w_0, i.e., 1/2 and 2, are arbitrary. However, $\Delta E^{(c)}$ can be defined more objectively as the difference between infinitely long voids (cylinders) and infinitely flat voids (penny-shaped cracks).

shape [43]. In the regime of moderate triaxialities, the cell model studies reported on here show that the sensitivity to initial void shape is influenced by matrix material anisotropy. This influence is so strong that it may either nullify the effect of void shape (e.g. material (iii) in Fig. 12) or exacerbate it, as is the case of materials (ib) and (iib) in Figs. 12 and 18, respectively. Typical trends can be summarized using the above notion of void shape sensitivity parameter $\Delta E^{(c)}$, as shown in Fig. 9b. In this regard, Benzerga et al. [58] used a heuristic combination of the models by Benzerga and Besson [32] and Gologanu et al. [38] in their modeling of anisotropic fracture. For weak coupling between void shape and matrix anisotropy effects, their heuristic combination is acceptable but the present results indicate the extent to which such heuristics is valid.

This study does not deal with the conditions under which voids nucleate in real materials. Any predictions made on the basis of the results reported here would need to be augmented with detailed nucleation analyses. Yet, voids are reported to nucleate at rather low macroscopic strain levels in various material systems (e.g., sulfides in steels and cracks in brittle phases). In addition, when void nucleation occurs due to brittle particle cracking, penny-shaped cracks form and blunt into the plastically flowing matrix.

Our findings for penny-shaped voids confirm that the influence of plastic anisotropy in ductile fracture is paramount. This was illustrated for EYT materials at a moderate triaxiality of 1 and the same behavior is expected at higher triaxialities which promote faster evolution of voids into equiaxed shapes. For all EYT materials that were considered, the cell model response was found to be independent of the specific choice of the "crack" aspect ratio so long as $w_0 \leq 1/10$. This is in agreement with the conclusions of Lassance et al. [52] who studied the case of isotropic matrices. As noted there, the ductility of isotropic materials containing penny-shaped cracks

is controlled by the relative void spacing. Since the latter was kept fixed in our investigation, we conclude that matrix anisotropy is another important microstructural parameter along with the relative void spacing. With respect to approximating penny-shaped cracks with equivalent spherical voids, our findings for some materials support the proposition made long ago by Pineau and Joly [50] who introduced the notion of an equivalent porosity f_0^e. Lassance et al. [52] established one limitation of such an approximation, namely the case of large particle/void volume fractions. The present investigation establishes another limit for materials endowed with a higher resistance in shear than their isotropic counterpart (Fig. 17). This limitation of the equivalent microstructure applies at all porosity levels.

Part of the effect of plastic anisotropy is associated with void growth. The other part can be associated with the way in which anisotropy affects the shift to the uniaxial straining mode, i.e., the onset and progress of void coalescence. It is not straightforward to apportion the two contributions from the cell model calculations alone. In the absence of an analytical quantitative model of void coalescence in anisotropic materials, one can document the values of the void volume fraction at incipient coalescence, i.e., at the onset of micro-scale localization. Fig. 20 illustrates the trends in terms of this "critical" porosity, designated $f^{(c)}$, versus stress triaxiality for three EYT materials. In all the cases shown, void coalescence took place by internal necking of the inter-void ligament. Fig. 20 illustrates that $f^{(c)}$ is significantly affected by the plastic anisotropy of the material and may vary as a function of the loading triaxiality even for an isotropic material. This finding emphasizes a point already made in the literature, e.g., [35, 43, 59], in that the use of a constant $f^{(c)}$ in the phenomenological approach to void coalescence is, in general, not adequate. At the rates of void growth preceding localization, a difference of half a percent in $f^{(c)}$ can lead to significant variations in the strain to coalescence $E^{(c)}$. What is important

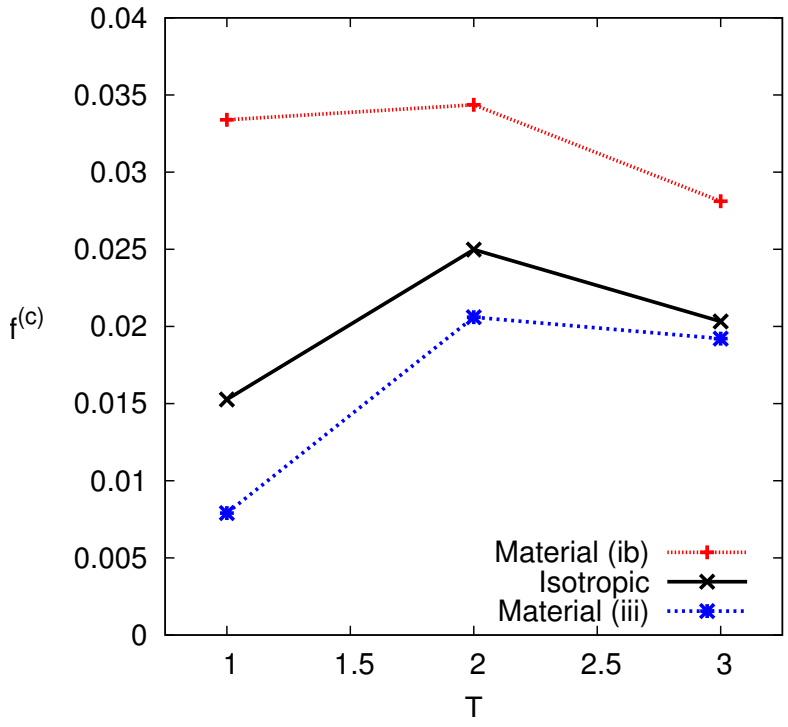

Fig. 20. Porosity at the onset of coalescence, $f^{(c)}$, versus stress triaxiality ratio, T, for initially spherical voids with $f_0 = 0.0001$ and three EYT matrix materials.

in Fig. 20 is that plastic anisotropy can lead to variations in $f^{(c)}$ that are stronger than those caused by the triaxiality alone. Capturing these effects requires micromechanics based models of void coalescence that take into account the cumulative effect of the deformation history in determining the critical conditions for the onset of coalescence.

The computations presented here were limited to transversely isotropic materials. Experimentally measured material anisotropies can be more general, and therefore the material properties used in this study are approximate axisymmetric representations of the range of material anisotropies observed experimentally. Yet, the effects of material anisotropy evidenced in this work are quite prominent. This suggests that even stronger effects may be expected in more realistic cases. The analysis of the latter would however require fully three-dimensional calculations. What is of particular practical importance is that plastic anisotropy effects are significant, unavoidable (e.g., due to processing) and sometimes beneficial. As such, they may prompt material designers to engineer anisotropy of certain types instead of limiting it. With this prospect in mind, this and other concurrent modeling efforts may help lay the theoretical foundations for such rational material design.

E. Conclusions

The effect of matrix material anisotropy on void growth and coalescence was investigated under a variety of axisymmetric loading conditions and for various initial microstructures representative of periodic void aggregates. The plastic anisotropy modeled here is a representation of material texture and grain elongation effects in polycrystalline materials. It can also represent the anisotropy of plastic flow in single crystals. The conclusions drawn from our results may be summarized as follows:

- The effect of plastic anisotropy of the matrix material appears to be a dominant

factor in the mechanics of porous plastic solids, at all stress triaxiality levels. Unlike the effect of void shape, its effect does not vanish at high levels of triaxiality. In addition, at low stress triaxiality, plastic anisotropy sets the extent to which the initial void shape affects the effective behavior of the porous material.

- The critical porosity for the onset of coalescence $f^{(c)}$, which generally depends on the stress triaxiality ratio, is found to depend strongly on the plastic anisotropy of the matrix.
- Since void growth and coalescence are but expressions of plastic distortion of the matrix material, the above effects of plastic anisotropy are qualitatively expected. However, the magnitude manifested by these effects is far more significant than has been appreciated in the literature.
- The computational results clearly illustrate the need for a fundamental coupling between plastic anisotropy and void shape effects for accurate modeling of ductile fracture in structural materials. In this context, there is a need for better experimental characterization of the plastic flow anisotropy of wrought structural materials under fully three-dimensional conditions.

CHAPTER III

A CONSTITUTIVE MODEL FOR PLASTICALLY ANISOTROPIC SOLIDS WITH NON-SPHERICAL VOIDS. PART I: THEORY*

A. Introduction

Failure in metallic structures at temperatures above the brittle-to-ductile transition typically occurs by the nucleation, growth and coalescence of microvoids [60]. Understanding the material-specific processes of ductile fracture is central to structural integrity assessment and to failure mitigation in various contexts, from metal forming to high strain-rate penetration phenomena. A generally accepted model of ductile fracture was developed in the 1980's by Tvergaard and Needleman [13] based on earlier developments in the micromechanics of void growth by McClintock [61], Rice and Tracey [11] and most notably Gurson [12]; see [62] for a review. However, many structural materials exhibit pronounced anisotropic deformation, damage and fracture behavior, which cannot be captured using the above isotropic model (Fig. 21). Part of this anisotropy is initial in that it is related to processing and fabrication routes. The other part is induced: the basic microstructural unit evolves under the large plastic deformations that precede fracture. The key microstructural features involved in anisotropic ductile damage include material texture, grain elongation, deformability of second-phase particles during processing and directionality in the spatial distribution of the latter. While damage initiation mainly occurs at second-phase particles, subsequent accumulation of damage (void growth) is affected by plastic deformation in the matrix.

---

*Reprinted with permission from "A constitutive model for plastically anisotropic solids with non-spherical voids" by Keralavarma, S. M. and Benzerga, A. A., 2010. J Mech Phys Solids 58, 874–901, Copyright [2010] Elsevier Ltd.

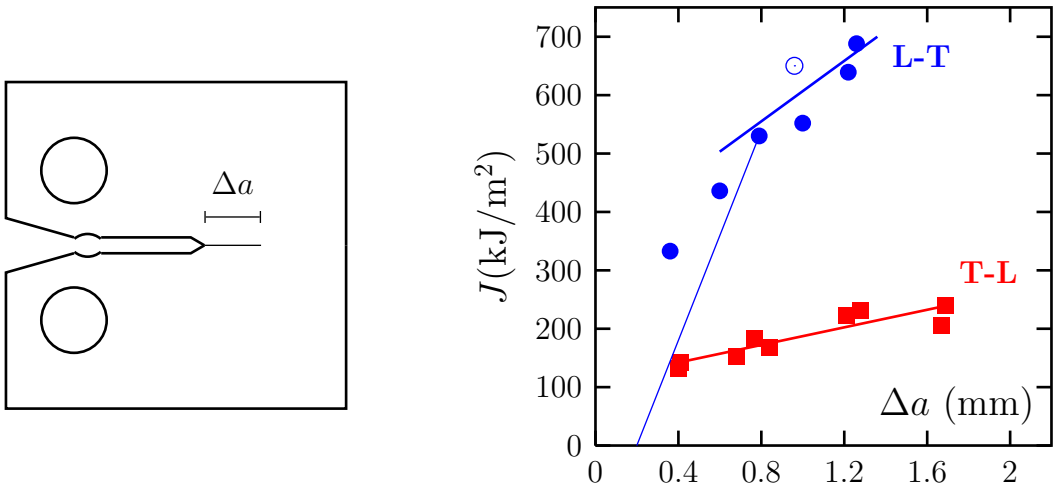

Fig. 21. Crack growth resistance curves of a tough pressure vessel C–Mn steel determined using compact-tension specimen testing for two loading orientations: L–T (load along axial direction L with crack extension, Δa, along transverse direction T) and T–L (vice-versa). Values of toughness, J_{Ic}, according to ASTM E-813-94 are 503kJ/m^2 and 121kJ/m^2, respectively. Adapted from [49].

Gurson [12] treated the nonlinear homogenization problem of a representative volume element (RVE) of a porous material subject to axisymmetric loading. His RVE consisted of a hollow *sphere* made up of a rigid, perfectly plastic and *isotropic* material containing a concentric *spherical* void. The outcome of his analysis was an effective yield criterion for the porous material along with an evolution law for the void volume fraction. His derivation was later shown to be amenable to Hill–Mandel homogenization of the kinematic kind, combined with limit-analysis of the chosen RVE subject to *arbitrary* loading conditions; (e.g. [16, 63]). A unique feature of Gurson's criterion is that it constitutes, for the chosen RVE, a rigorous upper bound, which also happens to lie very close to the exact criterion [16]. To account for initial and induced anisotropies, extensions of the Gurson model were developed in the 1990's to incorporate void shape effects [37, 38, 64, 65] and plastic anisotropy of

the matrix material [32]. Both have been shown to affect void growth to first order. Incorporating void shape effects based on an alternative variational principle using the concept of a linear comparison material [66] are also worthy of note [67, 68]. It seems reasonable to expect that plastic anisotropy and void shape effects will manifest themselves in the orientation dependence of toughness in some structural materials, as illustrated in Fig. 21.

Micromechanical unit-cell calculations of the type pioneered by Koplik and Needleman [29] have also documented the effect of void shape on void coalescence [42, 43]. This has motivated the development of improved models of void coalescence [43, 49, 56, 57, 59, 69–71]. For further practical implications of using anisotropic models in ductile fracture predictions, see the recent reviews by Pineau [72] and Pineau and Pardoen [60].

Based on the above extensions of the Gurson model, Benzerga et al. [58, 73] introduced a ductile fracture computational methodology, which accounts for all types of initial and induced anisotropy listed above. In particular, they proposed a heuristic combination of void shape and plastic anisotropy effects. Details may be found in [49]. More recently, Monchiet et al. [39] and Keralavarma and Benzerga [40] have tackled a Gurson–like homogenization problem to obtain a new yield function that truly couples plastic anisotropy and void shape effects. In both investigations, the RVE consisted of a hollow *spheroid* made up of a rigid, perfectly plastic and *orthotropic* material containing a confocal *spheroidal* void. The chief concern of both articles was the derivation of a new effective yield function, not the evolution of microstructure. While Monchiet et al. [39] derived an approximate yield criterion using a limited description of the microscopic deformation fields, Keralavarma and Benzerga [40] obtained more accurate results by considering a richer description of those fields. However, in the latter work, the void axis was taken to be aligned with one direction

of orthotropy of the matrix material and the loading was axially symmetric about the void axis. In this chapter, we develop a more general approximate solution applicable to (i) *non-axisymmetric* loadings; and (ii) under circumstances where the void axis is no longer constrained to be aligned with a principal axis of matrix orthotropy. The latter situation arises, for example, under off-axes loading of hot-rolled steels as a consequence of induced anisotropy, Fig. 22. In addition, we derive micromechanics-based evolution laws for the microstructure. We emphasize that while the remote loading is non-axisymmetric the void is approximated by a spheroid throughout the deformation. This approximation is of no consequence on the potential upper-bound character of the effective yield locus; it may be likened to approximating a void by a sphere in the Gurson model when deviatoric loadings are considered.

The chapter is organized as follows. In Section B we motivate further the need for improved models of void growth and coalescence by a set of finite-element calculations of voided unit-cells subject to imposed stress histories. Next, we recall the variational formulation of the effective yield criterion in Section B. In Section D the micromechanics problem is posed by specifying geometry, microscopic plasticity model and velocity fields. Section E is a self-contained derivation of the approximate effective yield function with details deferred to four appendices. In the following section, salient features of the derived yield surfaces are analyzed using data for three orthotropic materials. We close the model equations by developing laws for microstructure evolution in Section G along with some preliminary, but discriminating, comparisons with finite element calculations of voided cells.

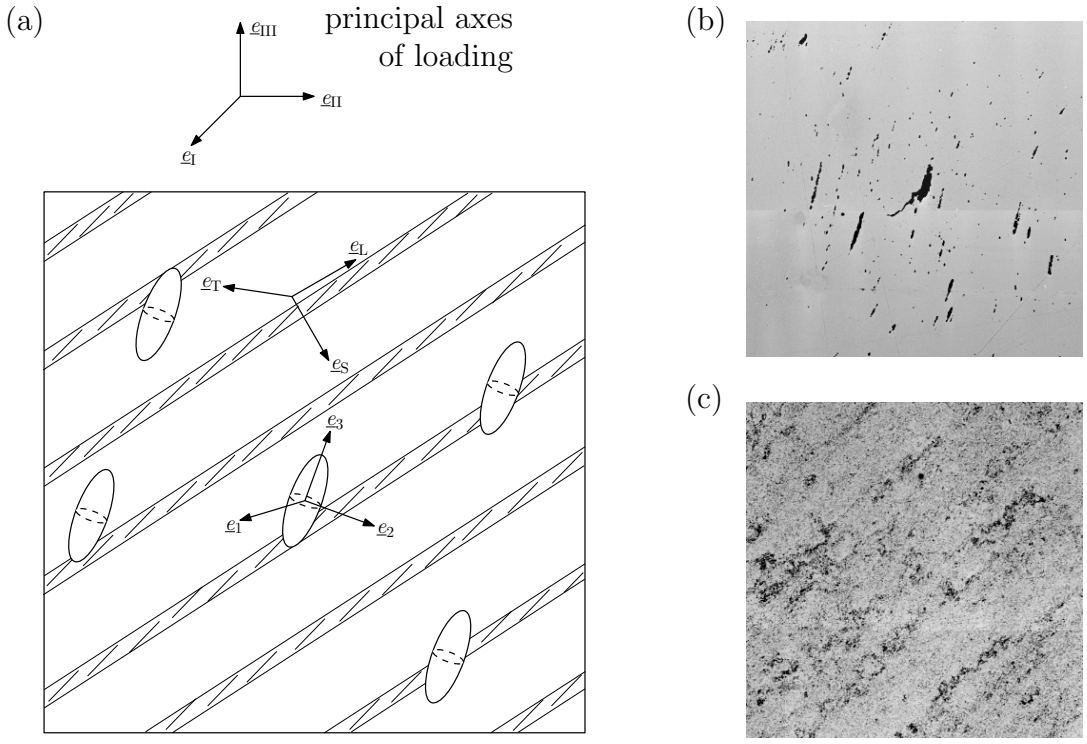

Fig. 22. (a) Sketch of porous material consisting of an aggregate of aligned spheroidal voids embedded in a plastically orthotropic matrix. (b) Actual configuration of void population in an initially dense steel after heavy deformation under off-axes triaxial loading [49]. (c) Etched cross-section of same specimen revealing its two-phase microstructure, ferrite (bright phase) and banded pearlite responsible for plastic anisotropy (dark phase). Orientation of void aggregate in (b) is not that of pearlite bands in (c) because of deformation-induced anisotropy.

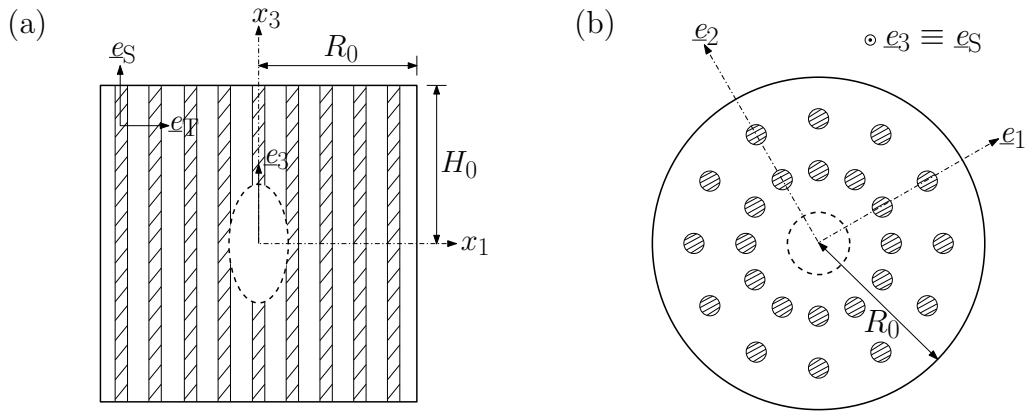

Fig. 23. Configuration of the cylindrical RVE considered in the finite element simulations. (a) Front view. (b) Top view. Void axis $\mathbf{e}_3$ and axis of transverse isotropy $\mathbf{e}_S$ are the same.

B. Finite Element Simulations

We present a set of finite element calculations on porous representative volume elements (RVE) to demonstrate the subtle coupling between the effects of void shape and material anisotropy and motivate the need for an improved model. In all simulations, the principal axes of the void, the axes of material orthotropy and the principal axes of the loading all coincide. Thus, the chosen configuration is considerably simplified from the general case sketched in Fig. 22. Yet, it illustrates important points while allowing for the analysis to be conducted under axisymmetric conditions.

The calculations are based on the concept of a unit-cell containing a void as elaborated upon by Tvergaard [28] and further developed by Koplik and Needleman [29]. A spheroidal void is embedded in an elastoplastic cylindrical matrix, as sketched in Fig. 23, with elastic constants $E = 210$ GPa and $\nu = 0.3$. The geometry of the unit-cell is characterized by the initial porosity, f_0, void aspect ratio, w_0, defined as the ratio of the axial to transverse semi-axes, and the cell aspect ratio, H_0/R_0. Invariance of material plastic flow properties about an axis $\mathbf{e}_S$ is assumed.

The latter is identified with the axis of the spheroidal void $\mathbf{e}_3$. The hatched bands in Fig. 23a schematically represent pearlite banding as in Fig. 22 and, more generally, any processing-induced texturing of the matrix material. More specifically, the matrix is taken to be plastically anisotropic of the Hill type, with the associated flow rule and power-law strain-hardening of the form $\bar{\sigma} = \sigma_{\mathrm{S}}(1 + \bar{\epsilon}/\epsilon_0)^N$, where $\bar{\sigma}$ and $\bar{\epsilon}$ are work-conjugate measures of matrix effective stress and plastic strain, respectively. To avoid confusion with the notion of *effective* properties, we will refer to $\bar{\epsilon}$ as the cumulative plastic strain. Here, $\epsilon_0 = 0.002$ is a constant strain offset, $N = 0.1$ is the hardening exponent and $\sigma_{\mathrm{S}} = 420$ MPa is the initial yield stress of the matrix material along $\mathbf{e}_{\mathrm{S}}$. The applied loading is taken to be axially symmetric about $\mathbf{e}_3$.

The computations are carried out using the object-oriented finite-element (FE) code ZeBuLoN [44] and a Lagrangian formulation of the field equations. The cell boundaries are constrained to remain straight so that the unit cell is representative of a periodic array of voids. Special boundary conditions are formulated such that, in any given calculation, the ratio γ of net axial stress, Σ_{33}, to net lateral stress, Σ_{11}, remains constant throughout. Stress triaxiality is measured by the ratio T of mean normal stress, Σ_{m}, to the von Mises effective stress, Σ_e, given by:

$$\Sigma_e = |\Sigma_{33} - \Sigma_{11}|, \quad \Sigma_{\mathrm{m}} = \frac{1}{3}(\Sigma_{33} + 2\Sigma_{11}), \quad T = \frac{\Sigma_{\mathrm{m}}}{\Sigma_e} = \frac{1}{3}\frac{2\gamma + 1}{|1 - \gamma|} \tag{3.1}$$

A Riks algorithm [74] is used to integrate the nonlinear constitutive equations in order to keep the stress ratio γ, and hence T, constant. T is taken to be unity in the calculations presented here. The effective response of the unit cell is defined in terms of the effective stress Σ_e above versus an effective strain, E_e, defined as follows:

$$E_e = \frac{2}{3}|E_{33} - E_{11}|; \quad E_{33} = \ln\left(\frac{H}{H_0}\right), \quad E_{11} = \ln\left(\frac{R}{R_0}\right) \tag{3.2}$$

where H and R are the current height and radius of the cylindrical unit cell, respec-

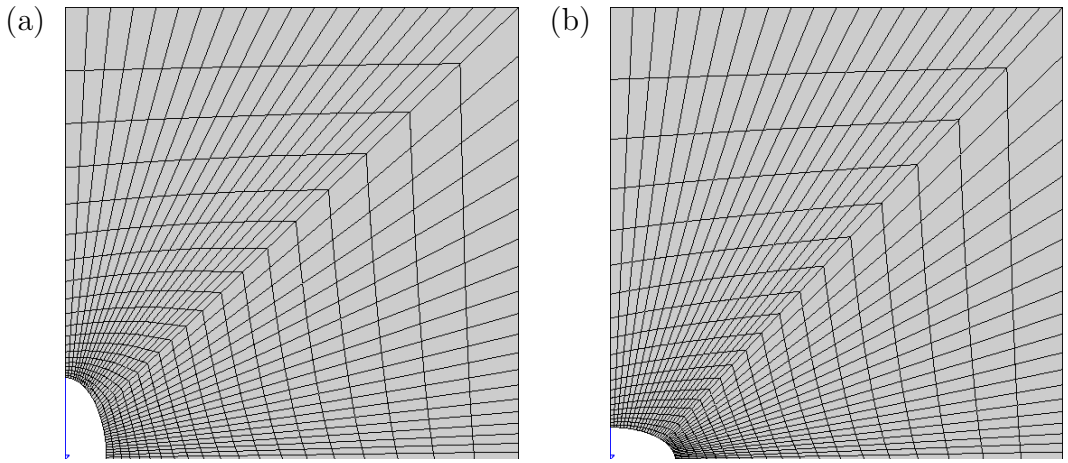

Fig. 24. Finite element meshes used in the unit-cell calculations with initial porosity $f_0 = 0.001$, cell aspect ratio $H_0/R_0 = 1$, and void aspect ratio (a) $w_0 = 2$, and (b) $w_0 = 1/2$.

tively, and H_0 and R_0 their initial values (Fig. 23).

In all calculations, $H_0/R_0 = 1$, the initial void volume fraction is fixed at $f_0 = 0.001$ while three values of the void aspect ratio are used: $w_0 = 1/2$ (oblate void), $w_0 = 1$ (spherical void) and $w_0 = 2$ (prolate void). Typical meshes are shown in Fig. 24, which consist of sub-integrated quadratic quadrilateral elements. Exploiting the symmetry of the problem, only one fourth of the domain is meshed. All material parameters are kept fixed except w_0 and the Hill anisotropy factors that characterize plastic flow in the matrix. Two sets of Hill coefficients are used which are representative of an aluminum alloy and a zirconium alloy and referred to as Material 1 and Material 2, respectively (Table III). The third set of values (Material 3) will be used later. In a reference calculation, the material is isotropic and the void spherical ($w_0 = 1$).

The effective responses of the anisotropic unit cells are compared in Fig. 25a with that of an isotropic solid (i.e., isotropic matrix and $w_0 = 1$). The effective stress is normalized by the matrix yield stress σ_S. The corresponding porosity versus effective

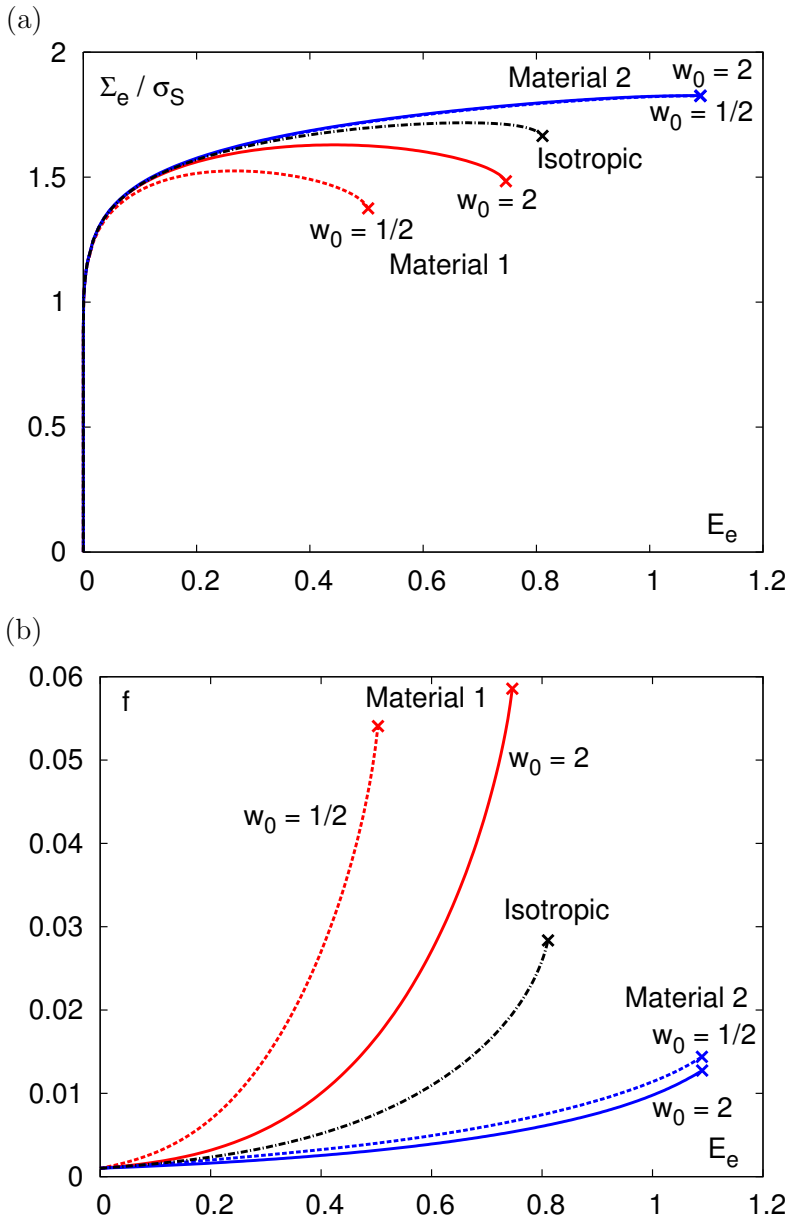

Fig. 25. Results of unit-cell calculations for two transversely isotropic matrix materials (Table III) containing either oblate ($w_0 = 1/2$) or prolate ($w_0 = 2$) voids. (a) Effective stress, Σ_e, normalized by the matrix yield stress in tension along $\mathbf{e}_S$, versus effective strain, E_e. (b) void volume fraction versus E_e. Key data include: initial porosity $f_0 = 0.001$; matrix hardening exponent $N = 0.1$; and stress triaxiality ratio $T = 1$. For comparison, results for initially spherical void in an isotropic matrix are also shown.

Table III. Matrix material anisotropy parameters, h_i, used in the numerical computations. h_i $(i = \mathrm{L}, \mathrm{T}, \mathrm{S}, \mathrm{TS}, \mathrm{SL}, \mathrm{LT})$ represent the diagonal elements of the Voigt representation of Hill's tensor in deviatoric stress space, $\mathbb{h}$, expressed in the frame of material orthotropy; see Section 2 for details.

	h_{L}	h_{T}	h_{S}	h_{TS}	h_{SL}	h_{LT}
Isotropic	1.000	1.000	1.000	1.000	1.000	1.000
Material 1	1.000	1.000	1.000	2.333	2.333	1.000
Material 2	1.000	1.000	1.000	0.500	0.500	1.000
Material 3	1.650	0.778	0.893	1.378	0.943	1.627

strain curves are shown in Fig. 25b. The calculations, which were terminated just at the onset of void coalescence, illustrate three typical trends. First, the effect of initial void aspect ratio w_0 is generally significant: in Material 1 there is nearly a 0.25 difference in effective strain between the $w_0 = 1/2$ and $w_0 = 2$ cases at incipient void coalescence. This result demonstrates the effect of initial void shape on void growth rates, in keeping with previous studies [43]. Next, at fixed value of w_0, changing the matrix anisotropy properties from Material 1 to Material 2 drastically affects the stress bearing capacity of the unit cell (Fig. 25a) as well as the rate of increase of porosity (Fig. 25b) with the effect being more dramatic for the oblate void ($w_0 = 1/2$). Finally, the combined effect of plastic anisotropy and void shape can yield unexpected trends as is the case for Material 2: the effect of initial void shape, which is invariably present in isotropic matrices, simply disappears within the range of w_0 considered here (Fig. 25). For reference, the results corresponding to the isotropic matrix with $w_0 = 1/2$ and $w_0 = 2$ fall in between the results for materials 1 and 2. They are not shown in Fig. 25 for the sake of clarity.

None of the available porous plasticity models capture all aspects of the behavior documented in Fig. 25. This includes the heuristic model of Benzerga et al. [58] who

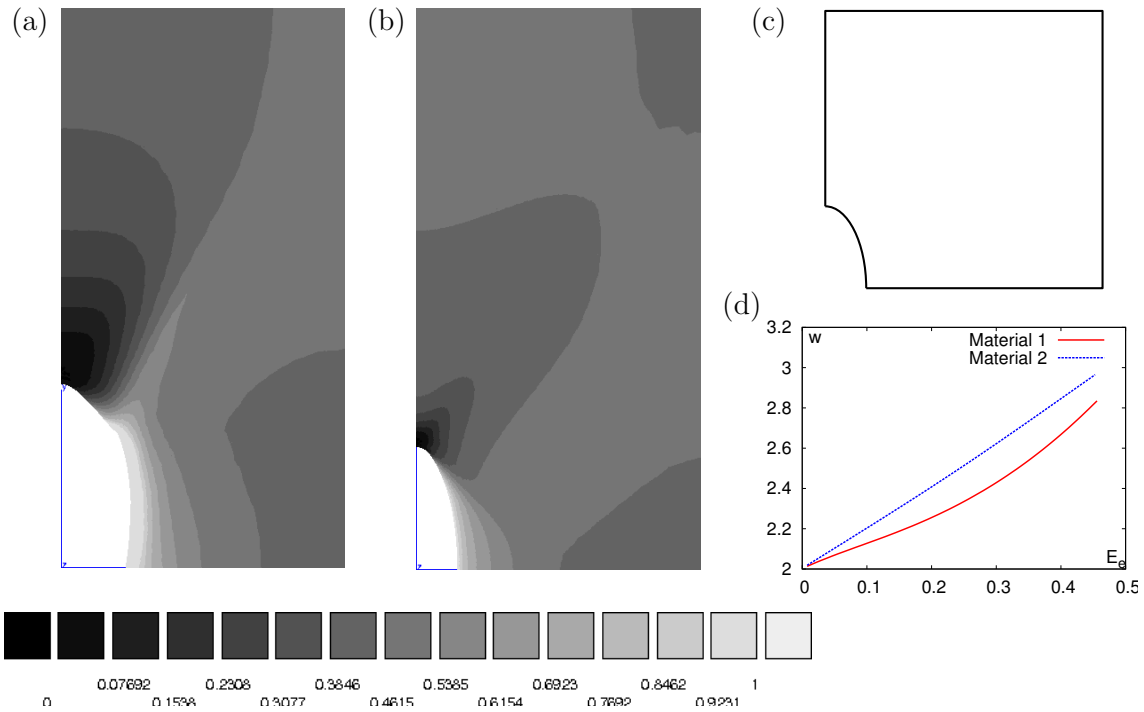

Fig. 26. Contours of cumulative plastic strain, $\bar{\epsilon}$, at a unit cell effective strain $E_e = 0.45$ and $T = 1$ using $f_0 = 0.001$, $w_0 = 2$, $H_0/R_0 = 1$, $N = 0.1$ and anisotropy parameters for (a) Material 1; and (b) Material 2 from Table III. (c) Initial state. (d) Evolution of void aspect ratio w. Nearly identical evolutions of void aspect ratio do not necessarily imply the same amount of void enlargement.

conjectured that the combined effect of void shape and plastic anisotropy is a simple superposition of separate effects. In fact, the effect of plastic anisotropy is more subtle than discussed above. Examination of the deformed configurations for an initially prolate cavity, Fig. 26a-c, shows that void growth depends on material anisotropy even when the void aspect ratio evolves in a nearly identical fashion (Fig. 26d). As previously shown in Fig. 25b, the porosity grows much faster in Material 1 than in Material 2 leading to a much lower ductility for the former. This is in contrast with existing void growth models [38, 43, 49], which would predict nearly identical evolutions of the porosity in these two materials.

In fact, the strong coupling between plastic anisotropy and void shape effects is

not surprising. Void growth is merely the expression of plastic deformation of the surrounding matrix. Physically, it is therefore expected that the ease, or difficulty, with which plastic flow takes place in the matrix will affect the rate of void growth. While the results in Figs. 25–26 provide a quantification of this coupling, it remains that such results hold for particular choices made for the initial microstructural parameters, loading history, etc. One can only carry out a finite number of such unit cell calculations. A more challenging task is to derive a mathematical plasticity model with an inherent predictive capability of coupled anisotropy effects as evidenced at the mesoscopic, unit-cell level. In doing so, the ambition goes beyond the restrictive case of transversely isotropic matrices and axisymmetric proportional loadings. On the other hand, derivation of such a mathematical model from first principles is currently not tractable without some basic restrictions. Chief among these are the neglect of elasticity and work hardening in the matrix material. In return, the derivation can be tackled using tools and concepts from limit analysis and nonlinear homogenization theory.

C. Variational Formulation of the Yield Criterion

The effective yield criterion of a porous anisotropic material is determined through homogenization of a representative volume element occupying domain Ω and containing voids that jointly occupy sub-domain ω. The kinematic approach of Hill–Mandel homogenization theory [75, 76] is used, wherein the RVE is subjected to uniform deformation-rate boundary conditions, i.e.,

$$v_i = D_{ij} x_j \qquad \text{on} \quad \partial\Omega \tag{3.3}$$

where $\mathbf{v}$ is the microscopic velocity field and $\mathbf{D}$ is a second-rank symmetric tensor, which specifies the loading. It is straightforward to show that the imposed boundary rate of deformation, $\mathbf{D}$, is equal to the volume average of the microscopic rate of deformation, $\mathbf{d}$, over the volume of the RVE. The corresponding macroscopic stress, $\boldsymbol{\Sigma}$, is defined in an analogous way as the volume average over Ω of the microscopic Cauchy stress, $\boldsymbol{\sigma}$. Hence,

$$D_{ij} = \langle d_{ij} \rangle_{\Omega}, \qquad \Sigma_{ij} \equiv \langle \sigma_{ij} \rangle_{\Omega}, \tag{3.4}$$

where the notation $\langle \cdot \rangle_{\Omega}$ is for volume averaging over Ω. For a porous material, (4.1) remains valid regardless of the extensions chosen for the fields $\boldsymbol{\sigma}$ and $\mathbf{d}$ within the void, provided that the boundary of the void remains traction free and the velocity field is continuous across the boundary. The Hill–Mandel lemma [75, 76] entails that the above defined macroscopic measures of stress and rate of deformation are work conjugate. It may be noted that in the lemma $\boldsymbol{\sigma}$ and $\mathbf{d}$ need not be related through a constitutive relation. For a rigid perfectly plastic matrix material with normality obeyed, the macroscopic, or effective, yield surface in stress space is determined using the classical limit-analysis theorem identifying the sets of potentially and actually sustainable loads [77], and is defined by

$$\Sigma_{ij} = \frac{\partial \Pi}{\partial D_{ij}}(\mathbf{D}) \tag{3.5}$$

Here, $\Pi(\mathbf{D})$ is the macroscopic plastic dissipation defined as the infimum of the volume-average of the microscopic plastic dissipation $\pi(\mathbf{d})$, the infimum being calculated over all admissible microscopic deformation fields. The above theorem and equation (3.5) also apply when elasticity is included if transformations are small. Physically, equation (3.5) means that among all microscopic diffuse modes of plastic deformation, those that result in the smallest average dissipation over the cell will

define "macroscopic" yielding. Formally,

$$\Pi(\mathbf{D}) = \inf_{\mathbf{d}\in\mathcal{K}(\mathbf{D})} \langle \pi(\mathbf{d}) \rangle_\Omega \tag{3.6}$$

where $\mathcal{K}(\mathbf{D})$ denotes the set of kinematically admissible microscopic deformations:

$$\mathcal{K}(\mathbf{D}) = \{\mathbf{d} | \exists \mathbf{v}, \forall \mathbf{x} \in \Omega,\, d_{ij} = \frac{1}{2}(v_{i,j} + v_{j,i}) \,\text{and}\, \forall \mathbf{x} \in \partial\Omega,\, v_i = D_{ij} x_j\} \tag{3.7}$$

For a given deviator $\mathbf{d}$, the microscopic plastic dissipation is defined as

$$\pi(\mathbf{d}) = \sup_{\boldsymbol{\sigma}^* \in \mathcal{C}} \sigma^*_{ij}\, d_{ij} \tag{3.8}$$

the supremum being taken over all microscopic stresses that fall within the microscopic convex $\mathcal{C}$ of elasticity.

Equations (3.5) through (4.15) represent a variational definition of the effective yield criterion. Actual derivation of the latter requires that the following be specified: (i) the geometry of the RVE; (ii) a micro-scale plasticity model, which enters through the term $\pi(\mathbf{d})$; and (iii) trial velocity fields defining the set $\mathcal{K}(\mathbf{D})$ for use in (4.13). These tasks are undertaken in the following section.

D. Problem Definition

Using the variational approach above, an effective yield criterion is sought for anisotropic porous materials subjected to arbitrary loadings. Aligned spheroidal voids are embedded in a rigid, plastically orthotropic matrix. Elasticity is thus neglected in the analysis so that (3.5) applies at finite strains. It will be included heuristically at the end within a hypoelastic framework. The microstructure orientation is defined by two triads: (i) $(\mathbf{e}_1, \mathbf{e}_2, \mathbf{e}_3)$ associated with the aggregate of spheroidal voids with $\mathbf{e}_3$ being their common axis and $\mathbf{e}_1, \mathbf{e}_2$ chosen arbitrarily; and (ii) $(\mathbf{e}_\mathrm{L}, \mathbf{e}_\mathrm{T}, \mathbf{e}_\mathrm{S})$ associated with

the directions of orthotropy of the matrix. The microstructural and matrix triads are not necessarily tied to each other; see Fig. 22a. Under an arbitrary macroscopic stress state with principal axes $(\mathbf{e}_{\mathrm{I}}, \mathbf{e}_{\mathrm{II}}, \mathbf{e}_{\mathrm{III}})$, initially spheroidal voids would develop into three-dimensional voids. This evolution is neglected in the present treatment:

Approximation $\mathcal{A}_1$: We approximate the void shape to be spheroidal at every stage of the deformation.

This approximation is similar to Gurson's assumption of spherical voids in his derivation of the isotropic criterion. It can be further justified on the basis that the objective is to develop an accurate estimate of the macroscopic yield criterion, not to determine the exact microscopic fields. Finding the latter is a challenging problem because of their expected dependence upon specific matrix flow characteristics and of other subtle nonlinear effects[1]. The microscopic velocity fields are important, however, in determining the evolution laws for some microstructural variables. The treatment of the evolution problem in Section G, therefore, will examine possible strategies to correct for the inaccuracies in the assumed velocity fields.

It is worth noting that while the homogenization procedure outlined in Section B is more easily tractable for spheroidal void shapes, alternative homogenization approaches using non-linear extensions of the Hashin-Shtrikman theory [66] have been effectively used for ellipsoidal void geometries. While earlier versions of such models [67, 68] did not provide good agreement with numerical estimates of the yield criterion at high stress triaxialities, recent extensions based on a second order homogenization procedure [78] provide approximate, but more accurate results. However,

[1] A typical example is the counterintuitive flattening of cavities under axial loading with sufficient amount of superposed hydrostatic stress.

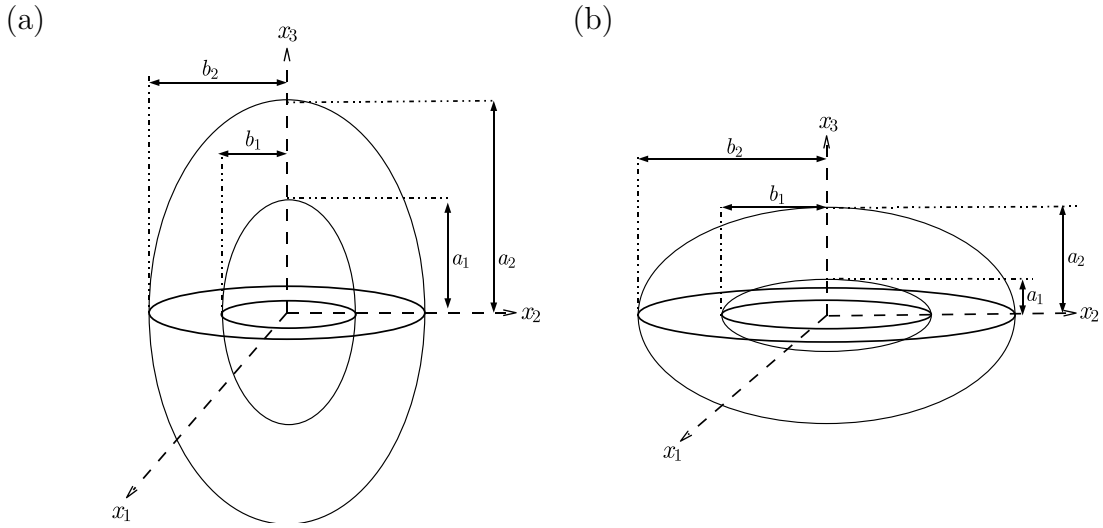

Fig. 27. Porous representative volume elements used in the derivation of the analytical yield criterion. The cases of prolate (a), and oblate (b) voids require separate treatments.

these models have not yet been extended to treat the case of plastically anisotropic matrices. In passing, we also note a recent formulation of admissible velocity fields by Leblond and Gologanu [79] for ellipsoidal voids. It remains to be seen whether the homogenization procedure of Section B is tractable in that case.

1. Geometry and Coordinates

Following previous works on void shape effects [37, 38, 64], we consider a spheroidal RVE containing a confocal spheroidal void, as shown in Fig. 27. Let a and b represent respectively the lengths of the axial and transverse semi-axes of the current confocal spheroid, and let $c = \sqrt{|a^2 - b^2|}$ represent the semi-focal length. Hereafter, the subscripts 1 and 2 shall represent variable values at the void and RVE boundaries, respectively. At fixed void orientation, the geometry is thus completely defined by two dimensionless parameters; the porosity, $f = |\omega|/|\Omega| = a_1 b_1^2 / a_2 b_2^2$, and the void aspect ratio, $w \equiv a_1/b_1$. For given values of f and w, the eccentricities of the inner

and outer spheroids may be uniquely determined from the relations

$$e_1^2 = \begin{cases} 1 - \dfrac{1}{w^2} & \text{(p)} \\ 1 - w^2 & \text{(o)} \end{cases}, \qquad \frac{(1-e_2^2)^n}{e_2^3} = \frac{1}{f}\frac{(1-e_1^2)^n}{e_1^3}, \qquad n = \begin{cases} 1 & \text{(p)} \\ 1/2 & \text{(o)} \end{cases} \tag{3.9}$$

where the shorthand notations (p) and (o) stand for prolate and oblate, respectively.

Due to the chosen geometry of the RVEs, we shall mainly employ the spheroidal coordinate system $(\lambda, \beta, \varphi)$ for the subsequent analysis. The base vectors of the spheroidal frame are defined by

$$\begin{aligned} \mathbf{e}_\lambda &= \{a \sin\beta \cos\varphi \mathbf{e}_1 + a \sin\beta \sin\varphi \mathbf{e}_2 + b \cos\beta \mathbf{e}_3\}/\sqrt{g_{\lambda\lambda}} \\ \mathbf{e}_\beta &= \{b \cos\beta \cos\varphi \mathbf{e}_1 + b \cos\beta \sin\varphi \mathbf{e}_2 - a \sin\beta \mathbf{e}_3\}/\sqrt{g_{\lambda\lambda}} \\ \mathbf{e}_\varphi &= -\sin\varphi \mathbf{e}_1 + \cos\varphi \mathbf{e}_2 \end{aligned} \tag{3.10}$$

$$g_{\lambda\lambda} \equiv a^2 \sin^2\beta + b^2 \cos^2\beta, \qquad \begin{cases} a = c \cosh\lambda, \ b = c \sinh\lambda & \text{(p)} \\ a = c \sinh\lambda, \ b = c \cosh\lambda & \text{(o)} \end{cases} \tag{3.11}$$

where $(\mathbf{e}_1, \mathbf{e}_2, \mathbf{e}_3)$ is the Cartesian base associated with the voids introduced above (also see Fig. 22c). With this choice of coordinates, the boundaries of the void and the RVE correspond to constant values of λ, designated λ_1 and λ_2 respectively. The eccentricity of the current confocal spheroid, e, is related to λ by the relation $e = 1/\cosh\lambda$.

2. Microscale Plasticity Model

The RVE is assumed to be made of a rigid ideal plastic orthotropic and incompressible material obeying the Hill quadratic yield criterion [47], which writes

$$\sigma_{\text{eq}} \equiv \sqrt{\frac{3}{2}\boldsymbol{\sigma} : \mathbb{p} : \boldsymbol{\sigma}} = \sqrt{\frac{3}{2}\boldsymbol{\sigma}' : \mathbb{h} : \boldsymbol{\sigma}'} \leq \bar{\sigma}, \qquad \mathbb{p} = \mathbb{J} : \mathbb{h} : \mathbb{J} \tag{3.12}$$

where the prime denotes the deviatoric part of a second order tensor and $\bar{\sigma}$ is the yield stress of the material in a reference direction. The fourth order tensor $\mathbb{p}$ denotes the Hill anisotropy tensor, $\mathbb{h}$ denotes the anisotropy tensor in the deviatoric stress space and $\mathbb{J}$ denotes the deviatoric projection operator defined by $\mathbb{J} \equiv \mathbb{I} - \frac{1}{3}\mathbf{I} \otimes \mathbf{I}$, where $\mathbb{I}$ and $\mathbf{I}$ are the fourth and second order identity tensors, respectively. The symbol $\otimes$ denotes the dyadic product, defined by $(\mathbf{I} \otimes \mathbf{I})_{ijkl} \equiv I_{ij} I_{kl}$. Typically, $\bar{\sigma}$ is chosen as the yield stress in one of the directions of orthotropy of the matrix material and the components of the anisotropy tensors $\mathbb{p}$ and $\mathbb{h}$ in (3.12) are scaled accordingly. The material obeys the associated flow rule, which may be written in the following form

$$\mathbf{d} = \frac{3}{2} \frac{d_{\text{eq}}}{\bar{\sigma}} \mathbb{p} : \boldsymbol{\sigma} \tag{3.13}$$

where d_{eq} is defined work-conjugate to σ_{eq} as the equivalent microscopic strain rate

$$d_{\text{eq}} = \sqrt{\frac{2}{3} \mathbf{d} : \hat{\mathbb{h}} : \mathbf{d}} \tag{3.14}$$

Here, $\hat{\mathbb{h}}$ is a formal inverse of tensor $\mathbb{h}$. It is defined as [32]

$$\hat{\mathbb{p}} \equiv \mathbb{J} : \hat{\mathbb{h}} : \mathbb{J}, \qquad \mathbb{p} : \hat{\mathbb{p}} = \hat{\mathbb{p}} : \mathbb{p} = \mathbb{J} \tag{3.15}$$

Both $\mathbb{h}$ and $\hat{\mathbb{h}}$ are symmetric positive definite tensors; i.e. $h_{ijkl} = h_{jikl} = h_{ijlk} = h_{klij}$ and $\forall \boldsymbol{\sigma} \neq \mathbf{0},\ \boldsymbol{\sigma} : \mathbb{h} : \boldsymbol{\sigma} > 0$. In the frame of material orthotropy (Fig. 22), $\mathbb{h}$ and $\hat{\mathbb{h}}$ may be expressed as diagonal 6×6 matrices using Voigt's condensation. The six Hill coefficients are then denoted h_{L}, h_{T}, etc. (see Table III). For a Hill material with associated flow rule, the microscopic plastic dissipation in (4.15) takes the form

$$\pi(\mathbf{d}) = \begin{cases} \bar{\sigma}\, d_{\text{eq}} & \text{(in the matrix)} \\ 0 & \text{(in the voids)} \end{cases} \tag{3.16}$$

3. Microscopic Velocity Fields

To describe plastic flow in the matrix, the velocity field is taken as a linear combination of two incompressible trial velocity fields

$$\forall \mathbf{x} \in \Omega \backslash \omega, \quad v_i(\mathbf{x}) = A v_i^A(\mathbf{x}) + \beta_{ij} x_j, \tag{3.17}$$

where scalar A and tensor $\boldsymbol{\beta}$ are parameters. Thus, $\mathbf{v}$ leads to an inhomogeneous deformation field, $\mathbf{d}^A$, responsible for void expansion, and a homogeneous field $\boldsymbol{\beta}$. Matrix incompressibility requires that the latter be a pure deviator ($\beta_{kk} = 0$). The above decomposition was also used in previous works [12, 32, 38, 39]. Here, however, the homogeneous part $\boldsymbol{\beta}$ is not required to be axisymmetric. The expansion velocity field, $\mathbf{v}^A$, is taken to be axisymmetric about the void axis and constructed from the family of incompressible velocity fields introduced by Lee and Mear [80]. Its components in spheroidal coordinates are:

$$\begin{cases} v_\lambda(\lambda,\beta) = c^2/\sqrt{g_{\lambda\lambda}}\,\{B_{00}/\sinh(\lambda) \\ \quad + \displaystyle\sum_{k=2,4,..}^{+\infty}\sum_{m=0}^{+\infty} k(k+1)[B_{km}Q_m^1(\zeta) + C_{km}P_m^1(\zeta)]P_k(\xi)\} \\ \qquad\qquad\qquad\qquad\qquad\qquad\qquad\qquad\qquad\qquad\qquad\qquad \text{(p)} \\ v_\beta(\lambda,\beta) = c^2/\sqrt{g_{\lambda\lambda}}\,\{\displaystyle\sum_{k=2,4,..}^{+\infty}\sum_{m=1}^{+\infty} m(m+1)[B_{km}Q_m(\zeta) \\ \qquad\qquad\qquad\qquad\qquad\qquad +C_{km}P_m(\zeta)]P_k^1(\xi)\} \end{cases} \tag{3.18}$$

$$\begin{cases} v_\lambda(\lambda,\beta) = c^2/\sqrt{g_{\lambda\lambda}}\,\{B_{00}/\cosh(\lambda) \\ \quad + \displaystyle\sum_{k=2,4,..}^{+\infty}\sum_{m=0}^{+\infty} k(k+1)i^m[i\,B_{km}Q_m^1(\zeta) + C_{km}P_m^1(\zeta)]P_k(\xi)\} \\ \qquad\qquad\qquad\qquad\qquad\qquad\qquad\qquad\qquad\qquad\qquad\qquad\qquad\qquad\qquad\qquad (o) \\ v_\beta(\lambda,\beta) = c^2/\sqrt{g_{\lambda\lambda}}\,\{\displaystyle\sum_{k=2,4,..}^{+\infty}\sum_{m=1}^{+\infty} m(m+1)i^m[i\,B_{km}Q_m(\zeta) \\ \qquad\qquad\qquad\qquad\qquad\qquad\qquad\qquad +C_{km}P_m(\zeta)]P_k^1(\xi)\} \end{cases} \tag{3.19}$$

where

$$\zeta \equiv \begin{cases} \cosh\lambda & \text{(p)} \\ i\,\sinh\lambda & \text{(o)} \end{cases} \quad ; \qquad \xi \equiv \cos\beta \tag{3.20}$$

In the above expressions, P_n^m and Q_n^m represent associated Legendre functions of the first and second kinds respectively, of order m and degree n [81], B_{km} and C_{km} are arbitrary real constants and $i^2 = -1$.

As discussed by Gologanu et al. [38], the condition of uniform boundary rate of deformation (3.3) formally fixes parameters A and $\boldsymbol{\beta}$ in a two-field approach such as (3.17). This may be seen by substituting the velocity field (3.17) into the macro-homogeneity condition $(4.1)_1$, which is itself a corollary of boundary condition (3.3); this yields:

$$D_{ij} = A\langle d_{ij}^A\rangle_\Omega + \beta_{ij} \tag{3.21}$$

Denoting $\mathbf{D}^A \equiv \langle \mathbf{d}^A\rangle_\Omega$ the contribution to $\mathbf{D}$ due to the expansion velocity field $\mathbf{v}^A$, it thus follows that parameters A and $\boldsymbol{\beta}$ are given by:

$$A = \frac{D_{\mathrm{m}}}{D_{\mathrm{m}}^A}, \quad \beta_{ij} = D_{ij} - \frac{D_{\mathrm{m}}}{D_{\mathrm{m}}^A}D_{ij}^A \tag{3.22}$$

where the subscript 'm' denotes the mean part of a tensor ($D_{\mathrm{m}} = D_{kk}/3$). Note that $\mathbf{D}^A$ is by definition axially symmetric about the void axis. In fact, the imposed boundary conditions imply further restrictions on the velocity fields. Since the second

deformation field in (3.17) is uniform by construction, equation (3.3) also requires that:

$$v_i^A = D_{ij}^A \, x_j \qquad \text{for} \quad \lambda = \lambda_2 \tag{3.23}$$

This condition implies that coefficients B_{km} and C_{km} of the Lee–Mear fields (4.28)–(4.29) obey the following linear constraints (see [38])

$$\begin{cases} e_2^3 B_{00}/(3(1-e_2^2)) + (3-e_2^2)F_2(\lambda_2)/\sqrt{1-e_2^2} - G_2(\lambda_2) = 0 & \text{(p)} \\ \\ -e_2^3 B_{00}/(3\sqrt{1-e_2^2}) + (3-2e_2^2)F_2(\lambda_2)/\sqrt{1-e_2^2} - G_2(\lambda_2) = 0 & \text{(o)} \end{cases} \tag{3.24}$$

$$F_k(\lambda_2) = G_k(\lambda_2) = 0, \qquad k = 4, 6, 8... \tag{3.25}$$

where

$$\begin{cases} F_k(\lambda) \equiv \displaystyle\sum_{m=0}^{+\infty} \left[B_{km} Q_m^1(\zeta) + C_{km} P_m^1(\zeta) \right] \\ G_k(\lambda) \equiv \displaystyle\sum_{m=1}^{+\infty} m(m+1) \left[B_{km} Q_m(\zeta) + C_{km} P_m(\zeta) \right] \end{cases} \quad \text{(p)}$$

$$\begin{cases} F_k(\lambda) \equiv \displaystyle\sum_{m=0}^{+\infty} i^m \left[i B_{km} Q_m^1(\zeta) + C_{km} P_m^1(\zeta) \right] \\ G_k(\lambda) \equiv \displaystyle\sum_{m=1}^{+\infty} m(m+1) i^m \left[i B_{km} Q_m(\zeta) + C_{km} P_m(\zeta) \right] \end{cases} \quad \text{(o)} \tag{3.26}$$

In the derivation of the effective yield criterion in closed form, only four terms in the Lee–Mear expansion are used. These correspond to factors B_{00}, B_{20}, B_{21} and B_{22}. Since the field $\mathbf{v}^A$ is defined only up to a multiplicative constant, coefficient B_{00} is taken as unity to normalize the field and the remaining factors are collectively referred to as B_{2m} $(m = 0, 1, 2)$. In the case of a spherical cavity, the fields related to the B_{2m} factors vanish and that related to B_{00} becomes spherically symmetric. The velocity fields corresponding to the coefficients C_{km} are not used since these fields do

not vanish at infinity as is required, so that one can recover the correct limit behavior for a vanishingly small value of the porosity. The chosen velocity fields are in fact identical to those used by Gologanu et al. [38] in their work on void shape effects and is a generalization of the fields used in the earlier works of Gologanu et al. [37,64] (B_{00} and B_{22}) and Garajeu [65] (B_{00} and B_{20}). Recent work by Monchiet et al. [39] using the Hill matrix also considered the fields B_{00} and B_{22} to describe the expansion field. However, we have chosen to use the above four fields to describe cavity expansion as this was found to yield a better correspondence with numerical estimates of the true yield criterion [40, 82]. In the case of isotropic matrices, comparison between the model developed by Gologanu et al. [38] using four fields and their earlier models using two fields has evidenced superior predictive capability of the former regarding the evolution of microstructure.

E. Approximate Analytical Yield Criterion

The macroscopic yield locus is given by the parametric equation (3.5) with the dissipation function rewritten as:

$$\Pi(\mathbf{D}) = \inf_{\mathbf{d}\in\mathcal{K}(\mathbf{D})} \langle \sup_{\boldsymbol{\sigma}^*\in\mathcal{C}} \sigma^*_{ij}\, d_{ij} \rangle_\Omega \tag{3.27}$$

With the choice (3.12)–(3.13) made for the matrix plasticity model and the choice (3.17)–(4.29) for the microscopic velocity fields, an estimate of $\Pi(\mathbf{D})$ is, in view of (3.16),

$$\Pi(\mathbf{D}) = \bar{\sigma}(1-f)\langle d_{\text{eq}}\rangle_{\Omega\setminus\omega} = \frac{\bar{\sigma}}{\Omega}\int_{\lambda_1}^{\lambda_2}\int_0^{\pi}\int_0^{2\pi} d_{\text{eq}} b\, g_{\lambda\lambda}\, \sin\beta\, d\varphi\, d\beta\, d\lambda \tag{3.28}$$

In this expression, d_{eq}, which is defined by (3.14), is evaluated for the specific set of chosen admissible velocity fields. Since a subset of $\mathcal{K}(\mathbf{D})$ is used, Eq. (3.28) delivers an

upper bound for the true dissipation. For notational convenience, this upper-bound value and other subsequent estimates are also designated $\Pi(\mathbf{D})$. As noted above, imposition of kinematic boundary conditions in terms of $\mathbf{D}$ formally determines the velocity field through (3.22) thus eliminating the need for explicit minimization in computing the macroscopic plastic dissipation, Eq. (3.27). However, the coefficients B_{km} appearing in the expression of $\mathbf{v}^A$ are left undefined, to be fixed later independently of the boundary conditions. Rewriting d_{eq} in terms of the fields $\mathbf{d}^A$ and $\boldsymbol{\beta}$, we get

$$d_{\text{eq}} = \sqrt{A^2 d_{\text{eq}}^{A^2} + {\beta_{\text{eq}}}^2 + \frac{4}{3} A \mathbf{d}^A : \hat{\mathbb{h}} : \boldsymbol{\beta}} \tag{3.29}$$

Here and subsequently, the meaning of subscript "eq" is consistent with definition (3.14) for deformation related quantities. Now, let

$$\langle d_{\text{eq}} \rangle_{(\beta,\varphi)} \equiv \frac{\int_0^\pi \int_0^{2\pi} d_{\text{eq}} g_{\lambda\lambda} \sin\beta \, d\varphi \, d\beta}{\int_0^\pi \int_0^{2\pi} g_{\lambda\lambda} \sin\beta \, d\varphi \, d\beta} = \frac{3}{4\pi(2a^2+b^2)} \int_0^\pi \int_0^{2\pi} d_{\text{eq}} g_{\lambda\lambda} \sin\beta \, d\varphi \, d\beta \tag{3.30}$$

be the average value of d_{eq} over coordinates β and φ. Then, using the change of variable $y = c^3/ab^2$, (3.28) becomes:

$$\Pi(\mathbf{D}) = \bar{\sigma} y_2 \int_{y_2}^{y_1} \langle d_{\text{eq}} \rangle_{(\beta,\varphi)} \frac{dy}{y^2} \tag{3.31}$$

which can be rigorously bounded from above by

$$\Pi(\mathbf{D}) = \bar{\sigma} y_2 \int_{y_2}^{y_1} \langle d_{\text{eq}}^2 \rangle_{(\beta,\varphi)}^{1/2} \frac{dy}{y^2} \tag{3.32}$$

using Hölder's inequality. We recall that subscripts 1 and 2 in the bounds of the integral refer to the inner void surface and outer surface of the RVE, respectively. Note at this juncture that the above change of variable to y singles out the case of a spherical cavity (for which $c \to 0$). A special treatment in that case leads to the criterion developed by Benzerga and Besson [32] since the velocity field $\mathbf{v}^A$ reduces to

a spherically symmetric field. We shall seek to recover this special case as the limit of the final criterion when $y_2 \to 0$. Now, from (3.29) we have

$$\langle d_{\mathrm{eq}}^2 \rangle_{(\beta,\varphi)} = A^2 \langle d_{\mathrm{eq}}^{A^2} \rangle_{(\beta,\varphi)} + {\beta_{\mathrm{eq}}}^2 + \frac{4}{3} A \langle d_{33}^A \rangle_{(\beta,\varphi)} \mathbf{Q} : \hat{\mathbb{h}} : \boldsymbol{\beta} \tag{3.33}$$

with

$$\mathbf{Q} \equiv -\frac{1}{2}(\mathbf{e}_1 \otimes \mathbf{e}_1 + \mathbf{e}_2 \otimes \mathbf{e}_2) + \mathbf{e}_3 \otimes \mathbf{e}_3 \tag{3.34}$$

Exact integration of (3.32) with the integrand specified through (3.33) and (4.5) is ruled out due to the complexity of the expression for d_{eq}^A. Anticipating approximations to come, in the spirit of [38], we define two new functions $F(u)$ and $G(u)$ through

$$\langle d_{\mathrm{eq}}^{A^2} \rangle_{(\beta,\varphi)} = F^2(u) u^2, \qquad \langle d_{33}^A \rangle_{(\beta,\varphi)} = F(u) G(u) u^2, \qquad u \equiv \begin{cases} y & \text{(p)} \\ \frac{y}{y+1} & \text{(o)} \end{cases} \tag{3.35}$$

thus operating a change of the spatial variable from y to u. This change of variable leaves the form of the integral in (3.32) unchanged for both prolate and oblate cavities. After rearranging, $\langle d_{\mathrm{eq}}^2 \rangle_{(\beta,\varphi)}$ may be written as

$$\langle d_{\mathrm{eq}}^2 \rangle_{(\beta,\varphi)} = \left[A \frac{F(u)}{\sqrt{\hat{h}_q}} \mathbf{Q} + \sqrt{\hat{h}_q} G(u) \boldsymbol{\beta} \right]_{\mathrm{eq}}^2 u^2 + H^2(u) {\beta_{\mathrm{eq}}}^2, \qquad H^2(u) \equiv 1 - \hat{h}_q G^2(u) u^2 \tag{3.36}$$

See above for the meaning of subscript "eq" and $\hat{h}_q$ is defined by

$$\hat{h}_q \equiv \frac{2}{3} \mathbf{Q} : \hat{\mathbb{h}} : \mathbf{Q} = \frac{\hat{h}_{11} + \hat{h}_{22} + 4\hat{h}_{33} - 4\hat{h}_{23} - 4\hat{h}_{31} + 2\hat{h}_{12}}{6} \tag{3.37}$$

$\hat{h}_{ij}$ above denote the Voigt-condensed components of the fourth-order tensor $\hat{\mathbb{h}}$, expressed in the basis associated with the void, hence the appearance of terms h_{23} etc. Since $\mathbf{Q}$ is axially symmetric about $\mathbf{e}_3$, it is clear that $\hat{h}_q$ is invariant with respect to the choice of axes $\mathbf{e}_1$ and $\mathbf{e}_2$ in Fig. 22.

Approximation $\mathcal{A}_2$: We simplify the spatial fluctuations of the microscopic rate of deformation by replacing functions $F(u)$, $G(u)$ and $H(u)$ in (3.36) by constants that approximately realize the minimum overall dissipation under some particular loading paths.

This permits evaluation of integral (3.32) in closed form. The accuracy of $\mathcal{A}_2$ can readily be assessed using numerical integration as illustrated in [40] for transversely isotropic materials under axisymmetric loadings. In general, however, $\mathcal{A}_2$ is an "uncontrolled" approximation in the sense that it does not necessarily preserve the upper-bound character of $\Pi(\mathbf{D})$ under all loading paths. In Appendix 1 we study the spatial fluctuations of the deformation to justify replacing $F(u)$, $G(u)$ and $H(u)$ by constants designated $\bar{F}, \bar{G}$ and $\bar{H}$, respectively. For a frozen microstructure, the value of $\bar{F}$ is chosen such that the analytical criterion yields a close approximation to the true yield criterion for purely hydrostatic loading, while $\bar{G}$ and $\bar{H}$ are chosen such that the analytical criterion provides a close match to the true yield criterion for purely deviatoric axisymmetric loading about the void axis. Here, by true yield locus we mean the locus defined by equations (3.5) and (3.28) evaluated using the four velocity fields chosen in Section 3 and determined numerically without approximations. The precise constants $\bar{F}$, $\bar{G}$ and $\bar{H}$ and their dependence upon f and w will be specified later.

Thus, substituting (3.36) in (3.32) in view of $\mathcal{A}_2$, we can write the plastic dissipation in the Gurson-like form

$$\Pi(\mathbf{D}) = \bar{\sigma} y_2 \int_{u_2}^{u_1} \sqrt{\tilde{A}_{\mathrm{eq}}^2 u^2 + \tilde{B}_{\mathrm{eq}}^2} \frac{du}{u^2} \tag{3.38}$$

where $\tilde{\mathbf{A}}$ and $\tilde{\mathbf{B}}$ are traceless tensors defined by

$$\tilde{\mathbf{A}} \equiv A\frac{\bar{F}}{\sqrt{\hat{h}_q}}\mathbf{Q} + \sqrt{\hat{h}_q}\bar{G}\boldsymbol{\beta}, \qquad \tilde{\mathbf{B}} \equiv \bar{H}\boldsymbol{\beta} \tag{3.39}$$

To obtain the closed form expression of the macroscopic yield locus, the components of $\mathbf{D}$ are to be eliminated from the parametric equation (3.5). $\mathbf{D}$ enters implicitly the equation above through A and $\boldsymbol{\beta}$. In Appendix 2 we provide the key steps for partial elimination of the parameters, leading to the following equation for the yield locus

$$q_2 C\frac{3}{2}\frac{\boldsymbol{\Sigma}:\mathbb{H}:\boldsymbol{\Sigma}}{\bar{\sigma}^2} + 2(g+1)(g+f)\cosh\left(q_1\kappa\frac{\boldsymbol{\Sigma}:\mathbf{X}}{\bar{\sigma}}\right) - (g+1)^2 - (g+f)^2 = 0 \tag{3.40}$$

where

$$\mathbb{H} \equiv (\mathbb{I} + \eta(\mathbf{X}\otimes\mathbf{Q}):\hat{\mathbb{p}}):\mathbb{p}:(\mathbb{I} + \hat{\mathbb{p}}:(\eta\mathbf{Q}\otimes\mathbf{X})), \tag{3.41}$$

$$\mathbf{X} \equiv \alpha_2(\mathbf{e}_1\otimes\mathbf{e}_1 + \mathbf{e}_2\otimes\mathbf{e}_2) + (1-2\alpha_2)\mathbf{e}_3\otimes\mathbf{e}_3 \tag{3.42}$$

and q_1 and q_2 are scalar-valued functions of $\boldsymbol{\beta}/A$. For example,

$$q_1 = \sqrt{1 + R_{\text{eq}}^2/\hat{h}_q}; \qquad \mathbf{R} \equiv \frac{(\mathbf{Q}:\hat{\mathbb{p}}:\mathbf{Q})\boldsymbol{\beta}/A - (\mathbf{Q}:\hat{\mathbb{p}}:\boldsymbol{\beta}/A)\mathbf{Q}}{\frac{3}{2}\bar{F}/\bar{G} + \mathbf{Q}:\hat{\mathbb{p}}:\boldsymbol{\beta}/A} \tag{3.43}$$

Expressions of the criterion parameters C, g, κ, η and α_2 are given in Appendix 3. They are tied to the constants involved in approximation $\mathcal{A}_2$ above, i.e., $\bar{F}$, $\bar{G}$ and $\bar{H}$ whose derivation is also given in Appendix 3. Most parameters depend on the anisotropy tensor $\mathbb{h}$; all of them are implicit functions of microstructural variables f and w. The effect of void orientation enters the criterion through tensors $\mathbf{Q}$ and $\mathbf{X}$ defined by (4.5) and (4.4), respectively, while matrix anisotropy enters via tensors $\mathbb{h}$ and $\hat{\mathbb{h}}$. An important formal difference with the model of Benzerga and Besson [32] is that the fourth order tensor $\mathbb{H}$, which may be termed the macroscopic plastic anisotropy tensor, is different from the microscopic anisotropy tensor $\mathbb{h}$. This difference stems from the fact that the expansion velocity field $\mathbf{v}^A$ used in the previous work was

spherically symmetric, whereas that used now is not. In the limit of a spherical cavity, $q_1 \to 1$ and so does q_2. We thus check that the criterion does not depend on the void orientation (see Appendix 2).

Finally, since the plastic dissipation $\Pi(\mathbf{D})$ is positively homogeneous of degree 1, elimination of the ratio $\boldsymbol{\beta}/A$, which appears through q_1 and q_2, from criterion (3.40) is possible, at least in principle. However, the resulting criterion would be unnecessarily complicated. For the sake of simplicity, therefore, we adopt the final approximation as follows:

Approximation $\mathcal{A}_3$: The derived yield criterion is approximated by replacing the coefficients q_1 and q_2 by unity in equation (3.40).

In Appendix 4 we provide some arguments pleading in favor of this approximation. The final form of the derived anisotropic yield criterion is thus written as $\mathcal{F}(\boldsymbol{\Sigma}) = 0$ with

$$\mathcal{F}(\boldsymbol{\Sigma}) = C\frac{3}{2}\frac{\boldsymbol{\Sigma} : \mathbb{H} : \boldsymbol{\Sigma}}{\bar{\sigma}^2} + 2(g+1)(g+f)\cosh\left(\kappa\frac{\boldsymbol{\Sigma} : \mathbf{X}}{\bar{\sigma}}\right) - (g+1)^2 - (g+f)^2 \quad (3.44)$$

where, in view of approximation $\mathcal{A}_3$, $\mathbb{H}$ is given by

$$\mathbb{H} \equiv \mathbb{p} + \eta(\mathbf{X} \otimes \mathbf{Q} + \mathbf{Q} \otimes \mathbf{X}) \quad (3.45)$$

$\mathbf{Q}$ by (4.5), $\mathbf{X}$ by (4.4) and the criterion parameters κ, α_2, g, C and η are provided in Appendix 3. Recall the definitions of the anisotropy tensors $\mathbb{p}$ and $\hat{\mathbb{p}}$ from (3.15).

In the special case of an isotropic Von Mises matrix ($\mathbb{h} = \hat{\mathbb{h}} = \mathbb{I}$) equation (4.2) reduces to the form proposed by Gologanu et al. [38]. However, Gologanu et al. had proposed the above form as a heuristic generalization of an axisymmetric criterion derived using a similar limit analysis. In the case of spherical voids in a Hill matrix,

from (4.50) one obtains $\lim_{w\to 1}\alpha_2 = 1/3$ and from (4.51) $C = 1$ and $\eta = 0$. Also, (4.48) reduces to

$$\kappa^{\mathrm{BB}} = \frac{3}{2}\sqrt{\frac{5}{(\hat{h}_q + 2\hat{h}_a + 2\hat{h}_t)}} = \frac{3}{2}\left[\frac{2}{5}\frac{h_{\mathrm{L}} + h_{\mathrm{T}} + h_{\mathrm{S}}}{h_{\mathrm{L}}h_{\mathrm{T}} + h_{\mathrm{T}}h_{\mathrm{S}} + h_{\mathrm{S}}h_{\mathrm{L}}} + \frac{1}{5}\left(\frac{1}{h_{\mathrm{TS}}} + \frac{1}{h_{\mathrm{SL}}} + \frac{1}{h_{\mathrm{LT}}}\right)\right]^{-\frac{1}{2}} \tag{3.46}$$

in terms of Hill's coefficients from Section 2 and the upper-bound yield criterion of Benzerga and Besson [32] is recovered. Note that κ^{BB} is an invariant of tensor $\mathbb{h}$ but $\hat{h}$, $\hat{h}_a$ and $\hat{h}_t$ are only transversely isotropic invariants. In particular, the Gurson yield function is obtained in the limit of spherical voids in an isotropic matrix since $\mathbb{h} = \mathbb{I}$ implies $\kappa^{\mathrm{BB}} = 3/2$.

In the limit of cylindrical voids in a Hill matrix with $\mathbf{e}_{\mathrm{S}} = \mathbf{e}_3$, we have $\lim_{w\to\infty}\alpha_2 = 1/2$ $C = 1$, $\eta = 0$ and (4.48) reduces to

$$\kappa^{\mathrm{cyl}} = \sqrt{\frac{3}{\hat{h}_t}} = \sqrt{3}\left[\frac{1}{4}\frac{h_{\mathrm{L}} + h_{\mathrm{T}} + 4h_{\mathrm{S}}}{h_{\mathrm{L}}h_{\mathrm{T}} + h_{\mathrm{T}}h_{\mathrm{S}} + h_{\mathrm{S}}h_{\mathrm{L}}} + \frac{1}{2h_{\mathrm{LT}}}\right]^{-\frac{1}{2}} \tag{3.47}$$

which is the result obtained by Benzerga and Besson [32][2]. In particular, the Gurson yield function for cylindrical cavities in a Von Mises matrix is recovered with $\kappa^{\mathrm{cyl}} = \sqrt{3}$ in that case.

F. Example Yield Loci

The yield surface defined by equation (4.2) may be visualized as the boundary of a convex region in the Haigh–Westergaard stress space (three-dimensional space with the principal stresses $\Sigma_{\mathrm{I}}, \Sigma_{\mathrm{II}}, \Sigma_{\mathrm{III}}$ as the Cartesian coordinates). It is conventional in plasticity theory to use cylindrical coordinates $z = \Sigma_{\mathrm{m}}$, $r = \sqrt{\boldsymbol{\Sigma}' : \boldsymbol{\Sigma}'} = \sqrt{2/3}\Sigma_e$ and θ such that $\cos(3\theta) = 27/2\det(\boldsymbol{\Sigma}'/\Sigma_e)$. As in equation (3.1), Σ_e and Σ_{m} are

[2]There are two typographical errors in [32] (i) the exponent 1/2 was dropped in print; and (ii) $\Sigma_{\alpha\alpha}$ should read $\Sigma_{11} + \Sigma_{22}$ after their equation (58).

the Von Mises effective stress and mean normal stress, respectively, and θ is the Lode angle. Cross-sections of the yield surface corresponding to the family of planes $\Sigma_{\rm m}$ = cste are called π-planes and the cross sections corresponding to θ = cste are called meridional planes. It is emphasized that, the yield function (4.2) being anisotropic, the shape of the yield surface in principal stress space will vary depending on the relative orientations of the principal axes of loading, the axes of orthotropy of the matrix and the axis of symmetry of the void.

In this section, we present cross-sections of the yield surface corresponding to special cases of loading. The first cross-section corresponds to triaxial loadings sharing a common value of $\Sigma_{\rm m}$. This cross-section represents the trace of the yield surface on a π-plane. The second cross-section corresponds to axisymmetric loading about the $\mathbf{e}_{\rm III}$ axis, $\mathbf{\Sigma} = \Sigma_{\rm m}\mathbf{I} + \Sigma^{'}/3(-\mathbf{e}_{\rm I}\otimes\mathbf{e}_{\rm I} - \mathbf{e}_{\rm II}\otimes\mathbf{e}_{\rm II} + 2\mathbf{e}_{\rm III}\otimes\mathbf{e}_{\rm III})$. The third cross-section corresponds to in-plane shear loading with a superposed hydrostatic stress, $\mathbf{\Sigma} = \Sigma_{\rm m}\mathbf{I}+\Sigma^{'}/\sqrt{3}(\mathbf{e}_{\rm I}\otimes\mathbf{e}_{\rm I}-\mathbf{e}_{\rm II}\otimes\mathbf{e}_{\rm II})$. Note that for the latter types of loading, the Von Mises effective stress $\Sigma_e = |\Sigma^{'}|$. Assuming that the Lode angle θ is measured with respect to the $\Sigma^{'}_{\rm III}$ axis in the π-plane, the above two cross-sections correspond to the traces of the yield surface on meridional planes defined by $\theta = n\pi$ and $\theta = (n+1/2)\pi$, respectively, with $n = 0, 1$. In all cases, the values of the stresses are normalized by a reference stress, $\bar{\sigma} \equiv \sigma_{\rm S}$, which is identified with the yield stress of the matrix material along direction of orthotropy $\mathbf{e}_{\rm S}$. Also, all examples below are shown for a porosity $f = 0.1$.

Four orthotropic materials are considered for the matrix. Their Hill coefficients are listed in Table III (see Section B). We consider two configurations of the microstructure, characterized by the orientation of the void axis relative to the axes of orthotropy of the matrix. In the first case, referred to as the "aligned" configuration, the void axis $\mathbf{e}_3$ is taken to be aligned with the $\mathbf{e}_{\rm S}$ axis of orthotropy. In the

Table IV. Orientations of the principal axes of loading relative to the microstructure, corresponding to the yield loci of Figs. 28–31.

Label	Loading orientation
L_1	$\mathbf{e}_{\mathrm{I}} = \mathbf{e}_{\mathrm{L}}, \mathbf{e}_{\mathrm{II}} = \mathbf{e}_{\mathrm{T}}, \mathbf{e}_{\mathrm{III}} = \mathbf{e}_{\mathrm{S}}$
L_2	$\mathbf{e}_{\mathrm{I}} = \mathbf{e}_{\mathrm{L}}, \mathbf{e}_{\mathrm{II}} = \mathbf{e}_{\mathrm{S}}, \mathbf{e}_{\mathrm{III}} = -\mathbf{e}_{\mathrm{T}}$
L_3	$\mathbf{e}_{\mathrm{I}} = \mathbf{e}_{\mathrm{L}}, \mathbf{e}_{\mathrm{II}} = \frac{1}{\sqrt{2}}(\mathbf{e}_{\mathrm{T}} + \mathbf{e}_{\mathrm{S}}), \mathbf{e}_{\mathrm{III}} = \frac{1}{\sqrt{2}}(-\mathbf{e}_{\mathrm{T}} + \mathbf{e}_{\mathrm{S}})$

second case, referred to as the "misaligned" configuration, an arbitrary orientation is chosen for the void axis relative to the matrix, $\mathbf{e}_3 = 1/7(2\mathbf{e}_{\mathrm{L}} + 3\mathbf{e}_{\mathrm{T}} + 6\mathbf{e}_{\mathrm{S}})$. In the case of the aligned configuration, the effective medium will be orthotropic with the same triad of orthotropy as the matrix material $(\mathbf{e}_{\mathrm{L}}, \mathbf{e}_{\mathrm{T}}, \mathbf{e}_{\mathrm{S}})$. In particular, when the matrix material is transversely isotropic about the $\mathbf{e}_{\mathrm{S}}$ axis (materials 1 and 2 from Table III), the effective medium will exhibit transverse isotropy about the $\mathbf{e}_{\mathrm{S}}$ axis. On the other hand, the misaligned configuration does not admit any orthotropic symmetry. Three loading cases are considered depending on the orientation of the principal axes of loading $(\mathbf{e}_{\mathrm{I}}, \mathbf{e}_{\mathrm{II}}, \mathbf{e}_{\mathrm{III}})$ relative to the material axes, Table IV. In cases L_1 and L_2, the principal axes of loading are aligned with the axes of orthotropy of the matrix, whereas L_3 corresponds to off-axis loading.

We first start with the case of materials containing spherical voids embedded in anisotropic matrices. In that case, the new criterion reduces to that of Benzerga and Besson [32]. The yield loci corresponding to all four materials from Table III are compared in Fig. 28 for various loading configurations. For loadings aligned with the matrix (L_1), Figs. 28(a) and (b) show the traces of the yield surfaces on the π-plane $\Sigma_{\mathrm{m}} = 0$ and the yield loci for axisymmetric loading about the $\mathbf{e}_{\mathrm{III}}$ axis, respectively. The yield loci in the π-plane for the isotropic matrix and materials 1–2 are perfect circles. This is a consequence of Hill coefficients h_1, h_2 and h_3 being equal in these

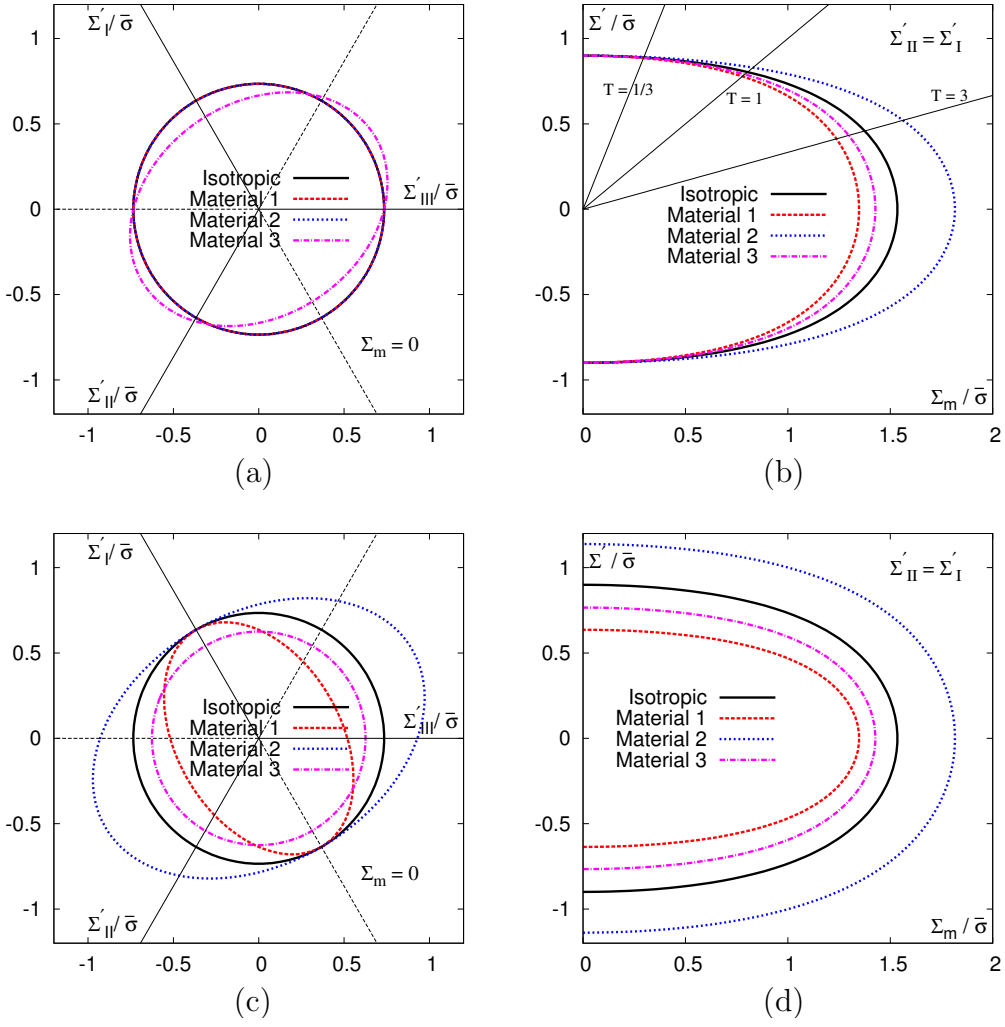

Fig. 28. Cross-sections of the yield surface for a spherical cavity with $f = 0.1$ and the four different anisotropic materials from Table III. The loading orientations L_1–L_3 correspond to Table IV. Orientation L_1 – (a) π-plane with $\Sigma_m = 0$ (b) axisymmetric loading with $\Sigma'_{II} = \Sigma'_I$. Orientation L_3 – (c) π-plane with $\Sigma_m = 0$ (d) axisymmetric loading with $\Sigma'_{II} = \Sigma'_I$. Stresses are normalized by the yield stress of the matrix material under uniaxial tension in the $\mathbf{e}_S$ direction of orthotropy.

materials. By way of contrast, the yield locus of Material 3 is an ellipse. In general, the elliptical shape of the yield locus on the π-plane is a signature of the Hill criterion assumed for the matrix and introduces a Lode angle dependence for the effective yield criterion. For reference, the yield loci of the sound matrices (i.e. for $f = 0$) are cylinders whose cross-sections are similar to the cross-sections in the π plane (shown in parts (a) of Fig. 28 and subsequent figures), but are bigger by a factor $1/(1 - f)$.

Since the yield function is indifferent to the sign of stress, the yield surface is symmetric with respect to inversion about the origin (point symmetry). Hence only the halves of the axisymmetric yield loci corresponding to $\Sigma_{\mathrm{m}} > 0$ are shown in Fig. 28b. For the spherical voids considered here, the axisymmetric yield loci are also symmetric with respect to the Σ_{m} axis. The radial lines in Fig. 28(b) correspond to proportional loading paths, i.e., with fixed stress triaxiality ratio T. In practice, values of T greater than 4 are rarely attained. Notice that even though the yield points themselves may be close to each other, the normals to the yield loci vary considerably from one material to another, especially towards higher values of T.

Figs. 28(c)-(d) show the corresponding yield loci for the off-axis loading case L_3. Here, all the yield traces in the π-plane are ellipses centered at the origin. The apparent Lode-angle dependence is thus exacerbated under off-axes loadings. Interestingly, in Fig. 28(c), one may notice that the yield locus for Material 3 is nearly circular in shape, indicating that the Lode angle dependence of the yield criterion may disappear depending on the orientation of loading relative to the material.

Next, consider the case of materials containing oblate voids with $w = 1/5$ in an isotropic matrix, Fig. 29. In this case, the new yield criterion coincides with that of Gologanu et al. [38]. Results for all loading orientations L_1–L_3 are shown superposed on each other. Figs. 29(a)-(b) show the π-plane cross-sections corresponding to $\Sigma_{\mathrm{m}} = 0$ and $\Sigma_{\mathrm{m}} = 0.9\Sigma^h$, respectively, where Σ^h designates the yield stress of the effective

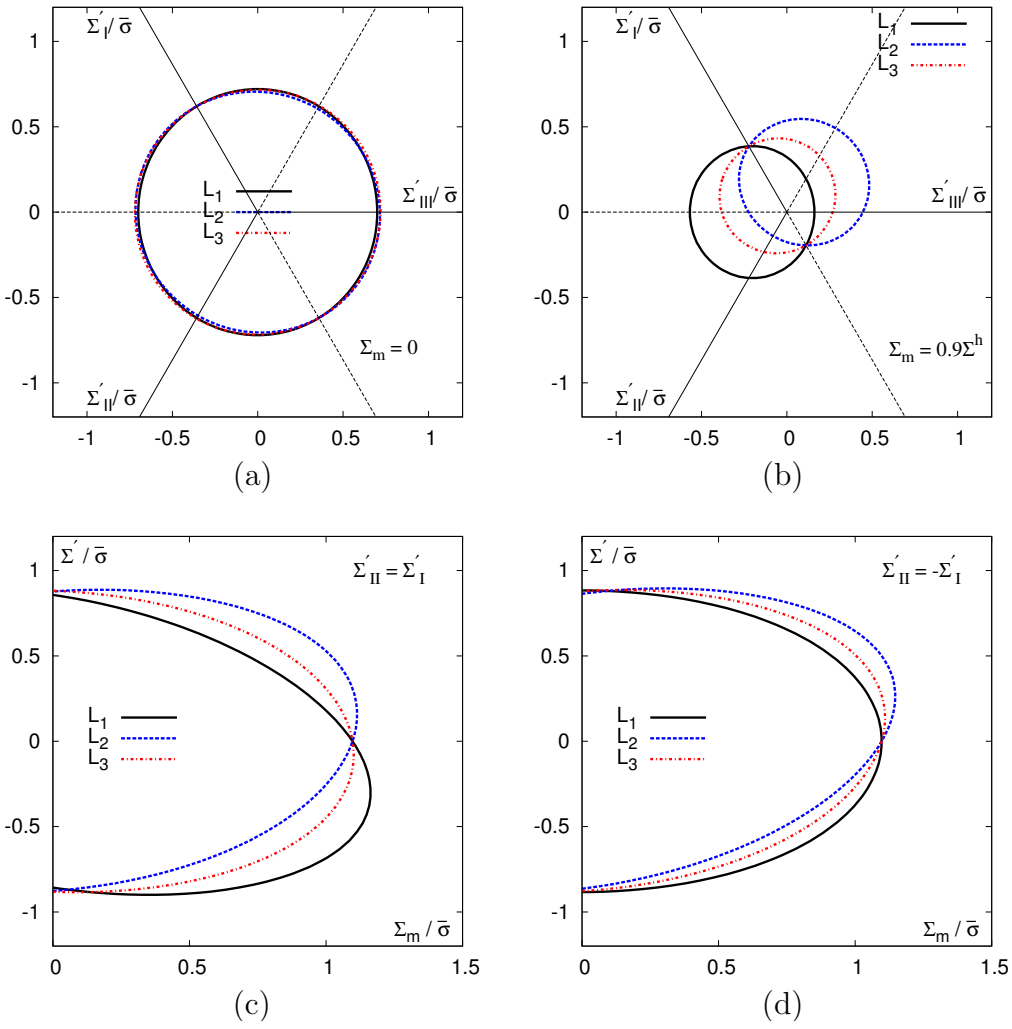

Fig. 29. Cross-sections of the yield surface for an oblate cavity with $f = 0.1$, $w = 1/5$ and an isotropic matrix. The loading orientations L_1–L_3 correspond to Table IV. (a) π-plane with $\Sigma_m = 0$ (b) π-plane with $\Sigma_m = 0.9\Sigma^h$ (c) axisymmetric loading with $\Sigma'_{II} = \Sigma'_I$ (d) in-plane shear with superposed hydrostatic stress, $\Sigma'_{II} = -\Sigma'_I$. Stresses are normalized by the yield stress of the matrix material under uniaxial tension in the $\mathbf{e}_S$ direction of orthotropy.

medium under pure hydrostatic loading. Although barely visible in Fig. 29(a), the non-spherical void shape leads to a slightly oval shape for the yield locus in the π-plane. However, the main effect of void shape is apparent for non-zero values of the mean stress as in Fig. 29(b). Depending on the loading orientation, the centroid of the yield locus moves away from the $\Sigma_{\mathrm{m}} = 0$ axis. This effect is also manifest in Figs. 29(c)-(d), which correspond to the cases of axisymmetric and transverse shear loadings, respectively, with a superposed hydrostatic stress. Note that, unlike in the case of spherical voids, these loci do not exhibit symmetry with respect to either coordinate axis.

Consider now the case of oblate voids (again with $w = 1/5$) embedded in an orthotropic matrix (Material 3) in an aligned configuration, i.e., $\mathbf{e}_3 = \mathbf{e}_{\mathrm{S}}$. The results summarized in Fig. 30 are the counterpart of the results in Fig. 29 when the isotropic matrix is replaced by Material 3. Notice that these yield loci inherit some of the characteristic features from both Figs. 28 and 29. The shape of the yield locus in the π-plane is primarily determined by the anisotropy of the matrix while the location of the centroid is primarily determined by the void shape. However, it is worth noting that the combined effect is not a simple superposition of a shape change due to material texture and a translation due to void shape. This is best seen from the fact that, unlike in Figs. 28(a) and (c), the π-plane yield loci are not ellipses, but assume a general oval shape. Also, the anisotropy of the matrix has a secondary influence on the location of the centroid. Similar results for prolate cavities (not shown) exhibit all the above characteristics, albeit to a lesser extent. The main difference between prolate and oblate cavities is that, all other conditions being the same, oblate cavities exhibit a greater sensitivity to the mean stress (i.e. lower yield stresses at larger values of Σ_{m}).

Finally, Fig. 31 shows the yield loci for the most general case of oblate cavities

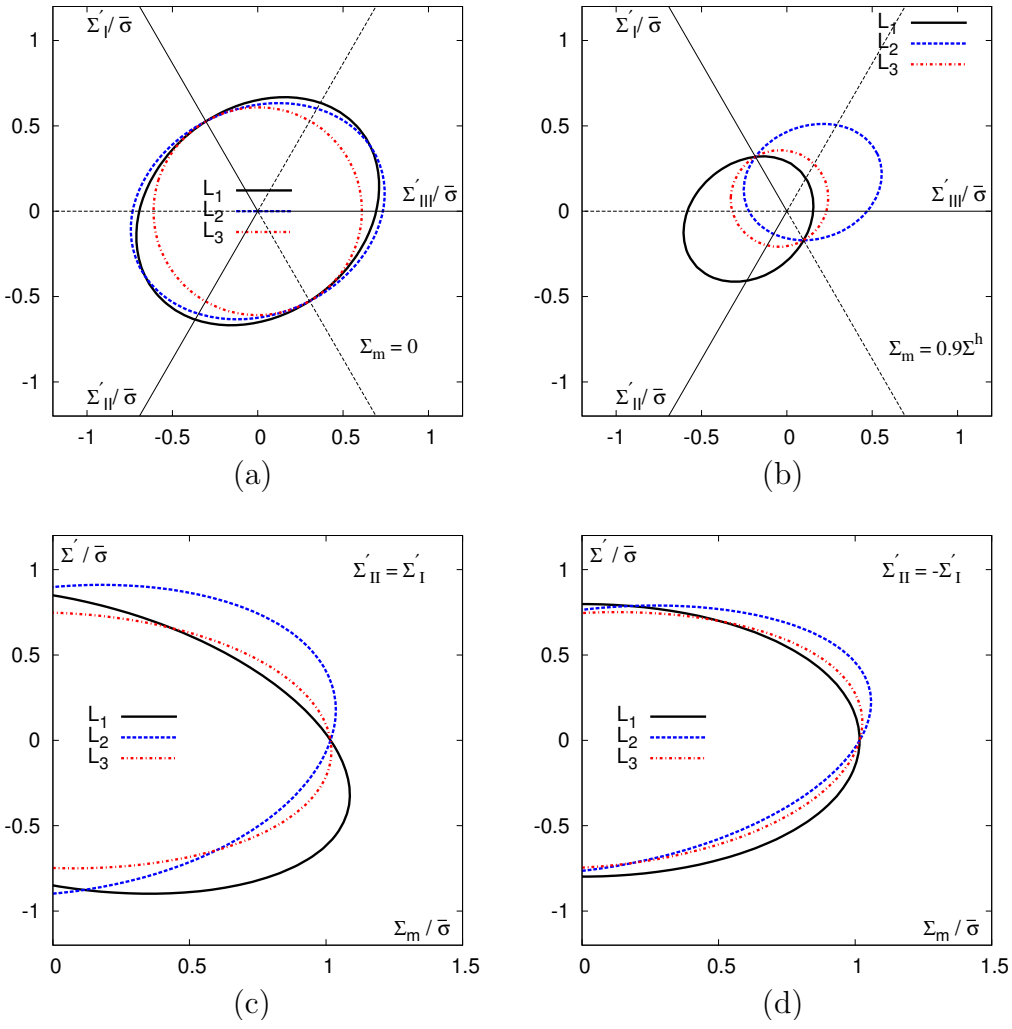

Fig. 30. Cross-sections of the yield surface for an oblate cavity with $f = 0.1$, $w = 1/5$ and Material 3 from Table III. Aligned microstructure with the void axis $\mathbf{e}_3 = \mathbf{e}_S$. The loading orientations L_1–L_3 correspond to Table IV. (a) π-plane with $\Sigma_m = 0$ (b) π-plane with $\Sigma_m = 0.9\Sigma^h$ (c) axisymmetric loading with $\Sigma'_{II} = \Sigma'_I$ (d) in-plane shear with superposed hydrostatic stress, $\Sigma'_{II} = -\Sigma'_I$. Stresses are normalized by the yield stress of the matrix material under uniaxial tension in the $\mathbf{e}_S$ direction of orthotropy.

($w = 1/5$) dispersed in an orthotropic matrix (Material 3) in a misaligned configuration ($\mathbf{e}_3 = 1/7(2\mathbf{e}_\mathrm{L} + 3\mathbf{e}_\mathrm{T} + 6\mathbf{e}_\mathrm{S})$). These results differ from those of Fig. 30 by the orientation chosen for the void axis $\mathbf{e}_3$. The π-plane yield loci in Figs. 31(a)-(b) reveal general oval shaped cross sections. Comparing Figs. 30(c)-(d) with Figs. 31(c)-(d) shows that there is a drastic reduction in the yield stresses at higher triaxialities in the case of the misaligned microstructure, indicating that the evolution of the microstructure due to sustained deformation can lead to significant weakening of the material.

While the analytical yield criterion, equation (4.2), has been derived using a rigorous variational approach, due to the approximations introduced in the derivations it is unclear whether the final result respects the upper-bound character of the approach. We have developed a numerical method to derive rigorous upper-bound yield loci for anisotropic materials containing spheroidal voids and subjected to axisymmetric loading about the void axis. The method is based on limit-analysis using a large number of velocity fields from the Lee-Mear decomposition [80], and has the property that it yields nearly exact results for the yield criterion in the particular case when the material exhibits transverse isotropy about the void axis. A more detailed study aimed at validation of the analytical criterion by comparison to the numerical upper-bound yield loci is presented in Chapter IV.

G. Microstructure Evolution

To close the constitutive formulation, evolution equations are needed for the microstructural variables that enter the criterion, i.e., void volume fraction, aspect ratio and orientation. Once these are specified, the constitutive equations can be integrated using a suitable scheme to obtain the stress-strain response of the material for

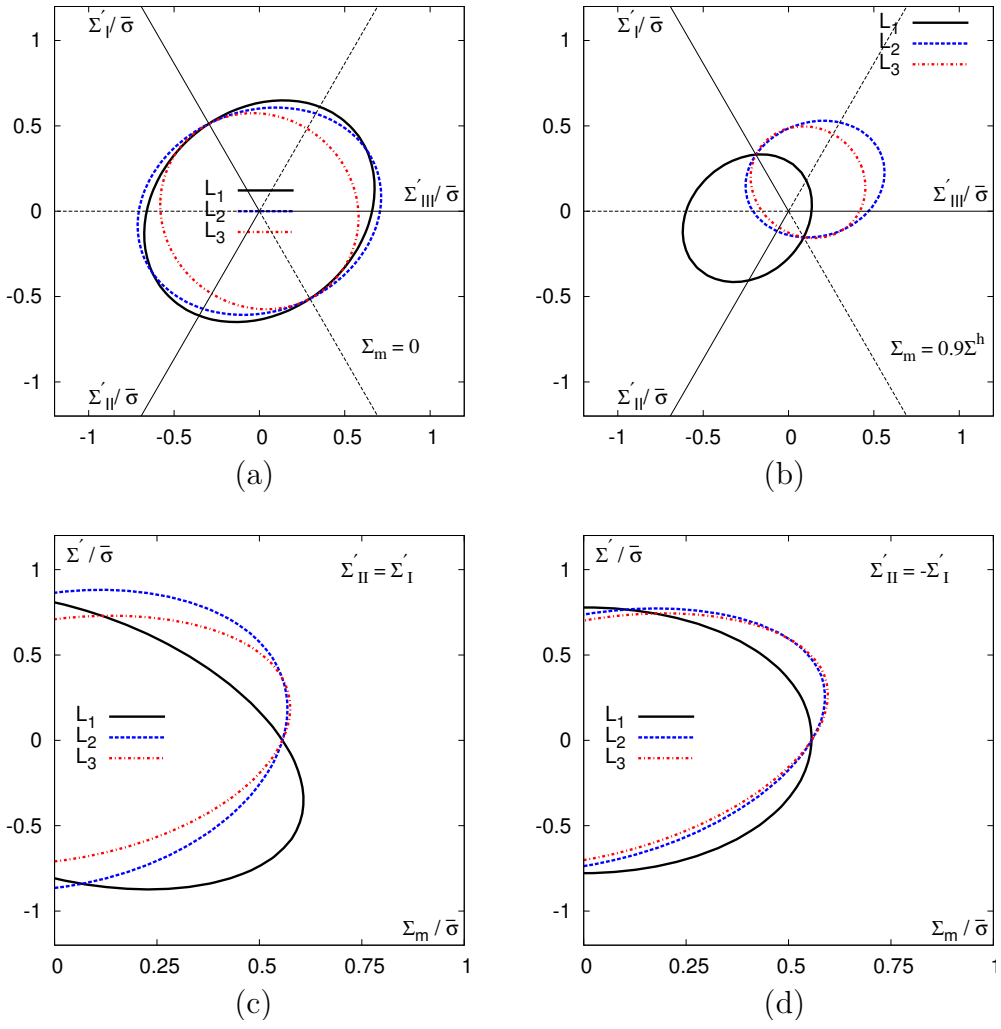

Fig. 31. Cross-sections of the yield surface for an oblate cavity with $f = 0.1$, $w = 1/5$ and Material 3 from Table III. Misaligned microstructure with the void axis $\mathbf{e}_3 = 1/7(2\mathbf{e}_\mathrm{L} + 3\mathbf{e}_\mathrm{T} + 6\mathbf{e}_\mathrm{S})$. The loading orientations L_1–L_3 correspond to Table IV. (a) π-plane with $\Sigma_\mathrm{m} = 0$ (b) π-plane with $\Sigma_\mathrm{m} = 0.9\Sigma^h$ (c) axisymmetric loading with $\Sigma'_\mathrm{II} = \Sigma'_\mathrm{I}$ (d) in-plane shear with superposed hydrostatic stress, $\Sigma'_\mathrm{II} = -\Sigma'_\mathrm{I}$. Stresses are normalized by the yield stress of the matrix material under uniaxial tension in the $\mathbf{e}_\mathrm{S}$ direction of orthotropy.

specified loading paths.

1. Evolution of Porosity

The evolution of void volume fraction, or porosity, follows directly from the assumption of an incompressible matrix so that

$$\frac{\dot{f}}{1-f} = D_{kk} \tag{3.48}$$

where $\mathbf{D}$ is entirely due to plastic deformation since elasticity is neglected. Given that the matrix obeys the normality flow rule, so does the effective material [12, 75]:

$$D_{ij} = \Lambda \frac{\partial \mathcal{F}}{\partial \Sigma_{ij}}(\mathbf{\Sigma}) \tag{3.49}$$

where $\mathcal{F}(\mathbf{\Sigma})$ denotes the yield function (4.2) and Λ the plastic multiplier. Combining (3.48) and the hydrostatic part of (4.9) we obtain the evolution equation for the porosity

$$\dot{f} = (1-f)\Lambda \frac{\partial \mathcal{F}}{\partial \Sigma_{\mathrm{m}}} \tag{3.50}$$

Thus, the evolution of porosity follows directly from the yield criterion. With the results of Figs 28-31 in mind, the following is worth noting. While the loci appear to be close to each other in the practical range of stress triaxialities the *normal* to the loci can vary considerably, even at low T. This has important implications for the evolution of the microstructure, as the evolution laws for the porosity and void shape are formulated in terms of the macroscopic plastic rate of deformation, which is normal to the yield locus. Hence, small differences in the yield loci can lead to large differences in the evolution of microstructural variables.

2. Evolution of Void Shape

a. Basic Form

Since the trial velocity field (3.17) contains a non-axisymmetric component, the model can be used to deliver evolution laws of two independent aspect ratios[3]. However, consistent with approximation $\mathcal{A}_1$, the void aspect ratio w is taken to represent the effective shape of the three-dimensional void, interpreting b_1 as the transverse semi-axis of an 'equivalent spheroid' whose volume equals that of the ellipsoid. For convenience, we define a void shape parameter $S \equiv \ln w$, so that $S > 0$ for prolate voids and $S < 0$ for oblate voids, Fig. 27. Thus,

$$\dot{S} = \frac{\dot{w}}{w} = \frac{\dot{a}_1}{a_1} - \frac{\dot{b}_1}{b_1} \tag{3.51}$$

To evaluate the right-hand side term in (3.51), we assume that the void is deforming homogeneously with rate of deformation $\mathbf{D}^v$, naturally defined by

$$D^v_{ij} = \langle d_{ij} \rangle_\omega = \frac{1}{2\omega} \int_{\partial\omega} (v_i n_j + v_j n_i) dS \tag{3.52}$$

where $\mathbf{n}$ is the unit normal to the boundary of the void. With the above interpretation in mind, it follows from (3.51) that

$$\dot{S} = D^v_{33} - \frac{1}{2}(D^v_{11} + D^v_{22}) \tag{3.53}$$

with the components of $\mathbf{D}^v$ calculated based on (3.52) and the chosen microscopic velocity fields in (3.17). Eliminating A and $\boldsymbol{\beta}$ using equations (3.69), we obtain

$$\mathbf{D}^v = \mathbf{D} + 3\left(\frac{1}{f}\mathbf{X}^v - \mathbf{X}\right) D_{\mathrm{m}} \tag{3.54}$$

---

[3]Note that such laws would be crude, since the assumed velocity fields of Section E do not depend on Hill's anisotropy factors. In actuality, the exact velocity field must be affected by the anisotropy.

where tensor $\mathbf{X}^v$ is defined similar to $\mathbf{X}$ in (4.4) with α_2 replaced by α_1. Combining (3.53) and (3.54) one gets

$$\dot{S} = \frac{3}{2} D'_{33} + 3 \left[\frac{1 - 3\alpha_1}{f} + 3\alpha_2 - 1 \right] D_{\mathrm{m}} \tag{3.55}$$

This equation constitutes the basic form for the evolution of void shape and does include an implicit dependence upon matrix anisotropy through the macroscopic rate of deformation, $\mathbf{D}$, which derives from yield criterion (4.2) by normality.

b. Alternative Approach

An alternative expression for the average rate of deformation of the void $\mathbf{D}^v$ was derived by Ponte Castañeda and Zaidman [67] using a micromechanical approach extending the classical Eshelby analysis [83] to the case of finite porosities. Their expression reads

$$\mathbf{D}^v = \mathbb{A} : \mathbf{D}, \qquad \mathbb{A} = [\mathbb{I} - (1 - f)\mathbb{S}]^{-1} \tag{3.56}$$

where $\mathbb{A}$ may be termed the strain concentration tensor and $\mathbb{S}$ is the Eshelby tensor for a spheroidal inclusion in an incompressible linear elastic isotropic matrix. One may use (3.56) in place of (3.54) in (3.53) to obtain an alternate estimate for the evolution of the shape parameter. Since a simple closed form expression for $\dot{S}$ of the type (3.55) can not be found in this case, implementing this approach involves evaluation of the strain concentration tensor $\mathbb{A}$, and hence $\mathbf{D}^v$, based on the current values of f and S and using (3.53) to evaluate $\dot{S}$. In this stiffness-based approach, the derived expression for $\mathbf{D}^v$ is independent of the microscopic velocity fields.

It must be emphasized, however, that neither the basic nor the alternate expression for $\mathbf{D}^v$ capture the complex effect of stress triaxiality that leads to cavity flattening under a major axial stress evidenced in finite element simulations [29, 84].

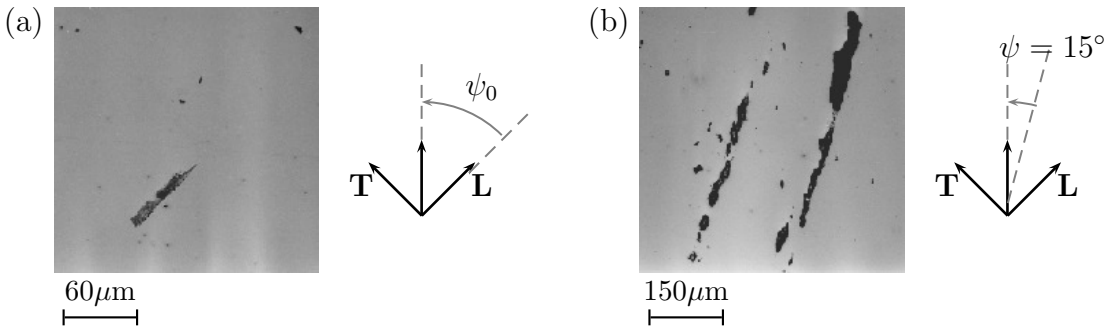

Fig. 32. Void rotation under off-axes triaxial loading of steel. (a) Initial configuration: elongated sulfide inclusion oriented at $\psi_0 = 45°$ from the vertical loading direction. (b) Deformed configuration: elongated cavities located in the neck of a notched bar and oriented at $\psi \approx 15°$ from the vertical loading direction.

In addition, similar FE calculations have revealed an effect of porosity on the magnitude of the deviatoric term in (3.55). This effect is implicitly contained in the alternate form (3.56), but the dependence is weaker than in FE calculations. Therefore, at present it does not seem to be possible to avoid completely all heuristics in the evolution law of void shape. In Chapter IV, we analyze possible heuristic extensions of (3.55). Here, it suffices to investigate the capability of this evolution law at capturing the nontrivial coupling between void growth and plastic anisotropy.

3. Evolution of Void Orientation

Under general loading conditions, the orientation of the void axis $\mathbf{e}_3$ evolves as a result of the macroscopic spin of the material in addition to the local plastic distortion. While the simplest proposal would be to assume that the spin rate of the voids is equal to the continuum spin, micrographic evidence of evolving material texture in notched tensile specimens [49] suggests that this is not necessarily the case (see Figure 32).

Based on a non-linear homogenization analysis, Kailasam and Ponte Castañeda

[68] have developed an expression for the void spin rate, which reads

$$\boldsymbol{\Omega}^v = \boldsymbol{\Omega} - \mathbb{C} : \mathbf{D} \tag{3.57}$$

where $\boldsymbol{\Omega}^v$ and $\boldsymbol{\Omega}$ represent the void and continuum spin tensors respectively. $\mathbb{C}$ represents the fourth order spin concentration tensor, which is given by

$$\mathbb{C} = -(1-f)\mathit{\Pi} : \mathbb{A} \tag{3.58}$$

where $\mathit{\Pi}$ is the Eshelby rotation tensor for a spheroidal inclusion in an incompressible linear matrix [83]. Simplified expressions for $\mathbb{S}$ and $\mathit{\Pi}$ for the cases of prolate and oblate spheroidal inclusions are provided in [83]. The evolution of the void orientation may then be obtained using the kinematical relationship

$$\dot{\mathbf{e}}_3 = \boldsymbol{\omega} \cdot \mathbf{e}_3, \qquad \boldsymbol{\omega} = \boldsymbol{\Omega}^v + \boldsymbol{\Omega}^l \tag{3.59}$$

where $\boldsymbol{\Omega}^l$ is an antisymmetric tensor given by

$$\Omega^l_{12} = 0, \quad \Omega^l_{i3} = \frac{w^2+1}{w^2-1} D^v_{i3} \qquad (i = 1, 2, \quad w \neq 1) \tag{3.60}$$

in the coordinate frame associated with the void (see [68]).

It may be remarked that the actual derivation of (3.57) assumes that the matrix is isotropic, and hence is strictly not applicable to the case of an anisotropic matrix like Hill's. Nevertheless, one can see that, as in equation (3.55) for the void shape evolution, equation (3.57) includes an implicit dependence of $\boldsymbol{\Omega}^v$ on material anisotropy through the macroscopic rate of deformation, $\mathbf{D}$. Hence, in the practical range of material anisotropy parameters, we may consider equation (3.57) as the best available estimate of the void spin rate.

4. Example

In this section, we compare the predictions of the analytical model, consisting of the yield function (4.2), flow rule (4.9) and the microstructure evolution laws (4.10) and (3.55), with the finite-element results presented in Section B for axisymmetric proportional loading at a moderate stress triaxiality ratio of $T = 1$. Since the materials considered are transversely isotropic, the void orientation does not change during loading ($\boldsymbol{\omega} \equiv \mathbf{0}$). For comparison, responses obtained using the alternative law for void shape evolution, i.e., equations (3.53) and (3.56), are also investigated. The constitutive equations are integrated using a backward Euler scheme. Strain hardening in the matrix is incorporated using the energy balance approach of Gurson [12], whereby the cumulative plastic strain $\bar{\epsilon}$ is evolved through

$$\boldsymbol{\Sigma} : \mathbf{D} = (1 - f)\bar{\sigma}\dot{\bar{\epsilon}} \tag{3.61}$$

The current yield stress in the matrix $\bar{\sigma}$ is determined using the same power law hardening model used in the FE calculations as described in Section B. Elasticity is included in the analytical model results using a hypoelastic form for the elastic constitutive law and assuming additive decomposition of the deformation rate tensor into elastic and plastic parts.

Figs. 33(a) and (b) show the stress versus strain and porosity versus strain curves predicted by the model. These results correspond to the unit-cell results of Figs. 25(a) and (b), respectively. Recall that the unit-cell results had evidenced a non-trivial coupling between the effects of void shape and plastic anisotropy of the matrix, the effect of void shape on the porosity rate being enhanced in the case of Material 1 and barely detectable in the case of Material 2. Comparison with the model predictions in Fig. 33(a)-(b) shows that the qualitative features of the unit-cell results are very well

reproduced by the model. In addition, the evolution of the void aspect ratio depicted in Fig. 33(c) shows that the model predictions yield a reasonably good match with the unit-cell results, which are summarized in Fig. 33(d). In the latter figure, the symbol (x) indicates the onset of void coalescence, which is not accounted for by the analytical model.

It is worth emphasizing that such qualitative behavior, notably the weak effect of void shape on void growth for material 2, is predicted without any heuristics in the evolution law (3.55). For better quantitative predictions, however, a heuristic "void interaction" parameter q could be introduced in the spirit of Gologanu et al. [38]. Further discussion of these issues may be found in Chapter IV. For comparison purposes, Fig. 34 shows the evolutions of porosity f and void aspect ratio w as predicted by the alternate evolution law for w due to [67] (see Section b). Just like the proposed model, the alternate model does a good a job at predicting the qualitative trends at $T = 1$ for both materials.

H. Conclusion and Outlook

Using nonlinear homogenization theory, limit analysis and elements from Eshelby micromechanics, a new model has been developed for plastically deforming solids containing spheroidal voids. Motivated by the experimental evidence of fracture and toughness anisotropy in a class of structural materials and by direct numerical simulations of void growth to coalescence, emphasis was laid on coupled effects of matrix material anisotropy and void shape. Notable among the model features are the following:

- A closed form expression for the effective yield locus was obtained which is applicable to arbitrary loadings, i.e, not necessarily aligned with the microstruc-

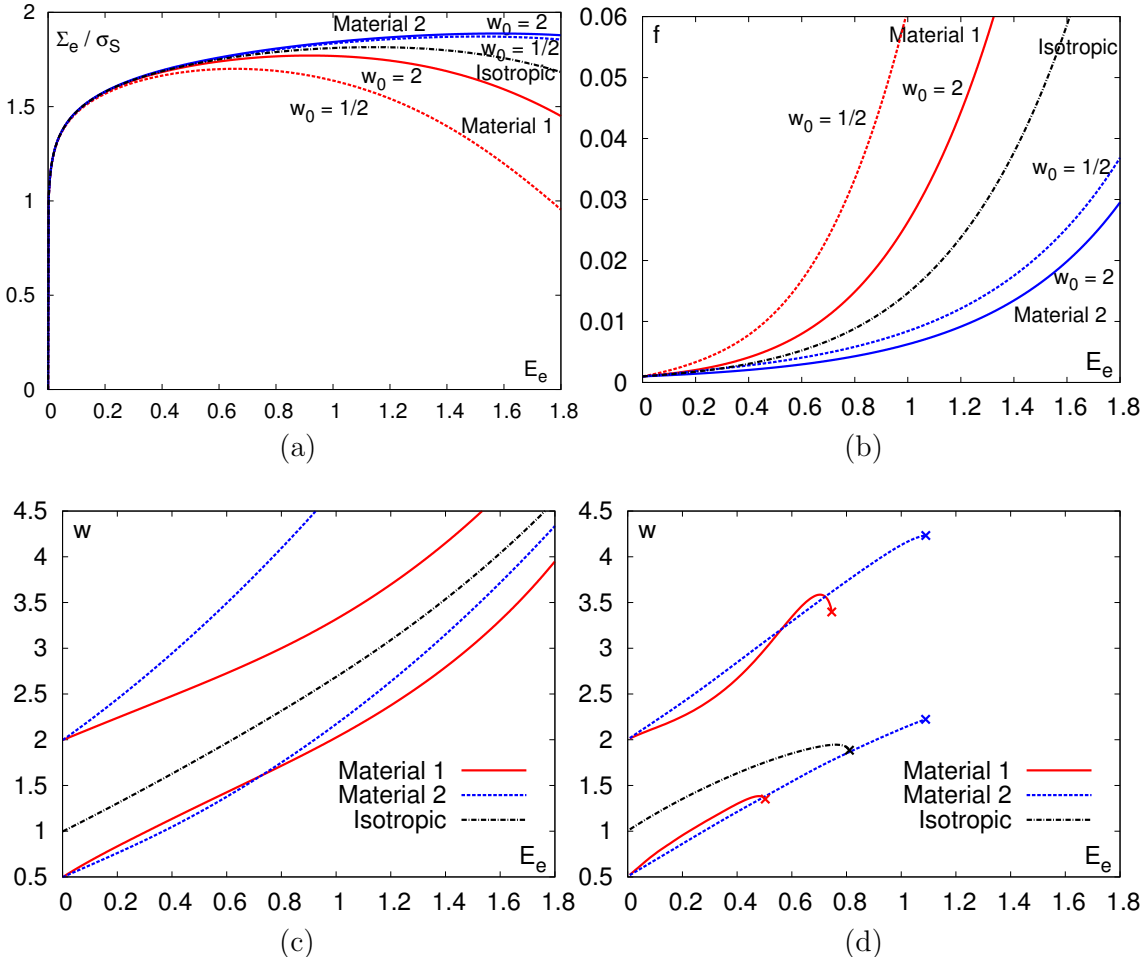

Fig. 33. Model predictions for the effective material response under axisymmetric loading, corresponding to the unit-cell results of Fig. 25, Section B: (a) Stress-strain response (b) Evolution of porosity (c) Evolution of void aspect ratio. The unit-cell results for the evolution of the void aspect ratio (not shown in Fig. 25) are shown in (d).

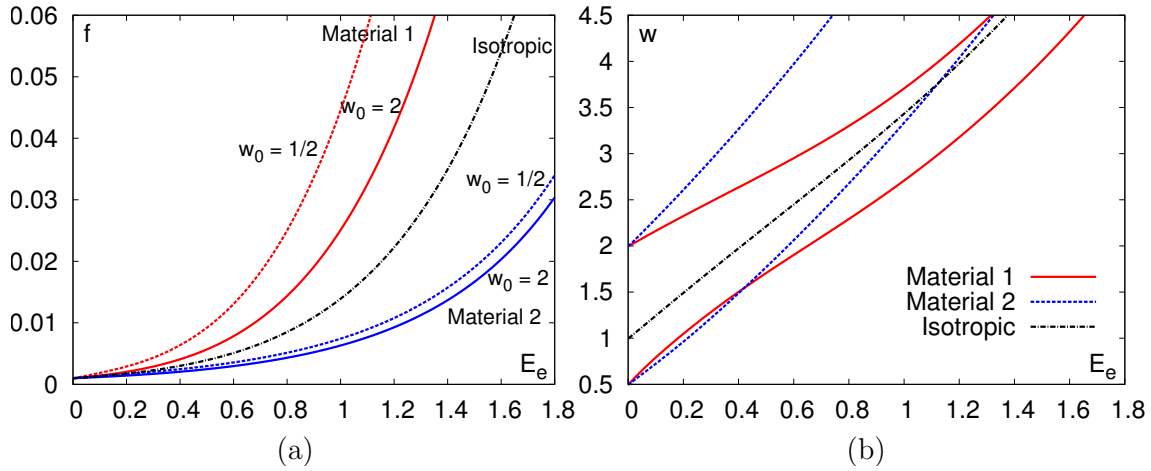

Fig. 34. Model predictions for the porosity f and void aspect ratio w using the alternate form (3.56) for void shape evolution in (3.53). Compare with Fig. 33(b) and (c).

ture, and arbitrary microstructures, i.e., principal directions of orthotropy not necessarily tied to the voids.

- The model has the capability to predict a much broader range of damage and fracture behaviors than with currently available models. For example, it picks up an apparent Lode-angle dependence as well as a shift of the yield surface in the π-plane for non vanishing amounts of hydrostatic stress.
- In the case of transversely isotropic materials and axisymmetric loadings, the model delivers quasi-exact results with any errors being associated with the cutoff in the velocity fields. It is demonstrated that the new yield criterion reduces to previously established results in the literature for the special cases of spheroidal voids in an isotropic matrix and spherical voids in a Hill matrix. The Gurson model is a special limit case of the model.
- Comparison with results of unit cell calculations using the finite element method has demonstrated the potential capabilities of the model at predicting complex microstructure evolution.

In addition, some of the model characteristics and limitations are common to other porous plasticity models, namely:

- Most attributes of the anisotropic plasticity model assumed at the microscale do not translate to the macroscale. In particular, the macroscopic behavior is not ideally plastic, it is sensitive to pressure and leads to dilation. In addition, macroscopic anisotropy evolves with deformation and carries the signature of the microstructure.
- Among the things that the model does not deliver for arbitrary loadings or general matrix anisotropies are the exact *microscopic* velocity fields. From the outset, this has not been the objective. The model delivers approximate but accurate *macroscopic* yield criteria.
- The closed form expression of the yield criterion was obtained using approximations that do not necessarily preserve the upper-bound character. For that reason, we have devoted a thorough numerical study to assess the approximations made (see Chapter IV). Complete validation of the new model would also require a critical assessment of microstructure evolution laws beyond the preliminary comparisons offered in Fig. 33. This requires comparison and calibration of the model against an extensive finite element investigation of anisotropic porous unit cells under controlled loading conditions of the type presented in Chapter II, which will be the subject of a forthcoming study.

I. Appendices

1. Rationale for Approximation $\mathcal{A}_2$

The microscopic deformation resulting from the trial expansion field $\mathbf{v}^A$ fluctuates within the RVE. Simplifying these fluctuations amounts to analyzing the variations

of functions $F(u)$ and $G(u)$ introduced in (4.33). We first examine the limits of these functions, aided by the Maple software. In the limit $u \to 0$ (i.e., spherical void) we get:

$$\lim_{u\to 0} F^2(u) = \lim_{y\to 0} \frac{1}{y^2} \langle d_{\text{eq}}^{A^2} \rangle_{(\beta,\varphi)} = \frac{4}{5}(\hat{h}_q + 2\hat{h}_t + 2\hat{h}_a), \tag{3.62}$$

and

$$\lim_{y\to 0} \langle d_{33}^{A} \rangle_{(\beta,\varphi)} = 0 \tag{3.63}$$

whereas in the limit $y \to \infty$ (i.e., cylindrical void in the prolate case and a "sandwich" in the oblate case) we obtain:

$$\begin{cases} \lim\limits_{u\to\infty} F^2(u) = \lim\limits_{y\to\infty} \dfrac{1}{y^2} \langle d_{\text{eq}}^{A^2} \rangle_{(\beta,\varphi)} & = 3\hat{h}_t & \text{(p)} \\ \lim\limits_{u\to 1} F^2(u) = \lim\limits_{y\to\infty} \langle d_{\text{eq}}^{A^2} \rangle_{(\beta,\varphi)} & = 9\hat{h}_q(3\pi B_{22} + 4B_{21})^2 + 6\hat{h}_a(\pi B_{21} + 12B_{22})^2 & \text{(o)} \end{cases} \tag{3.64}$$

and

$$\begin{cases} \lim\limits_{y\to\infty} \langle d_{33}^{A} \rangle_{(\beta,\varphi)} & = 0 & \text{(p)} \\ \lim\limits_{y\to\infty} \langle d_{33}^{A} \rangle_{(\beta,\varphi)} & = 12B_{21} + 9\pi B_{22} & \text{(o)} \end{cases} \tag{3.65}$$

where B_{21} and B_{22} were introduced in (4.28), $\hat{h}_q$ is defined by (3.37) and

$$\hat{h}_t \equiv \frac{\hat{h}_{11} + \hat{h}_{22} + 2\hat{h}_{66} - 2\hat{h}_{12}}{4}, \qquad \hat{h}_a \equiv \frac{\hat{h}_{44} + \hat{h}_{55}}{2}. \tag{3.66}$$

Here, $\hat{h}_{ij}$ are the components of tensor $\hat{\mathbb{h}}$ expressed using Voigt's condensation, with respect to the basis $(\mathbf{e}_i)$ associated with the voids[4]. The above limits call for some observations: (i) in the prolate case, $\langle d_{\text{eq}}^{A^2} \rangle_{(\beta,\varphi)}$ behaves asymptotically as y^2, hence the change of variable $u(y)$ in (4.33); (ii) in the oblate case, the asymptotic behavior at ∞ is different, hence the different mapping $u(y)$; and (iii) most importantly, all limits of $F(u)$ are finite. The only singular behavior is in the neighborhood of 0

[4]The values of $\hat{h}_t$ and $\hat{h}_a$ are invariant with respect to the choice of axes $\mathbf{e}_1$ and $\mathbf{e}_2$ transverse to the symmetry axis of the void.

for function $G(u)$, which is tied to the term $\langle d_{33}^A \rangle_{(\beta,\varphi)}$ via (4.33). This behavior is peculiar to the spherical void when considered in the limit $u \to 0$. Nevertheless, the corresponding term in equation (3.33) drops out rigorously in the limit of a spherical void due to the property (3.63), which is a consequence of the fact that the expansion velocity field $\mathbf{v}^{\mathrm{A}}$ reduces to a spherically symmetric field in the limit of a spherical void. Under such circumstances, the yield criterion can be derived without recourse to approximation $\mathcal{A}_2$ but the final expression would be consistent with that obtained in the general case using $\mathcal{A}_2$.

Next, we show that $F(u)$ behaves well in between the above limits. In doing so, we realize that the function to be studied is that for which the minimum overall dissipation is obtained when minimizing over the B_{2m} factors of the velocity field ($m = 0, 1, 2$). This function is denoted by $F^{\min}(u)$ for the sake of clarity. Numerically, $F^{\min}(u)$ may be determined for given plastic anisotropy, microstructural parameters f and w and for any loading path. The involved velocity fields do depend upon the plastic anisotropy tensor $\mathbb{h}$ through factors B_{2m}. For illustration, Figs. 35 and 36 (solid lines) show such functions $F^{\min}(u)$ for the isotropic matrix and one anisotropic material, for states of purely hydrostatic loading. Similar results were derived for the other materials listed in Table III. In the prolate case (Fig. 35) $F^{\min}$ is more conveniently plotted against the eccentricity e as the spatial variable within the RVE. The bounds for e and u in these plots depend on the specific choices made for porosity f and void aspect ratio w. The key point is that, despite their complicated expressions, the functions $F^{\min}(u)$ exhibit smooth variations between their finite limits. This is the rationale for replacing $F(u)$ with $\bar{F}$. The reasoning behind replacing $G(u)$ and $H(u)$ with constants is similar and leads to the proposed simplification of fluctuating deformation fields.

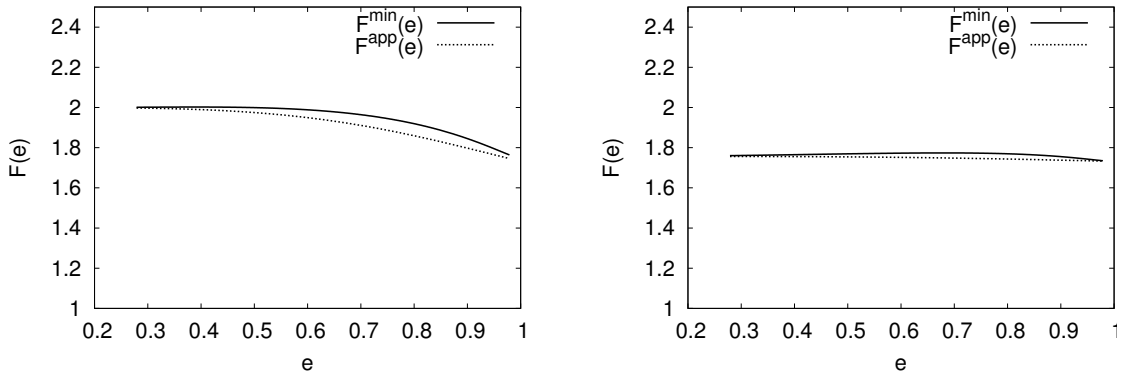

(a) (b)

Fig. 35. Numerically determined $F^{\min}(e)$ minimizing the overall dissipation under hydrostatic loading, and its approximate closed form $F^{\text{app}}(e)$ in (3.87) for a prolate void with $f = 0.001$ and $w = 5$: (a) Isotropic matrix; (b) Material 1 from Table III.

2. Derivation of Yield Criterion (3.40)

To obtain form (3.40) of the yield criterion, we first separate mean and deviatoric parts of $\boldsymbol{\Sigma}$ in the parametric equation (3.5) such that

$$\Sigma_{kk} = 3\frac{\partial \Pi}{\partial D_{kk}}, \qquad \Sigma'_{ij} = \frac{\partial \Pi}{\partial D'_{ij}} \tag{3.67}$$

Writing the axisymmetric tensor $\mathbf{D}^A$ in the form $D^A_{ij} = D^A_{kk} X_{ij}$ with tensor $\mathbf{X}$ given by (4.4) and using the expressions for the expansion velocity field $\mathbf{v}^A$ (4.28)–(4.29) in the boundary condition (3.23), one can show that

$$D^A_{kk} = 3y_2, \qquad \alpha_2 \equiv \frac{D^A_{11}}{D^A_{kk}} = \frac{1}{3} - \frac{b_2}{c} F_2(\lambda_2) \tag{3.68}$$

where $F_2(\lambda)$ is defined by (3.26). Using (4.4) and (3.68) in (3.22), D_{kk} and $\mathbf{D}'$ are related to A and $\boldsymbol{\beta}$ through

$$A = \frac{1}{3y_2} D_{kk}, \quad \boldsymbol{\beta} = \mathbf{D}' + \frac{1}{3} D_{kk}(\mathbf{I} - 3\mathbf{X}) \tag{3.69}$$

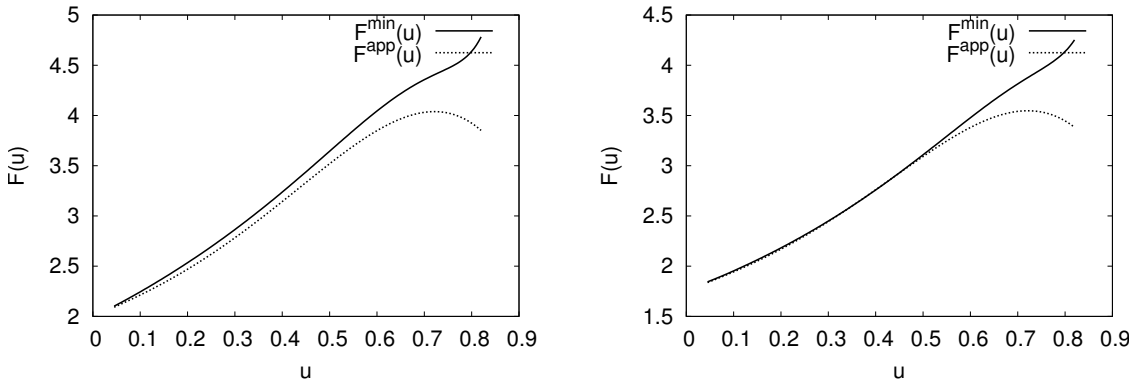

Fig. 36. Numerically determined $F^{\min}(u)$ minimizing the overall dissipation under hydrostatic loading, and its approximate closed form $F^{\text{app}}(e)$ in (3.88) for an oblate void with $f = 0.001$ and $w = 1/5$: (a) Isotropic matrix; (b) Material 1 from Table III.

Using the change of variables $(D_{kk}, \mathbf{D}^{'}) \rightarrow (A, \boldsymbol{\beta})$ equation (3.67) is rewritten in the form

$$3y_2\Sigma_{ij}X_{ij} = \frac{\partial \Pi}{\partial A}, \qquad \Sigma^{'}_{ij} = \frac{\partial \Pi}{\partial \beta_{ij}} \tag{3.70}$$

Next, use of the chain rule in conjunction with equation (3.39) yields

$$\frac{\partial \Pi}{\partial A} = \frac{\bar{F}}{\sqrt{\hat{h}_q}} \frac{\partial \Pi}{\partial \tilde{\mathbf{A}}} : \mathbf{Q}, \quad \frac{\partial \Pi}{\partial \boldsymbol{\beta}} = \sqrt{\hat{h}_q}\bar{G}\frac{\partial \Pi}{\partial \tilde{\mathbf{A}}} + \bar{H}\frac{\partial \Pi}{\partial \tilde{\mathbf{B}}} \tag{3.71}$$

where evaluation of the Jacobian must be carried out with care given that change of variable (3.39) is not one to one[5]. From expression (3.38) for the plastic dissipation, one formally gets

$$\frac{\partial \Pi}{\partial \tilde{\mathbf{A}}} = C_1 \frac{2}{3}\hat{\mathbb{p}} : \tilde{\mathbf{A}}, \quad \frac{\partial \Pi}{\partial \tilde{\mathbf{B}}} = C_2 \frac{2}{3}\hat{\mathbb{p}} : \tilde{\mathbf{B}}, \qquad \hat{\mathbb{p}} = \mathbb{J} : \hat{\mathbb{h}} : \mathbb{J}, \tag{3.72}$$

where C_1 and C_2 are positive scalar-valued functions. One can solve for the unknown C_1 by substituting $(3.72)_1$ in $(3.71)_1$. Using the above derived expression for $\partial\Pi/\partial\tilde{\mathbf{A}}$

[5]We keep the notation $\Pi(\tilde{\mathbf{A}}, \tilde{\mathbf{B}})$ for what should be $\tilde{\Pi}(\tilde{\mathbf{A}}, \tilde{\mathbf{B}})$

in (3.71) and upon simplification using (3.70), one obtains

$$\frac{\partial \Pi}{\partial \tilde{\mathbf{A}}} = \frac{(\boldsymbol{\Sigma} : \mathbf{X})}{\sqrt{\hat{h}_q}} \frac{2y_2}{\bar{F}} \hat{\mathbb{p}} : \{\mathbf{Q} + \mathbf{R}\}, \quad \frac{\partial \Pi}{\partial \tilde{\mathbf{B}}} = \frac{1}{\bar{H}} \left[\boldsymbol{\Sigma}' - \frac{2y_2 \bar{G}}{\bar{F}} (\boldsymbol{\Sigma} : \mathbf{X}) \hat{\mathbb{p}} : \{\mathbf{Q} + \mathbf{R}\} \right] \tag{3.73}$$

where the tensor $\mathbf{R}$ is defined by

$$\mathbf{R} \equiv \frac{[(\mathbf{Q} : \hat{\mathbb{p}} : \mathbf{Q})\boldsymbol{\beta}/A - (\mathbf{Q} : \hat{\mathbb{p}} : \boldsymbol{\beta}/A)\mathbf{Q}]}{\left[\frac{3}{2}\bar{F}/\bar{G} + (\mathbf{Q} : \hat{\mathbb{p}} : \boldsymbol{\beta}/A)\right]} \tag{3.74}$$

Notice that $\mathbf{R} \equiv \mathbf{0}$ if $\boldsymbol{\beta} \propto \mathbf{Q}$, i.e. for states of axisymmetric deformation about the void axis. Also note that, since $\boldsymbol{\beta}/A = 3y_2(\mathbf{D}/D_{kk} - \mathbf{X})$ from (3.69) and $y_2 \to 0$ for a spherical void, $\mathbf{R} \equiv \mathbf{0}$ in the limit case of a spherical void.

From the chain rule and the definitions of $\tilde{A}_{\text{eq}}$ and $\tilde{B}_{\text{eq}}$, we get

$$\left(\frac{\partial \Pi}{\partial \tilde{A}_{\text{eq}}}\right)^2 = \frac{3}{2} \frac{\partial \Pi}{\partial \tilde{\mathbf{A}}} : \mathbb{p} : \frac{\partial \Pi}{\partial \tilde{\mathbf{A}}}, \quad \left(\frac{\partial \Pi}{\partial \tilde{B}_{\text{eq}}}\right)^2 = \frac{3}{2} \frac{\partial \Pi}{\partial \tilde{\mathbf{B}}} : \mathbb{p} : \frac{\partial \Pi}{\partial \tilde{\mathbf{B}}}, \quad \mathbb{p} = \mathbb{J} : \mathbb{h} : \mathbb{J} \tag{3.75}$$

Finally, evaluation of the integral in (3.38) and elimination of the ratio $\tilde{A}_{\text{eq}}/\tilde{B}_{\text{eq}}$ between the expressions for $\partial\Pi/\partial\tilde{A}_{\text{eq}}$ and $\partial\Pi/\partial\tilde{B}_{\text{eq}}$ leads to the following equation of the macroscopic yield locus

$$\frac{1}{\bar{\sigma}^2} \left(\frac{\partial \Pi}{\partial \tilde{B}_{\text{eq}}}\right)^2 + 2(g+1)(g+f) \cosh\left(\frac{1}{\bar{\sigma} y_2} \frac{\partial \Pi}{\partial \tilde{A}_{\text{eq}}}\right) - (g+1)^2 - (g+f)^2 = 0 \tag{3.76}$$

Using $(3.73)_1$ in $(3.75)_1$ and the property that $\mathbf{Q} : \hat{\mathbb{p}} : \mathbf{R} = 0$, we see that

$$\frac{\partial \Pi}{\partial \tilde{A}_{\text{eq}}} = q_1 \frac{3y_2}{\bar{F}} (\boldsymbol{\Sigma} : \mathbf{X}), \qquad q_1 \equiv \sqrt{1 + \frac{R_{\text{eq}}^2}{\hat{h}_q}} \geq 1 \tag{3.77}$$

Similarly, using $(3.73)_2$ in $(3.75)_2$, we obtain

$$\left(\frac{\partial \Pi}{\partial \tilde{B}_{\text{eq}}}\right)^2 = \frac{q_2}{\bar{H}^2} \frac{3}{2} [\boldsymbol{\Sigma}' - \frac{2y_2 \bar{G}}{\bar{F}} (\boldsymbol{\Sigma} : \mathbf{X}) \hat{\mathbb{p}} : \mathbf{Q}] : \mathbb{p} : [\boldsymbol{\Sigma}' - \frac{2y_2 \bar{G}}{\bar{F}} (\boldsymbol{\Sigma} : \mathbf{X}) \hat{\mathbb{p}} : \mathbf{Q}] \tag{3.78}$$

where the dependency on tensor $\mathbf{R}$ is lumped into a parameter q_2

$$q_2 \equiv 1 + \frac{6y_2^2\bar{G}^2(\boldsymbol{\Sigma}:\mathbf{X})^2R_{\rm eq}^2 - 4y_2\bar{F}\bar{G}(\boldsymbol{\Sigma}:\mathbf{X})(\boldsymbol{\Sigma}:\mathbf{R})}{[\bar{F}\boldsymbol{\Sigma}' - 2y_2\bar{G}(\boldsymbol{\Sigma}:\mathbf{X})\hat{\mathbb{p}}:\mathbf{Q}]:\mathbb{p}:[\bar{F}\boldsymbol{\Sigma}' - 2y_2\bar{G}(\boldsymbol{\Sigma}:\mathbf{X})\hat{\mathbb{p}}:\mathbf{Q}]}, \qquad q_2 \leq 1 \tag{3.79}$$

The result that $q_2 \leq 1$ may be verified by evaluating $(\partial\Pi/\partial\tilde{B}_{\rm eq})^2$ by combining forms $(3.72)_2$ and $(3.73)_2$ for $\partial\Pi/\partial\tilde{\mathbf{B}}$ in $(3.75)_2$ and recalling that $\tilde{\mathbf{B}} = \bar{H}\boldsymbol{\beta}$. Also note that in the special cases of spherical void shapes or non-spherical voids subjected to axisymmetric deformation about the void axis $\mathbf{e}_3$, $\mathbf{R} \equiv \mathbf{0}$ and $q_1 = q_2 = 1$.

Using (3.77) and (3.78) in (3.76) leads to the desired result (3.40). In the latter, the criterion parameters are related to constants $\bar{F}$, $\bar{G}$ and $\bar{H}$ (Approximation $\mathcal{A}_2$) through

$$\kappa \equiv \frac{3}{\bar{F}}, \quad C \equiv \frac{1}{\bar{H}^2}, \quad \eta \equiv -\frac{2y_2\bar{G}}{\bar{F}}, \quad g \equiv \begin{cases} 0 & \text{(p)} \\ y_2 & \text{(o)} \end{cases} \tag{3.80}$$

while α_2 is defined by (3.68) above.

3. Criterion Parameters

a. Expressions

There are six parameters which depend on the microstructural variables f and w and on the anisotropy tensor $\mathbb{h}$: C, g, κ, η and α_2, listed by order of appearance in criterion (3.40) or its final form (4.2), and α_1, which mainly appears in the evolution law of w. We first provide their expressions in closed form then present their derivation in the following sections.

$$g = 0 \quad \text{(p)}; \qquad g = \frac{e_2^3}{\sqrt{1-e_2^2}} = f\frac{e_1^3}{\sqrt{1-e_1^2}} = f\frac{(1-w^2)^{\frac{3}{2}}}{w} \quad \text{(o)} \tag{3.81}$$

We recall that e_1 and e_2 are the eccentricities of the void and the outer boundary of the RVE, respectively. Both are implicit functions of f and w.

$$\kappa = \begin{cases} \sqrt{3}\left\{\dfrac{1}{\ln f}\left[\dfrac{2}{3}\ln\dfrac{1-e_2^2}{1-e_1^2}+\dfrac{3+e_2^2}{3+e_2^4}-\dfrac{3+e_1^2}{3+e_1^4}+\dfrac{1}{\sqrt{3}}\left(\tan^{-1}\dfrac{e_2^2}{\sqrt{3}}-\tan^{-1}\dfrac{e_1^2}{\sqrt{3}}\right)\right.\right. & \\ \left.\left.\qquad -\dfrac{1}{2}\ln\dfrac{3+e_2^4}{3+e_1^4}\right]\dfrac{4\hat{h}_q+8\hat{h}_a-7\hat{h}_t}{10}+\dfrac{4(\hat{h}_q+2\hat{h}_a+2\hat{h}_t)}{15}\right\}^{-1/2} & \text{(p)} \\ \dfrac{3}{2}\left(\dfrac{\hat{h}_q+2\hat{h}_a+2\hat{h}_t}{5}\right)^{-1/2}\left\{1+\dfrac{(g_f-g_1)+\frac{4}{5}(g_f^{5/2}-g_1^{5/2})-\frac{3}{5}(g_f^5-g_1^5)}{\ln\frac{g_f}{g_1}}\right\}^{-1} & \text{(o)} \end{cases} \tag{3.82}$$

where $\hat{h}_q$, $\hat{h}_t$ and $\hat{h}_a$ are defined by (3.37) and (3.66), and

$$g_f \equiv \frac{g}{g+f}, \quad g_1 \equiv \frac{g}{g+1}$$

$$\alpha_2 = \begin{cases} \dfrac{(1+e_2^2)}{(1+e_2^2)^2+2(1-e_2^2)} & \text{(p)} \\ \dfrac{(1-e_2^2)(1-2e_2^2)}{(1-2e_2^2)^2+2(1-e_2^2)} & \text{(o)} \end{cases} \tag{3.83}$$

$$\eta = -\frac{2}{3\hat{h}_q}\frac{\kappa Q^*(g+1)(g+f)\mathrm{sh}}{(g+1)^2+(g+f)^2+(g+1)(g+f)[\kappa H^*\mathrm{sh}-2\mathrm{ch}]}, \tag{3.84}$$

$$C = -\frac{2}{3}\frac{\kappa(g+1)(g+f)\mathrm{sh}}{(Q^*+\frac{3}{2}\hat{h}_q\eta H^*)\eta}, \quad \mathrm{sh} \equiv \sinh(\kappa H^*), \quad \mathrm{ch} \equiv \cosh(\kappa H^*)$$

where $H^* \equiv 2\sqrt{\hat{h}_q}(\alpha_1-\alpha_2)$ and $Q^* \equiv \sqrt{\hat{h}_q}(1-f)$.

$$\alpha_1 = \begin{cases} \left[e_1-(1-e_1^2)\tanh^{-1}e_1\right]/(2e_1^3) & \text{(p)} \\ \left[-e_1(1-e_1^2)+\sqrt{1-e_1^2}\sin^{-1}e_1\right]/(2e_1^3) & \text{(o)} \end{cases} \tag{3.85}$$

Note that the expressions of α_2 and α_1 are identical to those in [38] for isotropic matrices. $(3.81)_2$ derives directly from $(3.80)_4$ and $y_2 = c^3/a_2b_2^2$.

b. Derivation of κ and α_2

Most important among all criterion parameters are κ and α_2 which enter the "cosh" term in yield criterion (4.2). Both are affected by factors B_{2m} $(m = 0, 1, 2)$ of the velocity field. Note that α_2 enters the definition of the axisymmetric tensor $\mathbf{X}$ (4.4) which depends on the void axis $\mathbf{e}_3$. For consistency, it is required that the criterion be independent of the void orientation in the limit of a spherical void, which implies that $\mathbf{X}$ must reduce to an isotropic tensor (i.e. $\alpha_2 = 1/3$). We satisfy this requirement by constraining the parameters B_{2i} to be independent of material anisotropy so that α_2 remains independent of $\mathbb{h}$; see equation (3.68). To obtain κ, we start from $(3.80)_1$ where $\bar{F}$ is defined through

$$\bar{F} = \left(\ln \frac{u_1}{u_2}\right)^{-1} \inf_{[B_{20},B_{21},B_{22}]\in\mathbb{R}^3} \int_{u_2}^{u_1} F(u)\frac{du}{u} \tag{3.86}$$

by virtue of approximation $\mathcal{A}_2$. The true function that minimizes the above integral and the overall dissipation under purely hydrostatic loading was plotted in Figs. 35 and 36 as special cases of the family of functions designated $F^{\min}(u)$ in Appendix 1. In seeking a closed form expression for $\bar{F}$ and κ, we must approximate $F^{\min}(u)$ by a function $F^{\text{app}}(u)$ since the former can only be evaluated numerically[6]. This is done in two steps, in the spirit of [38]. First, the specific values of B_{20}, B_{21} and B_{22} are obtained by minimizing the integrand $F(u)$ in (3.86) and not the integral itself (or equivalently $\Pi(\mathbf{D})$). The existence of the minimum is guaranteed by the convexity of $F(u)$ in the triplet B_{2m} [82]. This yields expressions for B_{2m} in terms of e, the eccentricity of the current confocal spheroid[7]. The function $F(u)$ that

[6]There is an abuse of language here since $F^{\min}$ is in fact $F^{\min}(u; \mathbb{h}, B_{2m}(u_1, u_2, \mathbb{h}))$ whereas the sought approximation $F^{\text{app}}(u; \mathbb{h})$ lives in a different functional space.

[7]The expressions of Gologanu et al. [38] for B_{2m} also depended on e_2, due to the constraint (4.31). However, we choose to ignore this dependency, effectively con-

results from using the above values of B_{2m} has, however, a complicated expression and the integral (3.86) cannot be evaluated in closed form to calculate $\bar{F}$. Hence, in a second step, we recourse to heuristics. It is noted that this function has the form $\sqrt{\hat{h}_q F_q(e) + \hat{h}_t F_t(e) + \hat{h}_a F_a(e)}$ where the eccentricity e is used as the independent variable. Functions F_q, F_t and F_a are well approximated by functions of the form $C_1 \frac{(1-e^4)}{(3+e^4)^2} + C_2$, where C_1 and C_2 are determined by fitting the functions at the end points of the domain of e.

In the prolate case, the above procedure leads to the following approximate function $F^{\text{app}}(e)$

$$F^{\text{app}}(e) = \sqrt{\frac{9}{5}(4\hat{h}_q + 8\hat{h}_a - 7\hat{h}_t)\frac{(1-e^4)}{(3+e^4)^2} + 3\hat{h}_t} \qquad \text{(p)} \tag{3.87}$$

This approximation gives a close agreement with $F^{\min}(u)$, which minimizes the overall dissipation, regardless of the values of u_1 and u_2. In particular, $F^{\text{app}}(e)$ matches $F^{\min}(e)$ exactly in the limit cases of spherical ($e = 0$) or cylindrical ($e = 1$) void shapes. Fig. 35 compares the two functions for two different materials from Table III and a given microstructure ($f = 0.001$ and $w = 5$). In the case of oblate voids, however, the above procedure does not yield a satisfactory function $F^{\text{app}}(u)$ that minimizes the integral in (3.86). This is probably due to the stronger variations of $F^{\min}$ in that case, as illustrated in Fig. 36. We therefore propose the following heuristic function

$$F^{\text{app}}(u) = \sqrt{\frac{4}{5}(\hat{h}_q + 2\hat{h}_a + 2\hat{h}_t)}(1 + u + 2u^{5/2} - 3u^5) \qquad \text{(o)} \tag{3.88}$$

which captures the asymptotic behavior studied in Appendix 1. The quality of this approximation is illustrated in Fig. 36. It provides a reasonable approximation of

straining $\mathbf{v}^A$ to be homogeneous on every confocal spheroid, which is possible since B_{2m} are treated as functions of e rather than constants.

$F^{\min}(u)$.

Finally, parameter κ is obtained in either case by substituting F^{app} given by (3.87) or (3.88) into (3.86) then using equation $(3.80)_1$. For the prolate case, since the integral can still not be evaluated in closed form, the mean of $F^{\text{app}2}(e)$ is evaluated using equation (3.86) and the square root of this value is assigned to $\bar{F}$. It is verified numerically that for all values of e_1 and e_2, the two values are close to each other. The final expressions are given by (4.48). The determination of α_2 is based on the factors B_{2m} determined after step 1 of the above procedure. Based on definition (3.68), this leads to the expressions (4.50), which are identical to those obtained by Gologanu et al. [38] although the $B_{2m}(e)$ expressions used are not the same.

c. Parameters C and η

The parameters C and η are tied to the constants $\bar{G}$ and $\bar{H}$ by equations $(3.80)_{2,3}$. These are determined by forcing the approximate analytical yield locus to pass through and be tangent to known points on the exact two field yield locus (i.e. the yield locus defined by equations (3.5) and (3.28) without the approximations $\mathcal{A}_2$ and $\mathcal{A}_3$). Specifically, we seek to identify exact points on the yield locus for states of purely axisymmetric deformation for which $\boldsymbol{\beta} \propto \mathbf{Q}$. As can be inferred from $(3.69)_2$, this corresponds to stress states of the form $\boldsymbol{\Sigma} = \Sigma_{\text{m}}\mathbf{I} + \Sigma^{'}\hat{\mathbb{p}} : \mathbf{Q}$. In this case, the derivatives of the plastic dissipation, $\partial\Pi/\partial A$ and $\partial\Pi/\partial\beta_{ij}$ can be evaluated exactly for the points corresponding to $A = 0$, i.e., purely deviatoric loadings. Using equations (3.70), we obtain

$$\begin{aligned} \boldsymbol{\Sigma} : \mathbf{X} &= \pm 2\bar{\sigma}\sqrt{\hat{h}_q}(\alpha_1 - \alpha_2) \\ \boldsymbol{\Sigma}^{'} &= \pm\frac{2}{3}\frac{\bar{\sigma}}{\sqrt{\hat{h}_q}}(1-f)\hat{\mathbb{p}} : \mathbf{Q} \end{aligned} \tag{3.89}$$

In equation $(3.89)_1$, the parameter α_1 is defined in a manner similar to α_2 in (3.68), i.e., by

$$\alpha_1 \equiv \frac{D_{11}^{vA}}{2D_{11}^{vA} + D_{33}^{vA}} \tag{3.90}$$

where $\mathbf{D}^{vA}$ is the contribution to the average deformation rate of the void due to the velocity field $\mathbf{v}^A$, defined as in equation (3.52) with the components of $\mathbf{v}$ replaced by those of $\mathbf{v}^A$. The two algebraic equations that result from (i) substituting the above exact points in the equation of the analytical yield locus (4.2); and (ii) equating the slopes of the analytical and exact two-field yield loci at these points, can be solved for the values of the two unknown parameters $\bar{G}$ and $\bar{H}$, or equivalently C and η. This results in the expressions (4.51) given above.

Parameter α_1, which enters in both η and C through the term H^*, also enters the evolution law (3.55) of the void aspect ratio. Its expression is determined in a manner identical to that in [38]. Similar to the case of α_2, which was found to be closely approximated by a function of e_2 alone, it is assumed that α_1 depends only on e_1 (or S) and is independent of f. Then α_1 can be evaluated by letting the boundary of the RVE tend to infinity (i.e. $a_2, b_2 \to \infty$ or $f \to 0$). Under these circumstances, one must take $B_{20} = B_{21} = 0$ for the velocity fields to be bounded. The remaining parameter B_{22} is then fixed by the boundary conditions and the components of $\mathbf{D}^{vA}$ can be evaluated in closed form, thus leading to the final expression (4.52) using (3.90). In the limit of a spherical void $\lim_{w\to 1} \alpha_1 = 1/3$.

4. Rationale for Approximation $\mathcal{A}_3$

Since the first two terms in yield criterion (3.40) are non-negative quantities, it is clear that replacing q_1 and q_2 by lower bound estimates will lead to an upper bound to the yield criterion. However, as was shown in Appendix 2, $q_2 \leq 1$ and hence, in general,

approximation $\mathcal{A}_3$ does not preserve the upper bound character. In order to estimate the error entailed by $\mathcal{A}_3$, consider the case of small porosities, say $f < 0.1$. Tensor $\mathbf{R}$ is evaluated from its definition (3.74) using A and $\boldsymbol{\beta}$ from (3.69). A and $\boldsymbol{\beta}$ are determined by $\mathbf{D}$, which is evaluated from the yield function (3.40) using the normality rule and neglecting the derivatives of q_1 and q_2 with respect to $\boldsymbol{\Sigma}$. Expanding the resulting expression for $\mathbf{R}$ in a power series in the porosity f and keeping only the leading term, one may verify that $\mathcal{A}_3$ preserves the upper bound character for special loadings of the type $\boldsymbol{\Sigma}' = \mathbf{0}$ (hydrostatic loading) and $\boldsymbol{\Sigma} : \mathbf{X} = 0$ (equivalent of deviatoric loading for non-spherical voids). Also, we remark that approximation $\mathcal{A}_3$ is exact in certain special cases such as spherical voids or non-spherical voids subjected to axisymmetric deformation about the void axis, as shown in Appendix 2. For general loadings, one can show that the errors in the value of the yield function due to $\mathcal{A}_3$ are at least an order of magnitude smaller than f, which should be negligible for all practical purposes. Hence $\mathcal{A}_3$ is expected to be a good approximation at small porosities.

CHAPTER IV

A CONSTITUTIVE MODEL FOR PLASTICALLY ANISOTROPIC SOLIDS WITH NON-SPHERICAL VOIDS. PART II: NUMERICAL ASSESSMENT

A. Introduction

The basic phenomenology of ductile fracture involve the nucleation, growth and coalescence of micro-voids from inclusions and second phase particles. Continuum ductile fracture models based on the Gurson void growth model [12] have been very successful in modeling several macroscopic aspects of ductile fracture. Together with appropriate models of void nucleation and void coalescence, the Gurson model has been used to predict macroscopic aspects of ductile failure such as cup–cone fracture in round tensile bars [13] and the slant fracture in plane strain specimens [85]. The success of the Gurson model is partially due to the fact that the model is based on a rigorous micromechanical foundation and can be derived from homogenization and limit-analysis of a hollow ideal plastic spherical shell [86]. Detailed reviews of ductile fracture frameworks based on the Gurson model may be found in [15, 62]. However, the Gurson model predicts unrealistically high ductilities under low triaxiality conditions such as shear dominated loadings [15, 87]. Also, obtaining good quantitative predictions for material ductility and fracture strains using the Gurson model requires use of additional parameters, such as those introduced by Tvergaard and Needleman [13], whose physical significance is unclear.

The origins of some of these well documented limitations of the Gurson model are partially traceable to the fact that anisotropy, both due to texture development is wrought metals and due to the evolution of the void shape, are neglected. Accordingly, several investigators have developed extensions of the Gurson model to account

for the separate effects of void shape [37,38] and material texture [32]. Finite element studies by Benzerga [57] have shown that these microstruture-based enhancements are important in predicting some macroscopic aspects of ductile fracture. However, only recently have micromechanics-based models been developed that account for the combined effect of both forms of material anisotropy on the macroscopic response, including a model developed by the authors [39, 41]. Both the above models were developed based on the Hill-Mandel [75, 76] homogenization theory and an approximate limit-analysis of a spheroidal representative volume element (RVE), containing confocal spheroidal voids embedded in a Hill–type orthotropic matrix [47]. The main difference between the two recent models is that the authors used a larger set of trial velocity fields in the limit analysis, potentially yielding a more accurate estimate of the effective yield potential. The objective of the present chapter is to perform a detailed numerical assessment of the approximate analytical model of Keralavarma and Benzerga [41]. A brief summary of the analytical model is presented in section B for ease of reference. The performance of the model is assessed using two different approaches. In section C, a numerical method is developed to derive rigorous upper bounds to the yield loci for anisotropic materials subjected to axisymmetric stress states following a limit analysis procedure using a large number of trial velocity fields. The analytical yield criterion is validated by comparison with these numerically derived upper bound yield loci in section D. In section E, the analytical model is integrated for specified loading paths and the evolution equations for the microstructural variables are validated by comparing the model predictions with finite-element predictions for the same using micromechanical unit-cells.

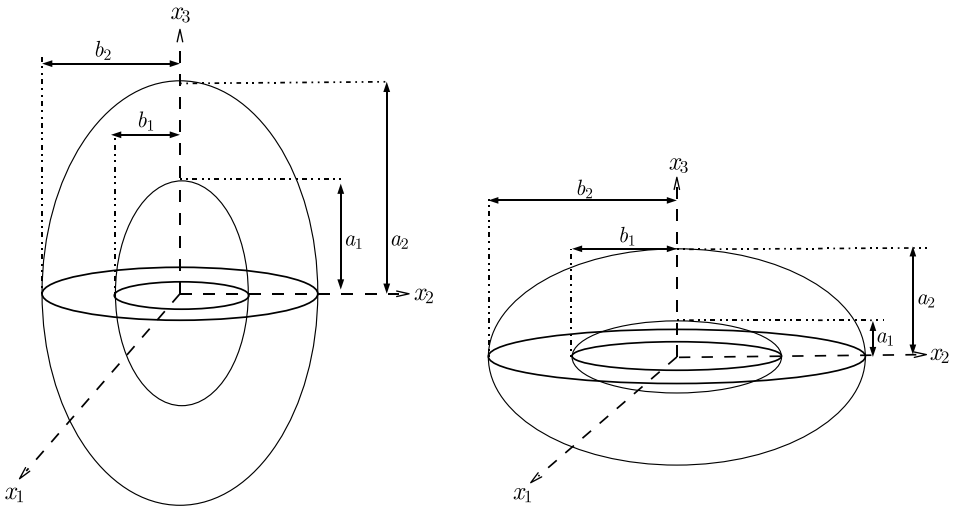

(a) (b)

Fig. 37. Porous representative volume elements (a) prolate (b) oblate

B. Model Synopsis

1. Yield Criterion

The effective or average constitutive response of an anisotropic porous material is derived by homogenization of the spheroidal RVE containing a confocal spheroidal void shown in Fig. 37. Following the Hill-Mandel homogenization approach, the macroscopic or 'average' stress, $\mathbf{\Sigma}$, and deformation rate, $\mathbf{D}$, for the RVE are given by

$$\mathbf{\Sigma} = \langle \boldsymbol{\sigma} \rangle_\Omega, \qquad \mathbf{D} = \langle \mathbf{d} \rangle_\Omega \tag{4.1}$$

where $\boldsymbol{\sigma}$ and $\mathbf{d}$ are the corresponding microscopic fields, Ω represents the volume of the RVE and the notation $\langle \cdot \rangle_\Omega$ represents the volume average over Ω. Following an approximate limit-analysis using a restricted set of trial velocity fields, the macroscopic

yield surface in stress-space was obtained as

$$\mathcal{F}(\boldsymbol{\Sigma}) = C\frac{3}{2}\frac{\boldsymbol{\Sigma}:\mathbb{H}:\boldsymbol{\Sigma}}{\bar{\sigma}^2} + 2(g+1)(g+f)\cosh\left(\kappa\frac{\boldsymbol{\Sigma}:\mathbf{X}}{\bar{\sigma}}\right) - (g+1)^2 - (g+f)^2 = 0 \quad (4.2)$$

where $\bar{\sigma}$ denotes the yield stress of the matrix in a reference direction and the fourth order tensor, $\mathbb{H}$, denotes the macroscopic plastic anisotropy tensor, defined by

$$\mathbb{H} \equiv \mathbb{p} + \eta(\mathbf{X}\otimes\mathbf{Q} + \mathbf{Q}\otimes\mathbf{X}) \quad (4.3)$$

Plastic anisotropy of the matrix enters the criterion above via the Hill anisotropy tensor, $\mathbb{p}$. The tensors $\mathbf{X}$ and $\mathbf{Q}$ are functions of the void orientation, given by

$$\mathbf{X} \equiv \alpha_2(\mathbf{e}_1\otimes\mathbf{e}_1 + \mathbf{e}_2\otimes\mathbf{e}_2) + (1-2\alpha_2)\mathbf{e}_3\otimes\mathbf{e}_3 \quad (4.4)$$

$$\mathbf{Q} \equiv -\frac{1}{2}(\mathbf{e}_1\otimes\mathbf{e}_1 + \mathbf{e}_2\otimes\mathbf{e}_2) + \mathbf{e}_3\otimes\mathbf{e}_3 \quad (4.5)$$

where $(\mathbf{e}_1, \mathbf{e}_2, \mathbf{e}_3)$ is a Cartesian frame introduced in Fig. 37 with $\mathbf{e}_3$ aligned with the void axis and the directions of $\mathbf{e}_1, \mathbf{e}_2$ chosen arbitrarily. Since the fourth order tensor $\mathbb{p}$ has a zero eigenvalue along the hydrostatic axis in stress space, it is convenient to define a variant of the Hill tensor in deviatoric stress space, $\mathbb{h}$, using the relation $\mathbb{p} = \mathbb{J} : \mathbb{h} : \mathbb{J}$. Here, $\mathbb{J}$ is the deviatoric projection operator given by $\mathbb{J} = \mathbb{I} - \frac{1}{3}\mathbf{I}\otimes\mathbf{I}$, where $\mathbb{I}$ and $\mathbf{I}$ are the fourth and second order identity tensors respectively.

In addition to the anisotropy tensor, $\mathbb{p}$, and the void orientation, the criterion depends on two non-dimensional variables that characterize the microstructure, the porosity, f, and the void shape parameter, S. The latter is defined by $S \equiv \ln w$, where w denotes the aspect ratio of the void. The variables f and S are related to

the eccentricities of the void, e_1, and the RVE, e_2, by

$$\begin{gathered}\frac{1}{1-e_1^2} = e^{2|S|} \\ \frac{(1-e_2^2)^n}{e_2^3} = \frac{1}{f}\frac{(1-e_1^2)^n}{e_1^3}, \qquad n = \begin{cases} 1 & \text{(p)} \\ 1/2 & \text{(o)} \end{cases}\end{gathered} \tag{4.6}$$

where the abbreviations (p) and (o) stand for prolate and oblate respectively. The parameter g that appears in (4.2) may be interpreted as a 'porosity-like' quantity that takes non-zero values only for oblate void shapes, given by

$$g \equiv \begin{cases} 0 & \text{(p)} \\ \dfrac{e_2^3}{\sqrt{1-e_2^2}} & \text{(o)} \end{cases} \tag{4.7}$$

In particular, a non-zero value of g for penny-shaped cracks, which is a limiting configuration of an oblate void as the porosity tends to zero, allows for predictions of porosity growth corresponding to the opening of the crack under certain types of loading. In contrast, the Gurson model does not predict damage growth in a material containing initial penny shaped cracks with a vanishing porosity.

The parameters C, η, κ and α_2 that appear in the yield criterion (4.2) are functions of the microstructural variables, f and S, defined above. In addition, these depend on material anisotropy via three scalar anisotropy factors, h, h_t and h_a, defined in term of the components of a tensor $\hat{\mathbb{h}}$ which is a formal inverse of the Hill tensor in deviatoric stress space $\mathbb{h}$ via the relation $\mathbb{J} : \mathbb{h} : \mathbb{J} : \hat{\mathbb{h}} : \mathbb{J} = \mathbb{J}$. The expressions for

the anisotropy factors read

$$h = \frac{\hat{h}_{11} + \hat{h}_{22} + 4\hat{h}_{33} - 4\hat{h}_{23} - 4\hat{h}_{31} + 2\hat{h}_{12}}{6}$$
$$h_t \equiv \frac{\hat{h}_{11} + \hat{h}_{22} + 2\hat{h}_{66} - 2\hat{h}_{12}}{4}, \qquad h_a \equiv \frac{\hat{h}_{44} + \hat{h}_{55}}{2} \tag{4.8}$$

where $\hat{h}_{ij}$ denote the components of the fourth order tensor $\hat{\mathbb{h}}$, expressed in Voigt notation, in the frame $(\mathbf{e}_1, \mathbf{e}_2, \mathbf{e}_3)$ of Fig. 37. It may be demonstrated that h is an invariant of the tensor $\hat{\mathbb{h}}$ while h_t and h_a are invariant with respect to the orientations of the axes $\mathbf{e}_1$ and $\mathbf{e}_2$. The expressions for the model parameters as functions of f, S and the anisotropy factors are provided in Appendix 1.

2. Microstructure Evolution Laws

The macroscopic plastic strain rate may be derived from the yield potential using the normality flow rule [12, 75], i.e.

$$D^p_{ij} = \Lambda \frac{\partial \mathcal{F}}{\partial \Sigma_{ij}}(\mathbf{\Sigma}) \tag{4.9}$$

where $\mathcal{F}$ denotes the yield function of equation (4.2) and Λ denotes the plastic multiplier. The evolution law for the porosity follows from the property of plastic incompressibility of the matrix

$$\dot{f} = (1 - f)\Lambda \frac{\partial \mathcal{F}}{\partial \Sigma_m} \tag{4.10}$$

where $\Sigma_m = \frac{1}{3}\Sigma_{kk}$ denotes the hydrostatic component of the stress.

The evolution law for the shape parameter is determined using an approximate method by assuming that the void shape remains spheroidal upon deformation. The proposed evolution law for the void shape is given by

$$\dot{S} = \phi D^{p'}_{33} + 3\left(\frac{1 - 3\alpha_1}{f} + 3\alpha_2 - 1\right) D_m \tag{4.11}$$

where $D_m = \frac{1}{3}D_{kk}$, $\mathbf{D}^{p'}$ denotes the deviatoric part of the plastic deformation rate and ϕ is a heuristic parameter introduced to correct for certain non-linear effects evidenced by finite-element calculations on porous unit-cells. The analytical expression for ϕ, which depends on the stress triaxiality T and the microstructure variables f and S, is provided in Appendix 1.

Apart from the evolution laws for f and S, an equation for the spin of the void axis, $\mathbf{e}_3$, was proposed in [41]. This is omitted here, since all the numerical results presented in this chapter correspond to special cases of loading where the rotation of the void axis is prevented.

C. Numerical Upper-Bound Yield Criterion

In this section, we present a numerical scheme for computing rigorous upper-bounds to the macroscopic yield loci for RVEs of the type illustrated in Fig. 37, i.e. thick spheroidal shells made of a Hill material and containing a confocal spheroidal void. We generalize the numerical method developed by Gologanu et al. [38] for spheroidal voids in a Von Mises matrix to the more general case of Hill orthotropic matrices. As in [38], we employ a large number of velocity fields derived from the family of axisymmetric incompressible velocity fields proposed by Lee and Mear [80] to describe the microscopic velocity field in the RVE. In addition, a homogeneous non-axisymmetric deformation field is incorporated so that the method can be applied to the case of orthotropic materials that do not respect transverse isotropy about the void axis. While rigorous upper-bound yield loci are obtained in all cases, the method has the property that the loci will be quasi-exact in the special case of materials that are transversely

isotropic about the void axis [1]. Moreover, since the velocity fields employed are a superset of the velocity fields used in the analytical derivations in [41], the numerical loci serve as a reference for validation of the choice of the trial velocity fields and the approximations used in the derivation of the closed form yield criterion. The formulation here is restricted to the case of axi-symmetric loading about the void axis, i.e. stress states of the form $\mathbf{\Sigma} = \Sigma_{11}(\mathbf{e}_1 \otimes \mathbf{e}_1 + \mathbf{e}_2 \otimes \mathbf{e}_2) + \Sigma_{33}\mathbf{e}_3 \otimes \mathbf{e}_3$, so that the resulting yield locus represents the intersection in stress space of the yield surface with the hyperplane of axisymmetric loading. For simplicity, we further restrict the analysis to the case where the void axis coincides with one of the axes of material orthotropy, although more general cases can be considered by a straightforward extension of the present formulation. In the following derivations, the Cartesian frame $(\mathbf{e}_1, \mathbf{e}_2, \mathbf{e}_3)$ of Fig. 37 is taken to coincide with the axes of orthotropy of the matrix.

1. Variational Definition of the Yield Locus

Limit-analysis yields the result that the macroscopic yield surface corresponds to the envelope of the hyper-planes in stress space, given by the parametric equation

$$\mathbf{\Sigma} : \mathbf{D} = \Pi(\mathbf{D}) \tag{4.12}$$

where $\Pi(\mathbf{D})$ is homogeneous function of degree one in the components of $\mathbf{D}$ denoted the macroscopic plastic dissipation [77]. In (4.12), the components of $\mathbf{D}$ act as parameters. $\Pi(\mathbf{D})$ is given by

$$\Pi(\mathbf{D}) = \inf_{\mathbf{d} \in \mathcal{K}(\mathbf{D})} \langle \pi(\mathbf{d}) \rangle_\Omega \tag{4.13}$$

$$\mathcal{K}(\mathbf{D}) = \{\mathbf{d} | \exists \mathbf{v}, \forall \mathbf{x} \in \Omega,\, d_{ij} = \frac{1}{2}(v_{i,j} + v_{j,i}) \,\text{and}\, \forall \mathbf{x} \in \partial\Omega,\, \mathbf{v} = \mathbf{D}.\mathbf{x}\} \tag{4.14}$$

[1] We assume that the velocity fields of Lee and Mear [80] represent the complete family of incompressible axisymmetric velocity fields.

where $\mathbf{v}$ is the trial velocity field, $\mathbf{d}$ denotes the microscopic deformation rate tensor and $\pi(\mathbf{d})$ is the microscopic plastic dissipation, which evaluates to

$$\pi(\mathbf{d}) = \bar{\sigma} d_{eq}, \qquad d_{eq} \equiv \sqrt{\frac{2}{3}\mathbf{d} : \hat{\mathbb{h}} : \mathbf{d}} \tag{4.15}$$

for a Hill material (see [41]). Considering the special case of axisymmetric loading about the void axis, one can see that the macroscopic stress and rate of deformation tensors must be of the form

$$\mathbf{\Sigma} = \Sigma_{11}(\mathbf{e}_1 \otimes \mathbf{e}_1 + \mathbf{e}_2 \otimes \mathbf{e}_2) + \Sigma_{33}\mathbf{e}_3 \otimes \mathbf{e}_3, \tag{4.16}$$

$$\mathbf{D} = D_{11}\mathbf{e}_1 \otimes \mathbf{e}_1 + D_{22}\mathbf{e}_2 \otimes \mathbf{e}_2 + D_{33}\mathbf{e}_3 \otimes \mathbf{e}_3 \tag{4.17}$$

Using (4.16) and (4.17) in (4.12), the yield point for an axisymmetric radial loading path may be written as

$$\Sigma_{11} = \frac{\Pi(D_{11}, D_{22}, D_{33})}{D_{11} + D_{22} + X D_{33}}, \qquad X \equiv \frac{\Sigma_{33}}{\Sigma_{11}} \tag{4.18}$$

where X is the ratio of the principal stresses. For axisymmetric loading, X is related to the stress triaxiality, T, by

$$X = \frac{9T}{3T - 1} - 2 \tag{4.19}$$

Noting that since $\Pi(\mathbf{D})$ is homogeneous of degree one in the components of $\mathbf{D}$ the right-hand side of (4.18) is homogeneous of degree zero, one may scale the components of $\mathbf{D}$ arbitrarily. For convenience we impose the constraint

$$D_{11} + D_{22} + X D_{33} = 1 \tag{4.20}$$

so that equation (4.18) becomes

$$\Sigma_{11} = \Pi(D_{11}, D_{22}, D_{33}) \tag{4.21}$$

$\Pi(D_{11}, D_{22}, D_{33})$ is calculated by evaluation of the infimum in equation (4.13) using a finite set of kinematically admissible trial velocity fields as defined by (4.14).

2. Trial Velocity Fields

The macroscopic deformation tensor in (4.17) may be written as a linear combination of an axisymmetric deformation rate, $\mathbf{D}^a$, and a pure shear deformation in the transverse plane of the RVE, $\mathbf{D}^s$, as

$$\begin{gathered} \mathbf{D} = \mathbf{D}^a + \mathbf{D}^s \\ \mathbf{D}^a = D^a_{11}(\mathbf{e}_1 \otimes \mathbf{e}_1 + \mathbf{e}_2 \otimes \mathbf{e}_2) + D^a_{33}\mathbf{e}_3 \otimes \mathbf{e}_3, \quad \mathbf{D}^s = D^s_{11}(\mathbf{e}_1 \otimes \mathbf{e}_1 - \mathbf{e}_2 \otimes \mathbf{e}_2) \end{gathered} \tag{4.22}$$

where

$$D^a_{11} = \frac{D_{11} + D_{22}}{2}, \quad D^a_{33} = D_{33}, \quad D^s_{11} = \frac{D_{11} - D_{22}}{2} \tag{4.23}$$

For the numerical evaluation of $\Pi(D_{11}, D_{22}, D_{33})$ in (4.21), using (4.13), we consider trial velocity fields of the form

$$\mathbf{v} = \mathbf{v}^a + \mathbf{D}^s \cdot \mathbf{x} \quad \Rightarrow \quad \mathbf{d} = \frac{1}{2}\left(\nabla\mathbf{v} + (\nabla\mathbf{v})^T\right) = \mathbf{d}^a + \mathbf{D}^s \tag{4.24}$$

where the first component, $\mathbf{v}^a$, is an axisymmetric velocity field and the second velocity field corresponds to a homogeneous pure shear deformation, $\mathbf{D}^s$, in the transverse plane of the RVE. From the kinematic boundary conditions, equation (4.14), we obtain

$$\mathbf{v} = \mathbf{D} \cdot \mathbf{x} \quad \Rightarrow \quad \mathbf{v}^a = \mathbf{D}^a \cdot \mathbf{x} \qquad \text{on} \quad \partial\Omega \tag{4.25}$$

We choose the field $\mathbf{v}^a$ from the family of incompressible axisymmetric velocity fields proposed by Lee and Mear [80], which is assumed to represent the complete set of such velocity fields. Due to the spheroidal geometry of the problem, we choose to work with the spheroidal coordinate system $(\lambda, \beta, \varphi)$, whose base vectors are defined

in the Cartesian frame of Fig. 37 as

$$\begin{aligned}
\mathbf{e}_\lambda &= \{a\sin\beta\cos\varphi\mathbf{e}_1 + a\sin\beta\sin\varphi\mathbf{e}_2 + b\cos\beta\mathbf{e}_3\}/\sqrt{g_{\lambda\lambda}} \\
\mathbf{e}_\beta &= \{b\cos\beta\cos\varphi\mathbf{e}_1 + b\cos\beta\sin\varphi\mathbf{e}_2 - a\sin\beta\mathbf{e}_3\}/\sqrt{g_{\lambda\lambda}} \\
\mathbf{e}_\varphi &= -\sin\varphi\mathbf{e}_1 + \cos\varphi\mathbf{e}_2
\end{aligned} \tag{4.26}$$

$$g_{\lambda\lambda} \equiv a^2\,\sin^2\beta + b^2\,\cos^2\beta, \qquad \begin{cases} a = c\,\cosh\lambda,\;\; b = c\,\sinh\lambda & \text{(p)} \\ a = c\,\sinh\lambda,\;\; b = c\,\cosh\lambda & \text{(o)} \end{cases} \tag{4.27}$$

In the spheroidal system, iso-λ surfaces are confocal spheroids with focal length, $2c$, so that the surfaces of the void and the RVE correspond to constant values of λ, designated λ_1 and λ_2 respectively. The eccentricity, e, of the current confocal spheroid is related to λ as $e = 1/\cosh\lambda$, with e_1 and e_2 denoting the eccentricities of the void and the RVE respectively. The components of the Lee-Mear velocity fields [80], expressed in spheroidal coordinates, are

$$\begin{cases}
v^a_\lambda(\lambda,\beta) = c^2/\sqrt{g_{\lambda\lambda}}\,\{B_{00}/\sinh(\lambda) \\
\quad + \displaystyle\sum_{k=2,4,..}^{+\infty}\sum_{m=0}^{+\infty} k(k+1)[B_{km}Q^1_m(w) + C_{km}P^1_m(w)]P_k(u)\} \\
 \\
v^a_\beta(\lambda,\beta) = c^2/\sqrt{g_{\lambda\lambda}}\,\{\displaystyle\sum_{k=2,4,..}^{+\infty}\sum_{m=1}^{+\infty} m(m+1)[B_{km}Q_m(w) \\
\qquad\qquad + C_{km}P_m(w)]P^1_k(u)\}
\end{cases} \quad \text{(p)} \tag{4.28}$$

$$\begin{cases} v^a_\lambda(\lambda,\beta) = c^2/\sqrt{g_{\lambda\lambda}}\,\{B_{00}/\cosh(\lambda) \\ \quad + \sum_{k=2,4,..}^{+\infty}\sum_{m=0}^{+\infty} k(k+1)i^m[i\,B_{km}Q^1_m(w) + C_{km}P^1_m(w)]P_k(u)\} \\ \qquad\qquad\qquad\qquad\qquad\qquad\qquad\qquad\qquad\qquad\qquad\qquad\qquad\qquad\qquad\qquad\qquad\qquad (o) \\ v^a_\beta(\lambda,\beta) = c^2/\sqrt{g_{\lambda\lambda}}\,\{\sum_{k=2,4,..}^{+\infty}\sum_{m=1}^{+\infty} m(m+1)i^m[i\,B_{km}Q_m(w) \\ \qquad\qquad\qquad\qquad\qquad\qquad\qquad\qquad\qquad\qquad +C_{km}P_m(w)]P^1_k(u)\} \end{cases} \tag{4.29}$$

where

$$w \equiv \begin{cases} \cosh\lambda & (\mathrm{p}) \\ i\,\sinh\lambda & (\mathrm{o}) \end{cases} ; \qquad u \equiv \cos\beta \tag{4.30}$$

In the above expressions, P^m_n and Q^m_n represent associated Legendre functions of the first and second kinds respectively, of order m and degree n [81], and B_{km} and C_{km} are arbitrary real constants. The requirement of homogeneous boundary strain rate, equation (4.25), leads to linear constraints on the values of coefficients B_{km} and C_{km}. These are given by [38]

$$\begin{cases} e_2^3 B_{00}/(3(1-e_2^2)) + (3-e_2^2)F_2(\lambda_2)/\sqrt{1-e_2^2} - G_2(\lambda_2) = 0 & (\mathrm{p}) \\ -e_2^3 B_{00}/(3\sqrt{1-e_2^2}) + (3-2e_2^2)F_2(\lambda_2)/\sqrt{1-e_2^2} - G_2(\lambda_2) = 0 & (\mathrm{o}) \end{cases} \tag{4.31}$$

$$F_k(\lambda_2) = G_k(\lambda_2) = 0, \qquad k = 4,6,8... \tag{4.32}$$

where

$$\begin{cases} F_k(\lambda) \equiv \sum_{m=0}^{+\infty}\,[B_{km}Q^1_m(w) + C_{km}P^1_m(w)] \\ G_k(\lambda) \equiv \sum_{m=1}^{+\infty} m(m+1)\,[B_{km}Q_m(w) + C_{km}P_m(w)] \end{cases} \quad (\mathrm{p}) \tag{4.33}$$

$$\begin{cases} F_k(\lambda) \equiv \sum_{m=0}^{+\infty} i^m\,[iB_{km}Q^1_m(w) + C_{km}P^1_m(w)] \\ G_k(\lambda) \equiv \sum_{m=1}^{+\infty} m(m+1)i^m\,[iB_{km}Q_m(w) + C_{km}P_m(w)] \end{cases} \quad (\mathrm{o})$$

From (4.25), we can show that the components of $\mathbf{D}^a$ are related to B_{km} and C_{km} by

$$D^a_{11} = \frac{3c^2}{a_2^2 - b_2^2}\left[G_2(\lambda_2) - \frac{3a_2}{b_2}F_2(\lambda_2)\right], \quad D^a_{33} = \frac{3c^2}{a_2^2 - b_2^2}\left[G_2(\lambda_2) - \frac{3b_2}{a_2}F_2(\lambda_2)\right] \tag{4.34}$$

Using (4.34) and (4.23), the additional constraint (4.20) may be written as

$$\frac{3c^2}{a_2^2 - b_2^2}\left[(2+X)G_2(\lambda_2) - 3\left(2\frac{a_2}{b_2} + X\frac{b_2}{a_2}\right)F_2(\lambda_2)\right] = 1 \tag{4.35}$$

Thus, the numerical evaluation of the yield point under axisymmetric loading, equation (4.21), corresponds to minimization of the plastic dissipation in (4.13) using trial velocity fields of the form (4.24), subject to linear constraints on the values of the multiplicative factors of the velocity fields B_{km} and C_{km}, given by equations (4.31), (4.32) and (4.35).

3. Numerical Minimization of the Plastic Dissipation

For given values of the microstructural parameters f and S, the eccentricities of the void and RVE may be obtained from equation (4.6). The semi-focal length, c, may be chosen arbitrarily since the problem is scale invariant. Combining (4.13) and (4.15), we may write the macroscopic plastic dissipation as

$$\Pi(\mathbf{D}) = \inf_{\mathbf{d}\in\mathcal{K}(\mathbf{D})} \bar{\sigma}\langle d_{eq}\rangle_\Omega, \qquad d_{eq} = \sqrt{\frac{2}{3}\mathbf{d} : \mathbb{h} : \mathbf{d}} \tag{4.36}$$

$\mathbf{d}$ is computed using the decomposition of the microscopic velocity field $\mathbf{v}$, in (4.24), where $\mathbf{v}^a$ is chosen to be a finite sub-set of the infinite double-series of the Lee-Mear fields in equations (4.28)-(4.29). Let us adopt the velocity fields corresponding to the coefficients B_{00}, B_{km} and C_{km}, where $k = 2, 4, 6, .., K$ and $m = 0, 1, 2, .., M$, which corresponds to a total of $N = K(M+1) + 2$ trial velocity fields. It is clear that $\mathbf{d}$ is a homogeneous linear function of the coefficients B_{00}, B_{km}, C_{km} and the in-plane

shear strain rate D^s_{11}. Let $[\mathbf{d}]$ stand for the Voigt representation of $\mathbf{d}$ in the frame $(\mathbf{e}_1, \mathbf{e}_2, \mathbf{e}_3)$. We may write

$$[\mathbf{d}] = [\mathcal{L}(\lambda, \beta, \varphi)][A] \tag{4.37}$$

where $[\mathcal{L}(\lambda, \beta, \varphi)]$ is a $6 \times N$ matrix whose components are functions of the coordinates $(\lambda, \beta, \varphi)$, and $[A]$ is a $N \times 1$ column vector defined as

$$[A] \equiv [B_{00} \quad [B_{km}]^T \quad [C_{km}]^T \quad D^s_{11}]^T \tag{4.38}$$

In (4.38), $[B_{km}]$ and $[C_{km}]$ denote column vectors of the corresponding Lee-Mear coefficients. The expression for d_{eq} may be written as

$$d_{eq} = \sqrt{\frac{2}{3}[A]^T[\mathcal{L}]^T[\hat{\mathbb{h}}][\mathcal{L}][A]} = \sqrt{[A]^T[\mathcal{M}][A]}, \qquad [\mathcal{M}] \equiv \frac{2}{3}[\mathcal{L}]^T[\hat{\mathbb{h}}][\mathcal{L}] \tag{4.39}$$

where $[\hat{\mathbb{h}}]$ is the 6×6 Voigt matrix of the anisotropy tensor $\hat{\mathbb{h}}$ in the frame $(\mathbf{e}_1, \mathbf{e}_2, \mathbf{e}_3)$. Since $(\mathbf{e}_1, \mathbf{e}_2, \mathbf{e}_3)$ is taken to be the frame of material orthotropy, $[\hat{\mathbb{h}}]$ will a diagonal matrix. The problem is now reduced to determination of the coefficients $[A]$ that minimize the plastic dissipation in (4.36). However, the components of $[A]$ are subject to the constraints given by equations (4.31), (4.32) and (4.35). These make a total of K linear equality constraints, which may be used to eliminate K of the N unknowns as

$$[A] = [\mathcal{C}][B] + [A_0] \tag{4.40}$$

where $[B]$ is an $(N - K) \times 1$ vector of the remaining unknowns, $[\mathcal{C}]$ is a constraint matrix and $[A_0]$ is a constant vector. Using (4.40) along with (4.39) in (4.36), we can write $\Pi(\mathbf{D})$ as

$$\Pi(\mathbf{D}) = \inf_{[B] \in \mathbb{R}^{N-K}} \Pi([B]) = \inf_{[B] \in \mathbb{R}^{N-K}} \bar{\sigma} \left\langle \sqrt{([\mathcal{C}][B] + [A_0])^T[\mathcal{M}]([\mathcal{C}][B] + [A_0])} \right\rangle_\Omega \tag{4.41}$$

The above represents an unconstrained minimization problem where $\Pi([B])$ is the objective function in $N-K$ variables, $[B]$, and the space of admissible values of $[B]$ is $\mathbb{R}^{N-K}$. Note that the existence and uniqueness of the minimum is guaranteed by the fact that $[\hat{\mathbb{h}}]$ is a positive definite matrix, which implies that $[\mathcal{M}]$ is positive semi-definite and hence the objective function is convex. The gradient of the objective function with respect to the unknowns, $[B]$ is given by

$$\frac{\partial \Pi}{\partial [B]} = \bar{\sigma} \left\langle \frac{[\mathcal{C}]^T[\mathcal{M}]([\mathcal{C}][B]+[A_0])}{\sqrt{([B]^T[\mathcal{C}]^T+[A_0]^T)[\mathcal{M}]([\mathcal{C}][B]+[A_0])}} \right\rangle_{\Omega} \tag{4.42}$$

The above problem can be solved for various values of the macroscopic stress triaxiality, T, to obtain individual points on the yield locus using equation (4.21). A program is developed to perform the above minimization using a conjugate gradient minimization algorithm [88]. In the following, the yield locus obtained using the above method will be referred to as the 'exact numerical yield locus'. The analytical criterion of section B is compared with the exact numerical yield loci for various microstructural parameters and material anisotropy coefficients in the following section.

D. Results

1. Yield Criterion

The numerical method of the previous section can be used to generate the yield locus for axisymmetric loading about the void axis, i.e. stress states of the form $\mathbf{\Sigma} = \Sigma_{11}(\mathbf{e}_1 \otimes \mathbf{e}_1 + \mathbf{e}_2 \otimes \mathbf{e}_2) + \Sigma_{33}\mathbf{e}_3 \otimes \mathbf{e}_3$. The analytical equation of the yield locus (4.2) for axisymmetric loading reads

$$\frac{h'C}{\bar{\sigma}^2}\left(\Sigma_{33}-\Sigma_{11}+\frac{3}{2}\eta\Sigma_h\right)^2 + 2(g+1)(g+f)\cosh\left(\kappa\frac{\Sigma_h}{\bar{\sigma}}\right) - (g+1)^2 - (g+f)^2 = 0 \tag{4.43}$$

where Σ_h is defined by $\Sigma_h \equiv \mathbf{\Sigma} : \mathbf{X} = 2\alpha_2\Sigma_{11} + (1 - 2\alpha_2)\Sigma_{33}$ and $h^{'}$ is defined similar to h in equation (4.8) using the components of the tensor $\mathbb{h}$ in place of those of $\hat{\mathbb{h}}$. The criterion also depends on the anisotropy factors h, h_t and h_a defined in (4.8). In the case when $(\mathbf{e}_1, \mathbf{e}_2, \mathbf{e}_3)$ coincides with the axes of orthotropy, the Voigt form of the tensors $\mathbb{h}$ and $\hat{\mathbb{h}}$ are diagonalized and they take on simplified expressions

$$h = \frac{\hat{h}_1 + \hat{h}_2 + 4\hat{h}_3}{6}, \quad h^{'} = \frac{h_1 + h_2 + 4h_3}{6}, \quad h_t = \frac{\hat{h}_1 + \hat{h}_2 + 2\hat{h}_6}{4}, \quad h_a = \frac{\hat{h}_4 + \hat{h}_5}{2} \tag{4.44}$$

In the above expressions, h_i and $\hat{h}_i$ $(i = 1..6)$ represent the diagonal elements of the Voigt matrix representation of the tensors $\mathbb{h}$ and $\hat{\mathbb{h}}$ respectively. These are related by (see [32])

$$\hat{h}_1 = \frac{-h_1 + 2h_2 + 2h_3}{h_1h_2 + h_2h_3 + h_3h_1}, \hat{h}_2 = \frac{2h_1 - h_2 + 2h_3}{h_1h_2 + h_2h_3 + h_3h_1}, \hat{h}_3 = \frac{2h_1 + 2h_2 - h_3}{h_1h_2 + h_2h_3 + h_3h_1},$$
$$\hat{h}_4 = \frac{1}{h_4}, \hat{h}_5 = \frac{1}{h_5}, \hat{h}_6 = \frac{1}{h_6} \tag{4.45}$$

It may also be noted that, in the case of transverse isotropy about the $\mathbf{e}_3$ axis, $h^{'} = 1/h$.

A detailed tabulation of the Hill anisotropy coefficients in practically important engineering materials was presented in [41]. For the numerical results presented here, we have chosen to work with a set of material parameters that are chosen to represent the observed range values of the Hill coefficients in [41] and previously used in [41]. Table V shows the values of the Hill coefficients for four different materials. The first row corresponds to an isotropic material, which is used as a reference. Materials 1 and 2 are transversely isotropic materials with properties similar to those analyzed in [32]. The properties of Material 1 are similar to those observed in thick Al sheets. Material 3 is not transversely isotropic and the properties are based on experimentally

Table V. Table of material anisotropy parameters used in the numerical computations.

Name	h_1	h_2	h_3	h_4	h_5	h_6
Isotropic	1.000	1.000	1.000	1.000	1.000	1.000
Material 1	1.000	1.000	1.000	2.333	2.333	1.000
Material 2	1.000	1.000	1.000	0.500	0.500	1.000
Material 3	1.650	0.778	0.893	1.378	0.943	1.627

determined values for commercially pure Titanium [2].

Figures 38(a)-(d) show the yield loci for the four materials from Table V for prolate cavities of aspect ratio, $w = 5$, and three different values of the porosity. The loci are plotted with the mean stress Σ_m as the abscissa and $\Sigma_{33} - \Sigma_{11}$ as the ordinate, whose absolute value equals the Von Mises effective stress for axisymmetric loading. The stresses are normalized by σ_3, the yield stress of the matrix in the $\mathbf{e}_3$ direction, which coincides with one of the axes of orthotropy in all the cases considered here. The numerical yield loci are plotted using discrete points, while the continuous lines correspond to the analytical criterion of equation (4.43). In all the results presented here, the numerical yield loci are calculated using twenty two trial velocity fields corresponding to the Lee-Mear coefficients B_{00}, B_{km}, C_{km} ($k = 2, 4$ and $m = 0..5$) and the homogeneous shear strain rate, D^s_{11}. It is clear from the figure that the analytical criterion provides a close agreement with the upper-bound numerical yield loci (which may be considered quasi-exact for the isotropic matrix and materials 1 and 2) over a wide range of values of the porosity and for all four material properties tested. It may also be mentioned that, while the new criterion in the case of prolate cavities

[2]Since the available data in the literature for Ti correspond to thin sheets [89], for which the out of plane strain ratios are not reported, these we assumed to be unity while calculating the data in Table V.

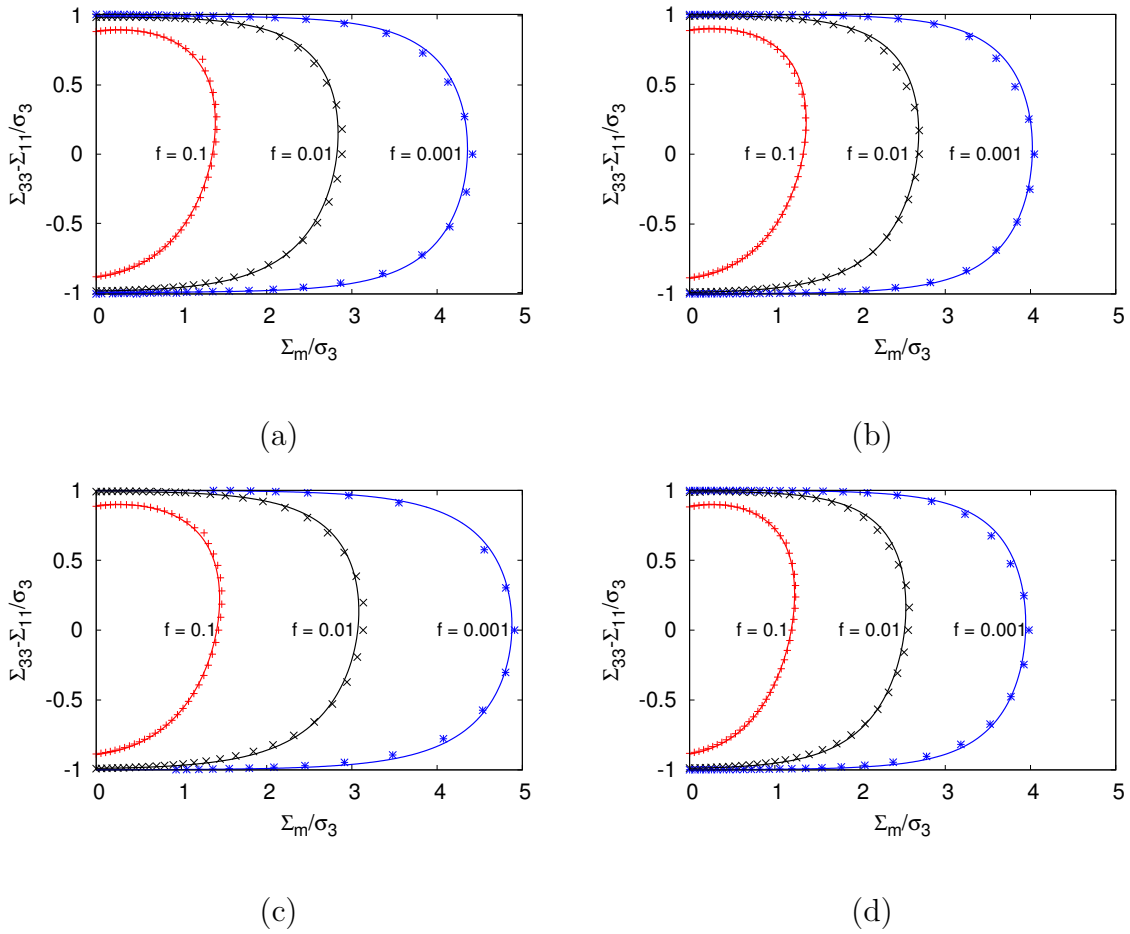

Fig. 38. Comparison of the analytical and numerical yield loci for prolate cavities. (a) Isotropic matrix (b) Material 1 (c) Material 2 (d) Material 3 and three values of the porosity, f. In all cases, $w = 5$. The solid lines correspond to the analytical criterion of equation (4.43).

and the isotropic matrix differs slightly from that of Gologanu et al. [38] due to the different approach adopted in the definition of the parameter κ, the loci of Fig. 38(a) are nevertheless in very good agreement with their results.

Similar results for oblate cavities of aspect ratio, $w = 1/5$, are presented in Figs. 39(a)-(d). The new criterion is again seen to agree closely with the numerical data. However, for certain values of the stress triaxiality, the analytical loci are seen to fall slightly inside the numerical yield loci. While it is preferable to always have the numerical points fall inside the analytical loci, since the former are known to be rigorous upper-bounds to the true values of the yield stress, the violations appear to be small in most instances.

In order to further characterize the yield criterion, we look at the variation of the yield point under axisymmetric loading for two values of the stress triaxiality, $T = 1$ and $T = 3$, as a function of the void aspect ratio. It may be noted that in practice, stress triaxialities in excess of 3 are rare and occur at blunted crack tips in a high strain hardening material. Figure 40 and 41 show the variation of the hydrostatic stress at yield, designated Σ_m^y, as a function of the void aspect ratio for $T = 1$ and $T = 3$ respectively. Subfigures (a)-(d) correspond the four different material properties from Table V. The discrete points represent the numerically determined values and the solid line corresponds to the analytical prediction from equation (4.43). Again, the analytical predictions are seen to be in good agreement with the numerical values for the yield points.

2. Evolution of Porosity

In general, validation of the microstructure evolution equations require the integration of the constitutive equations for specific loading paths and comparison with predictions from finite-element simulations on porous unit-cells. A preliminary study of

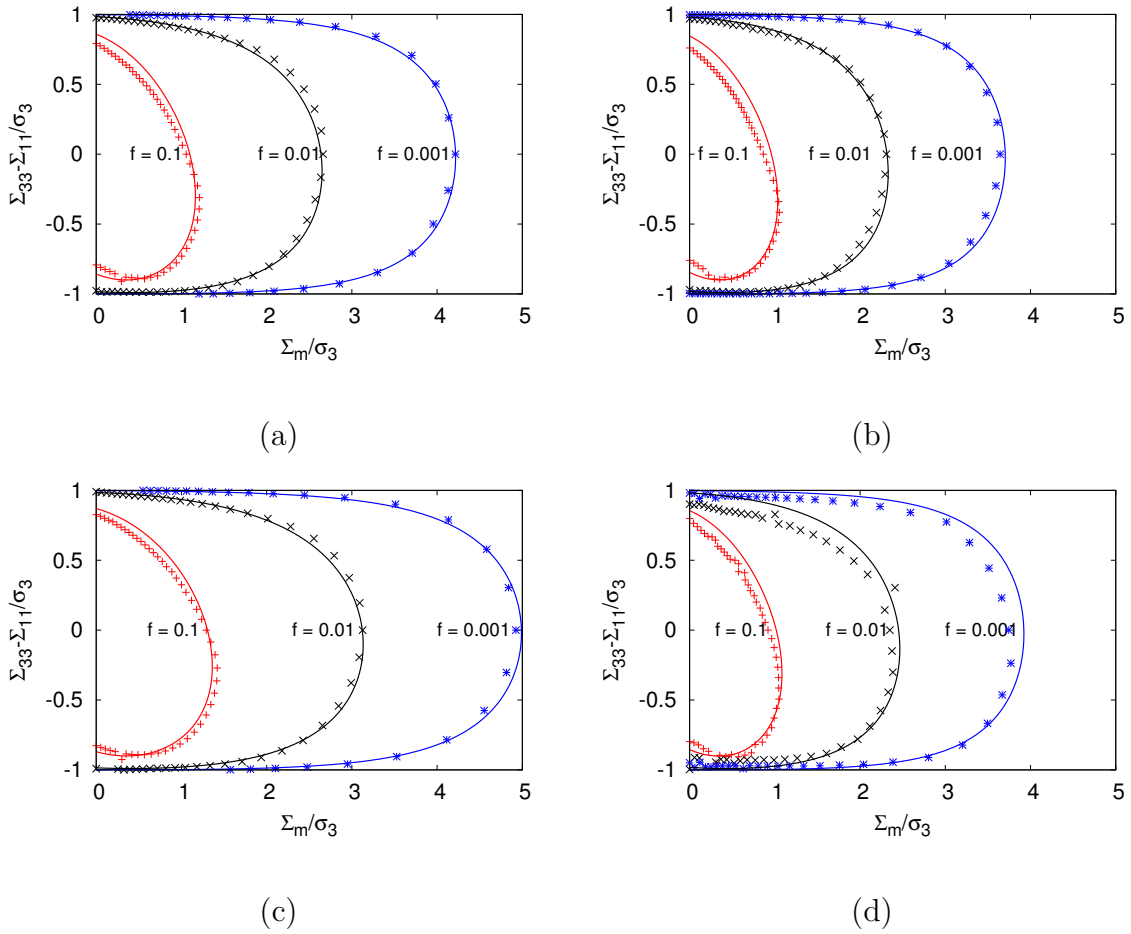

Fig. 39. Comparison of the analytical and numerical yield loci for oblate cavities. (a) Isotropic matrix (b) Material 1 (c) Material 2 (d) Material 3 and three values of the porosity, f. In all cases, $w = 1/5$. The solid lines correspond to the analytical criterion of equation (4.43).

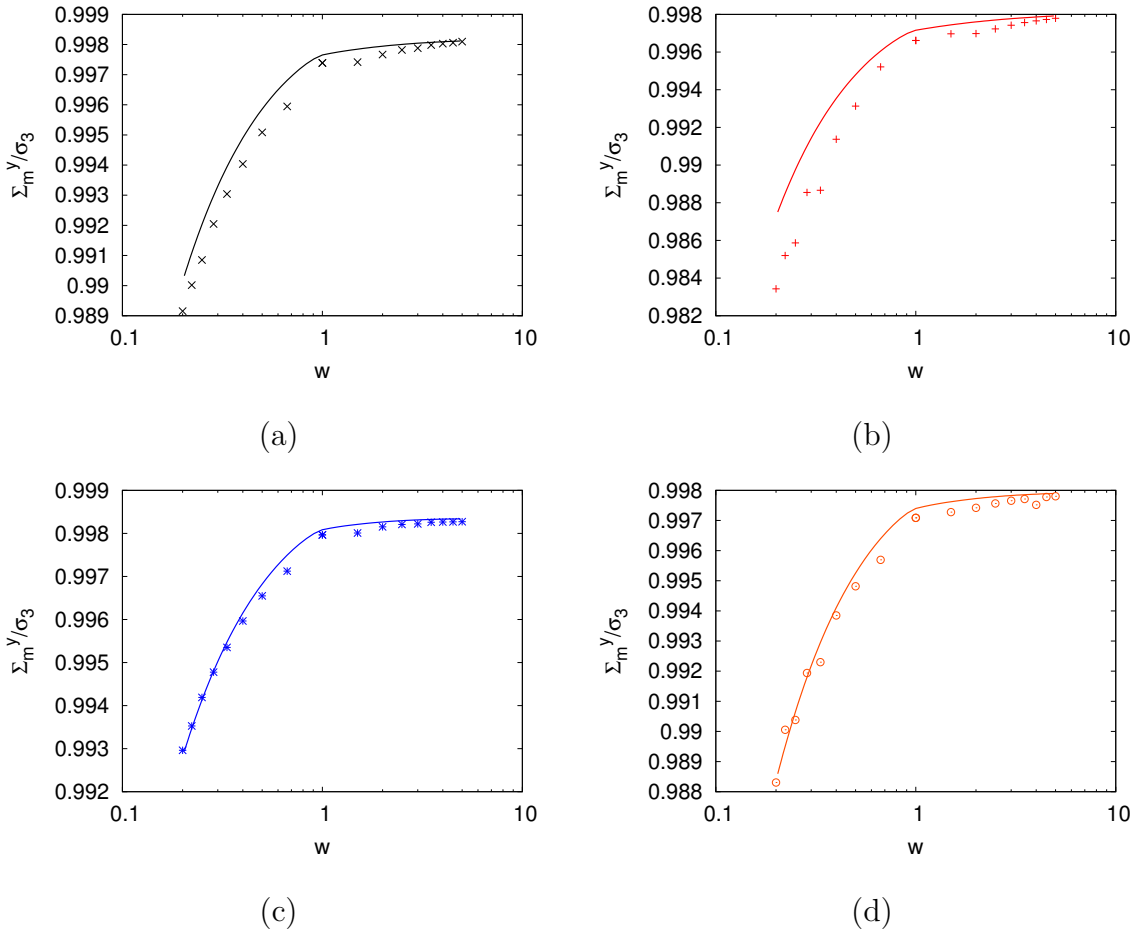

Fig. 40. Variation of the hydrostatic stress at yield, Σ_m^y, under proportional axisymmetric loading, as a function of the void aspect ratio, w, for porosity $f = 0.001$, and stress triaxiality, $T = 1$. (a) Isotropic matrix (b) Material 1 (c) Material 2 (d) Material 3. The discrete points are the numerically determined yield points, the solid line correspond to the analytical criterion of equation (4.43).

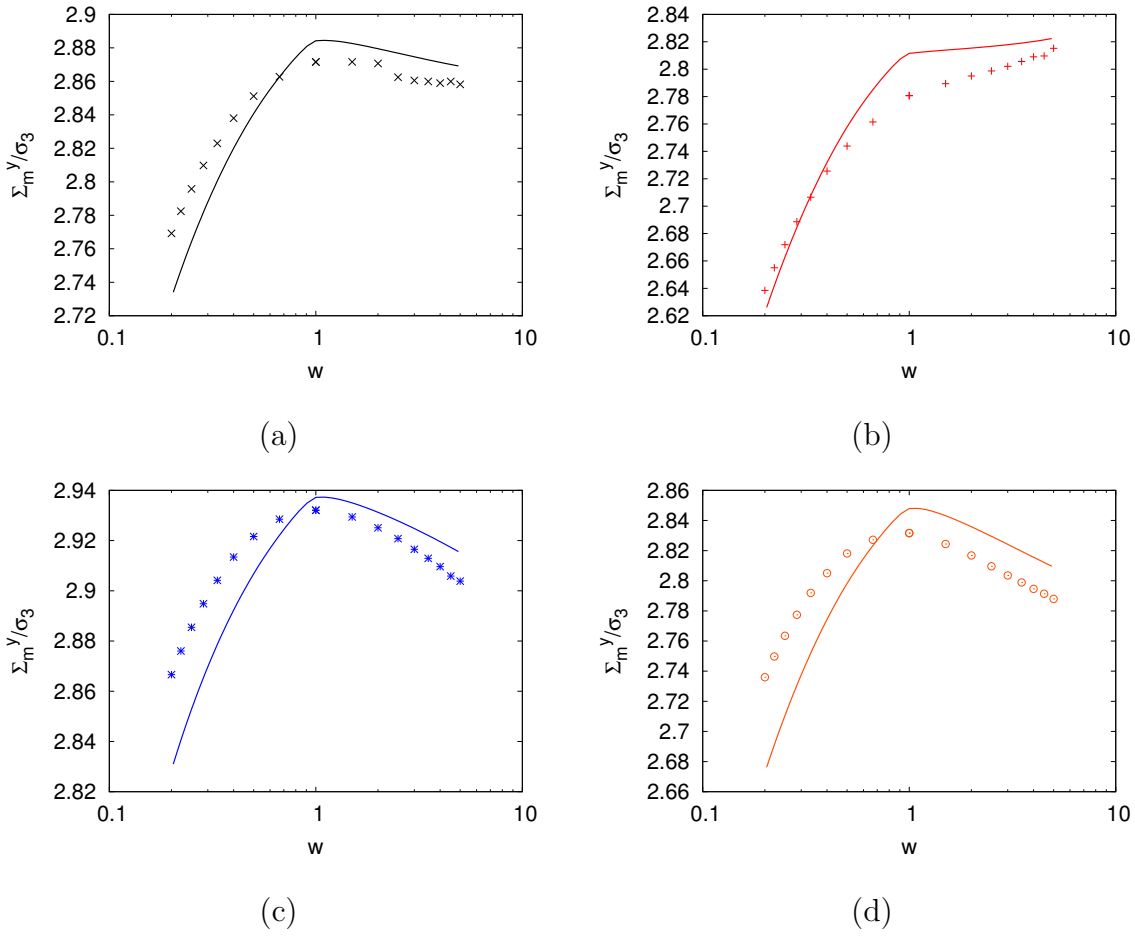

Fig. 41. Variation of the hydrostatic stress at yield, Σ_m^y, under proportional axisymmetric loading, as a function of the void aspect ratio, w, for porosity $f = 0.001$, and stress triaxiality, $T = 3$. (a) Isotropic matrix (b) Material 1 (c) Material 2 (d) Material 3. The discrete points are the numerically determined yield points, the solid line correspond to the analytical criterion of equation (4.43).

this type has been conducted and the results are presented in section E. However, one may also use the numerical limit-analysis approach to determine the macroscopic dilatancy, D_m, using the trial velocity fields that minimize the macroscopic plastic dissipation. In the case of transversely isotropic materials, since the Lee-Mear fields are assumed to span the space of axisymmetric velocity fields, the resulting value of $\dot{f}$ may be expected to be close to the true rate of porosity growth.

Figure 42 illustrate the variation of D_m/D_m^{sph} under axisymmetric loading as a function of the void aspect ratio, for $f = 0.01$, macroscopic stress triaxiality, $T = 1$, and three transversely isotropic materials from Table V. D_m^{sph} here corresponds to the value of D_m for a spherical void ($w = 1$). Note that since, in general, the spherical and the non-spherical RVEs have different yield points, and the materials being considered are not hardenable, the comparison is made for the case that the two RVEs have the same axial strain rate, i.e. $D_{33} = D_{33}^{sph}$. The actual value of D_m^{sph}, used in the calculations reported here, is obtained using a void with a vanishingly small eccentricity, which may be considered for all practical purposes to be a sphere. Discrete points in the figure correspond to numerically obtained values of D_m/D_m^{sph} using the method described in section C. The solid lines correspond to the model predictions using equations (4.9) and (4.43). In both the prolate and the oblate cases, the analytical predictions show acceptable agreement with the numerical results for the variation of D_m/D_m^{sph} with the void aspect ratio.

E. Finite-Element Simulations

The best means to validate the evolution equations for f and S is to compare them against direct finite element (FE) simulations on porous unit cells. However, a systematic study of this nature will require an extensive investigation involving a large

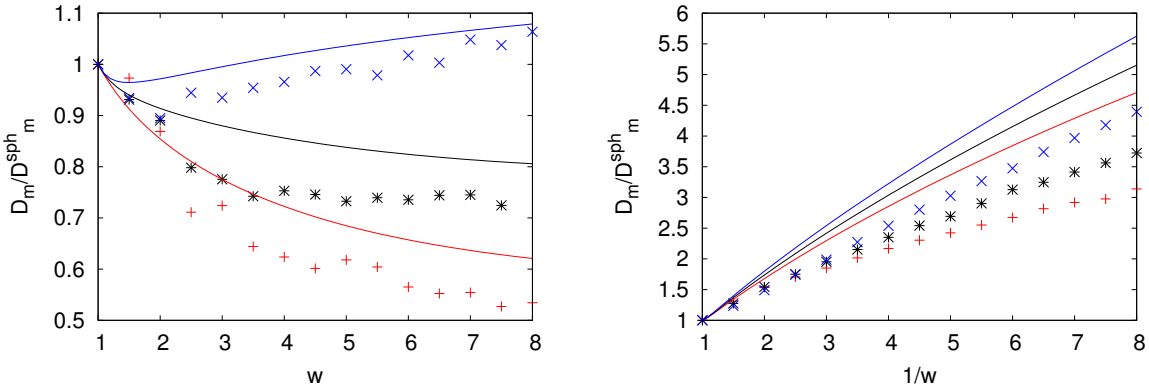

(a) (b)

Fig. 42. D_m/D_m^{sph} as a function of the void aspect ratio for (a) prolate cavities (b) oblate cavities, stress triaxiality, $T = 1$ and porosity, $f = 0.01$. The solid line corresponds to the predictions from the analytical model. Discrete points correspond to numerically determined values for Isotropic matrix ($*$), Material 1 ($+$) and Material 2 ($\times$) from Table V.

number of test cases, in the spirit of the previous works of [29,43,90] and others. This is especially true in the case of coupled void shape and anisotropy effects, where the parameter space to be explored is large. While such an investigation is beyond the scope of the present work, we present a limited set of two-dimensional axisymmetric finite element calculations for transversely isotropic matrices and axisymmetric states of loading, using the object–oriented finite element program, Zebulon, developed by Besson and Foerch [44, 91]. A cylindrical RVE, made of a transverse isotropic Hill matrix and containing a spheroidal void in the center, is subjected to proportional axisymmetric loading paths. The major stress is applied in the axial direction of the voids and the stress triaxiality is held constant through the simulation. The calculations presented are in fact similar to those in [32], using spheroidal voids instead of spherical ones.

Figure 43 shows typical RVEs used in the calculations and the details of the

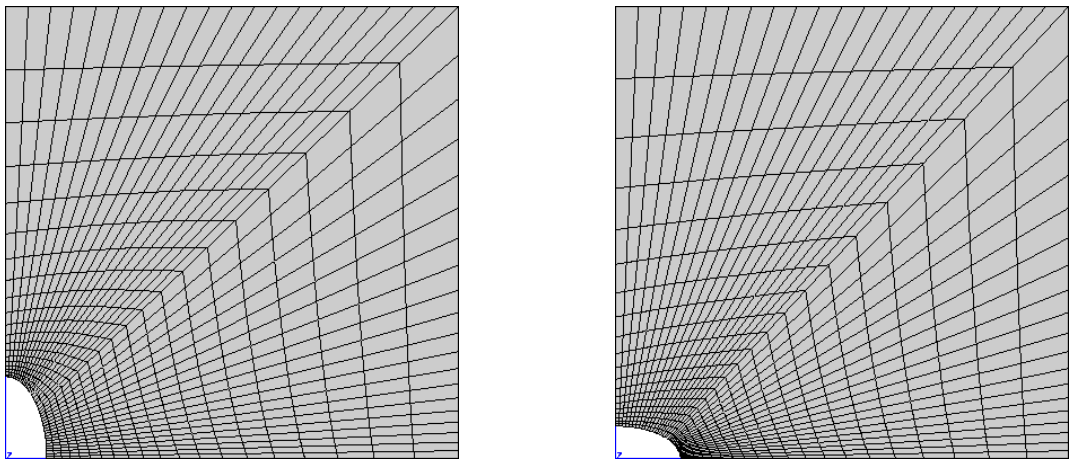

(a) (b)

Fig. 43. Finite-element meshes of the RVEs used for the unit cell calculations (a) prolate ($w = 2$) (b) oblate ($w = 1/2$). Porosity $f = 0.001$ for both cases.

meshes used. Exploiting the symmetry of the problem, only a quarter of the domain is modeled. The average stress-strain response for the unit-cell is obtained by plotting the variation of the Von Mises effective stress, $\Sigma_e = |\Sigma_{33} - \Sigma_{11}|$, as a function of the effective strain, $E_e = \frac{2}{3}|E_{33} - E_{11}|$, where the Cartesian coordinate system of Fig. 37 has been assumed. The evolution of porosity, f, and void aspect ratio, w, are compared with the model predictions from equations (4.10) and (4.11) respectively. The model constitutive equations are integrated using a convex cutting plane integration algorithm [92,93]. Attention is focused on the early stages of deformation, well before the onset of strain localization in the RVE, and the scope of the comparison is limited to discussing qualitative trends. Isotropic power-law hardening with an exponent $n = 0.1$ was assumed for the matrix in the FE computations. Strain hardening is incorporated into the model using a heuristic energy balance approach for the plastic work used in previous works [29, 43]. In addition, we incorporate a heuristic parameter, q_w, in the model, originally proposed by Tvergaard [14] in the context of the Gurson model, and later extended by Gologanu et al. [56] to be a function of the void

aspect ratio for spheroidal voids. With these heuristic corrections, the yield function for axisymmetric loading reads

$$\frac{h^{'}C}{\bar{\sigma}^2}\left(\Sigma_{33}-\Sigma_{11}+\frac{3}{2}\eta\Sigma_h\right)^2+2q_w(g+1)(g+f)\cosh\left(\kappa\frac{\Sigma_h}{\bar{\sigma}}\right)-(g+1)^2-q_w^2(g+f)^2=0 \tag{4.46}$$

where $\bar{\sigma}$ now denotes the *current* yield stress of the matrix and q_w is given by

$$q_w=1+2(q_s-1)\frac{w}{1+w^2} \tag{4.47}$$

The limiting value of q_w for a spherical cavity, q_s is taken to be 1.6 in the following calculations.

Figure 44 shows the comparison of the stress–strain response of the unit-cell to that obtained from integration of the model constitutive equations. These results correspond to axisymmetric proportional loading with a major axial stress ($\Sigma_{33} > \Sigma_{11}$) and a macroscopic stress triaxiality, $T = 1$. The initial porosity and void aspect ratios correspond to the meshes shown in Fig. 43. The Figs. 44(a)-(b) show the unit-cell and model responses respectively, for the initially prolate cavity of Fig. 43(a) and the Figs. 44(c)-(d) show the corresponding results for the initially oblate cavity of Fig. 43(b). It may be seen that the stress-strain response of the model is in close agreement with the FE results. Figure 45(a) and 45(b) show comparison of the evolution of porosity, f, as a function of the effective strain in the RVE, E_e, for the initially prolate cavity of Fig. 43(a). Figure 45(c) and 45(d) show comparison of the evolution of void aspect ratio, w, as a function of the effective strain for the same RVE. It is observed that the qualitative trends for the evolution of porosity and void shape with deformation for the three materials are correctly predicted by the analytical model. However, the unit-cell results for the evolution of the void aspect ratio, w, for Material 1 evidences an anomalous behavior at larger values of the effective strain.

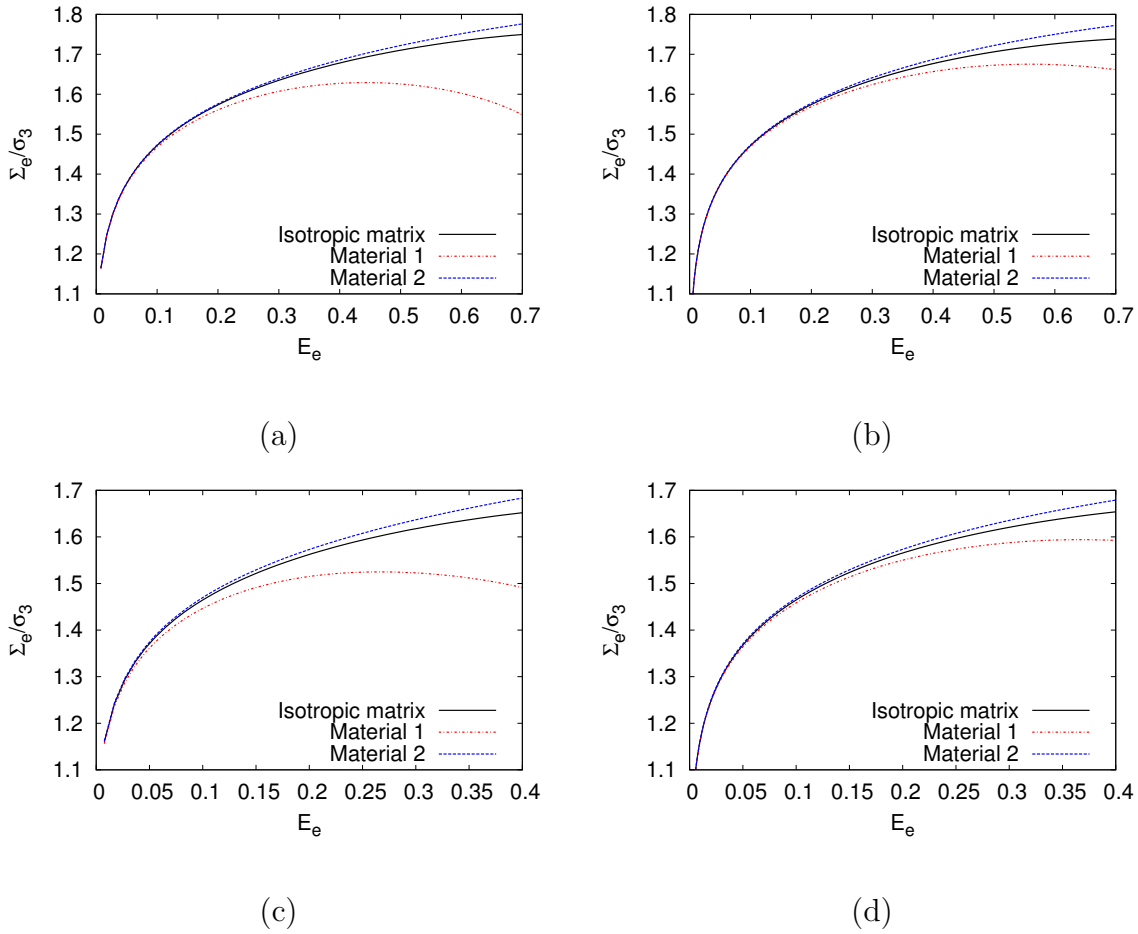

Fig. 44. Comparison of the stress–strain response from the FE calculations and the analytical model for initially prolate and oblate cavities (Figure 43) and three different materials from Table V. The results correspond to axisymmetric proportional loading with a stress triaxiality, $T = 1$. (a) FE results and (b) Model predictions for the initially prolate cavity. (c) FE results and (d) Model predictions for the initially oblate cavity.

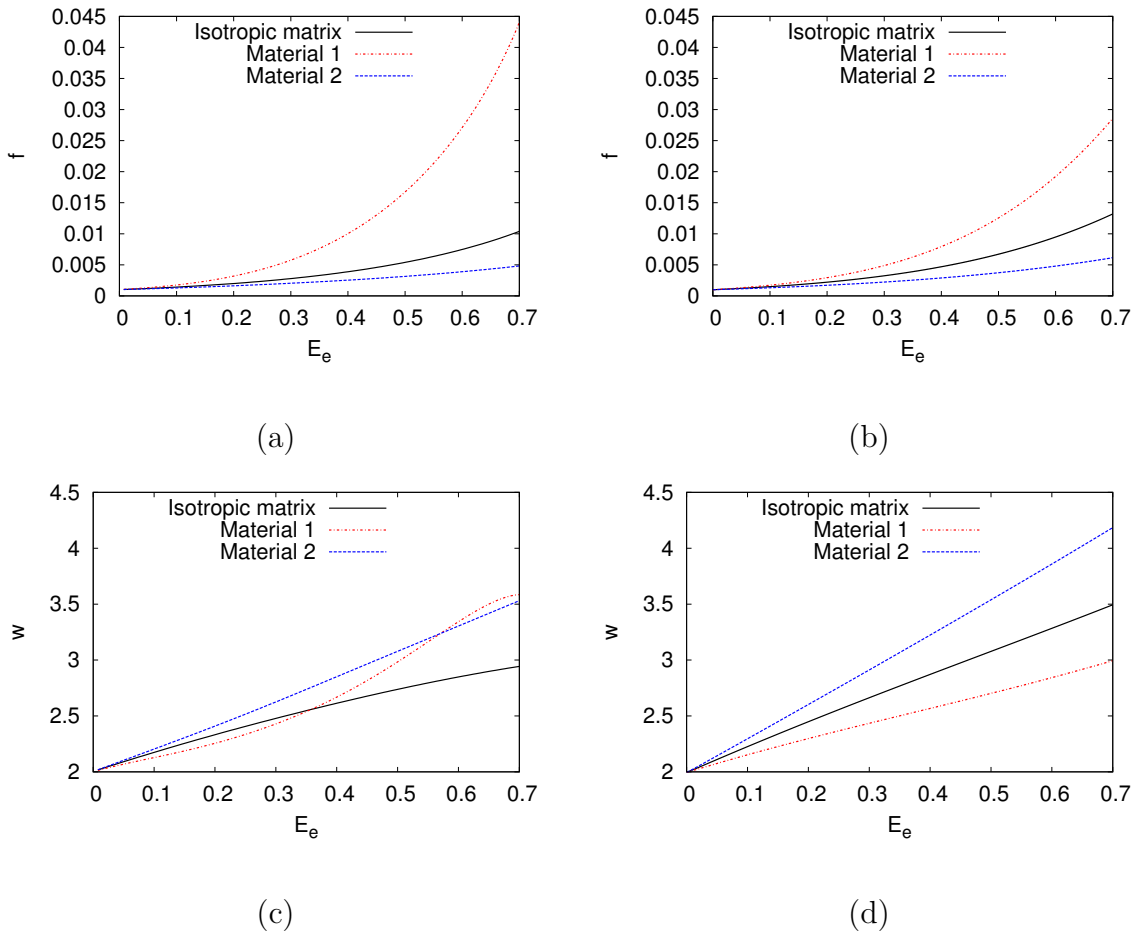

Fig. 45. Comparison of the unit cell response to the model results for the evolution of f and w, for an initially prolate cavity and three different materials from Table V. (a) FE results for the evolution of f (b) Model prediction for the evolution of f (c) FE results for the evolution of w (d) Model prediction for the evolution of w.

Examination of the corresponding deformed configuration of the unit-cell indicates that while the void shape remains roughly spheroidal for the isotropic matrix and Material 2, this is not true for Material 1 at large strains. Since the analytical model assumes that the void remains spheroidal during the deformation, such discrepancies may be expected in the case of certain types of material anisotropy.

Figures 46(a) and 46(b) show a similar comparison of the evolution of porosity, f, as a function of the effective strain in the RVE, E_e, for an initially oblate cavity. The initial porosity and void aspect ratio were $f_0 = 0.001$ and $w = 1/2$, corresponding to Fig. 43(b). Figures 46(c) and 46(d) show comparison of the evolution of void aspect ratio, w, as a function of the effective strain for the same RVE. Again, the model correctly predicts the qualitative trends for the evolution of f and w with deformation for the three materials studied, together with a reasonable quantitative agreement.

F. Conclusion

A numerical method to derive rigorous upper bound yield loci for spheroidal RVEs containing confocal spheroidal voids and subjected to axisymmetric stress states was developed. For a specified loading path in stress space, the yield point was obtained by conjugate gradient minimization of the plastic dissipation using a large number of axisymmetric velocity fields. The analytical model was also integrated to obtain the stress–strain history and evolution of the microstructural variables for a specified loading path using the convex cutting plane algorithm. The model predictions were compared with corresponding 'exact' results obtained from finite-element calculations. The main conclusions of this study are summarized below.

- Comparisons with numerical upper bound yield loci showed that the analyti-

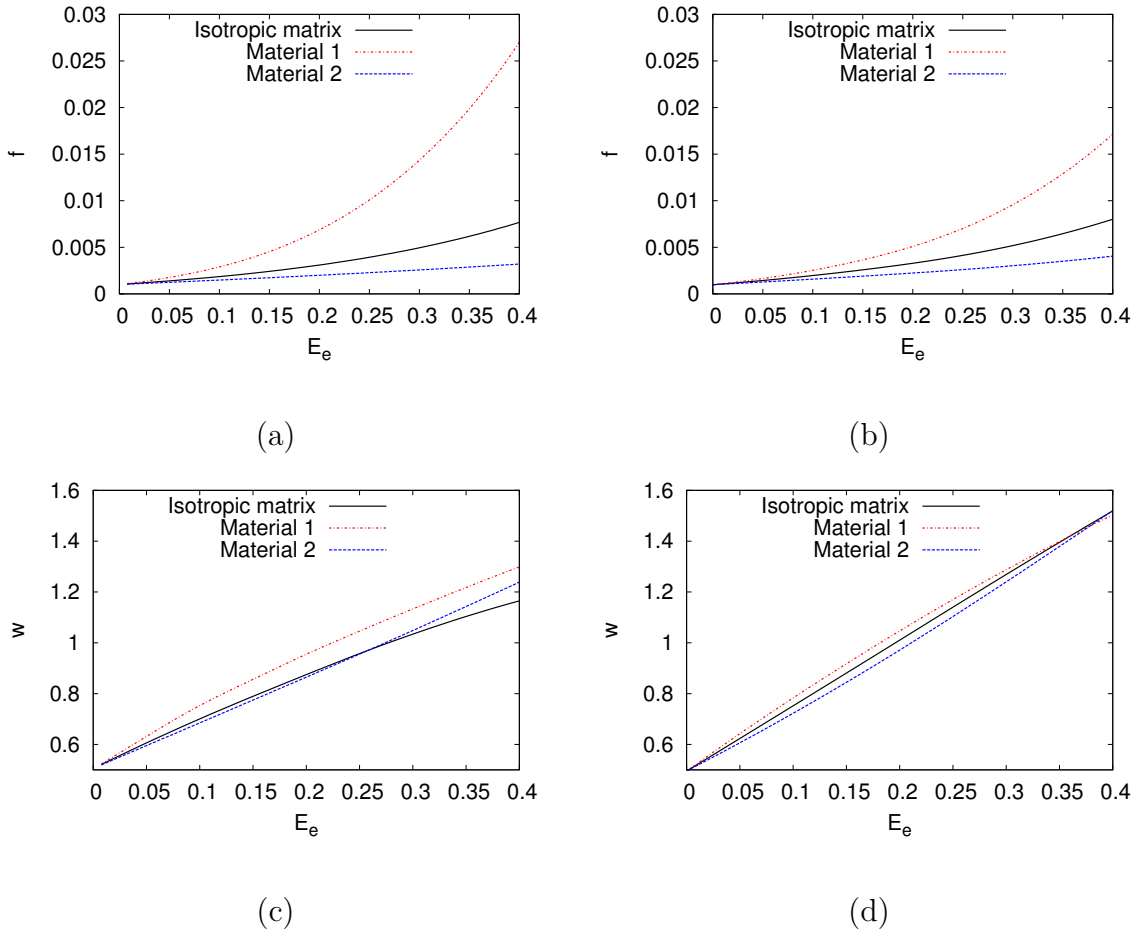

Fig. 46. Comparison of the unit cell response to the model results for the evolution of f and w, for an initially oblate cavity and three different materials from Table V. (a) FE results for the evolution of f (b) Model prediction for the evolution of f (c) FE results for the evolution of w (d) Model prediction for the evolution of w.

cal yield criterion of equation (4.2) respects the upper bound character of the homogenization approach for prolate cavities as well as provides a close approximation for the numerical yield loci at all triaxialities.

- Similar comparisons for oblate cavities also yielded good agreement albeit with larger deviations from the numerical loci, possibly as a result of the different approaches used to derive the prolate and oblate criteria. Also, possible violations of the upper bound character were observed for flat void shaped although the differences were small in all cases considered.
- Comparison of the model predictions for the evolution of the microstructure with finite-element predictions showed good agreement for the qualitative trends for the different types of material anisotropy considered. However, some deviations have been observed in cases where the void shape was found to deviate significantly from a spheroid as assumed in the analytical model.

G. Appendices

1. Expressions for the Model Parameters

The exponential term in the criterion (4.2) depends on two parameters, κ and α_2. κ is a measure of the pressure dependency of the yield surface, and is given by

$$\kappa = \begin{cases} \sqrt{3}\left\{\frac{1}{\ln f}\left[\frac{2}{3}\ln\frac{1-e_2^2}{1-e_1^2} + \frac{3+e_2^2}{3+e_2^4} - \frac{3+e_1^2}{3+e_1^4} + \frac{1}{\sqrt{3}}\left(\tan^{-1}\frac{e_2^2}{\sqrt{3}} - \tan^{-1}\frac{e_1^2}{\sqrt{3}}\right)\right.\right. & \text{(p)} \\ \qquad\qquad \left.\left. -\frac{1}{2}\ln\frac{3+e_2^4}{3+e_1^4}\right]\frac{4h+8h_a-7h_t}{10} + \frac{4(h+2h_a+2h_t)}{15}\right\}^{-1/2} & \\ \frac{3}{2}\left(\frac{h+2h_a+2h_t}{5}\right)^{-1/2}\left\{1 + \frac{(g_f-g_1)+\frac{4}{5}(g_f^{5/2}-g_1^{5/2})-\frac{3}{5}(g_f^5-g_1^5)}{\ln\frac{g_f}{g_1}}\right\}^{-1} & \text{(o)} \end{cases} \tag{4.48}$$

where

$$g_f \equiv \frac{g}{g+f}, \quad g_1 \equiv \frac{g}{g+1} \tag{4.49}$$

The argument of the 'cosh' also depends on the term $\mathbf{\Sigma} : \mathbf{X}$, where $\mathbf{X}$ is defined by (4.4). Since the tensor $\mathbf{X}$ is coaxial with the void, this term is in fact a weighted sum of the normal stress components in the axial and transverse directions of the void, where the weights depend on the value of the parameter α_2. α_2 is given by

$$\alpha_2 = \begin{cases} \dfrac{(1+e_2^2)}{(1+e_2^2)^2 + 2(1-e_2^2)} & \text{(p)} \\ \dfrac{(1-e_2^2)(1-2e_2^2)}{(1-2e_2^2)^2 + 2(1-e_2^2)} & \text{(o)} \end{cases} \tag{4.50}$$

The parameters C and η that appear in the square term of the yield criterion are given by

$$\begin{aligned} \eta &= -\frac{2}{3}\frac{\kappa Q^*(g+1)(g+f)\mathrm{sh}}{(g+1)^2 + (g+f)^2 + (g+1)(g+f)[\kappa H^* \mathrm{sh} - 2\mathrm{ch}]}, \\ C &= -\frac{\kappa h(g+1)(g+f)\mathrm{sh}}{(Q^* + \eta H^*)\eta}, \quad \mathrm{sh} \equiv \sinh(\kappa H^*), \quad \mathrm{ch} \equiv \cosh(\kappa H^*) \end{aligned} \tag{4.51}$$

where $H^* \equiv 2\sqrt{h}(\alpha_1 - \alpha_2)$ and $Q^* \equiv \sqrt{h}(1-f)$. H^* and Q^* depend on an additional parameter α_1 which is a function of the void shape alone. α_1 is given by

$$\alpha_1 = \begin{cases} \left[e_1 - (1-e_1^2)\tanh^{-1} e_1\right]/(2e_1^3) & \text{(p)} \\ \left[-e_1(1-e_1^2) + \sqrt{1-e_1^2}\sin^{-1} e_1\right]/(2e_1^3) & \text{(o)} \end{cases} \tag{4.52}$$

The evolution law for the void shape parameter, equation (4.11), depends on a heuristic parameter, ϕ, which is taken to be a function of the porosity, void shape and the macroscopic stress triaxiality, T, which is defined as the ratio of the mean stress to the Von Mises effective stress., i.e. $T \equiv \Sigma_m / \sqrt{\frac{3}{2}\mathbf{\Sigma}' : \mathbf{\Sigma}'}$. ϕ has the form

$$\phi \equiv 1 + \phi_f \phi_e \phi_T \tag{4.53}$$

where ϕ_f, ϕ_e and ϕ_T are functions of f, S and T respectively. These are given by

$$\phi_e(e_1) = \frac{9}{2}\frac{\alpha_1 - \alpha_1^{Gar}}{1-3\alpha_1},\ \phi_f(f) = (1-\sqrt{f})^2,\ \phi_T(T) = \begin{cases} 1-(T^2+T^4)/9 & \text{for}\,\epsilon = +1 \\ 1-(T^2+T^4)/18 & \text{for}\,\epsilon = -1 \end{cases} \tag{4.54}$$

The parameters ϵ and α_1^{Gar} are defined by

$$\epsilon = \text{sgn}(\Sigma_m \Sigma'_{33}), \quad \alpha_1^{Gar} = \begin{cases} 1/(3-e_1^2) & \text{(p)} \\ (1-e_1^2)/(3-2e_1^2) & \text{(o)} \end{cases} \tag{4.55}$$

CHAPTER V

RECENT EXTENSIONS OF THE 2.5D DISLOCATION DYNAMICS METHOD

A. Background

Plasticity in crystalline materials results from the collective motion of a large number of discrete dislocations. The experimentally observed flow strength and strain hardening rates are determined by the average behavior of a large number of defects at the nano and meso scales such as the population of dislocation nucleating sources, mobility of dislocations, their short range interactions with each other and with other crystal defects such as vacancies, precipitates, grain boundaries and free surfaces. Thus, unlike the elastic properties of a material, which may be determined in a straightforward fashion by consideration of the inter-atomic forces, the modeling of plasticity from first principles is difficult due to the variety of defects that contribute to the overall strength. Continuum models of crystal plasticity take a phenomenological approach informed by experimental observations such as the incompressibility of plastic flow and the dependence of the flow stress on the dislocation density on the individual slip systems through the Taylor hardening relation. However, the applicability of these continuum models to small scale systems is limited by several key factors: (i) lack of a natural length scale in the models and (ii) assumption of homogeneity of plastic flow in an elementary volume. Several recent experiments [5, 6, 94] have demonstrated that when specimen sizes are small enough for the above assumptions to be violated so that the fundamental discreteness of plasticity has an effect on the overall response, stochasticity and size effects emerge that can not be modeled using continuum mechanics. In such cases, "bottom up" modeling approaches such as atomistics or DD can provide an alternative approach to material design.

While the atomistic details of the dislocation cores are important in determining the short range interactions of dislocations, it has been observed that outside of the dislocation cores the long range fields of the dislocations are well represented by classical linear elasticity solutions [95]. Based on this observation, discrete dislocation plasticity uses a hybrid approach where discrete defects such as dislocations are modeled explicitly while the long range of interaction of these defects is modeled using continuum mechanics, leading to a tremendous reduction in the degrees of freedom. However, the DD method retains the essential discrete character of plasticity and embeds a physically relevant length scale, the dislocation Burgers vector. The central difference between DD and continuum models is that in DD the plasticity and hardening response of a material is an output from the model rather than an input through constitutive assumptions and as such can capture the size dependency in these properties.

Discrete dislocation dynamics models have been developed since the early 90's by several research groups [25,96–98] to investigate phenomena such as the formation of dislocation patterns. The models may be broadly classified into two categories, namely three dimensional (3D) and two dimensional (2D) DD models. The 3D models treat dislocations as line singularities in the form of loops or pinned segments that glide on well defined crystallographic slip systems in a three dimensional crystal. Full 3D DD simulations are computationally demanding, but potentially allows a more faithful representation of the physics of dislocation interactions. On the other hand, 2D models typically assume a simplified planar geometry, where dislocations are modeled as infinite straight line singularities that intersect the plane of analysis. In the simulations, the intersection points of the dislocations glide along in-plane projections of their respective slip systems. At the expense of some accuracy in the representation of the physics, 2D DD has enabled complex simulations such as

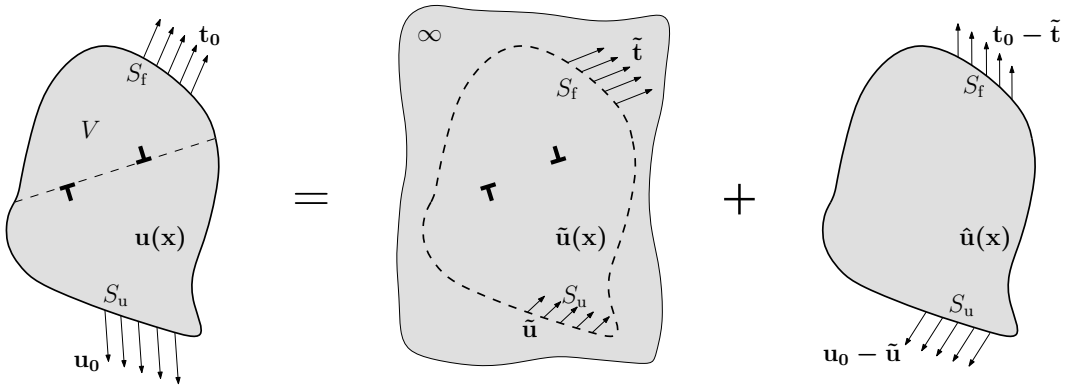

Fig. 47. Illustration of the superposition method for determination of the elastic fields in a dislocated body.

crack propagation, indentation, crack tip fields, strain hardening and void growth to be undertaken [99–103]. In the present dissertation, we focus our attention to one particular model of 2D DD originally developed by Van der Giessen and Needleman [25]. In the following sections, we present a brief review of the original model and an extension of their constitutive framework to account for strain hardening due to Benzerga et al. [26]. In the final section, we identify and discuss several limitations and gaps in the above constitutive framework that are addressed as part of this dissertation.

B. Dislocation Dynamics Model of Van der Giessen and Needleman

Van der Giessen and Needleman [25] developed a purely mechanical theory and simulation framework for low temperature plasticity through dislocation glide by neglecting temperature effects. Consider a linear elastic body of volume V containing a finite number of discrete dislocations in the form of dipoles as shown in Fig. 47. The dipole in the figure may represent the intersection of a dislocation loop with the plane of analysis. Within a small strain setting, superposition is used to decompose the overall elastic fields in the body as the sum of the infinite medium singular fields of the

discrete dislocations (the $\tilde{}$ fields) and a smooth complementary field that enforces the true boundary conditions of the problem (the $\hat{}$ field). Anywhere in the volume V of the sample, the displacements, strains and stresses are written as:

$$\mathbf{u} = \tilde{\mathbf{u}} + \hat{\mathbf{u}}, \qquad \boldsymbol{\epsilon} = \tilde{\boldsymbol{\epsilon}} + \hat{\boldsymbol{\epsilon}}, \qquad \boldsymbol{\sigma} = \tilde{\boldsymbol{\sigma}} + \hat{\boldsymbol{\sigma}} \tag{5.1}$$

The ($\tilde{}$) fields of the dislocations are themselves found as superposition of the singular fields of all dislocations in V,

$$\tilde{\mathbf{u}} = \sum_{i=1}^{N} \mathbf{u}^i, \qquad \tilde{\boldsymbol{\epsilon}} = \sum_{i=1}^{N} \boldsymbol{\epsilon}^i, \qquad \tilde{\boldsymbol{\sigma}} = \sum_{i=1}^{N} \boldsymbol{\sigma}^i, \tag{5.2}$$

with N the total number of dislocations in the sample. N generally changes in the course of a simulation due to the nucleation/annihilation of dislocations. The fields $\boldsymbol{\sigma}^i$, $\boldsymbol{\epsilon}^i$ and $\mathbf{u}^i$ corresponding to dislocation i in an extended homogeneous medium are known analytically [104]. However, these classical solutions for the dislocation fields have singularities at the dislocation positions and are hence not valid within the dislocation cores. Alternative non-singular approximations of the elastic fields of a dislocation, such as [105], may also be used within the above superposition framework. The governing equations for the image ($\hat{}$) fields are given by

$$\begin{aligned} \nabla \cdot \hat{\boldsymbol{\sigma}} &= 0 \qquad \text{in } V \\ \hat{\boldsymbol{\epsilon}} &= \frac{1}{2}\left(\nabla \otimes \hat{\mathbf{u}} + (\nabla \otimes \hat{\mathbf{u}})^T\right) \qquad \text{in } V \end{aligned} \tag{5.3}$$

with

$$\hat{\boldsymbol{\sigma}} = \mathcal{L} : \hat{\boldsymbol{\epsilon}} \qquad \text{in } V \tag{5.4}$$

where $\mathcal{L}$ denotes the tensors of elastic moduli of the material, $\otimes$ denotes the tensor product and the superscript T denotes tensor transposition. With S_f and S_u referring to the portions of the boundary on which tractions $\mathbf{T}_0$ and displacements $\mathbf{U}_0$ are

prescribed, respectively, the boundary conditions for the ($\hat{}$) fields are

$$\begin{aligned} \mathbf{n} \cdot \hat{\boldsymbol{\sigma}} &= \mathbf{T}_0 - \mathbf{n} \cdot \tilde{\boldsymbol{\sigma}} \qquad \text{on } S_{\mathrm{f}} \\ \hat{\mathbf{u}} &= \mathbf{U}_0 - \tilde{\mathbf{u}} \qquad \text{on } S_{\mathrm{u}} \end{aligned} \tag{5.5}$$

with $\mathbf{n}$ the outer unit normal.

Equations (5.3)-(5.5) represent a well-posed boundary value problem for the non-singular ($\hat{}$) fields, which is solved using the finite element method. The dislocation dynamics problem is solved in a time incremental manner where, at each increment of the deformation the elastic fields are determined using the current positions of the dislocations. The dislocation positions are updated between increments using the Peach-Koehler force, $\mathbf{f}^i$, which is a configurational force on dislocation i that acts to lower the overall potential energy and is defined as [25, 104]

$$\mathbf{f}^i = -\frac{\partial \Pi}{\partial \mathbf{x}^i} \tag{5.6}$$

where Π denotes the potential energy and $\mathbf{x}^i$ denotes the position of dislocation i. A careful analysis yields [25]

$$\mathbf{f}^i = \mathbf{t}^i \times \left[\left(\hat{\boldsymbol{\sigma}} + \sum_{j \neq i} \boldsymbol{\sigma}^j \right) \cdot \mathbf{b}^i \right] \tag{5.7}$$

where $\mathbf{t}^i$ is a unit vector along the tangent to the dislocation line and $\mathbf{b}^i$ is the Burgers vector. The Peach-Koehler force may be resolved into a glide component, f_g, and a climb component, f_c, along the slip plane tangent and normal directions respectively. I.e.

$$\mathbf{f}^i = f_g^i \mathbf{m}^i + f_c^i \mathbf{n}^i \tag{5.8}$$

where $\mathbf{n}^i$ denotes the slip plane normal and $\mathbf{m}^i = \mathbf{t}^i \times \mathbf{n}^i$. In [25], only the glide component is used to update the dislocation positions while the climb component is

ignored. A viscous drag type mobility law is assumed for dislocation glide

$$f_g^i = B_g v^i \tag{5.9}$$

with a constant drag factor B_g.

While the elastic boundary value problem framework described above is general and applies to three dimensional dislocated specimens, most numerical implementations of the same, including [25], use a two dimensional plane strain approximation where dislocation loops are represented as dipoles crossing the plane of analysis as illustrated in Fig. 47. These dislocation dipoles nucleate from randomly distributed point sources in the sample that idealize Frank-Read sources in three dimensions. A new dislocation dipole is nucleated when the modulus of the glide component of the Peach-Koehler force on a source exceeds a critical value of τ_{nuc} for a critical duration t_{nuc}. The dislocation structure is updated after checking for (i) nucleation of new dislocations from point sources, (ii) pinning of dislocations at randomly distributed point obstacles in the sample and their unpinning when the Peach-Koehler force exceeds the pinning strength $\tau_{\text{obs}} b$ where b is the modulus of the Burgers vector (iii) mutual annihilation of opposite signed dislocations when they cross each other or approach within a critical distance L_e on the same slip plane and (iv) exit of dislocations at the free boundaries leaving a slip discontinuity across their original slip plane. Thus, within the simulation framework, long range effects, including the effects of image forces due for example to the presence of free boundaries, are directly taken into account through the elasticity fields, while short range effects are accounted for through the constitutive rules (i)-(iv) described above.

C. 2.5D Constitutive Rules for Strain Hardening

While a two dimensional implementation of the DD framework described in the previous section provides a basic model of single crystal plasticity, it does not predict strain hardening under homogeneous deformation irrespective of whether singular or non-singular approximations of the elastic fields of the dislocations are used. The inability of 2D DD to predict strain hardening may be attributed to the absence of certain key ingredients in the model, namely the dynamic evolution of the density of dislocation sources and obstacles and absence of rules for short range interactions between dislocations on intersecting slip systems. In real crystals, dislocations on intersecting slip planes can form junctions [106] that can obstruct the flow of other dislocations. These junctions may either break away under further loading or stabilize by a variety of mechanisms including cross slip. Stable junctions can act as anchoring points for new Frank-Read sources in the specimen. Thus, the population of sources and obstacles in the specimen can evolve with the deformation. Another major effect neglected in the original model is the line tension effect that act to shrink dislocation loops. In order to remedy some of these shortcomings, Benzerga et al. [26] proposed a set of idealized constitutive rules in 2D that are inspired by the physics of dislocation interactions in 3D. The enhancements brought about by these additional constitutive rules allows for an adequate representation of strain hardening in 2D DD simulations with hardening rates that are comparable to experimental results [102, 107]. These constitutive rules, frequently referred to in the literature as '2.5D rules', are discussed below.

In the 2.5D formulation, two dislocations on intersecting slip planes can form a sessile junction if both dislocations fall within a critical radius of d^* from the intersection point at the end of an increment. These junctions may represent Lomer-Cottrel

locks in three dimensions and act as obstacles to dislocation motion on both the intersecting slip planes. Most of these "dynamic obstacles" may be destroyed by unzipping of the participating dislocations if the resolved shear stress at a junction I exceeds a critical value given by

$$\tau^I_{\text{brk}} = \beta_{\text{brk}} \frac{\mu b}{\mathcal{L}^I} \tag{5.10}$$

where μ denotes the shear modulus, $\mathcal{L}^I$ is the distance to the nearest junction on any of the intersecting slip planes and β_{brk} is a scaling factor for junction strength. However, a finite (small) probability, p, is assigned for the stabilization of these junctions by cross slip or other mechanisms at the scale of the junction cores so that they may not be destroyed under further loading. A probabilistic approach is needed due to the limited representation of the physics in the two-dimensional model. A stable junction I may act as an anchoring point for a new Frank-Read source with a nucleation strength given by

$$\tau^I_{\text{nuc}} = \beta_{\text{nuc}} \frac{\mu b}{\mathcal{L}^I} \tag{5.11}$$

where β_{nuc} is a source strength parameter (typically of the order of unity [108]) and $\mathcal{L}^I$ is the distance to the nearest junction on the slip plane on which τ^I_{nuc} is being resolved. The nucleation time for the source is given by

$$t^I_{\text{nuc}} = \gamma_{\text{nuc}} \frac{\mathcal{L}^I}{|\tau^I| b} \tag{5.12}$$

where γ_{nuc} is a material constant with the units of the drag factor and τ^I is the resolved shear stress at the junction I excluding the self-stress due to the participating dislocations. Notice that both the source strength and the nucleation time depends on a physically meaningful length scale so that the properties of the dynamic Frank-Read sources depend on the statistics of junction formation. Finally, the line tension force on 3D dislocation loops in is idealized in 2D as a mutually attractive force between

the two dislocations that comprise a dipole, given by

$$\mathcal{L}_i = -\alpha \frac{\mu b}{\mathcal{S}_d^i} \tag{5.13}$$

where $\mathcal{S}_d^i$ denotes the algebraic distance between the dislocations in the dipole and α is a scaling factor. The reader is referred to [26] for additional details including physical justifications for the above constitutive rules.

D. Limitations of the Model

Despite its success in modeling several aspects of crystal plasticity, the DD models currently in use suffer from certain limitations that we seek to address in this dissertation. These may be categorized into two broad areas, namely limitations in the computational framework that limit range of applicability of the method and limitations in the representation of the physics of dislocation motion and interactions. These are discussed below as a prelude to the developments presented in the next section. Applications of the enhanced DD model are presented in the subsequent chapters.

1. Algorithmic Limitations

By far the most computationally expensive operation in any DD simulation is the calculation of the Peach-Koehler interaction forces between the dislocations at each time increment. The complexity of this operation scales as $\mathcal{O}(N^2)$ where N denotes the total number of dislocations. For sufficiently large samples, the computation of the Peach-Koehler force becomes prohibitively expensive limiting the applicability of the framework to very large systems. Yet, this is an important limit case where the predictions of DD models have not been validated sufficiently by comparison with

predictions from continuum plasticity. Thus, in section E, we present two alternative approaches to address this issue, namely (i) code parallelization and (ii) implementation of the well known fast multipole method for many body dynamics.

The second limitation pertains to the treatment of slip discontinuities due to dislocations that exit the free surfaces in a sample. The current approach treats these as stress–free displacement discontinuities across the respective slip planes. However, in some multiply connected geometries such as porous or cracked specimens, these slip steps can lead to residual stresses in the sample. In order to treat such problems, we implement an enhanced finite element method for the solution of the ($\hat{}$) fields following the original proposal by Romero et al. [109] by embedding the discontinuities in the finite element formulation.

2. Limitations in the Representation of the Physics

One of the major limitations of most current DD frameworks is that they are based on a deterministic framework where thermally activated phenomena such as dislocation climb and bypass of obstacles are not adequately accounted for. Effectively, this limits the applicability of the DD models to low temperatures where thermal effects may be neglected. Nevertheless, there are several important engineering applications where thermal effects play a decisive role, such as in the creep of structural components. At high temperatures, crystalline materials contain a high concentration of point defects such as vacancies. Diffusion of vacancies into the dislocation core leads to the non-conservative climb motion of dislocations. In chapter VIII, we present a coupled formulation for DD and vacancy diffusion at elevated temperatures. This high temperature DD formulation is applied to the problem of dislocation creep in single crystals.

E. Recent Enhancements

This section contains a detailed discussion of the specific numerical algorithms that have been implemented to reduce the computation time for simulations involving a large number of dislocations ($N > 100000$) and to widen the scope of the 2D DD method to a more general class of boundary value problems. In the DD simulation methodology outlined in section B, the most critical operation in terms of the computation time is the calculation of the Peach-Koehler force on the dislocations at each time increment. The Peach-Koehler force, $\mathbf{f}^i$, on a dislocation i is given by

$$\mathbf{f}^i = \mathbf{t}^i \times \left[\left(\hat{\boldsymbol{\sigma}} + \sum_{j \neq i} \boldsymbol{\sigma}^j \right) \cdot \mathbf{b}^i \right], \qquad i, j = 1..N \tag{5.14}$$

As can be seen from the equation above, computation of the Peach-Koehler force on a system containing N dislocations is an operation of complexity $\mathcal{O}(N^2)$ due to the presence of the summation term over all dislocations. It must be mentioned here that an *ad hoc* solution to the above problem by using a cut off radius for mutual dislocation interactions can lead to large error due to the fact that the elastic fields of the dislocations are slowly decaying fields so that their influence extends over large distances (the stress field of the dislocations decays as $1/r$ with distance r from the dislocation core with the strain energy increasing as $\log r$). Therefore, achieving large dislocation densities in DD simulations in a realistic time span depends on finding efficient algorithms for computing the Peach-Koehler force. Alternate approaches towards achieving this objective are presented in the following two subsections.

1. Code Parallelization Using OpenMP

One relatively straightforward method for improving efficiency by leveraging the wide availability of multi-processor shared memory computing clusters is to parallelize

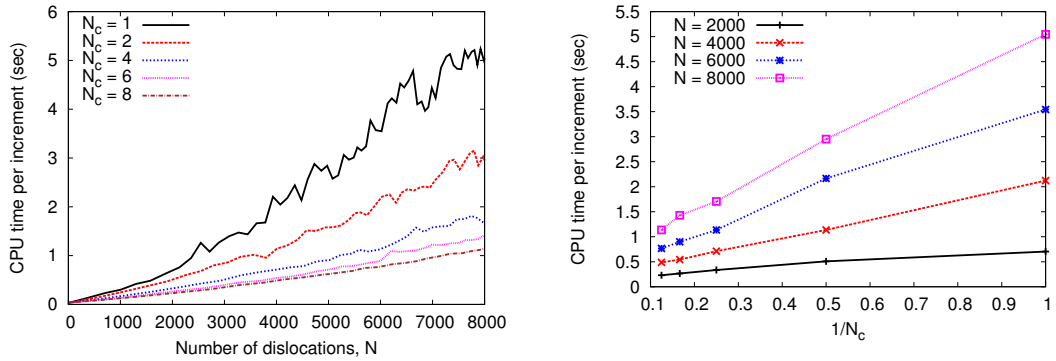

(a) (b)

Fig. 48. (a) Comparison of the computation time per increment as a function of the number of dislocations N for different values of the active core count N_c. (b) Scaling of the computation time with $1/N_c$ for different values of N.

the code. We have used the relatively standard OpenMP API [110] that is widely supported by all major compilers. Since the evaluation of expression (5.14) involves looping over a large number of dislocations, we make use of the OpenMP directives for automatic parallelization of program loops. In addition to the computation of $\mathbf{f}^i$ for updating dislocation positions, several other large loops in the code, including testing for nucleation from sources, cutting through point obstacles and break away of dislocation junctions, which involve computation of the Peach-Koehler force have been parallelized. The results of this effort are summarized in Fig. 48(a), which shows the computation time as a function of the number of dislocations N in a typical DD simulation. The different curves in Fig. 48(a) correspond to different number of active processing cores, N_c (upto 8). Fig. 48(b) shows the scaling of the computation time per increment as a function of the reciprocal of the number of processing cores N_c for different values of N. The results indicate that the computation time scales more or less inversely with the number of active cores.

Despite these improvements, the OpenMP approach suffers from two limitations.

First, unlike the case of massively parallel APIs, the scalability of OpenMP is limited by the number of cores available on a shared memory system, typically a node in a compute cluster, which is usually 8 or 16. Most importantly, while OpenMP yields a linear improvement in efficiency with core count, the increase in computation time is quadratic in the number of dislocations N. The dislocation count increases as the square of the sample size and for large systems the advantage of parallelization is quickly nullified. Tacking this problem calls for implementation of more refined algorithms that can reduce the computational complexity from $\mathcal{O}(N^2)$.

2. The Fast Multipole Method

The fast multipole method (FMM) was originally proposed by Greengard and Rokhlin [111] as an efficient numerical scheme for solving problems involving multibody interactions. We have used an adaptive version of FMM due to [112] that enables N-particle interactions to be computed in $\mathcal{O}(N)$ operations as against $\mathcal{O}(N^2)$ for direct evaluation. The adaptive multipole algorithm, explained in detail in [112], provides the key advantage that the $\mathcal{O}(N)$ scaling of the computation time is independent of the statistics of the particle population, which makes it ideal for DD simulations. In this section, the key lemmas and theorems of FMM are reformulated in the context of 2D DD simulations, followed by a brief summary of the algorithm implementation. The complex variable solution for an edge dislocation in an infinite medium is used in the formulation and the domain of interest is a subset of the complex plane $\mathbb{C}$.

The linear elasticity solution for an edge dislocation at position z_0 in an infinite elastic isotropic solid may be specified in terms of two complex potentials, $\Omega(z)$ and

$\omega(z)$ $(z, z_0 \in \mathbb{C})$, given by [113]

$$\Omega(z) = q \log(z - z_0), \qquad \omega(z) = \bar{q} \log(z - z_0) \tag{5.15}$$

$$q \equiv -i \frac{Eb}{8\pi(1 - \nu^2)} \tag{5.16}$$

where E and ν are the elastic modulus and Poisson's ratio respectively, $b = b_1 + ib_2$ is the Burger's vector and the overbar denotes complex conjugation. The stress field of the dislocation may be derived from the complex potentials using the formulae

$$\sigma_{11} + \sigma_{22} = 2(\Omega^{'}(z) + \overline{\Omega'(z)}) \tag{5.17}$$

$$\sigma_{11} - \sigma_{22} + 2i\sigma_{12} = -2(z\overline{\Omega''(z)} + \overline{\omega'(z)}) \tag{5.18}$$

It is clear from the above that the multipole expansions of the stress components of an edge dislocation can be constructed, given the expansions of the following two potentials

$$\phi_1(z) = \frac{q}{(z - z_0)}, \qquad \phi_2(z) = \frac{q}{(z - z_0)^2} \tag{5.19}$$

It is also obvious that given the multipole expansion of $(5.19)_1$, the expansion of $(5.19)_2$ can be obtained in straightforward way by differentiation of the former. In the following, the theorems and lemmas of FMM from [112] are restated in terms the potential of $(5.19)_1$. The numbering of the theorems and lemmas correspond to that in [112] and the proofs are omitted for brevity. The results presented here are analogous to the corresponding theorems and lemmas from [112] where a different complex potential $(\phi(z) = q \log(z - z_0))$ was used. Here, we use the complex potential

$$\phi(z) = \frac{q}{(z - z_0)} \tag{5.20}$$

which is in fact the derivative of $q \log(z - z_0)$. Hence, the expansions themselves can be derived by differentiating the corresponding results from [112]. However, the error

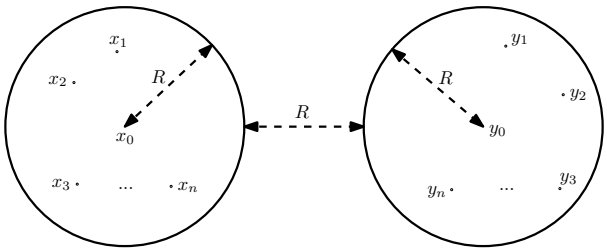

Fig. 49. Well separated sets of particles.

bounds are derived separately.

Theorem 2.1: For m dislocations Burgers vectors $b_i, i = 1, .., m$, located at points $z_i, i = 1, .., m$, with $|z_i - z_0| < R$, the potential at a point $z \in \mathbb{C}$ with $|z - z_0| > R$ is given by

$$\phi(z) = \sum_{k=0}^{\infty} \frac{a_k}{(z - z_0)^{k+1}}, \qquad a_k = \sum_{i=1}^{m} q_i (z_i - z_0)^k \tag{5.21}$$

where $q_i = q_i(b_i)$ is given by equation (5.16). Furthermore, for any $p \geq 1$,

$$\left| \phi(z) - \sum_{k=0}^{p} \frac{a_k}{(z - z_0)^{k+1}} \right| \leq \frac{A}{(c-1)} \left(\frac{1}{c} \right)^{p+1}, \; c = \left| \frac{z}{R} \right|, \; A = \frac{1}{R} \sum_{i=1}^{m} |q_i| \tag{5.22}$$

For "well separated" dislocations (i.e. $z > 2R$, see Fig. 49), an upper bound for the error is $A/2^{p+1}$.

Lemma 2.2: Given the multipole expansion of (5.21), for any point outside a circle, D, of radius $R + |z_0|$ and centered at the origin, the potential is given by

$$\phi(z) = \sum_{l=0}^{\infty} \frac{b_l}{z^{l+1}}, \qquad b_l = \sum_{k=0}^{l} a_k z_0^{l-k} \binom{l}{k} \tag{5.23}$$

with $\binom{l}{k}$ the binomial coefficients. Furthermore, for any $p \geq 1$,

$$\left| \phi(z) - \sum_{l=0}^{p} \frac{b_l}{z^{l+1}} \right| \leq \frac{A}{\left(1 - \left| \frac{|z_0| + R}{z} \right| \right)} \left| \frac{|z_0| + R}{z} \right|^{p+2} \tag{5.24}$$

with A defined in (5.22).

Lemma 2.3: Consider m dislocations with $q_i, i = 1..m$, located inside a circle D_1 of radius R and center at z_0, with $|z_0| > (c+1)R, c > 1$. Then, the corresponding multipole expansion (5.21) converges inside a circle D_2 of radius R centered at the origin. Inside D_2, the potential due to the dislocations is described by a power series

$$\phi(z) = \sum_{l=0}^{\infty} b_l z^l, \qquad b_l = -\frac{1}{z^{l+1}} \sum_{k=0}^{\infty} \frac{a_k}{z_0^k} \binom{l+k}{k} (-1)^k \tag{5.25}$$

Furthermore, for any $p \geq \max(2, 2c/(c-1))$, an error bound for the truncated series is given by

$$\left| \phi(z) - \sum_{l=0}^{p} b_l z^l \right| < \frac{4Ae(p+c)(c+1)}{c(c-1)} \left(\frac{1}{c}\right)^{p+1} \tag{5.26}$$

Lemma 2.4: For any complex z_0, z and $a_k, k = 1, .., n$,

$$\sum_{k=0}^{n} a_k (z - z_0)^k = \sum_{l=0}^{n} \left(\sum_{k=l}^{n} a_k \binom{k}{l} (-z_0)^{k-l} \right) z^l \tag{5.27}$$

Note that results 2.1–2.3 are the counterparts of similar results from [112] corresponding to the complex potential (5.20), while result 2.4 is unchanged from the above paper.

The implementation details of FMM are identical to that in [112], which contains a rigorous step-by-step description of the algorithm. What follows is an informal description of the main steps involved. The first step is the adaptive subdivision of the computational cell (assumed to be a square region without loss of generality) into a tree structure of square subcells such that no leaf cell contains more than a predefined number of dislocations (see Fig. 50). Next, the coefficients of the multipole

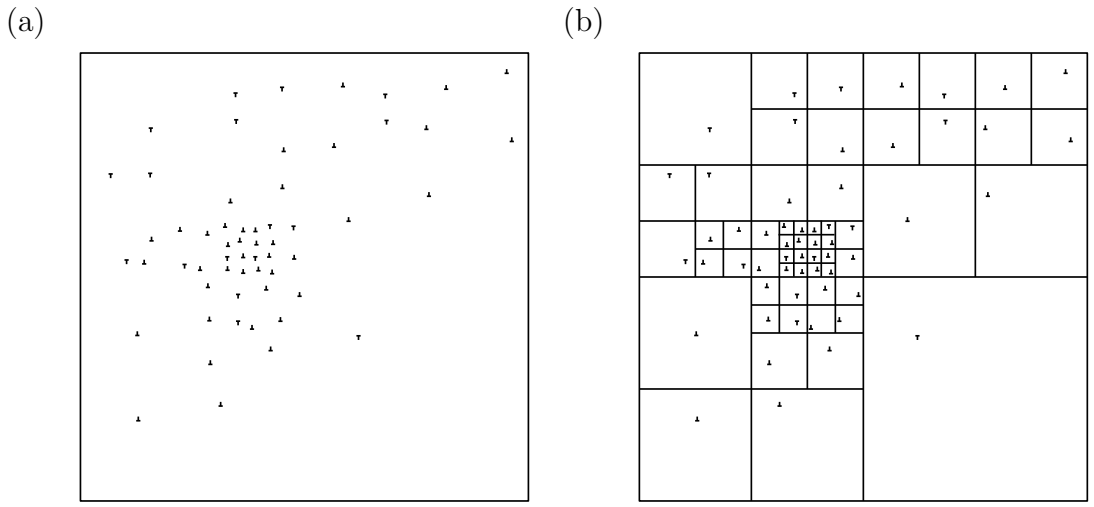

Fig. 50. (a) Square cell encompassing the domain of interest in a multibody simulation and (b) adaptive subdivision of the domain into a hierarchy of square subcells.

expansion for the stress field about the center of each cell are calculated. For leaf cells, this involves a direct application of Theorem 2.1, while for parent cells, the multipole expansion is established by combining together the multipole expansions of its four children by using Lemma 2.2. Finally, the Peach-Koehler forces on the dislocations in each leaf cell is calculated using the following steps: (i) the interactions between dislocations in the same leaf cell and every adjacent leaf cell are computed directly, (ii) the interactions with the dislocations in well separated cells are computed indirectly via the multipole expansions of the latter cells by shifting the centers of the expansion to that of the current leaf cell using lemmas 2.3 and 2.4. An implementation of the above algorithm using the dynamic memory allocation features of Fortran 90 due to [114] is adapted for use with the 2.5D DD code.

The FMM implementation in DD is validated by comparison of the Peach-Koehler forces computed using FMM vs. direct evaluation of the pairwise interactions. Fig. 51 shows a comparison of the compressive stress strain response and the evolution of the dislocation density for a $9.6 \times 3.2\,\mu\text{m}^2$ rectangular plane strain

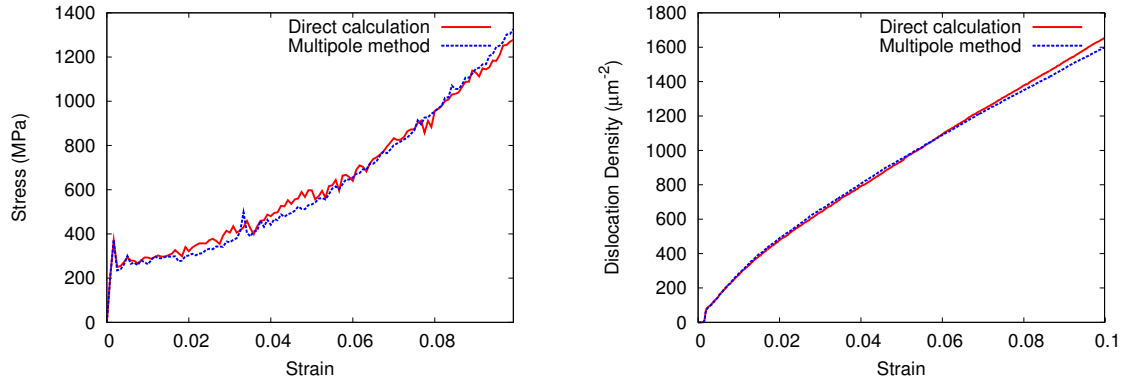

(a) (b)

Fig. 51. Comparison of DD results in plane strain compression for a $9.6 \times 3.2\,\mu\text{m}^2$ specimen using direct evaluation of the Peach-Koehler force vs. the FMM method. (a) Compressive stress vs. strain and (b) evolution of the dislocation density vs. strain.

specimen oriented for double slip. The solid curve corresponds to the direct method of evaluation of the Peach-Koehler force and the dashed curve corresponds to evaluation using FMM. Notice that while the two curves are identical initially, small differences manifest at larger strains due to the numerical fluctuations in the simulation. However, on average the two codes yield identical response irrespective of the specimen dimensions. Fig. 52(a) shows the comparison of the computation time for the Peach-Koehler forces as a function of the number of dislocations N. The figure shows the elapsed wall clock time from the beginning to the end of the Peach-Koehler force computations rather than the CPU time and is therefore subject to fluctuations due to variations in system load as is seen in Fig. 52(a). Use of FMM results in a dramatic reduction in the computation time, especially for large values of N. Further examination reveals that the scaling of the computation time with N is nearly linear up to very large values of N for the calculations using FMM. However, deviations from linearity are observed at very high N presumably due to the latency introduced

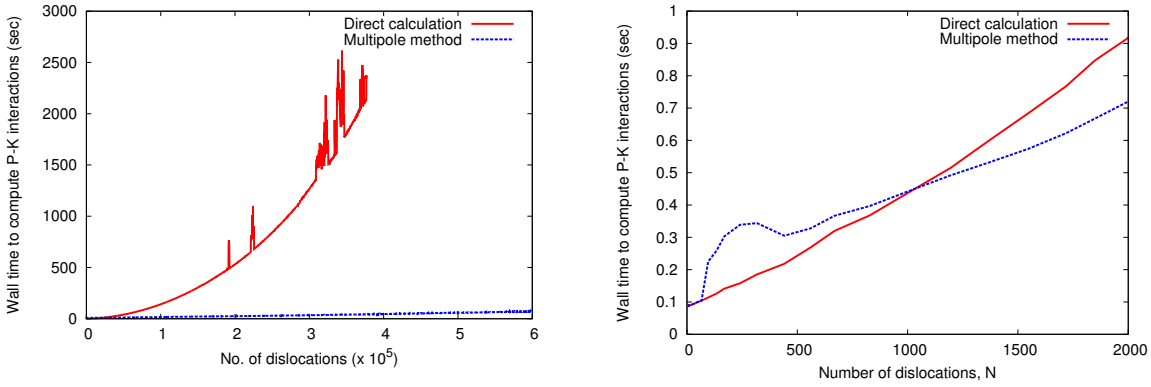

(a) (b)

Fig. 52. (a) Wall clock time for computation of the Peach-Koehler interactions as a function of the number of dislocations N and (b) zoom of the initial portion of the curve for $N < 2000$.

by the need to dynamically allocate large amounts of memory in the Fortran 90 implementation. Fig. 52(b) shows a zoom of the initial portion of the same curves for small values of N, which shows that the fixed computational cost associated with the use of the FMM algorithm dominates for small N leading to higher computation times. As will be shown in Chapter VI, use of FMM enables large simulations involving millions of dislocations that were not tractable before.

3. Non-convex and Multiply Connected Domains

The second major enhancement to the numerical framework involves the handling of slip discontinuities in the case of complex domain geometries such as non-convex or multiply connected domains. The need for this enhancement can be appreciated by examining the simple scenario illustrated in Fig. 53. Fig. 53(a) shows a convex domain containing a single Frank-Read source on a slip plane and subjected to simple shear deformation. Fig. 53(b) illustrates the same domain containing a void at the center and subjected to simple shear. Consider the case where both the sources have

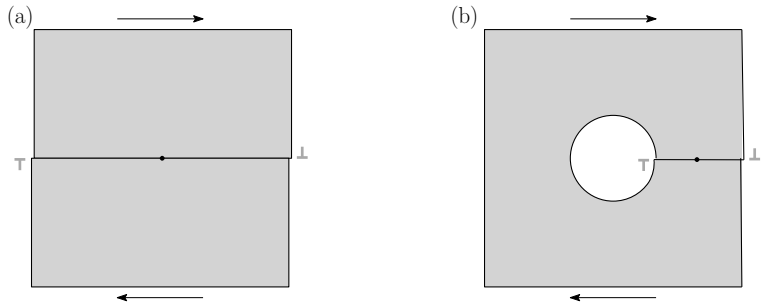

Fig. 53. Slip discontinuities in (a) simply connected and (b) multiply connected domains.

nucleated a dislocation dipole that have left the domain through glide as shown in the figure. In the case of Fig. 53(a) this leaves a stress free displacement discontinuity across the slip plane while the discontinuity can lead to residual stresses and strains in Fig. 53(b), which needs to be determined from the finite element solution. Proper handling of complex 2D domains is important in treating several important boundary value problems for porous or cracked specimens.

A computationally efficient approach for handling slip discontinuities in the context of DD has been proposed by Romero et al. [109], using the strong discontinuity method originally proposed by Simo et al. [115] for strain localization in plasticity. The superposition method of Van der Giessen and Needleman (Fig. 47) has been enhanced by including an additional discontinuous field (denoted by the $\check{}$ superscript) that accounts for the slip discontinuities dues to dislocations that exit the domain, as illustrated in Fig. 54.

$$\mathbf{u} = \tilde{\mathbf{u}} + \check{\mathbf{u}} + \hat{\mathbf{u}}, \qquad \boldsymbol{\epsilon} = \tilde{\boldsymbol{\epsilon}} + \check{\boldsymbol{\epsilon}} + \hat{\boldsymbol{\epsilon}}, \qquad \boldsymbol{\sigma} = \tilde{\boldsymbol{\sigma}} + \check{\boldsymbol{\sigma}} + \hat{\boldsymbol{\sigma}} \tag{5.28}$$

In the updated framework, the ($\tilde{}$) fields correspond to the infinite medium elastic fields of the dislocations that remain within the domain, the ($\check{}$) fields correspond to the residual stresses and displacements due to the slip discontinuities caused by

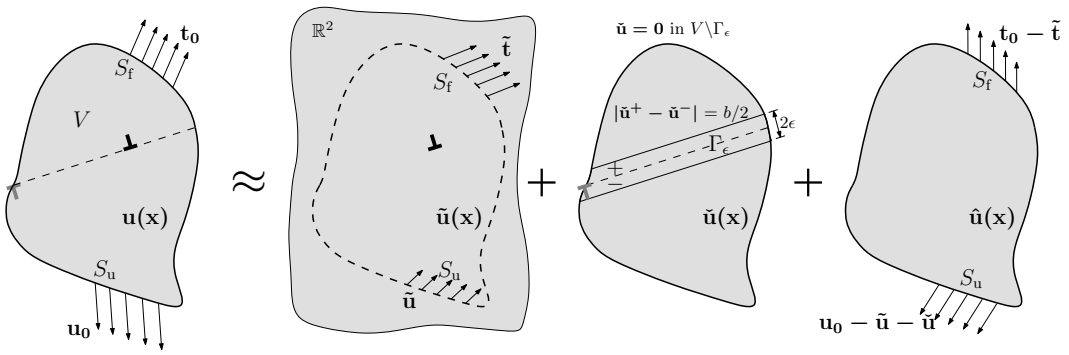

Fig. 54. The superposition method of [109] for solving linear elastic boundary value problems in arbitrary 2D domains containing discrete dislocations.

dislocation exit and the ($\hat{}$) fields are smooth non-singular fields that enforce the boundary conditions of the problem. The difference from the framework of [25] is that the ($\tilde{}$) fields no longer include the contribution from the slip discontinuities, since the latter are not known *a priori* in multiply connected domains. Instead, the discontinuities and associated residual stressed are abstracted into the ($\check{}$) fields and a combined finite element solution is obtained for the sum of the ($\check{}$) and the ($\hat{}$) fields using the following approach.

First, a trial solution for the discontinuous $\check{u}$ field is assumed such that it satisfies the following conditions. (i) The $\check{u}$ field is continuous everywhere except on the slip plane across which a discrete slip discontinuity exists and vanishes everywhere except in the ϵ neighborhood of these slip planes. The ϵ neighborhood is defined as the set of all points that lie at a distance not exceeding ϵ from the slip plane, where ϵ may be made arbitrarily small. (ii) The $\check{u}$ field has a discontinuity across the slip planes equal to $b/2$ times the signed number of dislocations that have exited from the slip plane. (iii) The gradient of the $\check{u}$ field is continuous everywhere. Let $\bar{u}, \bar{\epsilon}$ and $\bar{\sigma}$ be the elastic fields complementary to the assumed ($\check{}$) fields such their superposition yields the true linear elasticity solution for the combination of the ($\check{}$) and ($\hat{}$) fields for problems 2

and 3 from Fig. 54. The governing equations and the boundary conditions for the unknown ($\bar{}$) fields may then be written as

$$\mathrm{div}(\check{\boldsymbol{\sigma}} + \bar{\boldsymbol{\sigma}}) = 0 \qquad \text{in } V \tag{5.29}$$

$$\bar{\boldsymbol{\sigma}} = \mathbb{C}\bar{\boldsymbol{\epsilon}} \qquad \text{in } V \tag{5.30}$$

$$\bar{\boldsymbol{\epsilon}} = \frac{1}{2}(\nabla\bar{\mathbf{u}} + \nabla^t\bar{\mathbf{u}}) \qquad \text{in } V \tag{5.31}$$

$$(\check{\boldsymbol{\sigma}} + \bar{\boldsymbol{\sigma}})\mathbf{n} = \mathbf{t}_0 - \tilde{\boldsymbol{\sigma}}\mathbf{n} \qquad \text{on } S_t \tag{5.32}$$

$$\bar{\mathbf{u}} = \mathbf{u}_0 - \tilde{\mathbf{u}} - \check{\mathbf{u}} \qquad \text{on } S_u \tag{5.33}$$

An advantage of the above approach is that the solution for the unknown field $\bar{u}$ is smooth and need not account for the residual slip discontinuities. In the finite element implementation of this approach, the trial displacement field $\check{u}$ is constructed using the shape functions of those elements that are cut by the slip discontinuities such that it satisfies the three conditions established previously for the trial field. Additional details of the construction of the $\check{u}$ field and the actual algorithm for implementation in finite elements are provided in [109]. An important point to note is that the above approach has negligible computational overhead in DD simulations due to that fact that the stiffness matrix does not need to be modified at every increment and need to be computed and factorized only once.

The strong discontinuity approach has been implemented in finite elements using a procedure identical to that in [109]. On a related note, the finite element implementation in the existing 2.5D code was generalized such that arbitrary 2D meshes can be loaded from an external mesher and general four noded quadrilateral elements with four integration points can be used as opposed to the rectangular elements used previously. The updated code has been validated in several ways using elastic solutions for 2D problems (in the absence of dislocations) for which analytical solutions are

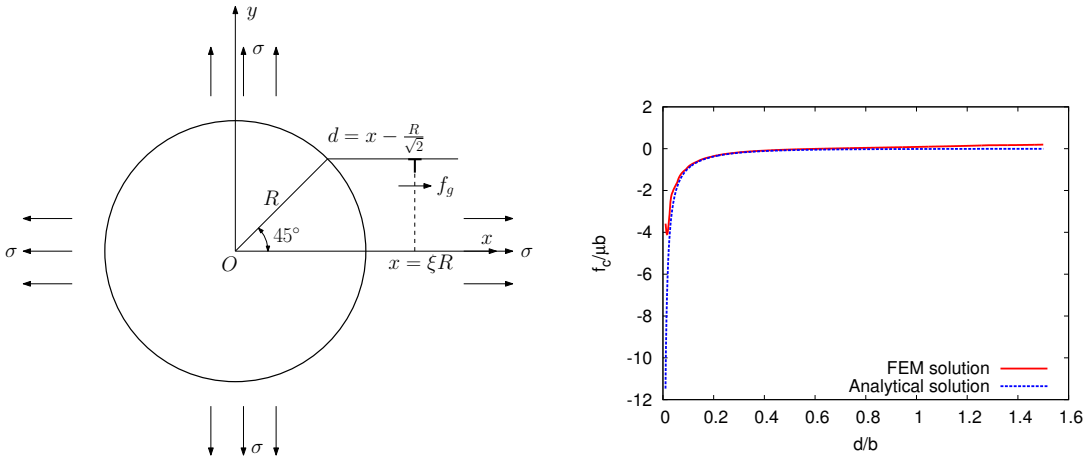

(a) (b)

Fig. 55. (a) Edge dislocation in the neighborhood of an isolated void in an infinite domain under equibiaxial tension σ and (b) comparison of the analytical and approximate finite element solutions for the Peach-Koehler glide force on the dislocation as a function of the dislocation position.

available. However, analytical solutions for finite domains containing dislocations are generally not available. An approximate comparison has been made for the case of an isolated dislocation in the neighborhood of a void in an infinite domain undergoing equibiaxial tension, for which an analytical solution is available from [116]. Fig. 55(a) illustrates the geometry and the loading conditions of the problem. An approximate finite element solution to the same problem is obtained by considering a square specimen of side $10R$ containing a concentric void of radius R. The Peach-Koehler glide force on a dislocation at $(x = \xi R, y = R/\sqrt{2})$ is given by

$$f_g = \sqrt{2}\sigma b \frac{\xi}{(\xi^2 + 1/2)^2} - \frac{\mu b}{\pi(1-\nu)} \frac{b}{R} \frac{\xi(\xi^4 + 1/4)}{(\xi^2 + 1/2)^2(\xi^4 - 1/4)} \tag{5.34}$$

where σ denotes the biaxial stress. Fig. 55(b) shows a comparison of the analytical and finite element solutions for f_g as a function of the dislocation position. The results show reasonably good agreement between the two solutions. The solutions begin to

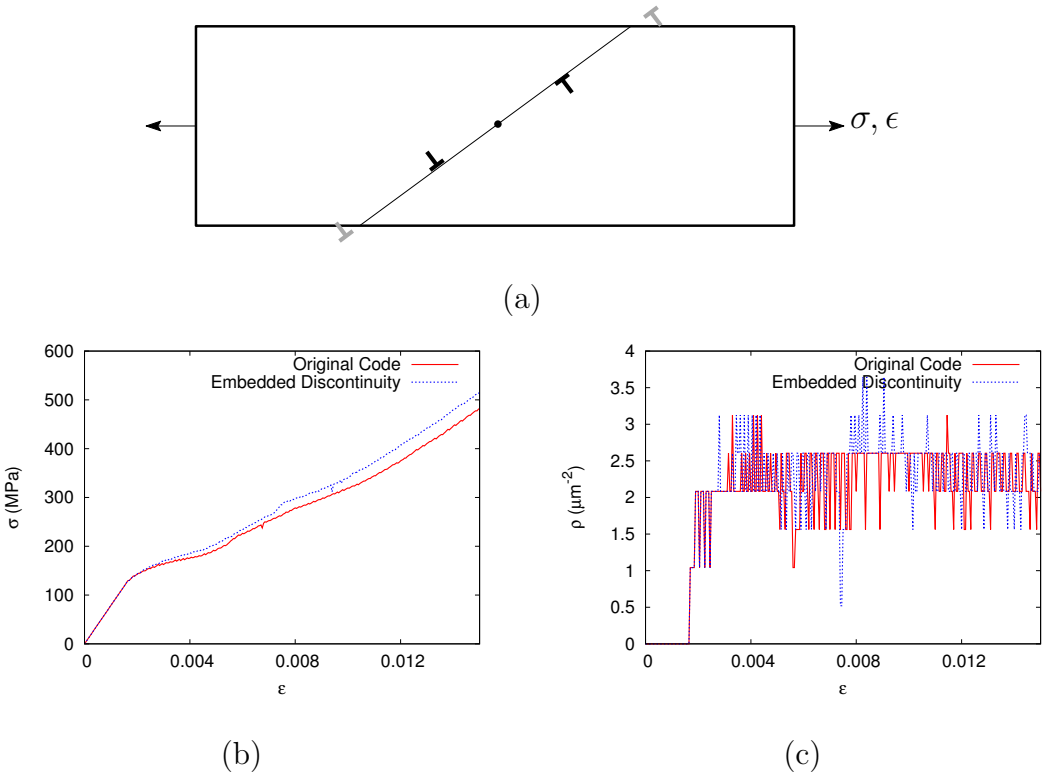

Fig. 56. (a) Plane strain tension specimen ($2.4 \times 0.8\mu m^2$) containing a single Frank-Read source. Comparison of (b) stress–strain response and (c) evolution of the dislocation density from the two codes.

diverge slightly far away from the void due to the fact that, unlike in the analytical model, a finite geometry is used in the finite element solution. As a test case for the embedded discontinuity approach, we compare the solutions from the original convex domain version of the DD code with the new code for a plane strain tension specimen containing an isolated Frank-Read source in the center (see Fig. 56(a)). Figs. 56(b) and (c) show the prediction for the evolution of the flow stress and the dislocation density respectively from the two versions of the code, which show very good agreement. In general, it has been observed that the two codes yield equivalent results on average for convex domain simulations.

4. Periodic Boundary Conditions

In spite of the huge improvements in efficiency brought by the implementation of the Fast Multipole method discussed in section 2, there are challenges in scaling the DD computations to billions of dislocations that are present in a typical bulk sample. On the other hand, it is of interest to study the asymptotic behavior of DD in the bulk limit where one can match predictions against readily available experimental data. One method of simulating bulk conditions in DD would be to subject a computational cell to periodic boundary conditions (PBC). However, one difficulty in using PBC with the DD boundary value problem framework described above is that analytical expressions for the ($\tilde{}$) fields are not available for general periodic arrays of edge dislocations in two dimensions. Therefore, we employ the same non-periodic fields for the ($\tilde{}$) and ($\breve{}$) fields as in the non-periodic case and enforce periodicity in the total fields through the solution for the ($\hat{}$) fields. This approach to obtain a periodic solution by superposition of three individual non-periodic fields has previously been employed by [103]. Note that, due to the non-periodicity of the unknown ($\hat{}$) fields, the stiffness matrix for the finite element problem will be non-symmetric.

We implement PBC by imposing multi-point constraints on the nodal degrees of freedom at the periodic boundaries as illustrated in Fig. 57. The constraint equations for the ($\hat{}$) fields may be written as

$$\hat{\mathbf{u}}^1 - \hat{\mathbf{u}}^2 = \boldsymbol{\epsilon}^\infty \cdot (\mathbf{x}^1 - \mathbf{x}^2) - \tilde{\mathbf{u}}^1 + \tilde{\mathbf{u}}^2 - \breve{\mathbf{u}}^1 + \breve{\mathbf{u}}^2 \tag{5.35}$$

$$\hat{\mathbf{t}}^1 - \hat{\mathbf{t}}^2 = -\tilde{\mathbf{t}}^1 + \tilde{\mathbf{t}}^2 - \breve{\mathbf{t}}^1 + \breve{\mathbf{t}}^2 \tag{5.36}$$

where the symbol $\mathbf{t}$ denotes the traction vector and the superscripts 1 and 2 correspond to the field values at periodic image nodes 1 and 2 as shown in Fig. 57 with position vectors $\mathbf{x}^1$ and $\mathbf{x}^2$ respectively. The above constraint equations are incorpo-

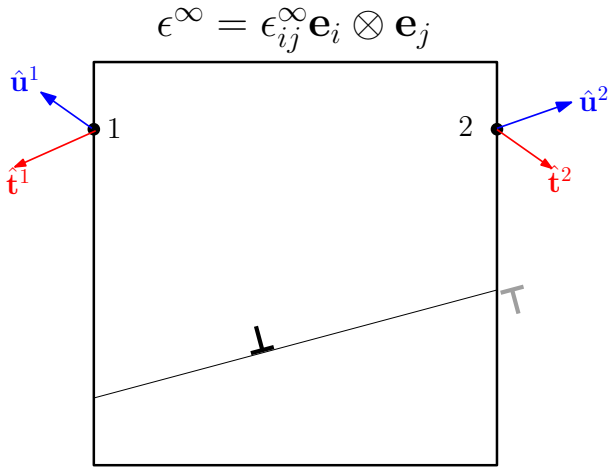

Fig. 57. Periodic boundary conditions enforced using multi-point constraint equations on the nodal tractions and displacements on the boundary.

rated directly into the global stiffness matrix. As a result of the above approach, the stiffness matrix loses its banded character and is stored as a general sparse matrix. An open source sparse matrix solver, LUSOL, is used to factorize and solve the finite element system of equations.

Periodicity is also ensured in the motion of dislocations in the DD simulations. When a dislocation exits the domain of analysis via an element edge on the periodic boundary, another dislocation is introduced into the domain through the periodic image of the element edge on the opposite boundary on the nearest entry point of a slip plane. However, the contribution of the dislocation to the slip discontinuity on its original slip plane is retained so as to ensure that one does not introduce spurious stresses at the periodic boundaries due to slip mismatch. Fig. 58 shows an example of the periodic stress field for a unit cell undergoing shear deformation and containing a single immobile dislocation dipole. Comparison of the results from a single cell analysis and a larger cell composed of four such unit cell clearly illustrates the periodicity in the computed finite element solution.

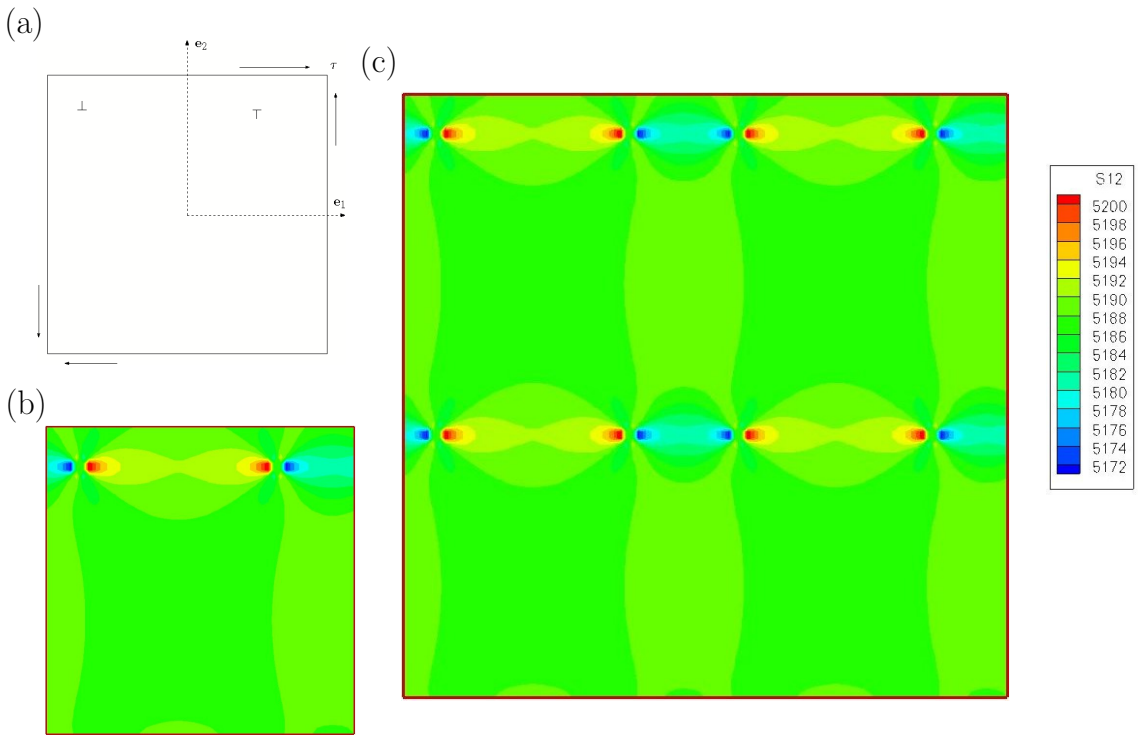

Fig. 58. (a) Unit cell containing a single dislocation dipole subjected to pure shear deformation (b) contours of τ computed using one periodic cell and (c) contours of τ computed using a larger periodic cell containing four smaller cells.

5. Dislocation Climb at Elevated Temperatures

As discussed in section D, simulation results obtained using the present DD framework are strictly applicable at low homologous temperatures when thermal effects such as creep and dynamic recovery are negligible. Nevertheless, there are several important engineering applications such as small scale electronic structures where one needs to account for the high temperature creep behavior of metallic components for their reliable operation. Since the applicability of continuum models at small scales is questionable, it is of interest to extend bottom up modeling techniques such as DD for modeling high temperature material behavior by accounting for relevant phenomena such as dislocation climb and vacancy diffusion. While most DD studies in the past have neglected dislocation climb or accounted for it using simplistic models, there have been several attempts in recent years to incorporate physics based models for dislocation climb within a DD simulation framework [117, 118]. In the present work, we generalize the 2D DD simulation framework of Van der Giessen and Needleman [25] to high temperatures by (i) developing a coupled framework for dislocation glide and climb by simultaneous solution of the linear elastic boundary value problem of section B with a boundary value problem for vacancy diffusion in a 2D domain and (ii) extending some of the key constitutive rules for dislocation glide in section B to be applicable at elevated temperatures. The resulting high temperature DD framework is applied to the solution of an example boundary value problem of the creep of micron sized single crystalline specimens under plane strain conditions. A detailed presentation of the development and application of the high temperature DD framework is deferred to Chapter VIII for space reasons.

CHAPTER VI

INVESTIGATION OF STRAIN HARDENING USING DISLOCATION DYNAMICS

A. Introduction

Demonstration of the existence of several interesting size effects on the strength of crystalline materials at small scales has been an area of significant scientific and technological interest in the past two decades. There is high interest in these phenomena from a technological perspective due to the recent advancements in manufacturing metallic components at micron scales and below for MEMS/NEMS applications. On the other hand, the question is of scientific interest due to the fact that properties such as material strength and hardening rates that were long considered to be intrinsic material properties turn out to be scale dependent. Early experiments by [21–23, 119] had demonstrated size effects on material strength under non-homogeneous loading conditions such as torsion of thin metallic wires, bending of thin foils and nanoindentation. It has been proposed that these size effects are related to the density of geometrically necessary dislocations (GND) that are required to accommodate the macroscopic strain gradient. Accordingly, several theories have been devised to account for these size effects within a framework of continuum plasticity by enhancing the constitutive laws to include gradients of the strains and stresses [23, 120, 121]. Simultaneously, this introduces a dependence on an intrinsic length scale and a connection to the microscopic mechanisms since the GND density is directly related to the plastic strain gradients. However, more recent experimental developments have challenged the basis of strain gradient plasticity theories by demonstrating that strong size effects can also manifest in sub-micron specimens in the absence of strain gradi-

ents under macroscopically homogeneous deformation. These recent experiments on micron and sub-micron diameter single crystalline pillars manufactured using focused ion beam machining and subjected to compression using flat tip nanoindenters has now been repeated by several groups [5–7, 122] who have confirmed the size dependence of flow strength. Some experiments using larger pillars ($\sim 1\mu$m) have also evidenced a dependence of the hardening rate on specimen size [123] although this effect has not received much attention in the literature.

Gradient based continuum models fail to explain these size effects for which alternative theories are needed. DD has emerged as a viable computational tool for modeling size dependent behavior at small scales due to several reasons: (i) inherently discrete nature of the method due to its dependence on a relevant physical length scale, the Burgers vector and (ii) availability of powerful computer hardware in recent years that makes possible large scale simulations. Several researchers have employed 3D [124–126] and 2D DD models [127, 128] to investigate the size dependence of flow strength. Based on these simulations, mechanisms such as dislocation starvation [126] and size dependence of the average nucleation strength of Frank-Read sources [127] have been invoked to explain the observed strengthening. However, systematic investigation of the size dependence of hardening rate on specimen size in larger pillars presents a challenge due to the large densities of dislocations needed for the Forest hardening mechanisms to operate. The usefulness of 3D DD is limited to relatively simple situations involving few dislocations due to the high computational cost of handling the complex interactions of dislocation loops among themselves and with the specimen boundaries. The advantage that 2D DD models have over 3D is that a 2D approximation allows for a significant reduction in the degrees of freedom, at the cost of some accuracy in the representation of the physics, allowing the computations to scale to large dislocation densities. In addition, use of the extended 2.5D constitutive

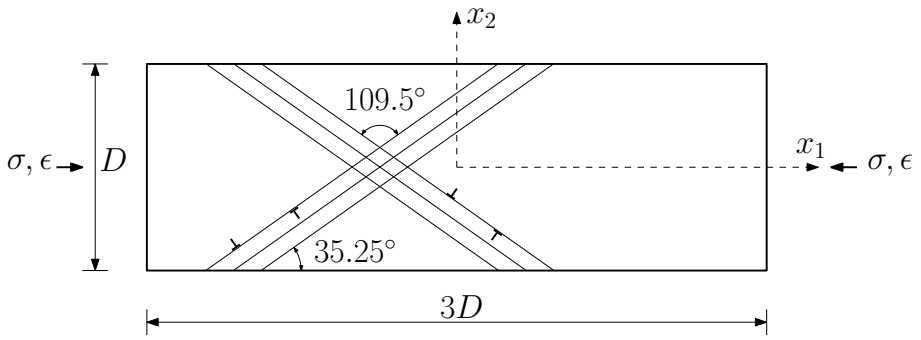

Fig. 59. Schematic of a plane strain compression specimen oriented for symmetric double slip.

rules presented in Chapter V allow for an adequate representation of strain hardening in multi-slip specimens [26]. Accordingly, 2.5D DD has recently been used to investigate the size effects on single crystal hardening rates, where the model predictions have been shown to be in good agreement with experiments [107,129]. However, some of the limitations of the 2D DD framework addressed in Chapter V had so far limited the scope of such investigations. As such, in the present chapter the enhanced DD framework is used to study the effect of specimen dimensions on strain hardening rates under idealized conditions. In particular, attention is focused on convergence of 2.5D DD predictions for the hardening rate under homogeneous deformation to bulk values in the limit of very large samples. Conditions approximating the latter limit is simulated in DD using computational cells subjected to periodic boundary conditions and subjected to shear loading.

B. Hardening in Single Crystal Compression

Consider a rectangular single crystalline specimen subjected to plane strain compression as illustrated in Fig. 59. The matrix is assumed to be a face centered cubic (FCC) single crystal oriented for quasi-plane strain deformation [130] where the $\mathbf{e}_1 - \mathbf{e}_2$ plane

coincides with the (110) crystallographic plane. The $\mathbf{e}_1$ axis is assumed to coincide with the $\langle 001 \rangle$ direction and the $\mathbf{e}_2$ axis coincides with the $\langle 1\bar{1}0 \rangle$ direction. The figure also shows the traces of the $\{111\}$ slip planes on the plane of the paper. We consider two intersecting slip systems corresponding to the $\langle \bar{1}12 \rangle$ and $\langle 1\bar{1}2 \rangle$ slip directions (in plane projections of the $\langle \bar{1}01 \rangle$ and $\langle 0\bar{1}1 \rangle$ slip systems respectively) with an included angle of approximately 109.5°. The crystal orientation considered corresponds to a symmetric double slip arrangement where the two slip system make an angle of 35.25° with respect to the $\mathbf{e}_1$ axis as shown in the figure.

The specimen is initially stress and dislocation free and contain a random distribution of point sources and obstacles distributed on slip planes spaced $20b$ apart. Although the source and obstacle densities vary as a function of the deformation due to the dynamic creation/destruction of junctions, initial densities of static sources and obstacles is taken to be 150 and 600 μm^{-2} respectively. These rather high values of the initial defect densities are chosen such that the simulation results are representative of larger micropillars where the strength is flow controlled rather than nucleation controlled. The surfaces at $x_2 = \pm D/2$ are traction free and the shear stress vanishes at $x_1 = \pm 3D/2$. A uniform displacement $u_1 = \pm U/2$ is prescribed along $x_1 = \pm 3D/2$. Rotation of the tensile axis is not restricted. The average compressive stress, σ, and strain, ϵ, are calculated as

$$\sigma = -\frac{1}{D}\int_{-D/2}^{D/2} \sigma_{11}(\pm 3D/2, x_2)\, \mathrm{d}x_2, \qquad \epsilon = -\frac{U}{3D} \tag{6.1}$$

Young's modulus $E = 70$ GPa and Poisson's ratio $\nu = 0.33$ corresponding to values for Aluminum are used for the matrix. The modulus of the Burger's vector $b = 0.25$ nm is assumed on all slip systems. The drag factor is taken to be $B = 10^{-4}$ Pa s and a constant value of $\tau_{\text{obs}} = 150$ MPa is used for the obstacle strength. A normal distribution of initial source strengths τ_{src} is assumed with an average value of 50

MPa and a standard deviation of 10 MPa and a constant nucleation time of $t_{\text{nuc}} = 10$ ns is assigned for all sources as in previous 2D DD studies [25, 103, 131]. The values used for the 2.5D parameters that affect the properties of dislocation junctions are $\beta_{\text{nuc}} = 1$, $\beta_{\text{brk}} = 10\beta_{\text{nuc}}$, $\gamma_{\text{nuc}} = 1000B$, $d^* = 6b$ and $p = 0.01$. A constant strain rate of 10^{-4} s^{-1} is used in all the simulations. The compressive response of the specimens are studied as a function of the specimen size for values of D ranging from $0.4 - 25.6\mu$m.

Fig. 60(a) and (b) compare the stress–strain response and evolution of the dislocation density for self-similar single crystals of varying size D. Due to the particular initial conditions chosen for the problem, where the statistics of the initial Frank-Read source strengths are independent of the specimen size, the simulations do not show a size effect on the initial yield stress. However, a size dependency in the flow stress emerges as a result of the evolving dislocation configurations leading to smaller specimens showing a higher rate of strain hardening, consistent with the previous study of Guruprasad et al. [129]. Here, unlike in earlier investigations we have been able to scale the computations to much larger values for the specimen size and dislocation count thanks to the efficient handling of the Peach-Koehler interactions using the fast multipole method. In fact, the largest specimen simulated contained over two million dislocations at the end of the simulation. Note that the higher flow stresses in Fig. 60(a) are accompanied by higher dislocation densities shown in Fig. 60(b). In the plasticity of bulk crystals, the average flow stress per slip system, $\mathcal{T}$, is related to the dislocation density, ρ, on the slip system through the well-known Taylor hardening relation

$$\mathcal{T} = A\mu b\sqrt{\rho} \tag{6.2}$$

where A is a dimensionless constant in the range 0.3–0.5 [132]. The average slip system flow stress $\mathcal{T}$ is equal to the resolved shear stress calculated from the average

(a)

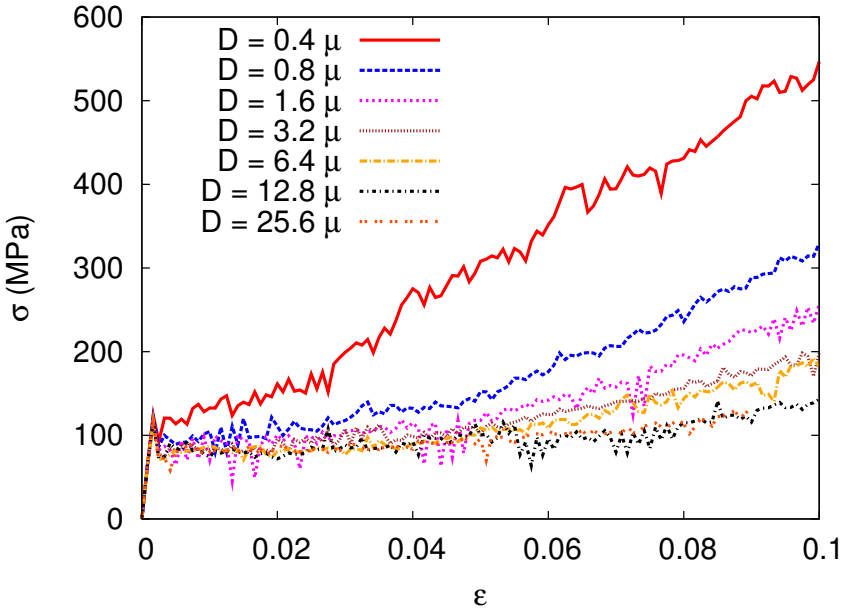

(b)

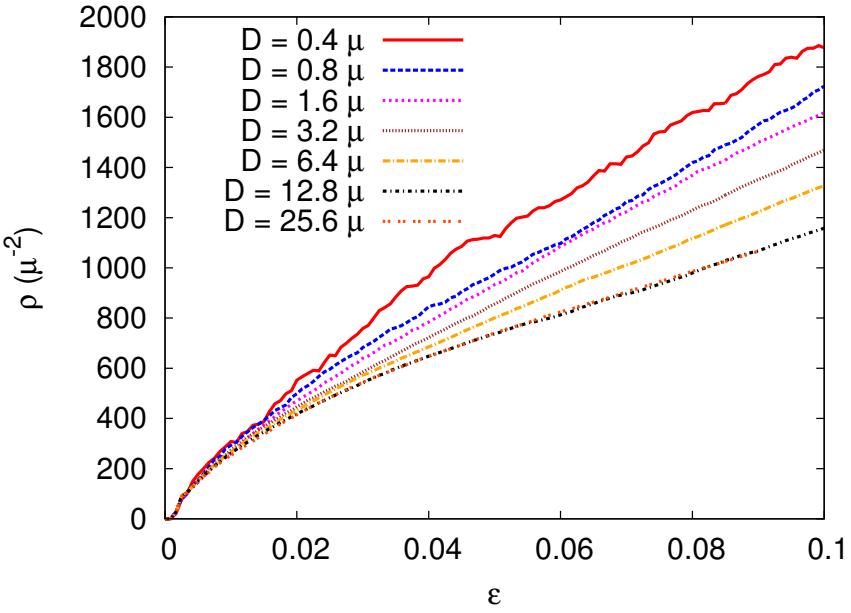

Fig. 60. Mechanical response of self-similar single crystalline specimens subjected to plane strain compression: (a) average stress σ vs. average strain ϵ and (b) dislocation density ρ vs. ϵ.

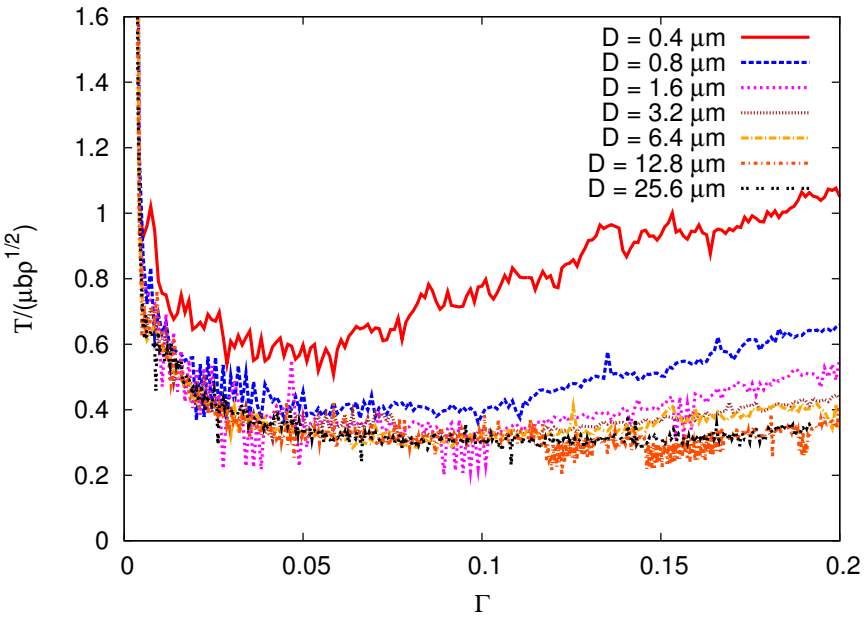

Fig. 61. Variation of the slip system flow stress $\mathcal{T}$, normalized by $\mu b\sqrt{\rho}$, as a function of the work conjugate shear strain Γ corresponding to the compression results of Fig. 60 for different specimen sizes.

global stresses using the appropriate Schmid factor, f_s. For the compression specimen of Fig. 59, we have $\mathcal{T} = f_s\sigma$. Due to the symmetric double slip arrangement considered, both slip systems have an identical Schmid factor $f_s = 0.47$. Fig. 61 plots the variation of the flow stress $\mathcal{T}$, normalized by $\mu b\sqrt{\rho}$, as a function of a shear strain, $\Gamma \equiv \epsilon/f_s$, work conjugate to $\mathcal{T}$. Notice that while the ratio $\mathcal{T}/(\mu b\sqrt{\rho})$ tends to a more or less constant value during the steady state hardening regime for the largest specimens considered, as expected based on the Taylor relation, progressively larger deviations are observed towards smaller specimen sizes. As noted in [129], this result indicates a breakdown of Taylor law at the micron scale. Fig. 62 compares the dislocation structures at the end of the simulation ($\epsilon = 0.1$) for compression specimens of two different sizes $D = 0.04$ μm and $D = 3.2$ μm. Notice that the distribution of the positive and negative dislocations exhibit greater inhomogeneity for the smaller sam-

(a)

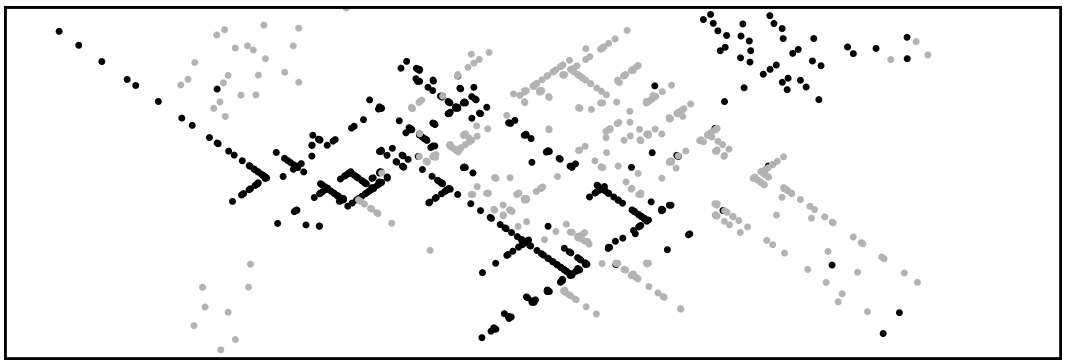

(b)

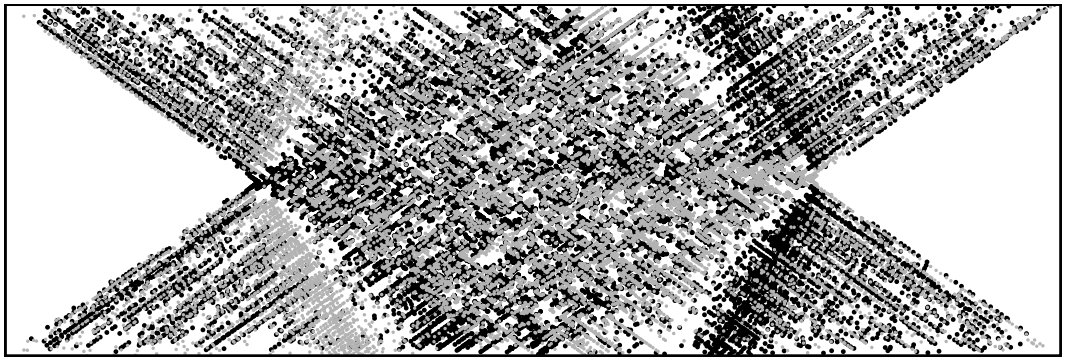

Fig. 62. Dislocation structures at $\epsilon = 0.1$ for compression specimens of sizes (a) $D = 0.4$ μm and (b) $D = 3.2$ μm. Black dots represent positive dislocations while gray dots represent negative dislocations.

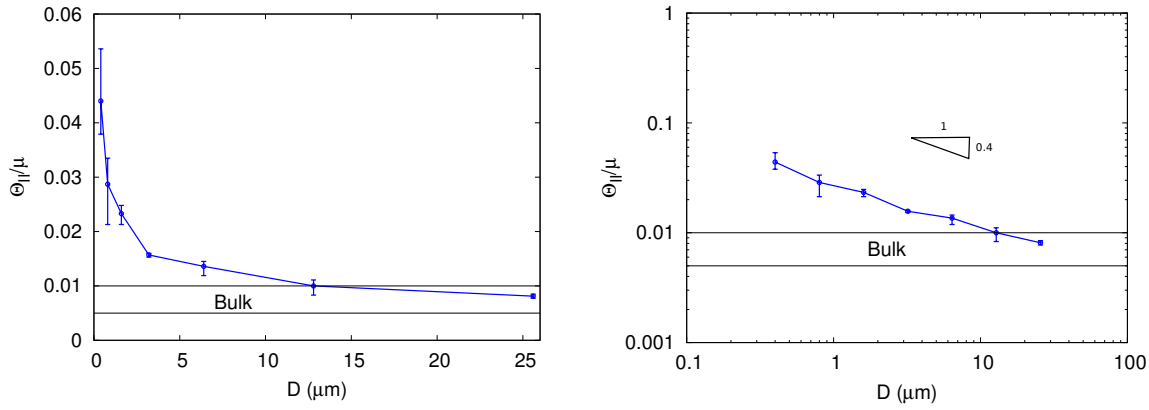

(a) (b)

Fig. 63. (a) Scaling of the average steady state hardening rate Θ_{II} as a function of specimen size D and (b) the same data on a log–log plot.

ple size compared to the large compression specimen. This indicates that although both specimens have an overall zero net Burgers vector, local fluctuations in the dislocation distribution can lead to the emergence of GNDs at intermediate scales. This fact was used by Guruprasad and Benzerga [129] to arrive at an effective measure of the local GND density which correlated well with the observed size effects. The reader is referred to [102] for additional details of a phenomenological theory of strain hardening using two internal state variables, the dislocation density and an effective GND density.

Fig. 63 shows the scaling of the steady state hardening rates, Θ_{II}, estimated from these simulations as a function of the specimen size. Average values of Θ_{II} estimated from multiple realizations of the initial source and obstacle populations are reported along with the associated scatter. Using the standard approach of crystal plasticity, the hardening rates are estimated based on the tangent to the flow stress $\mathcal{T}$ vs. shear strain Γ, work conjugate to $\mathcal{T}$, for the slip systems. I.e.

$$\Theta_{\text{II}} = \frac{\partial \mathcal{T}}{\partial \Gamma}, \qquad \mathcal{T} = f_s \sigma, \quad \Gamma = \epsilon / f_s \tag{6.3}$$

Θ_{II} is related to the tangent to the stress–strain curves of Fig. 60 as $\Theta_{\mathrm{II}} = f_s^2(\partial\sigma/\partial\epsilon)$. From Fig. 63(a), one can see that as we approach large specimen sizes the variation in the hardening rate with D tends to level off and approach a plateau. From experimental results for the plasticity of bulk single crystals, the steady state 'stage II' hardening rates have a universal range of values from $\mu/200 - \mu/100$, independent of the material, temperature and strain rate [133]. This range of values is marked by the horizontal band in Fig. 63. We can see that for the largest specimen considered the average Θ_{II} value from the simulations falls within the experimental range. Note that the hardening obtained in DD simulations are a result of a convolution of several factors such as the statistics of junction formation, junction breaking and dynamic source formation. In a simplified 2D framework, each of these mechanisms are modeled using approximate constitutive rules (2.5D rules) discussed in Chapter V, section C with associated parameters, some of whose range of values are estimated from experiments or lower scale molecular dynamics (MD) simulations (see [26]) while others are not. The convergence of the asymptotic hardening rates obtained from DD with the bulk values may be viewed as an indirect validation of the parameter ranges used in the 2.5D DD simulations. Examining the same data on a log–log scale in Fig. 63(b) shows an approximately linear behavior indicating that, similar to the well documented scaling of the flow stress in the literature, the hardening rates also scales with the specimen size according to a power law with an exponent of ~ 0.4.

C. Simulation of the Bulk Limit Using Periodic Boundary Conditions

In order to further investigate the asymptotic behavior of the hardening rate obtained from DD simulations in the bulk limit, we examine the response of a square cell from a bulk crystalline specimen whose response under pure shear loading is simulated

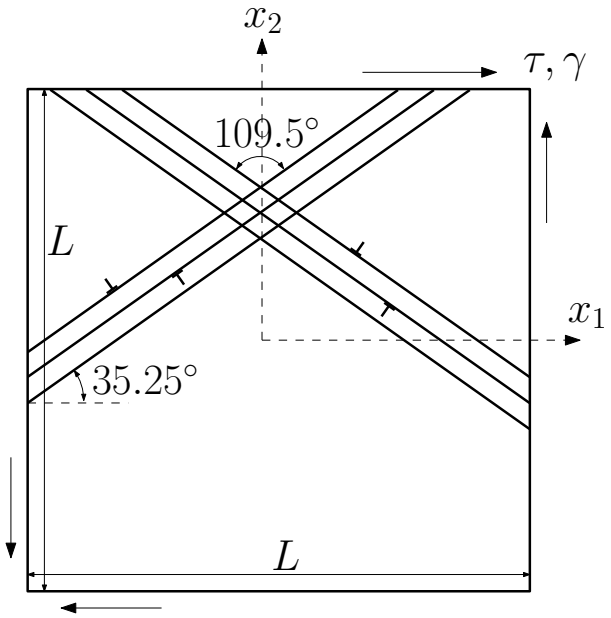

Fig. 64. Schematic of a square periodic unit cell from a bulk sample subjected to pure shear loading.

approximately using periodic boundary conditions (PBC). A symmetric orientation for the crystal is again chosen relative to the loading direction, corresponding to a Schmid factor $f_s = 0.33$ ($\mathcal{T} = f_s\tau$), as illustrated schematically in Fig. 64. Note that the cell size, L, in these simulations is an artificial length parameter that has no physical significance. Therefore, it is required that a sufficiently large value is chosen for the cell size L such that the simulation results are independent of L. Fig. 65(a) shows the average shear stress, τ, vs. the shear strain, γ, response for periodic cells with sizes in the range $L = 0.5$–8μm. Fig. 65(b) shows the corresponding evolution of the dislocation density with strain. It is clear from these results that choice of $L < 1\mu$m can lead to results that depend on the cell size and are hence not representative of a bulk sample. Such a result is expected due to the discrete nature of the system, which means that very small sample sizes lead to stochasticity in the results due to the system containing too few dislocations. For the purposes of this

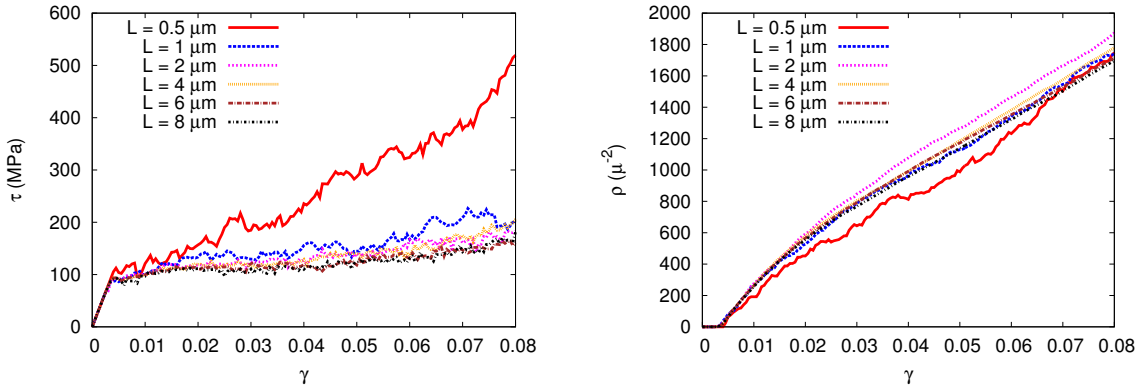

Fig. 65. (a) Average shear stress τ vs. shear strain γ and (b) dislocation density ρ vs. γ for periodic cells with different values of the cell size L subjected to pure shear deformation.

section, we use cell sizes $L = 2$–8 to simulate bulk behavior using PBCs.

Fig. 66 compares the resolved shear stress $\mathcal{T}$ vs. shear strain Γ response for the slip systems between the PBC simulations and the compressions simulation from Fig. 60 corresponding to the largest specimen size $D = 25.6\mu$m. Results obtained from three different sizes of the periodic cell $L = 2, 4$ and 8 are included in Fig. 66. Notice that the hardening rates obtained from the two sets of simulations for very different types of boundary conditions are quite similar. Fig. 67 shows the data from Fig. 63(b) overlaid with the hardening rates obtained from the PBC simulations for the different cell sizes. The hardening rate data obtained from the PBC simulations fall completely within the bulk range of hardening rates, $\mu/200 - \mu/100$, while the free boundary simulations converge towards this band for larger specimen sizes as expected.

In Fig. 68, we compare the strain hardening results from 2.5D DD with predictions based on the Taylor relation, equation (6.2). The PBC simulations show good agreement with the Taylor relation (6.2) with a value of $A \approx 0.3$. A close agreement

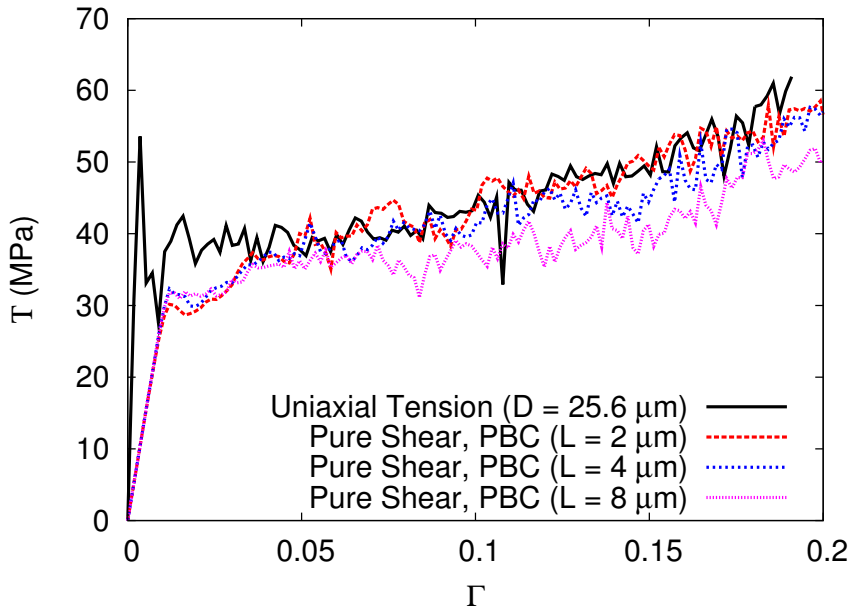

Fig. 66. Comparison of the resolved shear stress $\mathcal{T}$ vs. resolved shear strain Γ curves between the PBC simulations and free boundary simulations for the largest specimen size D.

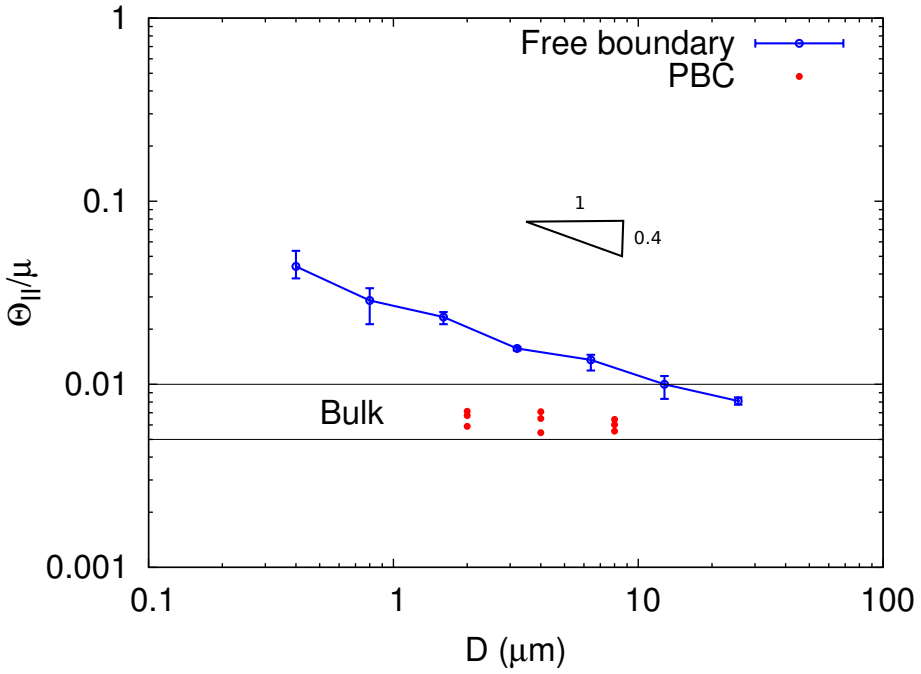

Fig. 67. Log–log plot from Fig. 63(b) overlaid with the hardening rates obtained from the PBC simulations for different cell sizes.

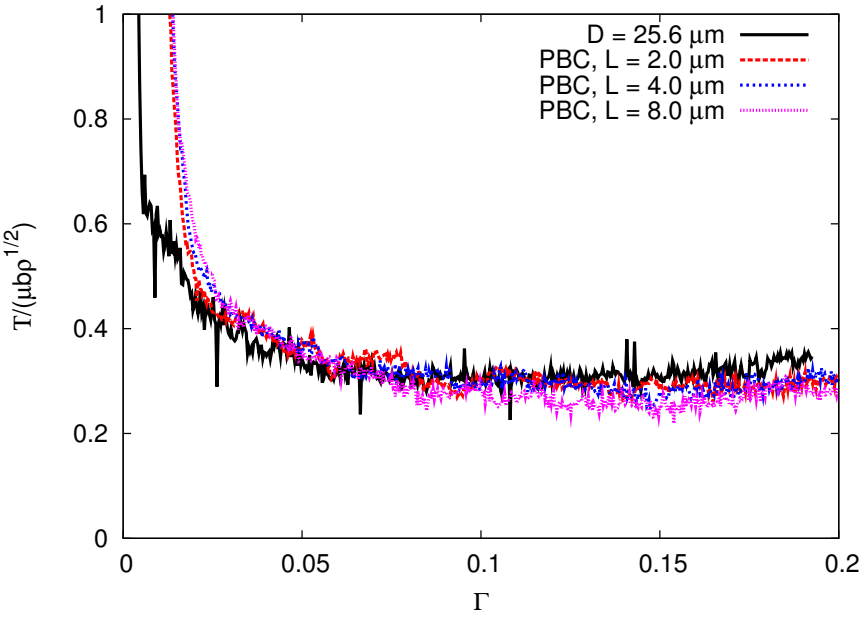

Fig. 68. Variation of the slip system flow stress $\mathcal{T}$, normalized by $\mu b\sqrt{\rho}$, as a function of the work conjugate shear strain Γ obtained from the PBC simulations. Corresponding curve for the largest compression specimen $D = 25.6\mu$m from Fig. 61 is included for reference.

may also be noted between the PBC results and the free boundary compression simulations for the largest specimen size. This provides additional evidence of the correct asymptotic behavior of the 2.5D DD simulation method in the bulk limit. Fig. 69 compares the dislocation structures at $\Gamma = 0.2$ obtained from the free boundary simulation for $D = 25.6$ μm and the PBC simulation for the three cell sizes considered. Due to the large number of dislocations in the sample, only a 2×2 μm^2 region from the center of the respective specimens are shown. Interestingly, while the compression sample shows a rather homogeneous distribution of the positive and negative dislocations consistent with the fact that a large specimen size is used, the PBC simulations reveal a greater degree of clustering of the positive and negative dislocations. This indicates that the artificial periodicity being enforced through the cell size L may have some effect on the dislocation distribution obtained. However, this effect does not appear to impact the effective hardening rate obtained, which is consistent with the Taylor relation irrespective of the cell size. Guruprasad and Benzerga [102] had proposed a phenomenological constitutive law of size dependent hardening using 2.5D DD compression simulations of the type presented in section B. Based on the premise that the size effects observed in the pillar compression experiments at the micron scales may result from the emergence of a dislocation substructure due to interaction with the specimen boundaries, they extended the widely used Kocks-Mecking-Estrin model of work hardening [134, 135] to include a term that depends on the average GND density at a suitably defined resolution. Their proposed expression for the hardening rate reads [102]

$$\Theta_{\text{II}} = \Theta^{\infty} + \delta\mu\frac{\rho_G}{\rho} \tag{6.4}$$

where Θ^{∞} is the size independent athermal hardening rate predicted by the Kocks-Mecking-Estrin model, ρ_G is the GND density and δ is a non-dimensional parameter.

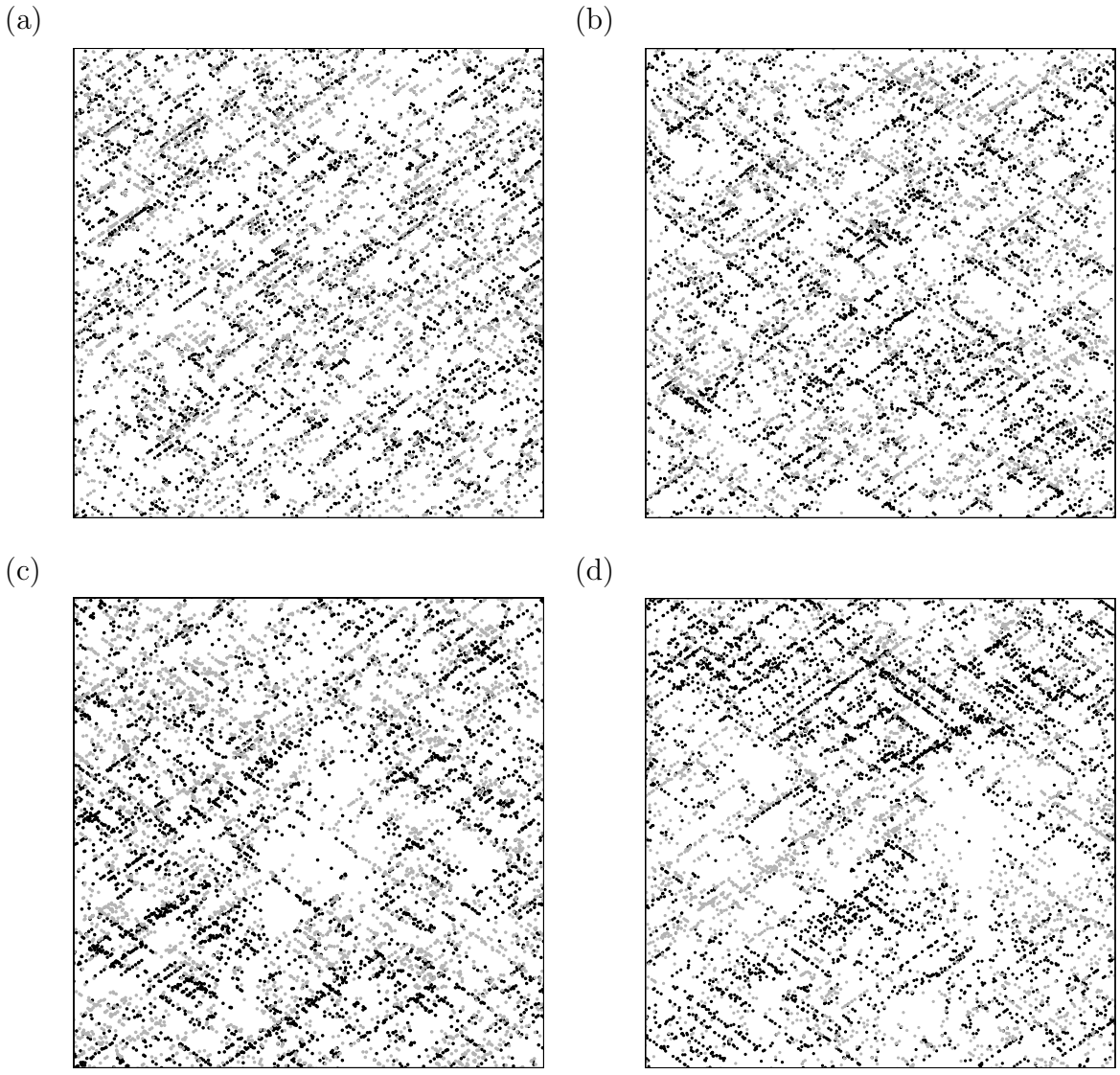

Fig. 69. Dislocation structures at $\Gamma = 0.2$ inside a 2 μm $\times$ 2 μm block of material extracted from the center of (a) $D = 25.6$ μm compression specimen and periodic cells subjected to simple shear (b) $L = 2$ μm, (c) $L = 4$ μm and (d) $L = 8$ μm. Black dots represent positive dislocations while gray dots represent negative dislocations.

The GND density is a resolution dependent quantity defined as [136]

$$\rho_G = \frac{||\mathbf{B}||}{b} \tag{6.5}$$

where $\mathbf{B}$ denotes the net Burgers vector in a domain of volume ω at the chosen resolution, b is the material Burgers vector magnitude and $||\cdot||$ denotes the Euclidean norm. Guruprasad and Benzerga [102] have demonstrated that in 2.5D DD simulations of pillar compression, the ratio of an *effective* measure of the GND density, $\bar{\rho}_G$, defined as the average of the resolution dependent GND density in equation (6.5) over the entire computational domain, to the total dislocation density ρ remained roughly constant during the steady state hardening regime. Moreover, the steady state value of $\bar{\rho}_G/\rho$ decreased monotonously with increasing specimen size, which was used to show that equation (6.4) using $\bar{\rho}_G$ in place of ρ_G yielded a good agreement with the hardening rates obtained from DD. Fig. 70(a) shows the evolution of the ratio $\bar{\rho}_G/\rho$ as a function of the resolved shear strain Γ corresponding to our compression simulations from section B. $\bar{\rho}_G$ is calculated as the averaging the value of ρ_G over horizontal strips of height 50 nm as in [102]. Notice that the ratio $\bar{\rho}_G/\rho$ is constant during the steady state hardening regime for all samples and decreases monotonously as a function of the specimen size consistent with the results of Gurupasad and Benzerga. For comparison, Fig. 70(b) shows the evolution of $\bar{\rho}_G/\rho$ for the PBC simulations from section C for the three unit cell sizes. While a constant value of $\bar{\rho}_G/\rho$ is obtained in all the PBC simulations, this value is seen to depend on the cell size L. Also, as the cell size increases, $\bar{\rho}_G/\rho$ tends to a constant value that is different from zero and is in fact higher than the value obtained from the free boundary simulations for the largest specimen sizes. However, we have seen that despite these differences, the hardening rates obtained from the PBC simulations are in close agreement with each other and with the largest free boundary specimens. This implies that the hardening

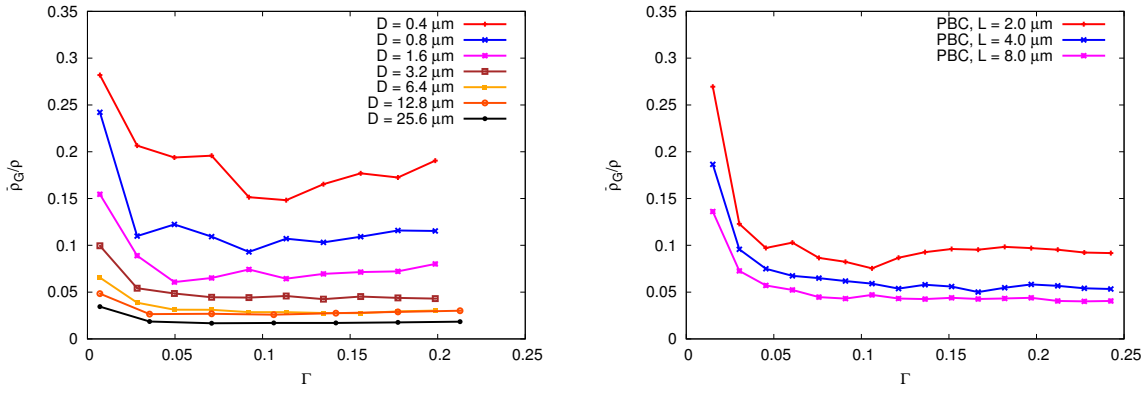

(a) (b)

Fig. 70. Ratio of the effective GND density $\bar{\rho}_G$ computed using horizontal strips of 50 nm height to the total dislocation density ρ as a function of the resolved shear strain Γ for (a) the compression simulations for different sample sized D and (b) pure shear simulations using PBCs for different cell sizes.

law proposed by Guruprasad and Benzerga [102] does not apply to the PBC simulation results and may need to be generalized for arbitrary boundary conditions. Nevertheless, their key observation that a coarse grained measure of the dislocation substructure, $\bar{\rho}_G/\rho$, remains constant during steady state hardening regime holds true in all the simulations presented here, which indicates that an alternate form of equation (6.4) that depends on ρ_G/ρ could be used to capture the size effects under arbitrary imposed loading conditions.

D. Conclusion

The strain hardening behavior of single crystals has been analyzed using the 2.5D dislocation dynamics framework of Benzerga et al. [26], containing enhanced constitutive rules for the physics of dislocation interactions in multiple slip systems. Advances in the numerical methods used in computing the dislocation–dislocation interactions and the treatment of the boundary conditions enable larger sample sizes, containing

millions of dislocations, to be simulated and predictions under multiple loading configurations to be compared, unlike in the previous investigations of Guruprasad et al. [129]. Particular attention is paid to the asymptotic behavior of 2.5D DD simulations in the limit of bulk samples. The latter limit is simulated approximately using periodic boundary conditions. The main conclusions from this study are summarized below.

- Convergence of the size-dependent athermal hardening rates Θ_{II} obtained from 2.5D DD simulations to the experimental range of $\mu/200$–$\mu/100$ has been demonstrated using (i) very large finite specimens containing millions of dislocations and (ii) unit cells of appropriate sizes subjected to pure shear and periodic boundary conditions.
- In the bulk limit, 2.5D DD simulations predict similar athermal hardening rates irrespective of the type of loading imposed (compression or shear).
- The simulation results are consistent with the phenomenological Taylor hardening law, relating the flow stresses to the dislocation density, in the bulk limit. However, unlike in continuum modeling, the hardening relation in DD is a prediction rather than a constitutive assumption. The correct scaling of the flow stress with the dislocation density emerges from the statistics of dislocation interactions in large dynamic systems, in accordance with a set of constitutive rules defined at the scale of the discrete dislocations.
- The phenomenological constitutive law for size dependent hardening proposed by Guruprasad and Benzerga [102] is found to be inconsistent with the simulation results using periodic boundary conditions. This indicates that their expression for the athermal hardening rate derived from plane strain compression simulations may not be generalizable to arbitrary boundary conditions.

CHAPTER VII

DISCRETE DISLOCATION PLASTICITY SIMULATIONS OF VOID GROWTH IN SINGLE CRYSTALS WITH HARDENING

A. Introduction

The growth and coalescence of micro-voids is recognized as the primary mechanism for crack initiation and propagation in ductile materials. In many structural materials, voids initiate by cracking or debonding of second phase particles at the micron scale [15]. Subsequent growth of these voids is mediated by the plastic deformation of the surrounding material under the imposed remote loading conditions. Models of void growth have relied on continuum mechanics to describe the deformation of the matrix material. Homogenization-based constitutive models [12, 15] are widely used to predict the evolution of ductile damage in finite element simulations of structural response involving large deformations, such as in metal forming and failure analysis. With a few exceptions [137, 138], these models lack an internal length scale, which implies that they predict no dependence of the void growth rates on the absolute size of the voids.

Investigation of void size effects in ductile materials is relevant to a number of technologically important applications. Some high-strength structural steels are engineered with a population of second phase particles whose sizes are in the sub-micron range and nucleate sub-grain voids [139]. Other examples are nanostructured materials with low alloy content, such as interstitial-free steels, where voids may nucleate from grain boundary triple points or shear band intersections due to the limited availability of second phase particles [140]. In such cases, void growth rates may be expected to depend on the size of the voids and anisotropy of the crystalline

matrix. There is compelling experimental evidence that plasticity at sub-micron length scales is inherently scale dependent. The existence of these size effects have been conclusively demonstrated experimentally under imposed specimen level strain gradients [20–22] and under macroscopically homogeneous loading [94]. In the specific case of void growth, the relevant length scales of interest are the void size and the void spacing. Continuum damage models, being scale independent, do not predict any dependence of the void growth rate on either of these variables, while the onset of void coalescence, defined as the transition from a diffuse to a localized mode of plasticity in the matrix, depends on the ratio of the void size to void spacing [15]. However, various theoretical investigations using scale dependent plasticity models have indicated a dependence of void growth rates on the *absolute* void size, with the growth rates being significantly slower when the void sizes are small enough to be comparable to the internal length scale of the model [24, 141, 142]. To the authors' knowledge this effect has not been subjected to a thorough experimental investigation to date.

Generalized continuum models such as strain gradient plasticity that depend on an internal length scale have previously been used to investigate void size effects from a theoretical perspective. Early results by Fleck and Hutchinson [141] and Huang et al. [24] considering isolated spherical or cylindrical voids in an isotropic matrix using different formulations of strain gradient plasticity have indicated a sharp increase in the flow stresses and reduction in the void growth rates when the void size is reduced below a micron or so. Later investigations of void size effects using isotropic strain gradient plasticity theories [142–144] and strain gradient formulations of crystal plasticity [145] have confirmed the trend of slower growth rates for smaller voids. The effects of plastic flow anisotropy through the crystal orientation have also been analyzed by several researchers using classical models of crystal plasticity [146–148].

They have concluded that crystal orientation does affect void growth rates under low triaxiality loadings. However, classical plasticity models do not account for the size effects due to the lack of an inherent length scale while gradient plasticity models depend on a heuristic length scale parameter that needs to be fitted from experiments or lower scale simulations.

A more fundamental approach involves the use of bottom up modeling techniques such as atomistic or dislocation dynamics (DD) simulations to investigate void size effects. Unlike continuum theories, these models are inherently more suited to the investigation of size dependent phenomena due to their intrinsic dependence on a physically meaningful length scale such as the lattice parameter or the dislocation Burgers vector. Although molecular dynamics has previously been used to study void growth in a single crystalline matrix [149, 150], the void sizes have been limited to a few nanometers due to computational limitations and the focus had been on studying the mechanisms of void expansion by dislocation emission. DD provides a computationally efficient alternative that allows the consideration of much larger unit cells and void sizes. Previous DD studies of void growth have employed a two dimensional model of a cylindrical void in a crystalline matrix subjected to plane strain loading. Hussein et al. [103] simulated the response of a periodic array of rectangular voids using a representative unit cell subjected to periodic boundary conditions. Segurado et al. [131] studied the mechanical response of an isolated single crystal containing a circular cylindrical void subjected to plane strain loading. The above studies have demonstrated strong size effects under high triaxiality loading for void sizes below a micron. However, size effects were negligible under low triaxiality loading such as pure shear [103]. Also, recent DD studies of Segurado at al. [151] have demonstrated a dependence of the void growth rates on the crystal orientation at low triaxialities.

While the above DD studies have provided insight into the conditions for ductile void enlargement at small scales, some limitations of these studies are notable. Both the above investigations used a formulation of DD that does not exhibit strain hardening under uniaxial loading conditions, due to the fact that short range interactions of dislocations between intersecting slip planes such as junction formation are neglected. On the other hand, real crystals exhibit a multi-stage hardening response under uniaxial loading. Hardening can have an important effect on void growth rates due to the fact that the material surrounding the expanding voids is subjected to large plastic strains. Thus the void will be surrounded by a shell of strain hardened matrix which will have an effect on the void growth rates. Capturing this effect requires enhancements to the DD formulation to account for strain hardening. Also, the previous studies of Segurado and Llorca [131, 151] considered isolated crystals with boundaries that are impenetrable to dislocations leading to high hardening rates due to slip blocking at the boundaries. Thus, their results are more representative of the response of a grain in a polycrystalline material rather than single crystals.

The objective of the present chapter is to investigate void growth in a single crystalline material containing a periodic distribution of voids using DD. A two dimensional approximation of the void and representative volume element (RVE) geometry is used as in the above works. However, we employ an enhanced DD model using an extended set of constitutive rules developed by Benzerga et al. [26] for interactions of dislocations among multiple slip systems (frequently referred to as 2.5D constitutive rules in the literature). The above model has been successfully used to predict size effects under homogeneous loading [127,129] and to yield strain hardening rates comparable to experimental values [102]. The elastic boundary value problem formulation for DD follows the approach of Romero et al. [109] using finite elements with embedded discontinuities, allowing for the treatment of non-convex and mul-

tiply connected domains. Here, the boundary value problem formulation has been enhanced to account for periodic boundary conditions so that the simulation results are representative of a porous crystal containing a periodic array of voids. The details of the boundary value problem formulation and the constitutive rules for dislocation interactions are presented in the following section.

B. Dislocation Dynamics Problem Formulation

Consider a large single crystalline specimen containing a periodic array of cylindrical voids as shown schematically in Fig. 71(a). The material is subjected to plane strain loading by an imposed remote deformation field $\mathbf{E}$, with the strain components $E_{13} = E_{23} = 0$ in the Cartesian frame shown in Fig. 71. The effective mechanical response of the void-matrix composite is obtained by simulating the stress–strain behavior of the unit cell shown in Fig. 71(b) containing discrete dislocations and subjected to doubly periodic boundary conditions. This approach involves an inherent approximation that the statistics of the distribution of dislocations in the unit cell is representative of the bulk material, which is only accurate for unit cells that are sufficiently large when compared to the average dislocation spacing. The geometry of the unit cell may be characterized by the void diameter, D, the void volume fraction, $f = \pi D^2/4L_1L_2$, and the cell aspect ratio, $\lambda = L_2/L_1$. In most calculations we assume $\lambda = 1$, in which case the symbol $L(= L_1 = L_2)$ is used to denote the unit cell size. Physically, L represents the void spacing. The matrix is assumed to be a face centered cubic (FCC) single crystal oriented for quasi-plane strain deformation [130] where the $\mathbf{e}_1$–$\mathbf{e}_2$ plane coincides with the (110) crystallographic plane. The mechanical response of the composite may be simulated by subjecting the RVE shown in Fig. 71(b) to doubly periodic boundary conditions consistent with the imposed remote deformation rate.

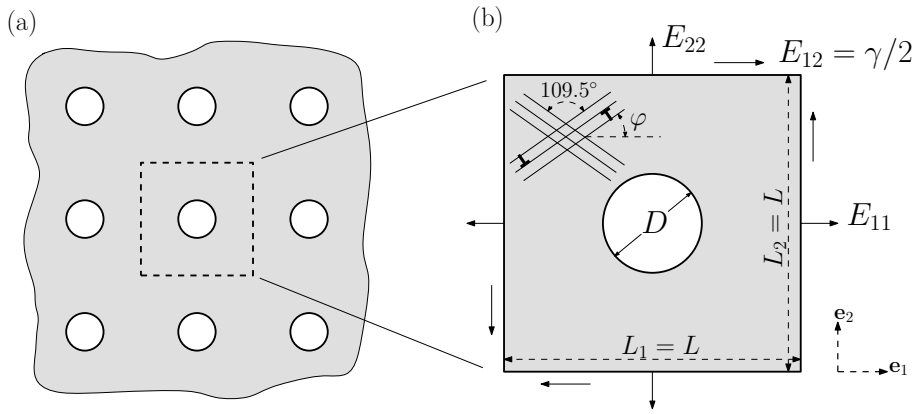

Fig. 71. (a) Schematic of a periodically voided crystalline microstructure and (b) the representative volume element subjected to doubly periodic boundary conditions.

Fig. 71(b) also shows the traces of the $\{111\}$ slip planes on the plane of the paper. We consider two intersecting slip systems corresponding to the $\langle\bar{1}12\rangle$ and $\langle1\bar{1}2\rangle$ slip directions (in plane projections of the $\langle\bar{1}01\rangle$ and $\langle0\bar{1}1\rangle$ slip systems respectively) with an included angle of approximately 109.5°. The angle φ in Fig. 71(b) corresponds to the angle of the $\langle\bar{1}12\rangle$ slip system with respect to the $\mathbf{e}_1$ direction.

The DD framework is based on the original formulation of Van der Giessen and Needleman [25], which treats dislocations as line singularities in a linear elastic continuum that glide along well defined slip systems. In two dimensions, the dislocations are represented as points that represent infinitely long straight edge segments that extend into the plane of the paper. In this formulation, plasticity emerges naturally from the collective motion of discrete dislocations and not as a consequence of constitutive assumptions at the continuum level. A recent extension of the above formulation by Romero et al. [109] that allows for efficient treatment of complex multiply connected domains is adopted in the voided cell calculations presented here. For a given instantaneous arrangement of the dislocations, the elastic fields in the domain, V, of the RVE depicted in Fig. 71 are obtained from the superposition of three distinct fields

within a small strain approximation,

$$\boldsymbol{\sigma} = \tilde{\boldsymbol{\sigma}} + \check{\boldsymbol{\sigma}} + \hat{\boldsymbol{\sigma}}, \qquad \mathbf{u} = \tilde{\mathbf{u}} + \check{\mathbf{u}} + \hat{\mathbf{u}} \tag{7.1}$$

where $\boldsymbol{\sigma}$ and $\mathbf{u}$ stand for the periodic stress and displacement fields respectively. In (7.1), the $\tilde{(\,)}$ fields represent the elastic fields due to the dislocations in the unit cell in an infinite domain and are obtained as the superposition of the individual elastic fields of each dislocation, i, which are known analytically from classical solutions in the literature [104].

$$\tilde{\boldsymbol{\sigma}} = \sum_i \boldsymbol{\sigma}^i, \qquad \tilde{\mathbf{u}} = \sum_i \mathbf{u}^i \tag{7.2}$$

One may note that the $\tilde{(\,)}$ fields are *not* periodic as they do not include the contributions from the periodic images of the dislocations outside the domain V. When the dislocations leave the domain through free boundaries such as the void boundary in Fig. 71(b), they leave behind a displacement discontinuity across their original slip planes equal in magnitude to half the Burgers vector. $\check{\mathbf{u}}$ is a discontinuous displacement field specially constructed such that it evaluates to zero everywhere except in the neighborhood of the slip planes, where it has a discontinuity equal to half the net Burgers vector due to all the dislocations that have exited the domain from that slip plane. Additional details of the construction of the $\check{\mathbf{u}}$ field including its implementation within the finite element framework are detailed in [109]. Finally, the $\hat{(\,)}$ fields are complementary elastic fields that enforce the true boundary conditions of the problem namely the traction free condition at the void boundaries and the periodicity of the tractions and displacement at the boundaries of the unit cell. This method of obtaining periodic solutions for the elastic fields from the superposition of non-periodic fields has previously been employed by Hussain et al. [103]. The unknown fields in equation (7.1), namely the $\hat{\mathbf{u}}$ and the combined stress field $\check{\boldsymbol{\sigma}} + \hat{\boldsymbol{\sigma}}$, are

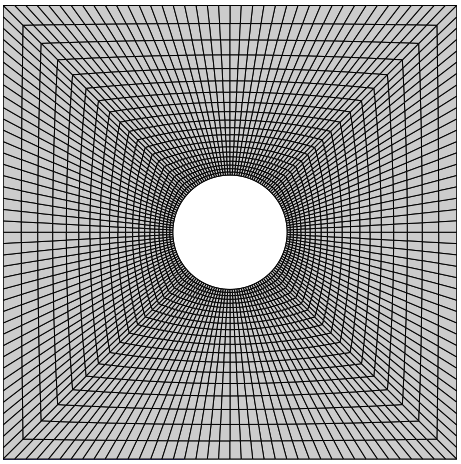

Fig. 72. A typical mesh used in the finite element calculations for the voided unit cells.

solved for using the finite element method. Note that the unknown fields are smooth since the singular and discontinuous fields are known analytically, justifying the use of the finite element method.

A typical mesh, consisting of bilinear quadrilateral elements, used in the finite element computations is shown in Fig. 72. The details of the finite element formulation, including the governing equations, have been presented elsewhere [109] and will not be repeated here. The boundary conditions for the unknown fields in (7.1) may be derived from the traction free conditions at the boundary of the void and the periodicity of the tractions and displacements at the cell boundaries in Fig. 71(b). These are

$$\begin{aligned} (\check{\boldsymbol{\sigma}} + \hat{\boldsymbol{\sigma}}) \cdot \mathbf{n} &= -\tilde{\boldsymbol{\sigma}} \cdot \mathbf{n} && \text{(at the void boundary)} \\ \left.\begin{aligned} \hat{\mathbf{u}}_1 - \hat{\mathbf{u}}_2 &= \mathbf{E} \cdot (\mathbf{x}_1 - \mathbf{x}_2) - \tilde{\mathbf{u}}_1 + \tilde{\mathbf{u}}_2 - \check{\mathbf{u}}_1 + \check{\mathbf{u}}_2 \\ \hat{\mathbf{t}}_1 - \hat{\mathbf{t}}_2 &= -\tilde{\mathbf{t}}_1 + \tilde{\mathbf{t}}_2 - \check{\mathbf{t}}_1 + \check{\mathbf{t}}_2 \end{aligned}\right\} & && \text{(at the cell boundaries)} \end{aligned} \tag{7.3}$$

where the subscripts 1 and 2 correspond to the field values at periodic image nodes with position vectors $\mathbf{x}_1$ and $\mathbf{x}_2$ respectively and $\mathbf{t} = \boldsymbol{\sigma} \cdot \mathbf{n}$ represents the traction

vector with $\mathbf{n}$ as the unit normal vector at the boundary. Note that imposition of the multi-point constraints $(7.3)_2$ resulting from the periodic boundary conditions leads to an unsymmetric stiffness matrix.

The dislocations move on their respective slip planes in accordance with the Peach-Koehler force, which is a configurational force that acts to lower the overall potential energy of the sample and thus depends on the long range pairwise interactions between the dislocations and the image fields due to the boundary conditions. The expression for the Peach-Koehler force on a dislocation i reads [25]

$$f^i = \mathbf{m}^i \cdot \left(\hat{\boldsymbol{\sigma}} + \sum_{j \neq i} \boldsymbol{\sigma}^j \right) \cdot \mathbf{b}^i \tag{7.4}$$

where $\mathbf{m}^i$ is the slip plane normal and $\mathbf{b}^i$ is the Burgers vector. A drag type mobility law is used for the instantaneous velocity, v^i, of dislocation i,

$$f^i = Bv^i \tag{7.5}$$

where B denotes the drag factor. At every increment of the loading, the finite element solution yields the elastic fields based on the current positions of the dislocations. A forward Euler integration method with a suitably small time step is used to update the dislocation positions and the solution proceeds in an iterative manner. Any dislocations that cross the void boundaries are removed from the sample while dislocations that cross the periodic cell boundaries reenter the sample through the corresponding element edge on the opposite face of the cell on the nearest entry point of a slip plane. The slip contributions due to dislocations that exit and reenter the domain through the periodic boundaries are retained in order to avoid spurious singularities at the boundaries. Additional details of the implementation of periodic boundary conditions within the DD simulation framework may be found in [152].

While the elastic fields are sufficient to capture the long-range interactions between the dislocations, additional constitutive rules are required to capture the short-range interactions of the dislocations among themselves and with obstacles, which depend on atomistic phenomena at the scale of the dislocation cores. Previous investigations of void growth using DD [103, 131, 151] have used simple constitutive rules for short-range interactions originally introduced in [25]. These include the nucleation of dislocations from a predefined set of static Frank-Read sources when the resolved shear stress on a source exceeds a critical value of τ_{nuc} for a critical nucleation time, t_{nuc}, their pinning and unpinning at randomly distributed obstacles with a specified pinning strength, τ_{obs}, and mutual annihilation of opposite signed dislocations when they cross each other or approach within a critical distance on the same slip plane. While these constitutive rules have been used successfully to model a variety of phenomena where discrete dislocation effects are important, such as indentation [101], ductile crack propagation [99], etc, they do not predict strain hardening under uniaxial loading conditions. Strain hardening is characterized by the dynamics evolution of the population of dislocation sources and obstacles in the sample due to three dimensional effects such as the formation of junctions between dislocations on intersecting slip planes, which can act as both obstacles to dislocation motion and/or anchoring points for new dislocation sources. In the specific case of void growth, it is conceivable that localized hardening due to large plastic straining in the neighborhood of the voids can inhibit further void growth. In order to investigate these issues, we employ an enhanced constitutive description for short range dislocation interactions proposed by Benzerga et al. [26] using two dimensional idealizations of some three dimensional dislocation phenomena (referred to alternatively in the text as hardening constitutive rules or 2.5D rules). The capabilities of the enhanced model in predicting the strain hardening rates in single crystals and size effects at small scales have been

demonstrated previously [102, 127, 129].

In the 2.5D formulation, two dislocations on intersecting slip planes can form a sessile junction if both dislocations fall within a critical radius of d^* from the intersection point at the end of an increment. These junctions may represent Lomer-Cottrel locks in three dimensions and act as obstacles to dislocation motion on both the intersecting slip planes. Most of these "dynamic obstacles" may be destroyed by unzipping of the participating dislocations if the resolved shear stress at a junction I exceeds a critical value given by

$$\tau^I_{\text{brk}} = \beta_{\text{brk}} \frac{\mu b}{\mathcal{L}^I} \tag{7.6}$$

where μ denotes the shear modulus, $\mathcal{L}^I$ is the distance to the nearest junction on any of the intersecting slip planes and β_{brk} is a scaling factor for junction strength. However, a finite (small) probability, p, is assigned for the stabilization of these junctions by cross slip or other mechanisms at the scale of the junction cores so that they may not be destroyed under further loading. A probabilistic approach is needed due to the limited representation of the physics in the two-dimensional model. A stable junction I may act as an anchoring point for a new Frank-Read source with a nucleation strength given by

$$\tau^I_{\text{nuc}} = \beta_{\text{nuc}} \frac{\mu b}{\mathcal{L}^I} \tag{7.7}$$

where β_{nuc} is a source strength parameter (typically of the order of unity [108]) and $\mathcal{L}^I$ is the distance to the nearest junction on the slip plane on which τ^I_{nuc} is being resolved. The nucleation time for the source is given by

$$t^I_{\text{nuc}} = \gamma_{\text{nuc}} \frac{\mathcal{L}^I}{|\tau^I| b} \tag{7.8}$$

where γ_{nuc} is a material constant with the units of the drag factor and τ^I is the resolved shear stress at the junction I excluding the self-stress due to the participating

dislocations. Notice that both the source strength and the nucleation time depends on a physically meaningful length scale so that the properties of the dynamic Frank-Read sources depend on the statistics of junction formation. The key feature of the 2.5D approach is the dynamic evolution of the source and obstacle population that collectively determines the observed strain hardening rates. The reader is referred to [26] for additional details including physical justifications for the above constitutive rules.

C. Simulation Results

The initial conditions for all the simulations presented in this chapter correspond to a stress and dislocation free unit cell (Fig. 71(b)) containing a random distribution of point sources and obstacles distributed on slip planes spaced $20b$ apart, where b denotes the modulus of the Burgers vector. Although the source and obstacle densities vary as a function of the deformation due to the dynamics creation/destruction of junctions, initial densities of static sources and obstacles is taken to be 150 and 600 μm^{-2} respectively. Two types of boundary conditions are analyzed corresponding to pure shear ($E_{12} = \gamma/2$, other $E_{ij} = 0$) and equibiaxial deformation ($E_{11} = E_{22}$, other $E_{ij} = 0$), which represent two extreme cases of loading with a zero average triaxiality and a very high value of the triaxiality respectively. The average stress tensor, $\mathbf{\Sigma}$, for the unit cell is evaluated using the micromechanical relationship

$$\Sigma_{ij} = \frac{1}{V}\int_V \sigma_{ij} \mathrm{d}V = \frac{1}{V}\int_S t_i x_j \mathrm{d}S \tag{7.9}$$

where S denotes the surface of the RVE. Some calculations are also performed under proportional loading conditions with a specified value of the stress ratio, $\theta = \Sigma_{22}/\Sigma_{11}$. In the latter case, for a specified value of the imposed strain E_{11} (and with $E_{12} = 0$),

Table VI. Tabulation of the important loading and microstructure related parameters used in the DD simulations.

Property	Values
D (μm)	0.252, 0.505, 1.01, 1.51
f	0 (no void), 0.05
λ	1, 1.44, 2.25
L (μm)	1, 2, 4, 6, 8
φ	35.25° (symmetric double slip)
Matrix behavior	Non-hardening (2D rules) Hardening (2.5D rules)
Loading types	Pure shear ($E_{11} = E_{22} = 0$) Equibiaxial deformation ($E_{11} = E_{22}, E_{12} = 0$) Proportional loading with constant $\theta = \Sigma_{22}/\Sigma_{11}$

the unknown lateral strain component E_{22} is evaluated using the additional constraint equation

$$\int_S t_2 x_2 \mathrm{d}S = \theta \int_S t_1 x_1 \mathrm{d}S \tag{7.10}$$

which is incorporated into the global stiffness matrix. All the simulations are performed at a uniform strain rate of 2000 s^{-1} for the non-zero components of the imposed strain rate tensor $\dot{\mathbf{E}}$. Unless explicitly mentioned otherwise, the void volume fraction $f = 0.05$ and cell aspect ratio $\lambda = 1$ in all the calculations. Additional calculations are also performed for a sound material ($f = 0$) to serve as a reference. Table. VI summarizes the values of some of the loading and microstructure related parameters used in the calculations.

Young's modulus $E = 70$ GPa and Poisson's ratio $\nu = 0.33$ corresponding to values for Aluminum are used for the matrix. The modulus of the Burger's vector

$b = 0.25$ nm is assumed on all slip systems for simplicity. The drag factor is taken to be $B = 10^{-4}$ Pa s and a constant value of $\tau_{\text{obs}} = 150$ MPa is used for the obstacle strength. A normal distribution of initial source strengths τ_{src} is assumed with an average value of 50 MPa and a standard deviation of 10 MPa and a constant nucleation time of $t_{\text{nuc}} = 10$ ns is assigned for all sources as in previous 2D DD studies [25, 103, 131]. The values used for the 2.5D parameters that affect the properties of dislocation junctions are $\beta_{\text{nuc}} = 1$, $\beta_{\text{brk}} = 5\beta_{\text{nuc}}$, $\gamma_{\text{nuc}} = 1000B$, $d^* = 6b$ and $p = 0.01$. These values have been used in previous investigations of size effects at micron scales under homogeneous loading conditions [107] and have been shown to predict bulk values of the athermal hardening rates in single crystals in the limit of very large samples.

1. Dense Matrix under Pure Shear

The case of a crystalline material with zero porosity subjected to pure shear loading is examined first to investigate the effect of the RVE sizes chosen and to establish a reference for comparison with the voided cell calculations. A uniform grid of square finite elements is used in these calculations. The crystal orientation with respect to the $\mathbf{e}_1 - \mathbf{e}_2$ coordinate frame established in Fig. 71 is chosen to be $\varphi = 35.25°$, which corresponds to a symmetric double slip arrangement under the imposed loading conditions.

Fig. 73 shows comparisons of the stress–strain response and evolution of the dislocation density under pure shear using a non-hardening matrix (2D rules) and a hardening matrix (2.5D rules) for different unit cell sizes corresponding to $L = 0.5$ to 8 μm. Notice that the effect of the cell size on the evolution of the flow stress and the dislocation density is small in both sets of calculations for $L \geq 1$. However, for values of $L < 1$ μm, a pronounced cell size effect if observed, indicating that these cells are not statistically representative of the porous crystal as they may contain too

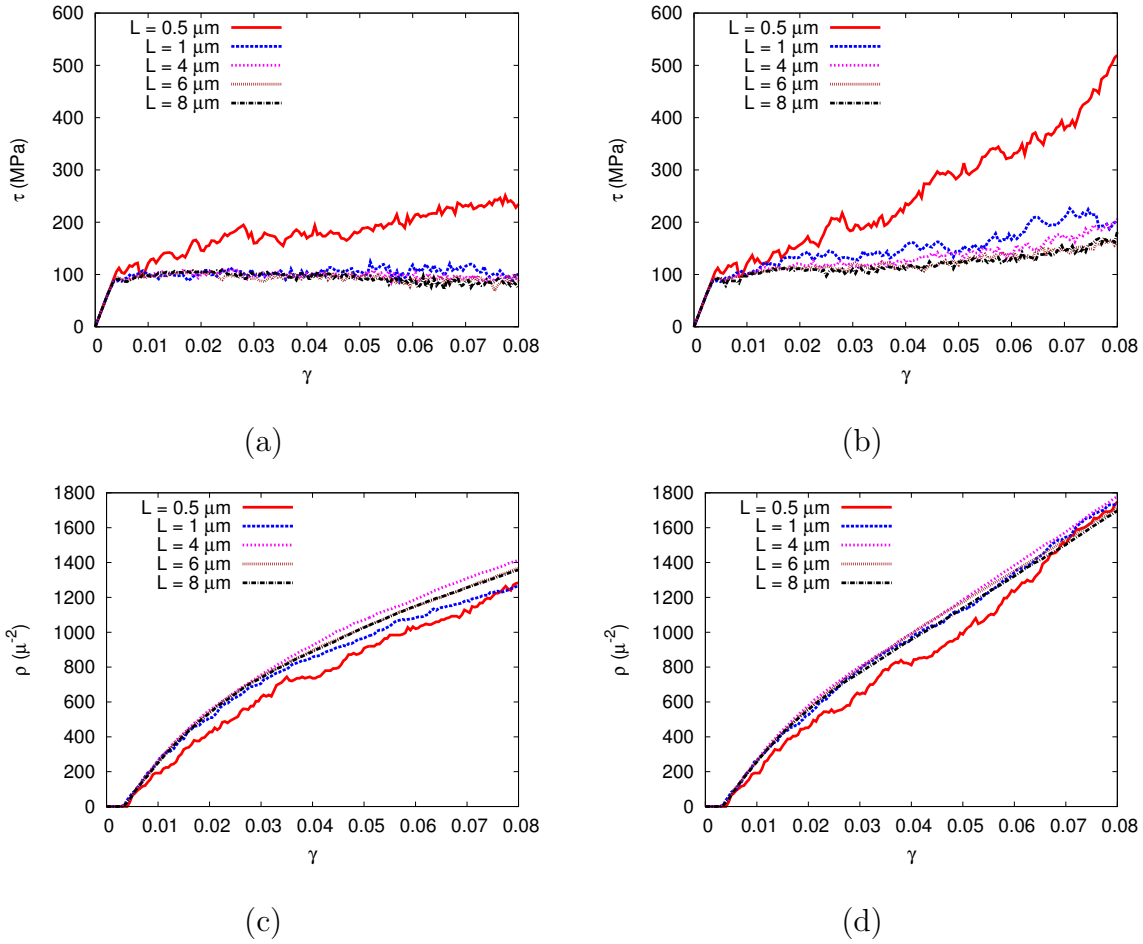

Fig. 73. Effective response of the matrix material subjected to pure shear loading using unit cells of different sizes. Average shear stress, τ, vs shear strain, γ, using (a) non-hardening constitutive rules and (b) hardening constitutive rules. Dislocation density, ρ, vs shear strain, γ, using (a) non-hardening constitutive rules and (b) hardening constitutive rules.

few sources and dislocations. While the crystals do not exhibit any strain hardening using the 2D constitutive rules, the use of 2.5D rules lead to significant hardening at high shear strains. The athermal hardening rates for FCC single crystals, defined as the slope of the resolved shear stress vs. a work conjugate shear strain graph on the slip systems in the steady state (stage II) hardening regime, have a universal range of values from $\mu/200$ – $\mu/100$, independent of the material, temperature and strain rate [133]. Estimating the hardening rate from Fig. 73 using a least square fit in the range $\gamma = 0.02 - 0.08$ yields, after appropriate corrections using the Schmid factor, a range of $0.005\mu - 0.008\mu$ with an average value of 0.006μ. Thus the simulated bulk hardening rates are close to the lower end of the experimental range for bulk single crystals.

Any effect of the cell size L in these simulations would be due to the lack of statistical representativity of the chosen unit cells. In order to avoid such effects in the results presented in the following sections, one needs to quantify the deviations from bulk behavior as a function of the cell size. For this purpose, we define an *ad hoc* scalar measure of the cell size dependence of the flow stress, $\varepsilon(L)$, as the root mean squared value of the deviation in the flow stress of a sample of size L from that of the largest simulated cell size ($L = 8\mu$m) normalized by the latter value and averaged over the strain range $\gamma = 0.02 - 0.08$. I.e.

$$\varepsilon(L) \equiv \left[\left\langle \left(\frac{\tau(L)}{\tau(8\mu m)} - 1 \right)^2 \right\rangle_{\gamma=2-8\%} \right]^{1/2} \tag{7.11}$$

where $\langle \cdot \rangle$ denotes averaging over the specified range of strains. Fig. 74 shows the variation of the quantity ε as a function of the cell size L for the case of the hardening matrix (Fig. 73(b)). Notice that large deviations from bulk behavior are observed for cell sizes below $L = 1\mu$m. Based on these results, we use cell sizes $L \geq 1\mu$m in

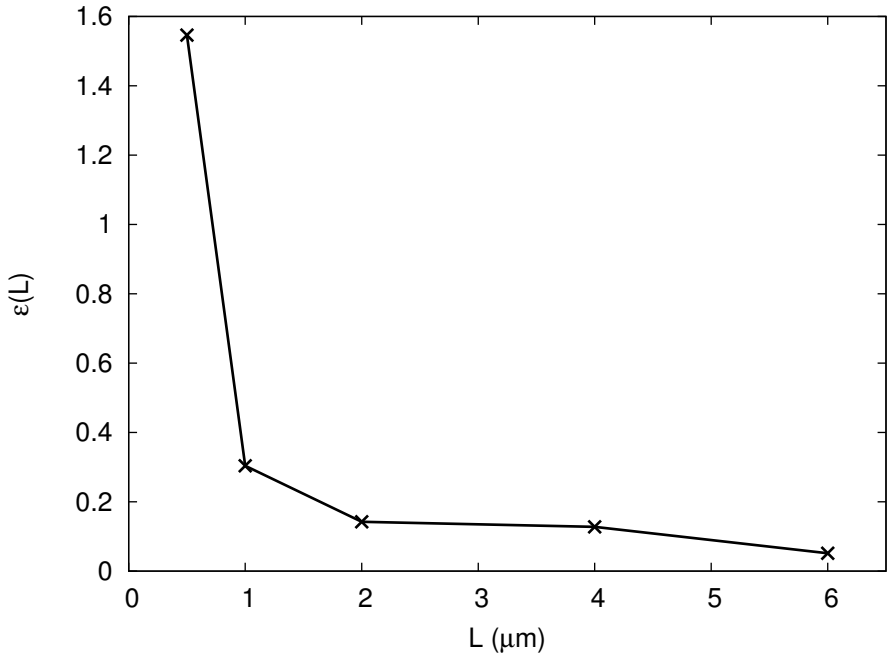

Fig. 74. Variation of the quantity $\varepsilon(L)$ that measures the cell size dependence of the flow stress as a function of L.

the rest of this chapter to study void size effects. Finally it is noted that, while the relative absence of a cell size effect has been established above in the case of pure shear loading, similar trends were also observed for crystals subjected to uniaxial tension along the $\mathbf{e}_1$ direction. These results are omitted for brevity.

2. Effective Response: Pure Shear vs. Biaxial Deformation

The effect of void size on the mechanical response of a porous crystal is investigated in this section using self-similar unit cells of the type shown in Fig. 71(b). The crystal orientation is kept fixed at $\varphi = 35.25^\circ$ and two types of boundary conditions, pure shear and equibiaxial deformation, are considered. Previous investigations of a similar nature by Hussein et al. [103] using 2D DD and assuming a square geometry for the voids had evidenced little size effects at low triaxialities, while significant size

effects were observed under high triaxiality loading. Here, we examine the effect of hardening in the matrix on the size effects on the average stress–strain response and the void growth rates.

Figs. 75(a) and (b) show the stress–strain response of four porous self-similar unit cells with $f = 0.05$ and containing voids of diameter $D = 0.252\mu$m, $D = 0.505\mu$m, $D = 1.01\mu$m and $D = 1.51\mu$m (corresponding to $L = 1, 2, 4$ and 6μm respectively) under pure shear loading and assuming non-hardening and hardening constitutive rules for the matrix respectively. The former exhibits no strain hardening on the average shear stress vs. shear strain behavior irrespective of the void size and are in broad agreement with the results of Hussein et al. [103]. On the other hand, Fig. 75(b) exhibits a strain hardening behavior similar to that observed for the sound matrix as a result of the dynamic junction formation arising from the 2.5D constitutive rules. Also, an effect of the void size on the hardening rate may be observed in Fig. 75(b). Recall that no size effect was observed under pure shear in section 1 for the same cell sizes ($L = 1$–6) in the absence of voids. Examination of the corresponding dislocation density curves in Figs. 75 (c) and (d) reveal some interesting trends. For the case of the non-hardening matrix, the dislocation densities for the different cell sizes are comparable initially. However, at larger strains, the dislocation densities are found to be large for the larger void sizes. Comparison with the dislocation density plots for the dense matrix (Fig. 73(c)) shows that for the case of the smallest void size, $D = 0.252$ μm, the evolutions of the dislocation density are similar to that of a dense matrix. In other words, the void has no effect on the evolution of the flow stress or the dislocation density. However, for the larger cell sizes the dislocation density is larger in the porous material compared to a dense material at equivalent shear strains, and the difference is seen to increase as the void size increases. These results can be rationalized based on the stress concentration around the voids. In the absence

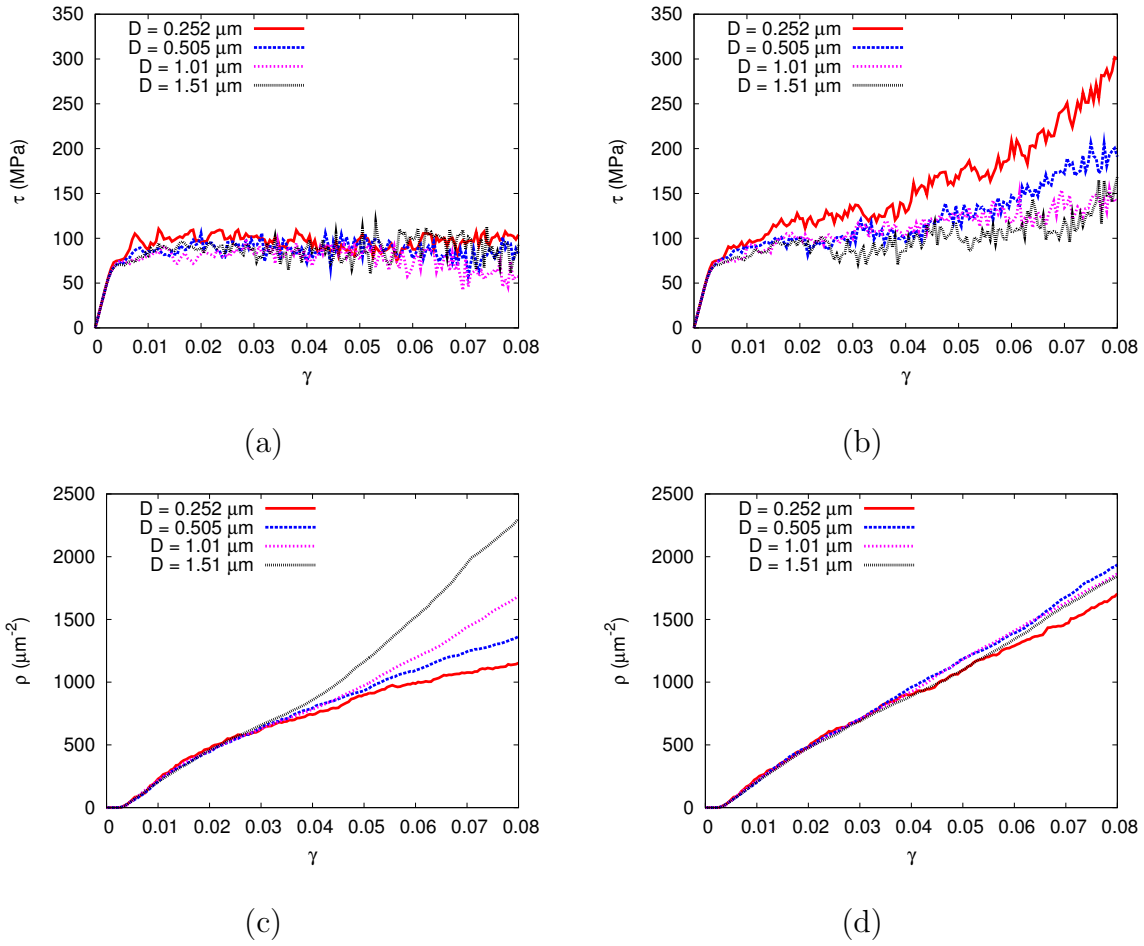

Fig. 75. Mechanical response of voided unit cells with $f = 0.05$ ($L/D = 3.96$) and four different void sizes subjected to pure shear deformation. Top Row: shear stress τ vs. shear strain γ for (a) non-hardening matrix and (b) hardening matrix. Bottom Row: dislocation density ρ vs. γ for (a) non-hardening matrix and (b) hardening matrix.

of dislocations, the distribution of stresses will be similar for all the (self-similar) unit cells considered. However, since a constant density of Frank-Read sources is used in all cases, the number of available dislocation nucleating sources in the high stress regions will be larger for the larger void sizes, resulting in a higher dislocation density. However, the evolution of the flow stress is apparently unaffected by the different evolutions of the dislocation density and show no size dependence. Adding the 2.5D rules for strain hardening appears to negate the above behavior and the dislocation densities are comparable irrespective of the void size. This is likely due to local hardening around the voids due to junction formation that leads to shutdown of the sources around the voids. However, a clear size dependence of the flow stress is evident with the smaller voids yielding a larger flow stress. The origins of this effect are unclear.

Figs. 76(a) and (b) compare the stress–strain response of the same unit cells under equibiaxial deformation using non-hardening and hardening constitutive rules respectively. The graph plots the in-plane hydrostatic stress, $(\Sigma_{11} + \Sigma_{22})/2$, as a function of the work conjugate unit cell volumetric strain, E_v, given by $E_v = E_{11} + E_{22}$. In this case, a marked size effect may be observed in both the figures with the smaller void sizes leading to a significantly harder response. The trends obtained in Fig. 76(a) are in agreement with those obtained by [103], while the hardening rates are significantly lower when compared to the results of Segurado and Llorca [131] using an isolated single crystalline specimen identical to the one in Fig. 71(b) with slip blocking at the boundaries. However, the inclusion of 2.5D constitutive rules in Fig. 76(b) alters the results somewhat due to dynamic junction formation, which leads to significant hardening at higher values of the overall strain for the case of the larger unit cells.

In order to investigate further the origin of these size effects, we look at the

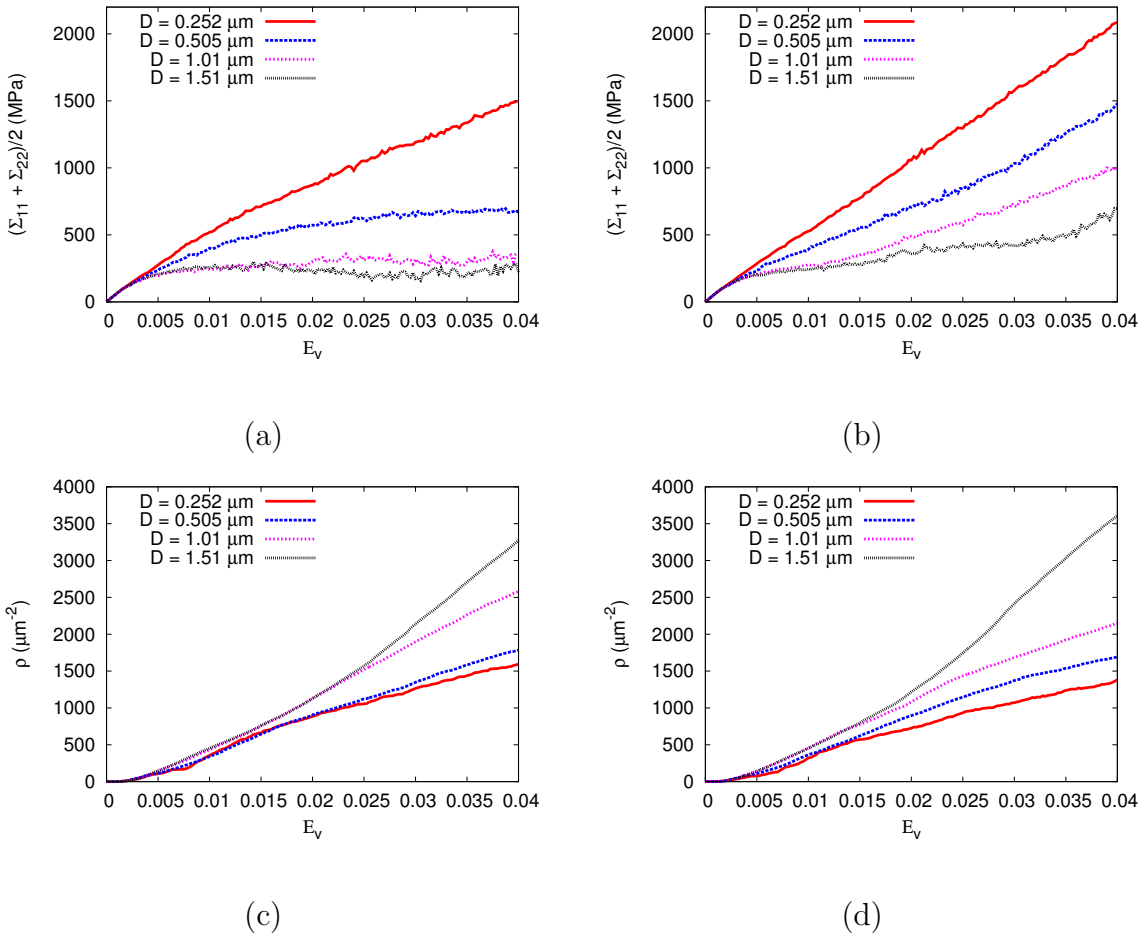

Fig. 76. Mechanical response of voided unit cells with $f = 0.05$ and four different void sizes subjected to equibiaxial deformation. Top Row: mean normal in-plane stress $(\Sigma_{11}+\Sigma_{22})/2$ vs. volumetric strain $E_v = E_{11}+E_{22}$ for (a) non-hardening matrix and (b) hardening matrix. Bottom Row: dislocation density ρ vs volumetric strain E_v for (c) non-hardening matrix and (d) hardening matrix.

contours of total slip, Γ, in the matrix at a given state of the macroscopic strain, for the different unit cell sizes. Γ is a non-negative scalar field that measures the extend of plastic deformation in an elementary volume and is defined as

$$\Gamma = \int_0^t \dot{\Gamma}\ \mathrm{d}t, \qquad \dot{\Gamma} \equiv \sum_{\kappa} |\dot{\gamma}^{\kappa}|, \qquad \dot{\gamma}^{\kappa} = s_i^{\kappa} \dot{\epsilon}_{ij} m_j^{\kappa} \tag{7.12}$$

where κ denotes the slip system number and $\mathbf{m}^{\kappa}$ and $\mathbf{s}^{\kappa}$ are unit vectors along the slip plane normal and slip direction respectively. In the case of pure shear, Figs. 77(a) and (b) compare the contours of Γ at $\gamma = 0.04$ for the smallest and largest cell sizes examined corresponding to $L = 1\mu$m and $L = 6\mu$m respectively. It is clear from these figures that plastic slip is distributed fairly uniformly throughout the cell in the case of pure shear loading. On the contrary, similar contour plots for the case of equibiaxial deformation at $E_v = 0.02$ show a much more inhomogeneous slip distribution with most of the slip being localized in the neighborhood of the voids. As discussed previously, for a given random distribution of the Frank-Read sources in the specimen with a constant average density, the availability of sources close to the void will increase as the void size increases. At low triaxialities, such as under pure shear loading, the resolved shear stress on the slip planes will be high on average throughout the unit cell, resulting in dislocation nucleation and glide on multiple slip planes as observed in Fig. 77(a) and (b). On the contrary, under equibiaxial loading, the resolved shear stress will be low away from the voids (and will be exactly zero in the absence of voids) implying that dislocation nucleation and plastic flow will be strongly dependent on the availability of sources close to the periphery of the voids where the shear stresses are concentrated. Since the latter increases as the void size increases, we obtain the strong size effects in Fig. 79(b). Additional evidence that the effective size dependent hardening behavior obtained under equibiaxial loading is linked to source limited behavior around the voids is obtained from examination

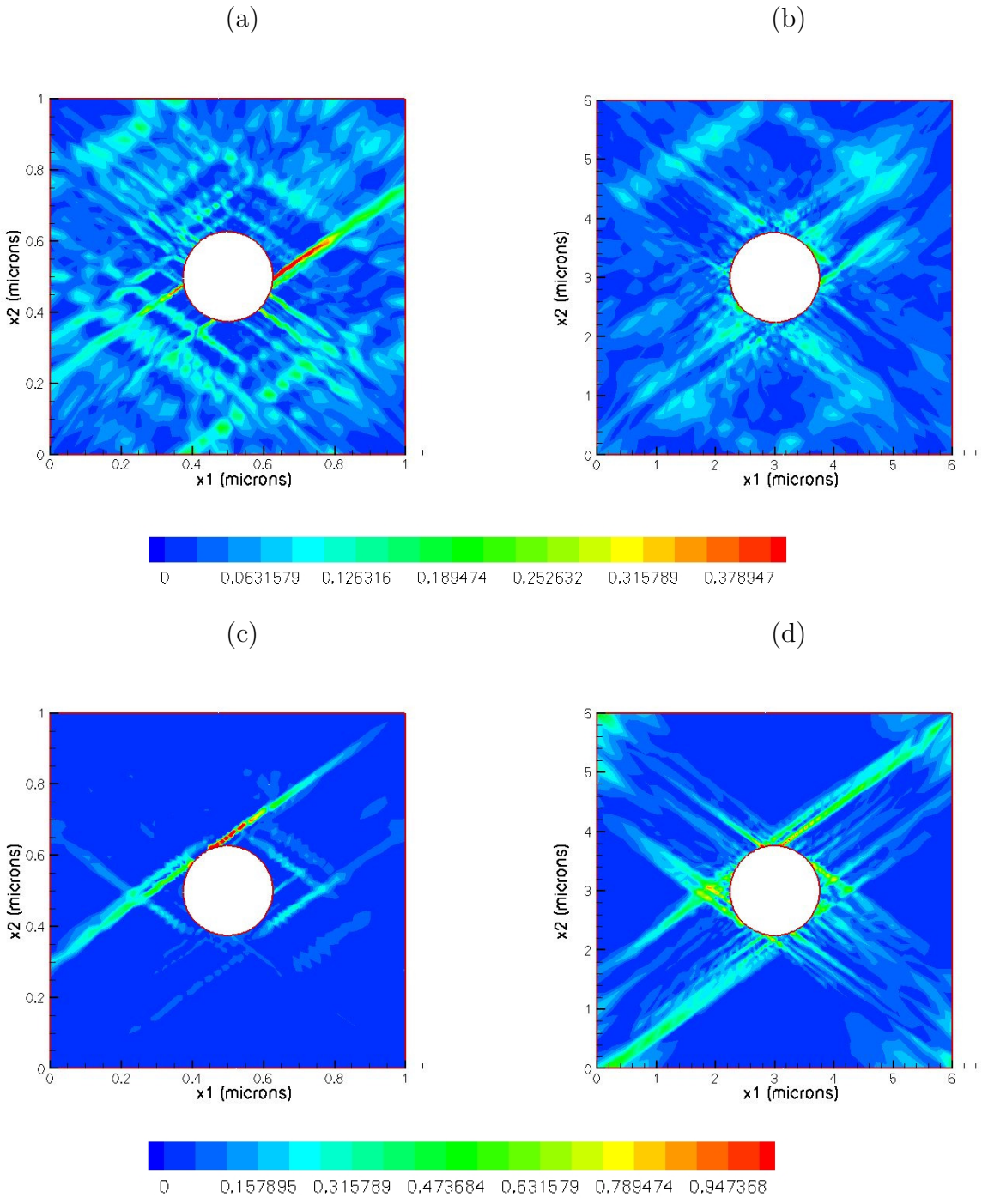

Fig. 77. Top Row: Contours of total slip Γ at $\gamma = 0.04$ corresponding to pure shear loading and a hardening matrix for different cell sizes (a) $L = 1\mu$m ($D = 0.252\mu$m) (b) $L = 6\mu$m ($D = 1.51\mu$m). Bottom Row: Corresponding contours for equibiaxial loading at $E_v = 0.02$ and two different cell sizes (c) $L = 1\mu$m ($D = 0.252\mu$m) (d) $L = 6\mu$m ($D = 1.51\mu$m).

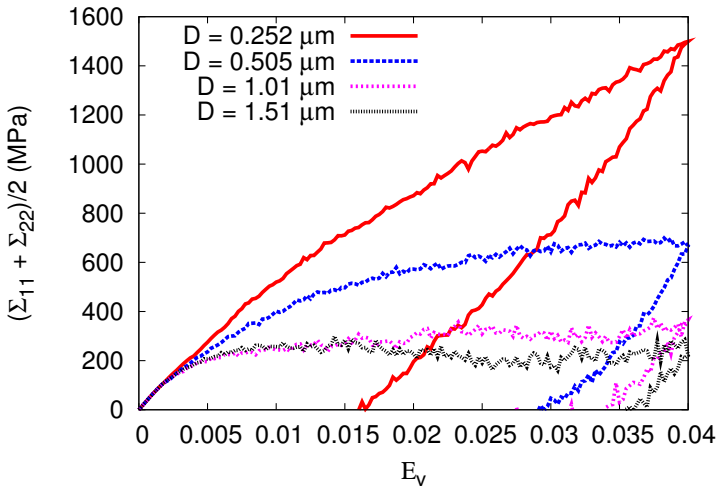

Fig. 78. Stress–strain response upon unloading from a total strain of $E_v = 0.04$ corresponding to the results of Fig. 76(a).

of the dislocation density, ρ, vs. strain curves in Fig. 76(c) and (d). For a single crystal undergoing homogeneous deformation, the flow stress is proportional to the square root of the dislocation density via the Taylor hardening relation. On the other hand, in Fig. 76(c) the harder unit cells are observed to have a lower dislocation density, which is a clear indication of the type of behavior commonly referred to in the literature as exhaustion hardening. Fig. 78 shows the response of the same unit cells upon unloading from a total volumetric strain $E_v = 0.04$. The recoverable (elastic) portion of the total strain is seen to be larger for the smaller void sizes, which provided further evidence of source limited behavior in smaller unit cells.

While the results in Figs. 75 and 76 correspond to individual realizations of the initial Frank-Read source and obstacle distribution in the sample, several computations have been performed for each case corresponding to different random initial configurations with the same average source and obstacle densities. Fig. 79 shows a summary of these simulations in terms of the scaling of the flow stress as a function

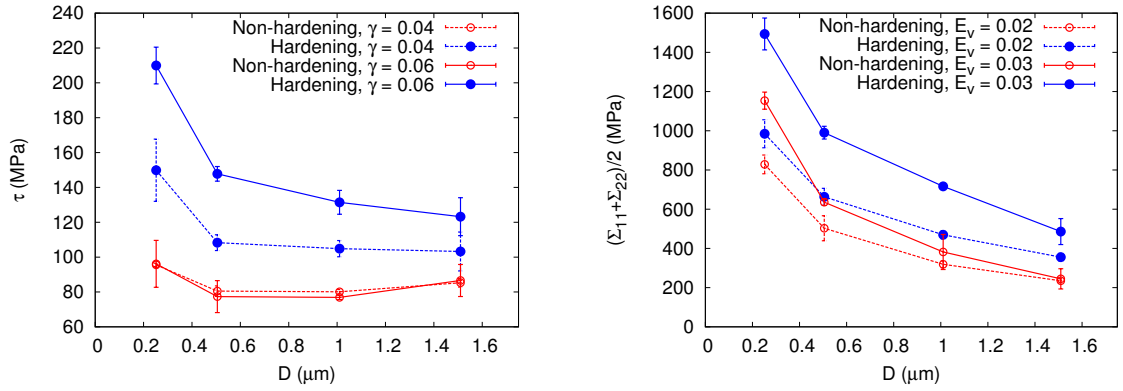

(a) (b)

Fig. 79. Scaling of the flow stress as a function of the void diameter under (a) pure shear and (b) equibiaxial deformation. Results using both non-hardening and hardening matrix are shown.

of the void diameter at two different values of the overall strain. The results for pure shear loading, Fig. 79(a), shows no size effect on the evolution of the flow stress in the case of the non-hardening matrix while a clear size effect is observed in the case of a hardenable matrix. On the other hand, under equibiaxial deformation, Fig. 79(b), significant size effects are obtained in the case of both types of matrix behavior with the smaller voids yielding a much harder overall response.

3. Void Growth Rates

In this section, we examine the effect of the imposed loading on the void growth rates through the evolution of the void volume fraction f. Assuming unit thickness in the out-of-plane direction, f is calculated at each increment as the ratio of the current void area and unit cell area, which are estimated using the nodal displacements obtained from the finite element solution. It must be mentioned here that the trends discussed for f are qualitative only due to the fact that a small strain finite element framework is being used, which implies that the cumulative expansion of the voids and the

associated softening in the overall stress–strain behavior are not well captured in the simulations. Also, the void volume fraction includes the contribution from the elastic dilation of the cell in addition to the plastic part due to dislocation slip. Nevertheless, it is instructive to look at the qualitative trends for the void growth as a function of the loading.

Fig. 80(a) shows the void volume fraction as a function of the imposed shear strain under pure shear loading (corresponding to the stress–strain response in Fig. 75(a)) and in the absence of hardening in the matrix. Fig. 80(b) shows similar results for the case of the hardening matrix corresponding to Fig. 75(b). Notice that, as expected, both sets of simulations show negligible void growth under pure shear loading irrespective of the void size. However, significant void growth is observed under equibiaxial loading, Figs. 76(c) and (d), which exhibit a clear size effect with the larger voids growing faster. This size effect is clearly associated with the plastic deformation due to dislocation glide, since a pure elasticity calculation will yield no size effects. The trends are consistent with the previous results of [131] using an isolated voided crystal model. Comparisons of the void growth rates with and without hardening in the matrix (Figs. 80(d) and (c) respectively) show that strain hardening around the voids leads to slower void growth for all void sized compared to the case of a non-hardening matrix.

Analytical models of void growth in a ductile matrix have shown that void growth rates have an exponential dependence on the hydrostatic component of the stress through the stress triaxiality ratio. In order to better investigate the effect of the stress state on the void growth rates, we subject the unit cells to proportional loading by imposing a constant stress ratio using the constraint condition in equation (7.10). Fig. 81 shows the void volume fraction as a function of the strain E_{11} under proportional loading with different values of the stress ratio $\theta = \Sigma_{22}/\Sigma_{11}$ ranging from

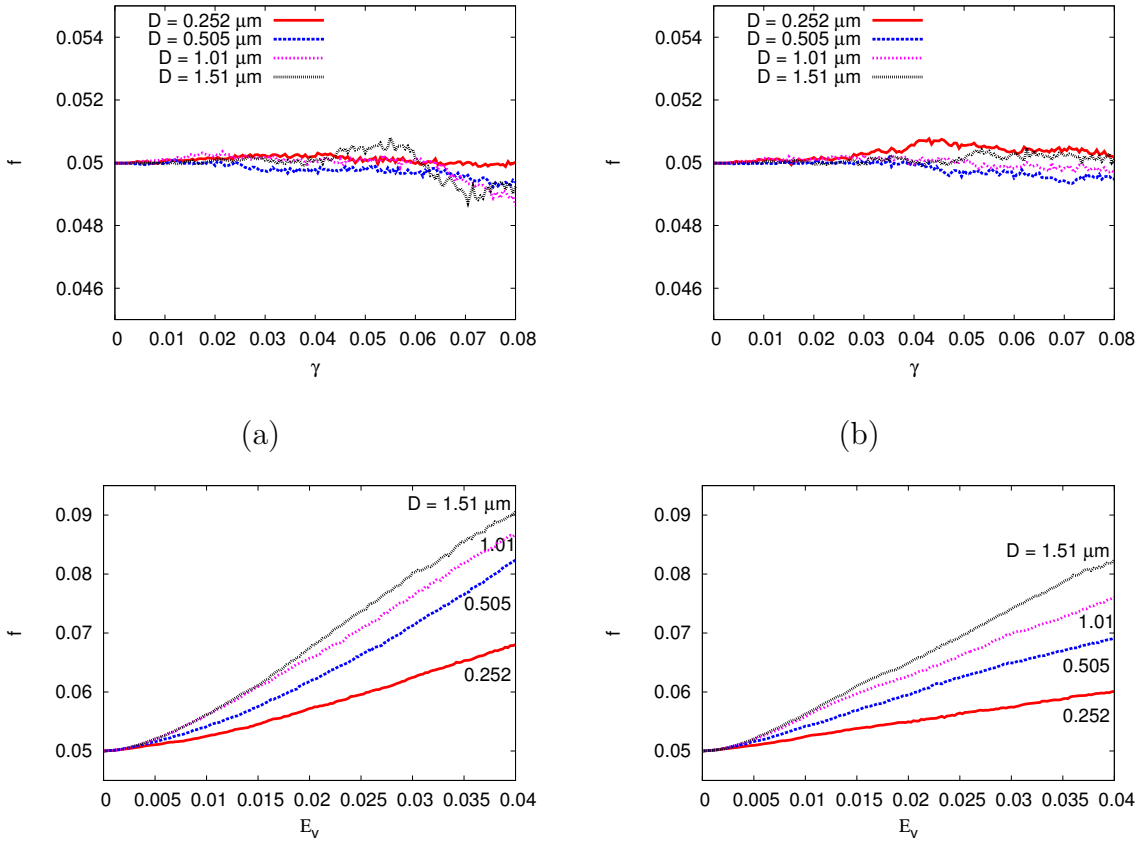

Fig. 80. The void volume fraction f vs. shear strain γ under pure shear loading for (a) non-hardening matrix and (b) hardening matrix. f vs. volumetric strain $E_v = E_{11} + E_{22}$ under equibiaxial loading for (c) non-hardening and (d) hardening matrix behavior.

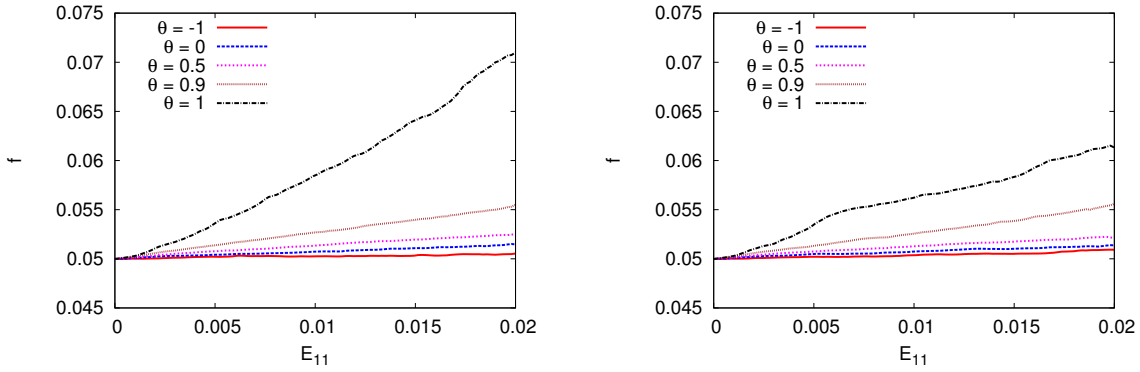

(a) (b)

Fig. 81. The void volume fraction f as a function of the strain E_{11} for a unit cell with $D = 0.505$ μm under proportional loading for different values of the stress ratio θ: (a) non-hardening matrix, (b) hardening matrix.

$\theta = -1$ (pure shear) through $\theta = 0$ (uniaxial tension) to $\theta = 1$ (in-plane hydrostatic tension). All the results correspond to a unit cell with $L = 2\mu$m. The results clearly show a non-linear dependence of the void growth rates on the stress ratio. Low triaxiality loading in the range $\theta = -1$ to 0 results in negligible void growth while the void growth rates increase rapidly as θ approaches a value of unity. Comparison of the results in Fig. 81(a) and (b) using a non-hardening matrix and a hardening matrix respectively show that strain hardening in the matrix tends to inhibit void growth rates. Figs. 82(a) and (b) show the scaling of the void volume fraction as a function of θ for two values of the strain E_{11}, which confirm the strongly non-linear dependence of the void growth rates on θ. The effect of hardening in the matrix is apparent at higher strains with void growth being slower in general than for a non-hardening material subject to similar loading history.

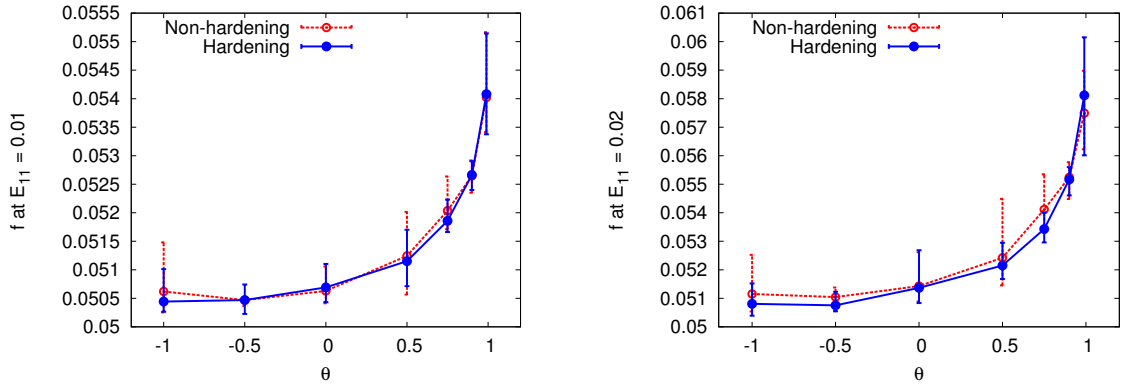

(a) (b)

Fig. 82. The scaling of the void volume fraction f at (a) $E_{11} = 0.01$ and (b) $E_{11} = 0.02$ as a function of the imposed stress ratio θ for unit cells with initial void size $D = 0.505$ μm subjected to proportional loading.

4. Effect of Void Spacing

Periodic microstructures of the type studied here (see Fig. 71) introduce two geometric length scales that are of relevance to the problem, namely the void diameter D and the mean void spacing L (assuming $L_1 = L_2 = L$). The size effects demonstrated in section 2 correspond to self similar microstructures ($L/D =$ constant) with different values of the void size D. Therefore, the impact of the void spacing L on the magnitude of the size effects seen in Fig. 76 is unclear. Here, we investigate the material response under equibiaxial loading and 2D constitutive rules for porous materials with a fixed void spacing ($L = 6\mu$m) and the four different void sizes investigated in section 2. Fig. 83(a) shows comparisons of the in-plane mean normal stress vs. the volumetric strain, while Fig. 83(b) shows the evolution of the porosity. Note that, since the materials being compared have different values for the initial porosity f_0, the evolution of the change in porosity $f - f_0$ is plotted for ease of comparison. Comparing the results in Fig. 83(a) with those in Fig. 76(a) for the same

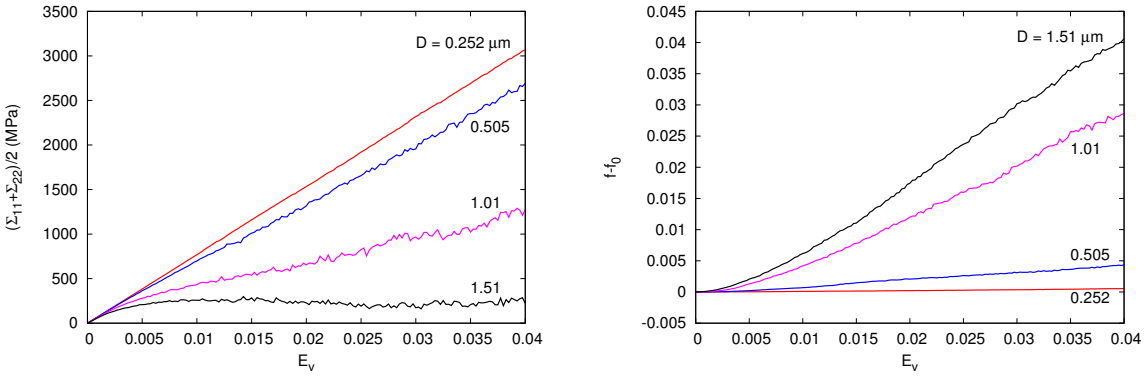

(a) (b)

Fig. 83. Mechanical response of unit cells of fixed size $L = 6\mu$m and four different values of the void size D, subjected to equibiaxial deformation: (a) in-plane mean normal stress $(\Sigma_{11} + \Sigma_{22})/2$ vs. volumetric strain E_v and (b) $f - f_0$ vs. E_v.

void diameters, one can see that for a given void size, the flow stresses are larger for the unit cells with the larger void spacing. Similarly, comparison of the void growth rates between Fig. 83(b) and Fig. 80(c) shows that, for a given void size, void growth rates are smaller for materials with the larger void spacing. It is clear from these results that the size effects in section 2 do not depend solely on the void size, but also on the spacing between the voids. In fact, the above trends are consistent with expectations based on continuum theories that void growth is faster in materials with a larger average porosity. For a given value of D, the material with a larger L has a lower porosity and therefore exhibits slower growth of porosity.

Another interesting test case involves alternate distributions of voids for a given void size and volume fraction, i.e. different values of $\lambda = L_2/L_1$ for given values of f and D. Under these conditions continuum theory predicts that, void growth is insensitive to the value of λ as long as the mode of plasticity in the matrix is diffuse and not localized between the voids. Fig. 84(a) and (b) show the stress–strain response

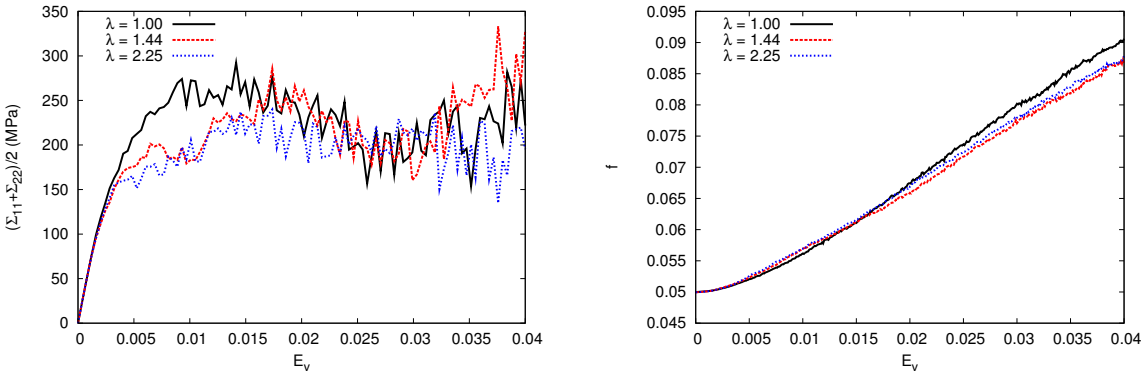

(a) (b)

Fig. 84. Mechanical response of unit cells with $f = 0.05$, $D = 1.51\mu$m and three different values of the unit cell aspect ratio λ, subjected to equibiaxial deformation: (a) in-plane mean normal stress $(\Sigma_{11} + \Sigma_{22})/2$ vs. volumetric strain E_v and (b) f vs. E_v.

and the evolution of f respectively for three unit cells with $f = 0.05$, $D = 1.01\mu$m and three values of λ corresponding to $\lambda = 1, 1.44$ and 2.25. The simulations show no influence of the cell aspect ratio on the effective material response, in line with the expectations based on continuum theory.

D. Conclusions

A formulation of discrete dislocation plasticity that accounts for strain hardening within a simplified two dimensional setting has been used to study the effect of void size on the mechanical response of porous single crystals. A modified boundary value problem framework that accounts for multiply connected domains is used and bulk response is simulated using periodic boundary conditions. Within the limitations of a small strain model, trends for the dependence of void growth rates on void size have also been discussed. The main conclusions from the study are listed below.

- In the absence of hardening in the matrix, no void size effects are observed for

the flow stress under pure shear (low triaxiality) loading conditions. However, a strong void size dependence of the flow stress is observed under biaxial (high triaxiality) loading with smaller voids leading to a harder effective response. The behavior under both types of loading are consistent with an explanation based on source limited plasticity around the voids.

- The use of hardening (2.5D) constitutive rules generally leads to higher flow stresses under both types of loadings considered. In addition, void size effects are observed under both low and high triaxiality loading.
- Void growth rates are found to be slower for smaller sized voids, consistent with findings from previous studies. In general, strain hardening in the matrix is seen to yield slower void growth rates compared to a non-hardening matrix.
- Practically, the slower growth rates for sub-micron sized voids evidenced in the discrete dislocation calculations implies that in a ductile specimen with a given population of voids, crack growth and fracture will be primarily influenced by the distriution of larger voids while the smaller voids have an insignificant influence.

CHAPTER VIII

DISLOCATION DYNAMICS AT HIGH TEMPERATURE

A. Introduction

The microscopic mechanisms of inelastic deformation in crystalline materials depends on several factors such as the temperature, strain rate and the applied stress levels. At low homologous temperatures, $T/T_{\mathrm{m}} \sim 0.1$ where T_{m} denotes the melting point, plastic deformation is essentially controlled by the glide of dislocations and their athermal interactions with other dislocations, precipitates, grain boundaries, etc. While temperature does play a role in some dislocation events at low temperature such as cross-slip and affects the macroscopic response under certain conditions, such as the stage III hardening of a single crystal, dislocations are confined to glide on their slip planes due to the low concentration of point defects at low temperatures. On the other hand at higher homologous temperatures, $T/T_{\mathrm{m}} > 0.4$, dislocations can bypass obstacles by climb normal to their slip planes aided by the diffusion of point defects into the dislocation cores. Dislocation climb is an important microscopic mechanism for creep and dynamic recovery phenomena and may control the rate of deformation under some circumstances [153, 154]. Typical metals at low temperature exhibit a rather well distinguished yield point for the resolved shear stress, τ, below which little or no dislocation glide occurs on a slip system. When loaded beyond this nominal yield point, plastic flow and dislocation multiplication lead to strain hardening until the flow stress equals the imposed stress so that further plastic flow is possible only by increasing the applied load. The strain hardening is correlated with the dislocation density through the well known empirical Taylor relationship. However, at higher temperatures, metals exhibit creep behavior at loads well below their

yield stress where sustained deformation occurs without an associated increase in the shear stress or the microstructural variables such as the dislocation density. Creep is a thermally activated mode of inelastic deformation whose rate depends on several competing microscopic deformation mechanisms. Part of the strain rate results from mass transport through the diffusive flow of vacancies through the crystal lattice from regions of low hydrostatic pressure to regions of higher pressure. This mode of deformation, known as Nabarro-Herring creep [155, 156], is dominant in single crystals or relatively large grain polycrystals at low stresses and high temperatures. Another mode of diffusional creep in polycrystals is due to the diffusion of vacancies through the grain boundaries. Due to the significantly higher mobility for the vacancies along the grain boundaries, this so called Coble creep [157] can dominate at lower temperatures when lattice diffusion is negligible. At higher values of the resolved shear stress, in the range $0.0001\mu - 0.001\mu$ where μ denotes the shear modulus of the material, dislocations play an important role in creep. Sessile dislocations can bypass obstacles by climbing out of their slip planes through absorption or emission of vacancies [158]. At high temperatures the concentration of vacancies in the bulk material is sufficient to aid dislocation climb while at lower temperatures the dislocation cores can act as conduits for rapid diffusion of vacancies.

It is clear from the above that creep is a complex deformation mode composed of several competing microscopic mechanisms. Phenomenological models of creep have been extensively used by material scientists to model the different regimes of inelastic deformation in polycrystals and the transition between them. Typical models of creep use a power law relationship between the shear strain rate, $\dot{\gamma}$, the resolved shear stress τ and the average grain size, $\bar{d}$, of the form

$$\dot{\gamma} \propto \tau^n \bar{d}^{-p} \tag{8.1}$$

where the values of the exponents n and p and the constant of proportionality are typically determined by a combinations of assumptions regarding the microscopic mechanisms and fitting to experimental data. All the different types of creep described previously can be modeled using the generic relationship (8.1) for different values of the exponents n and p. For example, the diffusional creep modes are generally described by a stress exponent $n = 1$ and grain size exponent $p = 2$ for Nabarro-Herring creep and $p = 3$ for Coble creep. On the other hand, dislocation creep is characterized by a wide range of stress exponents from $n = 3$ to $n = 10$. For a given material system, it is customary to graphically summarize the relationship between the temperature, stress and strain rates using maps of the type shown n Fig. 85 for polycrystalline Aluminum. Originally proposed by Ashby and Frost [153, 159], these maps are constructed by extensive tabulation of the experimental data and using rate equations of the form (8.1) to interpolate between them. The diagram plots the contours of constant strain rate on a graph with the homologous temperature along the abscissa and the logarithm of the shear stress (labeled σ_s in the figure) normalized by the material shear modulus along the ordinate. The graph is divided into regions where the different creep mechanisms predominate. The boundaries of the different regions are determined approximately as the locus of the points where the competing modes of creep yield equal strain rate according to the phenomenological rate equations of type (8.1). The reader is referred to the book by Frost and Ashby [153] for detailed methodology used in the construction of these maps and extensive data on a variety of metals and alloys.

While the microscopic mechanisms of plasticity and creep and the fundamental role played by defects such as dislocations, vacancies and grain boundaries have been appreciated by materials scientists for a long time, the computational tools required to simulate the collective behavior of such defects have only been made available re-

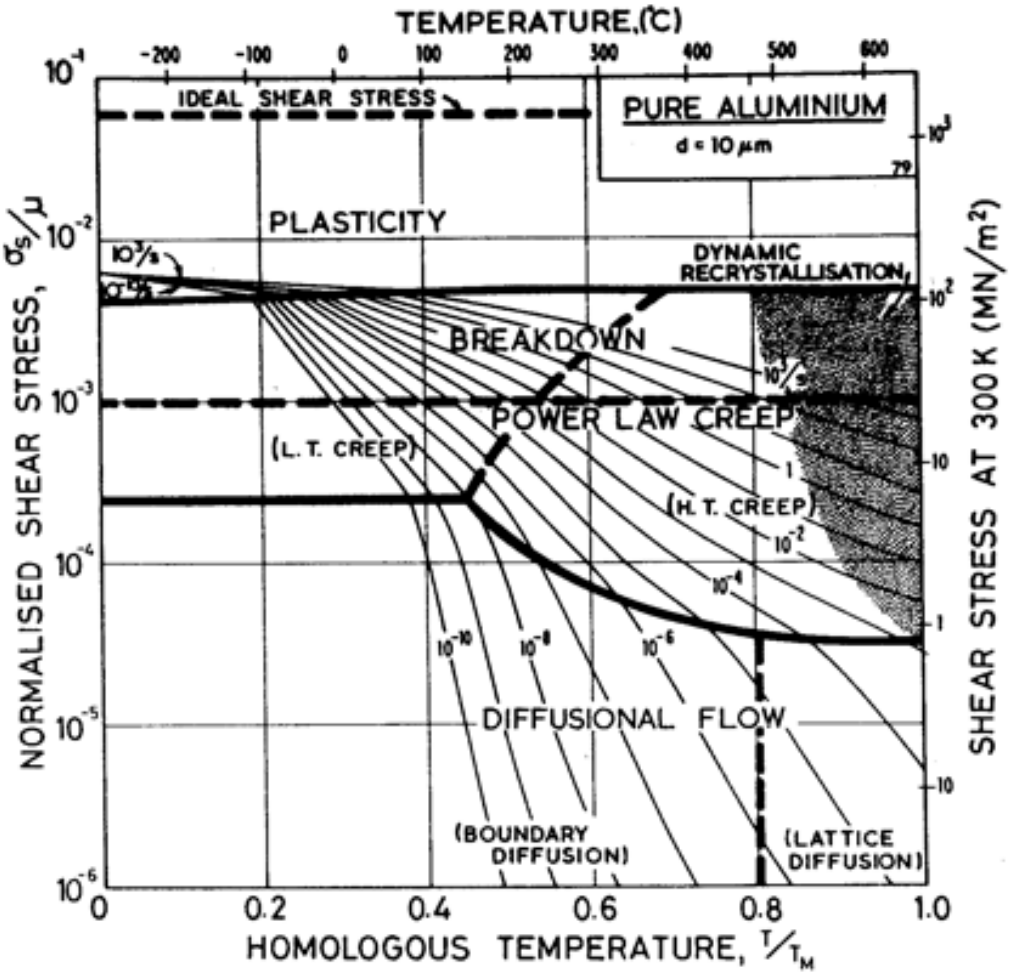

Fig. 85. Deformation mechanism map for polycrystalline Al adapted from [153].

cently, leading to reliance on phenomenological modeling approaches. While the latter have worked well for modeling creep in traditional polycrystalline metals and alloys, their applicability to small scale systems and newly developed ultra-fine grained and nanocrystalline materials remains unclear. In fact, recent experimental evidence indicates deviations from bulk behavior for the creep behavior of single crystals [160] and fine grained polycrystals [8]. Even in conventional polycrystals, while the phenomenological constitutive rule (8.1) applies, there is little fundamental understanding of the observed stress and grain size exponents [153]. There is a tremendous scope for bottom up modeling approaches such as molecular dynamics and DD to contribute towards understanding of high temperature behavior in small scale systems. Since the central role played by material defects such as dislocations and vacancies is well understood, a hybrid modeling approach such as DD using continuum mechanics to model bulk behavior while using discrete representation of the defects provides an effective and scalable bottom up modeling strategy. Since the DD approach has proved successful in understanding plasticity from a fundamental perspective, it is reasonable to expect that, with appropriate extensions to the physics, one can gain fundamental insight into material behavior at elevated temperatures.

One of the key ingredients required for mesoscopic simulation of creep and other thermally activated phenomena is a framework for modeling dislocation climb and diffusion. Currently, most of the DD studies neglect the climb motion of dislocations altogether since, at low homologous temperatures, the effect of climb on plasticity is negligible compared to dislocation glide. However, it is expected that at high homologous temperatures climb will have a significant effect due to increased mass transport through diffusion. Diffusion of vacancies and dislocation climb are coupled effects in the sense that climb is a non-conservative motion that leads to the emission or absorption of point defects and the diffusion of the latter under imposed pressure

and concentration gradients leads to an "osmotic" force on the dislocations normal to their slip planes. Thus DD at finite temperatures involves the concurrent solution of two coupled boundary value problems, one for the elastic fields in the deforming material and the other for the concentration of the point defects. The few previous DD studies that attempted to include the effects of dislocation climb have used a heuristic climb model similar to the viscous drag model typically used for dislocation glide. These include both three dimensional [161, 162] and two dimensional [97, 163] DD studies. In particular, these studies ignore the effects of vacancy diffusion on climb motion altogether. On the other hand, it is worth mentioning that at high temperatures and/or high vacancy supersaturations, dislocations may climb even in the absence of a Peach-Koehler force due to the effect of the osmotic force, which is not captured by the "glide-like" models. Recently Mordehai et al. [117] developed a 3D DD framework where the effect of the osmotic force is explicitly accounted for, using equilibrium solutions for the climb rate of dislocations due to vacancy diffusion into the dislocation core in a prescribed uniform vacancy field. This framework has been used to study the shrinkage/expansion of prismatic dislocation loops [117] and the annealing of dislocations [164] in a bulk material under conditions of vacancy supersaturation. Another recent work by Gao et al. [118] attempts to include the effect pipe diffusion of vacancies through the dislocation cores in a 3D DD simulation, using analytical estimates of the climb velocity that depend on the core diffusion parameters. However, such models have so far not been used in more complex simulations involving macroscopic gradients of the vacancy field as in a creep simulation, presumably due to the complexity inherent in full 3D DD simulations. In fact, discrete dislocation plasticity has so far not been used to predict creep rates of crystalline materials as a function of temperature to the best of our knowledge.

In the present work, we propose a simulation strategy for creep boundary value

problems by explicitly solving the dynamic equations of dislocation motion and vacancy diffusion in a simplified 2D setting. The 2D DD model of Van der Giessen and Needleman [25] is enhanced to account for the interactions of discrete dislocations with thermally generated vacancies, which is modeled using a continuum concentration field as in the work of [117]. However, unlike in the above work, the effect of free boundaries and specimen level gradients in the vacancy concentration field and their interactions with discrete dislocations are naturally accounted for in the formulation. The 2D approach, while restrictive in terms of the richness of the physical mechanisms that can be modeled, allows a greater variety of boundary value problems to be studied and greater strains and dislocation densities to be achieved in the simulations. The detailed formulation of the coupled boundary value problems of dislocation dynamics and vacancy diffusion are described in the following section. An example boundary value problem of creep in single crystalline tensile samples is solved and the results are discussed in subsequent sections.

B. Formulation of the Dislocation Climb Problem

As mentioned in the introduction, the 2D DD formulation of Van der Giessen and Needleman needs to be extended to include the physics of vacancy diffusion and dislocation climb at high temperatures. However, dislocation glide and climb are kinetic processes that occur over widely differing time scales. A quick calculation shows that dislocation glide velocities exceed the climb velocity by several orders of magnitude even at high homologous temperatures. Therefore, simulation of a slow process such as creep using DD presents a challenge in terms of resolving both the dislocation glide (time scales of the order of nanoseconds) and climb (time scales of the order of milliseconds or higher) events within realistic computation times. We

work around this issue by assuming that dislocation climb is the rate controlling event and adopting separate time steps for resolving the dislocation glide and climb events in the simulation. The above assumption is consistent with the model proposed by several researchers [104,154] where creep results from the thermally activated climb of dislocations from local equilibrium positions. Hence, we model the overall deformation as a sequence of glide and climb steps rather than as a continuous process occurring simultaneously. The glide steps are responsible for the rearrangement of dislocations between local equilibrium positions on their respective slip planes (stuck at obstacles, for instance) and consequently for most of the macroscopically observed strain. The climb process, occurring over a much longer time scale, sets the overall strain rate by determining the rate at which dislocations are able to bypass obstacles through thermally activated climb. In this framework, the glide steps are performed using the same procedure as in the Van der Giessen and Needleman model with minor changes to account for the effect of temperature on some of the constitutive rules described in Chapter V. The climb steps are computed using a coupled formulation involving vacancy diffusion and DD described below.

1. Governing Equations for Vacancy Diffusion

Consider an elastic body of volume V containing a set of discrete edge dislocations $1..N$ as shown in Fig. 86. The core region of a dislocation i is denoted C^i, $\tilde{C} = \bigcup^i C^i$ denotes the core regions of all the dislocations in the sample and $\hat{V} = V \setminus \tilde{C}$ denotes the volume of the body excluding the core regions of all the dislocations. The body is subjected to arbitrary tractions $\mathbf{t}^0$ on its boundary denoted ∂V. Let $\mathbf{x}$ denote the spatial position within the domain V, t denote the time and $c(\mathbf{x}, t)$ denote a continuous field of the fractional vacancy concentration in V, defined as the ratio of the number of vacancies to the number of lattice sites in an elementary volume. It is

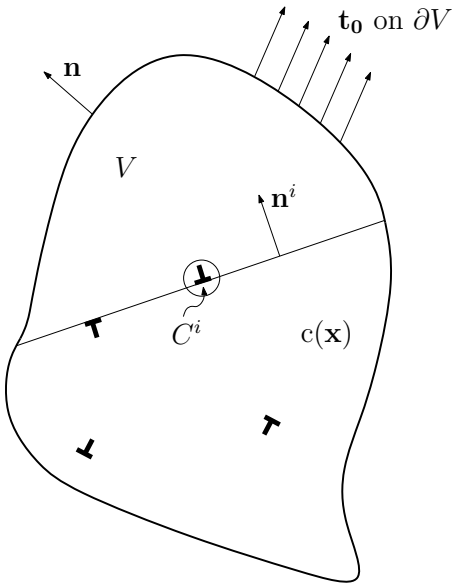

Fig. 86. Schematic sketch of an elastic body containing discrete dislocations and a concentration field $c(\mathbf{x})$ of vacancies subjected to tractions on the external boundary.

assumed that any vacancy that enters the core regions of a dislocation is immediately absorbed by the dislocation (no pipe diffusion) so that $c(\mathbf{x}, t) \equiv 0$ in $\tilde{C}$. The Gibbs free energy, G, of the body may be written as

$$G \equiv H - TS = G(c(\mathbf{x}, t), \mathbf{x}^i(t)) \tag{8.2}$$

where H, T and S denote the enthalpy, absolute temperature and entropy respectively and $\mathbf{x}^i(t)$ denotes the position of dislocation i ($i = 1..N$). The kinetic equations of vacancy diffusion and dislocation climb may be determined from the thermodynamic variational principle of Cocks et al. [165, 166], which states that the rate of evolution of the system is given by a stationary value of the functional

$$\mathit{\Pi} = \dot{G} + \Psi \tag{8.3}$$

where the overdot denotes the time rate of change and Ψ is a dissipation potential that contains the contribution from the kinetic processes in the system. The following derivation is a straightforward generalization of the analysis of Gao and Cocks [166] to the case of a system containing multiple dislocations.

The total Gibbs free energy of the body may be written as

$$G = \int_V g \, \mathrm{d}V - \int_{\partial V} (\mathbf{t}_0 \cdot \mathbf{n}) u_n \, \mathrm{d}S \tag{8.4}$$

where $g = g(c(\mathbf{x}, t), \mathbf{x}^i(t))$ denotes the Gibbs free energy density in V, $\mathbf{n}$ denotes the surface normal and the second term on the right-hand side represents the contribution to the total Gibbs free energy due to the work done by the surface tractions as a result of the displacement of the boundary normal to itself, u_n, by Nabarro-Herring creep. The Gibbs free energy density g is a function of the elastic and vacancy fields in V,

$$g = h - Ts \tag{8.5}$$

where h and s are the enthalpy and entropy per unit volume, given respectively by [167]

$$h = \frac{1}{2}\boldsymbol{\sigma} : \boldsymbol{\epsilon} + \left[\frac{E_f}{\Omega} - p\frac{\Omega_v}{\Omega}\right] c - \boldsymbol{\sigma} : \boldsymbol{\epsilon}, \qquad s = -\frac{k}{\Omega}\left[c \log c + (1-c)\log(1-c)\right] \tag{8.6}$$

In the above, $\boldsymbol{\sigma}$ and $\boldsymbol{\epsilon}$ denote the stress and strain fields in the body respectively, $p = -\mathrm{tr}(\boldsymbol{\sigma})/3$ denotes the hydrostatic pressure field, E_f denotes the formation energy of a single vacancy (energy required to break the atomic bonds), Ω denotes the atomic volume, Ω_v denotes the relaxation volume of a vacancy and k denotes the Boltzmann constant. The relaxation volume Ω_v is the local reduction in volume as a result of formation of a vacancy and is typically a fraction of the atomic volume, i.e. $0 < \Omega_v/\Omega < 1$. Within the core regions of the dislocations $\tilde{C}$, all the terms in g involving the vacancy concentration c vanish identically due to the assumption that $c \equiv 0$,

while the elastic strain energy term is singular due to the use of the singular elastic fields of the dislocations in the elastic solution (see chapter V, section B). Therefore, as proposed by Van der Giessen and Needleman [25], the core energies are calculated by use of the divergence theorem to convert the volume integrals over C^i to surface integrals over ∂C^i. Using (8.5) and (8.6) in (8.4), the total Gibbs free energy may be written in the form

$$G = G_1(\mathbf{x}^i(t)) + G_2(c(\mathbf{x},t), p(x^i(t))) \tag{8.7}$$

where G_1 denotes the contribution from the mechanical strain energy

$$G_1 = \int_{\hat{V}} \frac{1}{2}\boldsymbol{\sigma} : \boldsymbol{\epsilon} + \sum_{i=1}^{N} \int_{\partial C^i} \frac{1}{2}\mathbf{t}\cdot\mathbf{n}\ \mathrm{d}S - \int_{\partial V} \mathbf{t}_0 \cdot \mathbf{u}\ \mathrm{d}S \tag{8.8}$$

and G_2 denotes the contribution from the thermally generated vacancies

$$G_2 = \int_{\hat{V}} \left[\frac{E_f}{\Omega} - p\frac{\Omega_v}{\Omega}\right] c + \frac{kT}{\Omega}\left[c\log c + (1-c)\log(1-c)\right]\ \mathrm{d}V - \int_{\partial V} (\mathbf{t}_0\cdot\mathbf{n}) u_n\ \mathrm{d}S \tag{8.9}$$

Note that the second and third terms in (8.8) have been obtained using the divergence theorem. The rate of change of the Gibbs free energy $\dot{G}$ may be written as

$$\dot{G} = -\sum_{i=1}^{N} \mathbf{f}^i \cdot \mathbf{v}^i + \int_{\hat{V}} \left(\mu_v \dot{c} - \frac{\Omega_v}{\Omega} c\dot{p}\right)\ \mathrm{d}V + \int_{\partial V} (\mathbf{t}^0\cdot\mathbf{n})(\mathbf{J}\cdot\mathbf{n})\ \mathrm{d}S \tag{8.10}$$

where $\mathbf{f}^i$ denotes the Peach-Koehler configurational force on a dislocation i, $\mu_v \equiv \partial g/\partial c$ denotes the chemical potential of the vacancies and $\mathbf{J}$ denotes the volumetric flux of the vacancies. The expression for the Peach-Koehler force $\mathbf{f}^i$ in a system containing multiple dislocations has been derived by Van der Giessen and Needleman [25] (see chapter V, section B), which reads

$$\mathbf{f}^i = -\frac{\partial G_1}{\partial \mathbf{x}^i} = \mathbf{t}^i \times \left[\left(\hat{\boldsymbol{\sigma}} + \sum_{j\neq i} \boldsymbol{\sigma}^j\right)\cdot \mathbf{b}^i\right] \tag{8.11}$$

where $\mathbf{t}^i$ is a unit vector along the tangent to the dislocation line and $\mathbf{b}^i$ is the Burgers

vector. The chemical potential for the vacancies μ_v is given by

$$\mu_v = \frac{\partial g}{\partial c} = \frac{kT}{\Omega}\left[\frac{E_f}{kT} - \frac{p\Omega_v}{kT} + \log\frac{c}{(1-c)}\right] \tag{8.12}$$

Ignoring the elastic fields of the vacancies themselves, the pressure field is a function of the position of the dislocations, i.e. $p = p(x^i(t))$, so that one may write

$$\dot{p} = \sum_{i=1}^{N} \frac{\partial p}{\partial \mathbf{x}^i} \cdot \mathbf{v}^i \tag{8.13}$$

Substituting (8.13) in (8.10) yields

$$\dot{G} = \int_{\hat{V}} \mu_v \dot{c}\ \mathrm{d}V + \int_{\partial V} (\mathbf{t}^0 \cdot \mathbf{n})(\mathbf{J}\cdot\mathbf{n})\ \mathrm{d}S - \sum_{i=1}^{N} (\mathbf{f}_d^i + \mathbf{f}^i)\cdot\mathbf{v}^i, \quad \mathbf{f}_d^i \equiv \int_{\hat{V}} c\frac{\Omega_v}{\Omega}\frac{\partial p}{\partial \mathbf{x}^i}\ \mathrm{d}V \tag{8.14}$$

where $\mathbf{f}_d^i$ is a drag force arising from the interaction of the moving dislocations with the vacancy field. This drag force originates due to the fact that the chemical potential of the vacancies depends on the pressure field $p(\mathbf{x}^i)$ so that changes in p due to the motion of the dislocations gives rise to a thermodynamic force on the dislocations.

From the principle of conservation of mass, $\mathbf{J}$ and $\dot{c}$ are related by the continuity equation.

$$\dot{c} = -\nabla \cdot \mathbf{J} \qquad \text{in } \hat{V} \tag{8.15}$$

Further, from our assumption that dislocation motion is restricted to pure climb during the climb time steps, we have $\mathbf{v}^i = v_c^i \mathbf{n}^i$, where $\mathbf{n}^i$ denotes the normal to the slip plane of dislocation i. In such case, conservation of mass can also be invoked to relate the dislocation climb velocity v_c^i to the flux of vacancies into or away from the dislocation core, since climb is a non-conservative motion that must be accompanied by the production/absorption of vacancies at the dislocation core. We obtain the

climb velocity from the mass conservation condition as

$$v_c^i = \frac{1}{b^i} \int_{\partial C^i} \mathbf{J} \cdot \mathbf{n} \, \mathrm{d}S \tag{8.16}$$

where b^i is the magnitude of the Burgers vector for dislocation i and the unit normal $\mathbf{n}$ points into the dislocation core. Note that the above integral must be independent of the size of the dislocation core C^i by the continuity condition since dislocations are the only sources or sinks of vacancies in the body. Substituting (8.15) and (8.16) in (8.14) and using the divergence theorem, we get

$$\dot{G} = \int_{\hat{V}} \nabla\mu_v \cdot \mathbf{J} \, \mathrm{d}V - \int_{\partial V} \mu_v \mathbf{J} \cdot \mathbf{n} \, \mathrm{d}S + \int_{\partial V} (\mathbf{t}^0 \cdot \mathbf{n})(\mathbf{J} \cdot \mathbf{n}) \, \mathrm{d}S - \sum_{i=1}^{N} \frac{1}{b^i} (f_o^i + f_{dc}^i + f_c^i) \int_{\partial C^i} \mathbf{J} \cdot \mathbf{n} \, \mathrm{d}S \tag{8.17}$$

where f_{dc}^i denotes the climb component of the drag force $\mathbf{f}_d^i$ and $f_o^i = \mu_v b^i$ is the so called osmotic force in the climb direction. During the climb time steps, we assume that energy dissipation in the system is entirely due to the diffusive flux of the vacancies, for which a quadratic form for the dissipation potential Ψ is assumed following [166].

$$\Psi = \frac{1}{2} \int_{\hat{V}} \frac{1}{\bar{D}} \mathbf{J} \cdot \mathbf{J} \, \mathrm{d}V \tag{8.18}$$

where the constant $\bar{D}$ is related to the diffusivity of the material. Using (8.17) and (8.18) in (8.3) and taking the first variation with respect to the vacancy flux yields

$$\delta\Pi = \int_{\hat{V}} \left(\nabla\mu_v + \frac{\mathbf{J}}{\bar{D}} \right) \cdot \delta\mathbf{J} \, \mathrm{d}V + \int_{\partial V} (\mathbf{t}^0 \cdot \mathbf{n} - \mu_v)(\delta\mathbf{J} \cdot \mathbf{n}) \, \mathrm{d}S - \sum_{i=1}^{N} \frac{1}{b^i} (f_o^i + f_{dc}^i + f_c^i) \int_{\partial C^i} \delta\mathbf{J} \cdot \mathbf{n} \, \mathrm{d}S \tag{8.19}$$

From (8.19), one can write the local form of the governing equations for vacancy

diffusion as

$$\mathbf{J} = -\bar{D}\nabla\mu_v \qquad \text{in } \hat{V} \tag{8.20}$$

$$\mu_v = \mathbf{t}^0 \cdot \mathbf{n} \qquad \text{on } \partial V \tag{8.21}$$

$$\mu_v = -\frac{1}{b^i}(f^i_{dc} + f^i_c) \qquad \text{on } \partial C^i \tag{8.22}$$

Equation (8.20) is the constitutive law for vacancy diffusion, which reduces to the Fick equation in the absence of pressure gradients, i.e.

$$\mathbf{J} = -D\nabla c \tag{8.23}$$

where D is the vacancy diffusion coefficient. Using (8.12) in (8.20) assuming $\nabla p = \mathbf{0}$ and comparing with (8.23) we obtain

$$\bar{D} = \frac{D\Omega}{kT}c(1-c) \tag{8.24}$$

The diffusion coefficient D in solids depends strongly on the temperature and weakly on the pressure. Here we neglect the pressure dependence of D, so that a constant value of D, independent of the dislocation positions, is used throughout the specimen. An Arrhenius type equation is used to express the temperature dependence of D

$$D = D_0 \exp\left(-\frac{E_m}{kT}\right) \tag{8.25}$$

where E_m is the vacancy migration energy and the pre-exponential term D_0 is the asymptotic value of the vacancy diffusion coefficient at very high temperatures [104].

At each increment, we solve for the vacancy field using the continuity equation (8.15) and equation (8.20) to relate the vacancy flux to the gradients of c and p and subject to the boundary conditions (8.21) and (8.22). Note that the pressure field p and the Peach-Koehler forces f^i_c are known from the solution of the elastic boundary

value problem. Finally, the vacancy flux $\mathbf{J}$ on ∂C^i is coupled to the climb velocity v_c^i via equation (8.16), which is used to update the dislocation positions and the simulation proceeds in an iterative manner.

2. Climb Velocity of an Edge Dislocation

Using the simulation framework in the previous section for a large scale DD simulation presents a major difficulty due to the fact that one would need to resolve the cores of the dislocations (O($\sim$ 1 nm)) in the numerical discretization. Moreover, since the dislocations themselves are mobile, one would need to adaptively re-mesh the domain so as to track the moving core regions. In order to resolve this difficulty, we assume a separation of scales where the macroscopic gradients in the vacancy fields have a characteristic length scale that is at least an order of magnitude larger than the radius of the dislocation cores. This allows us to tackle the vacancy diffusion problem using a relatively coarse mesh (O($\sim$ 100 nm)). Further, the dislocation climb velocities are determined analytically using equation (8.16) and several simplifying assumptions regarding the vacancy flux in the neighborhood of a dislocation core, as described below.

Consider an isolated edge dislocation in a remote vacancy concentration field c_∞ as shown in Fig. 87. For the purpose of the analytical solution, we assume that a constant $c = c_\infty$ is imposed at each point on the circumference of a cylinder of radius r_∞, assumed to be much larger than the dislocation core radius, r_d ($r_\infty \gg r_d$). On the inner cylinder ($r = r_d$), we assume that vacancies are in thermomechanical equilibrium with the dislocation, in which case the concentration is given by [104]

$$c_d = c_0 \exp\left(-\frac{f_c \Omega}{bkT}\right), \qquad c_0 = \exp\left(-\frac{E_f}{kT}\right) \tag{8.26}$$

where c_0 is the equilibrium vacancy concentration at temperature T and b is the

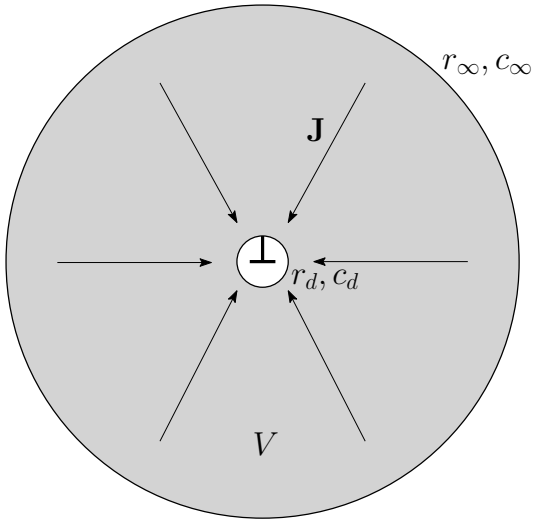

Fig. 87. Diagram illustrating the simplifying assumptions used in the analytical solution for the dislocation climb velocity.

modulus of the Burgers vector. The climb velocity of the dislocation can be obtained by calculating the flux of vacancies into the dislocation core by solving the diffusion boundary value problem for the domain of Fig. 87. Mordehai et al. [117] have obtained an analytical estimate of the climb velocity using the simplifying assumptions of (i) steady state conditions (no time dependence) and (ii) radial symmetry of the vacancy flux (no angular dependence). In this case, the continuity equation reduces to

$$\nabla^2 c = \frac{1}{r}\frac{\mathrm{d}}{\mathrm{d}r} r \frac{\mathrm{d}c(r)}{\mathrm{d}r} = 0 \tag{8.27}$$

The analytical solution of (8.27) subject to given values of c on the inner and outer boundaries may be obtained in a straightforward way to yield

$$c(r) - c_\infty = \frac{(c_\infty - c_d)}{\log\left(r_\infty / r_d\right)} \log\left(\frac{r}{r_\infty}\right) \tag{8.28}$$

Calculating the flux $\mathbf{J} = -D\nabla c$ from (8.28) and using equation (8.16), we obtain the

dislocation climb velocity as (see [117])

$$v_c^i = -\frac{2\pi}{\log\left(r_\infty/r_d\right)}\frac{D}{b}(c_d - c_\infty) \tag{8.29}$$

Notice that the dislocation climb velocity vanishes when $c_d = c_\infty$, i.e. the remote vacancy concentration field is equal to the equilibrium vacancy concentration around the dislocation core c_d. Using equation (8.26) for c_d and rearranging, we obtain

$$-f_c = \frac{bkT}{\Omega}\log\left(\frac{c_\infty}{c_0}\right) \approx b\mu_v = f_o \tag{8.30}$$

where the term involving the relaxation volume Ω_v and second and higher order terms in c in the expression for the chemical potential (8.12) are neglected. Thus, the stationary condition for the climb velocity corresponds to the balance of thermodynamic forces on the dislocation.

In our simulation framework, equation (8.29) is used to compute the dislocation climb velocity at each increment. The remote concentration c_∞ is estimated by interpolating the c field obtained from the solution of the global diffusion boundary value problem to the position of each dislocation. While the length parameter r_∞ may be physically interpreted as the average spacing between the dislocations, we assume a constant value of $r_\infty = 100r_d$ for simplicity. However, note that the v_c is not very sensitive to the choice of r_∞ due to the term appearing in the logarithm. Further, the production/consumption of vacancies due to dislocation climb is accounted for by adding a source/sink term to the mass conservation equations. Consequently, the governing equations for the global boundary value problem (8.15) and (8.20)–(8.22)

are amended as

$$\dot{c} = -\nabla \cdot \mathbf{J} + \dot{c}_{\text{src}} \qquad \text{in } V \tag{8.31}$$

$$\mathbf{J} = -\bar{D}\nabla\mu_v \qquad \text{in } V \tag{8.32}$$

$$\mu_v = \mathbf{t}^0 \cdot \mathbf{n} \qquad \text{on } \partial V \tag{8.33}$$

A positive climb step of a dislocation requires the absorption of a single vacancy into the dislocation core while a negative climb step requires the emission of a single vacancy. Consequently, the source/sink term, $\dot{c}_{\text{src}}$, is estimated from the net climb velocity of all the dislocations in an elementary volume $\mathrm{d}V$ such that

$$\dot{c}_{\text{src}}\ \mathrm{d}V = -(\sum_i v_c^i)b^2 \tag{8.34}$$

where the algebraic sum of the dislocation climb velocities is calculated over all dislocations in the elementary volume $\mathrm{d}V$.

3. Constitutive Rules for Dislocation Glide

As mentioned previously, the formulation of the dislocation glide problem is essentially unchanged from the original framework of Van der Giessen and Needleman described in Chapter V. However, some of the constitutive rules therein needs enhancement to account for the effect of temperature on the constitutive parameters. First, the elastic modulii of materials vary as a function of temperature with the stiffness usually reducing with increasing temperature. Within the isotropic elasticity approximation, this is accounted for by assuming that the shear modulus μ is a material dependent function of temperature, i.e. $\mu = \mu(T)$. Next, the phonon drag factor B_g relating the glide component of the Peach-Koehler force to the dislocation velocity for mobile dislocations, equation (5.9), is also a function of the temperature with the drag usually

increasing linearly with the temperature. A theoretical estimate of the drag factor from [104] gives

$$B_g = \frac{3kT}{b^2 c_s} \tag{8.35}$$

where c_s is the speed of shear waves in the material. In the simulations, we use a linear scaling for the drag factor of the form $B_g(T) = B_g^0 T/T_0$ where B_g^0 is an experimentally determined value of the drag factor at a reference temperature, T_0. Finally, the physics of short range interactions between the dislocations and obstacles needs to be updated to account for the thermally activated bypass of obstacles. This mechanism is precluded in the original low temperature formulation, where a dislocation pinned at an obstacle can only be released if the Peach-Koehler force on the dislocation exceeds $\tau_{\text{obs}} b$, where τ_{obs} is an athermal strength parameter for the obstacle. However, in the high temperature formulation we allow for the possibility of dislocations to bypass obstacles by thermal activation at sub-critical values of the Peach-Koehler force using a probabilistic formulation proposed by Frost and Ashby [153] in the context of determining the drift velocity of a dislocation in a regular array of obstacles. Based on their analysis, at the end of each glide increment we allow for a dislocation to bypass an obstacle with a probability given by

$$p_{\text{act}} = \exp\left[-\frac{\Delta F}{kT}\left(1 - \frac{|f_g|}{\tau_{\text{obs}} b}\right)\right] \tag{8.36}$$

where f_g is the glide component of the Peach-Koehler force on the pinned dislocation and ΔF is the activation energy required to overcome the obstacle. Values for the latter are expected to range from $0.2\mu b^3 - 2\mu b^3$ for weak to strong obstacles. In our simulations, we use a value of $\Delta F = \mu b^3$ for the activation barrier. Apart from the modifications proposed above, the remaining constitutive rules for short range dislocation interactions are unchanged from that of Chapter V.

C. Numerical Implementation and Validation

At every time step, we need to obtain solutions for the elastic fields and the vacancy concentration fields in the sample. The former are obtained from the solution of a time independent linear elastic boundary value problem using the governing equations (5.3) and the boundary conditions (5.5) from Chapter V. The dislocation fields ($\tilde{}$ fields) in the superposition solution are obtained from the current positions of the dislocations at the end of each increment. On the other hand, the solution for the vacancy concentration field is obtained by solving a time dependent initial/boundary value problem subjected to the governing equations (8.31) and (8.32) subjected to the boundary conditions (8.33). The solutions to both problems are obtained using the finite element method. The finite element implementation of the linear elasticity problem is unchanged from that in [25] and will not be repeated here. This section contains a brief summary of the finite element formulation for the vacancy diffusion problem. We note that both the solutions to the elasticity and diffusion problems are obtained using the same finite element grid consisting of bilinear quadrilateral elements with four integration points.

Combining the two equations (8.31) and (8.32) for vacancy diffusion and using equation (8.12) for the chemical potential, we may write

$$\dot{c} = D\nabla^2 c - \frac{D\Omega_v}{kT}\nabla \cdot [c(1-c)\nabla p] + \dot{c}_{\text{src}} \tag{8.37}$$

which is non-linear in c due to the presence of the term $c(1-c)$. However, since typically $c \ll 1$, we may neglect the c^2 term and write

$$\dot{c} = D\nabla^2 c - \frac{D\Omega_v}{kT}\nabla \cdot c\nabla p + \dot{c}_{\text{src}} \qquad \text{in } V \tag{8.38}$$

The solution to (8.38) is obtained subject to Dirichlet boundary condition for c, which

may be obtained from (8.33) combined with (8.12) to write

$$c = c_0 \exp\left(\frac{\mathbf{t}^0 \cdot \mathbf{n}\Omega}{kT}\right) \qquad \text{on } \partial V \tag{8.39}$$

where c_0 is the equilibrium vacancy concentration defined in (8.26) and $\mathbf{t}^0$ and $\mathbf{n}$ are the traction and unit normal vectors at the boundary respectively. The weak form for equations (8.38) and (8.39) may be written as

$$\int_V v\dot{c}\ \mathrm{d}V = -D\int_V \nabla v \cdot \nabla c\ \mathrm{d}V + \frac{D\Omega_v}{kT}\int_V c\nabla v \cdot \nabla p\ \mathrm{d}V + \int_V v\dot{c}_{\mathrm{src}}\ \mathrm{d}V \tag{8.40}$$

where $v \in \mathcal{V}$ is an arbitrary test function belonging to the function space

$$\mathcal{V} = \{w : V \to \mathbb{R}, \qquad w = 0 \ \text{ on } \partial V\} \tag{8.41}$$

In each finite element V_e, the solution to (8.40) is written in the form $c = c_i(t)\psi_i^e(\mathbf{x})$, where summation over the repeated index $i(i = 1..4)$ is assumed, $c_i(t)$ denotes the time dependent value of the vacancy concentration at the nodes and $\psi_i^e(\mathbf{x})$ are the shape functions for element e. Using the usual procedure to evaluate and assemble the global equations, we obtain the discrete system of implicit ordinary differential equations

$$[C](\{\dot{c}\} - \{\dot{c}_{\mathrm{src}}\}) = [K]\{c\} \tag{8.42}$$

where $[C]$ and $[K]$ denote the damping and stiffness matrices respectively, $\{c\}$ denotes the vector of nodal values for c and the vector $\{c_{\mathrm{src}}\}$ denotes the contribution from non-conservative processes to the change in concentration at the nodes. The latter is a known quantity which is estimated approximately from the total climb velocity of the dislocations within each element, which is extrapolated to the nodes. Also note that the stiffness matrix contains a non-symmetric component due to the contribution from the pressure gradient within the domain, given by the second term on the right

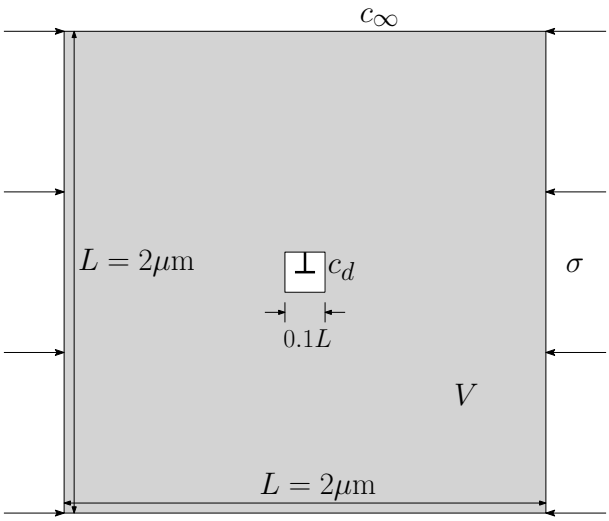

Fig. 88. Schematic of the steady state diffusion problem for the climb velocity of an edge dislocation in an imposed vacancy field.

hand side of equation (8.40). This part of the stiffness matrix is recalculated at the beginning of each climb increment from the known pressure gradient field from the solution of the elasticity problem. The set of ODEs (8.42) are integrated in time using the implicit sparse ODE solver DLSODIS from the open source ODEPACK software [168], which is capable of integrating both stiff and non-stiff systems of ODEs.

The finite element implementation of the diffusion problem is validated by comparing the numerical solutions with known analytical solutions for special cases of both steady and non-steady diffusion. As a first test case, we look at the same problem of steady state dislocation climb as in Section 2 (subsection 2) using the finite element method. Consider a square block of material of side L and at temperature T containing a single edge dislocation at the center as shown in Fig. 88. The block is subjected to plane strain compressive stress σ, as shown in figure, so that the climb component of the Peach-Koehler force on the dislocation $f_c = \sigma b$. The domain is discretized using square finite elements such that the dislocation lies at the center of

the central element. In order to obtain a close correspondence with the conditions of the analytical solution (see Fig. 87), we impose a uniform vacancy concentration field $c = c_\infty$ at the external boundary, $\max(|\text{x1}|, |\text{x2}|) = \text{L}/2$, and the concentration of vacancies in thermodynamic equilibrium with the dislocation c_d, given by equation $(8.26)_1$, at an internal boundary defined by $\max(|\text{x1}|, |\text{x2}|) = \text{L}/20$, as illustrated in Fig. 88. The steady state vacancy diffusion equation $\nabla^2 c = 0$ is solved in the shaded domain of Fig. 88 using the above mentioned Dirichlet conditions on the two boundaries. The dislocation climb velocity is estimated from the mass conservation condition of equation (8.16), by numerically evaluating the integral on the right hand side for the flux of vacancies into the dislocation core via the inner boundary. Note that the boundary conditions of the numerical solution in Fig. 88 differs from that of the analytical solution in Fig. 87 (equation (8.29)) due to the different geometries considered. Nevertheless, one may expect that the functional dependence of the climb velocity on the stress σ, temperature T and the imposed remote vacancy field c_∞ will be similar between the two solutions, with any differences appearing through the 'geometry factor', $2\pi/\log(r_\infty/r_d)$, in equation (8.29).

Fig. 89(b) shows the contours of the vacancy field c obtained from the finite element solution with the corresponding mesh shown in Fig. 89(a). One can see that far from the two boundaries the solution for c exhibits an approximately radial symmetry as assumed in the analytical solution. Fig. 90(a)–(c) plots the analytical and finite element solutions for the climb velocity, v_c, as a function of the stress σ for at three different temperatures, $T = 300, 400$ and 500 K and three different remote vacancy concentrations corresponding to equilibrium ($c_\infty = c_0$), vacancy supersaturation ($c_\infty = 1.2c_0$) and vacancy subsaturation ($c_\infty = 0.8c_0$). Note that a logarithmic scale is used for the ordinate since the climb velocity depends exponentially on the stress and temperature. Also note that the absolute value of the climb velocity is

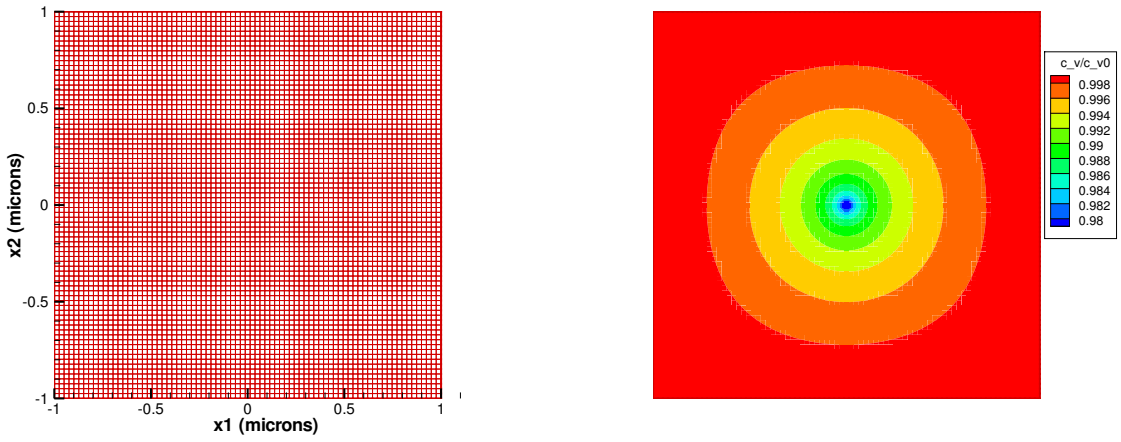

(a) (b)

Fig. 89. (a) Finite element discretization of the domain of Fig. 88 and (b) contours of the vacancy field c from the finite element solution normalized by the equilibrium concentration c_0.

plotted in Fig. 90(c) due to the fact that the climb velocity can become negative at sufficiently low values of the remote vacancy concentration due to the outward diffusive flow of vacancies. The results show a fixed offset between the two sets of curves corresponding to the analytical and FEM solutions indicating that the two velocities differ by a constant numerical factor, which is more clearly exhibited in Fig. 90(d) where we plot the ratio of the two velocity estimates. Recall that in the actual DD simulations, we proposed to use equation (8.29) to estimate the climb velocity of the dislocations at each time step in order to avoid having to resolve the dislocation cores in the simulations. In effect, the results in Fig. 90 serve as a validation test case for our finite element implementation and a justification for the use of equation (8.29) for the climb simulations.

Another test case considered for the solution of the unsteady diffusion problem of equation (8.38) is the case of a semi-infinite block of material that is subjected to a

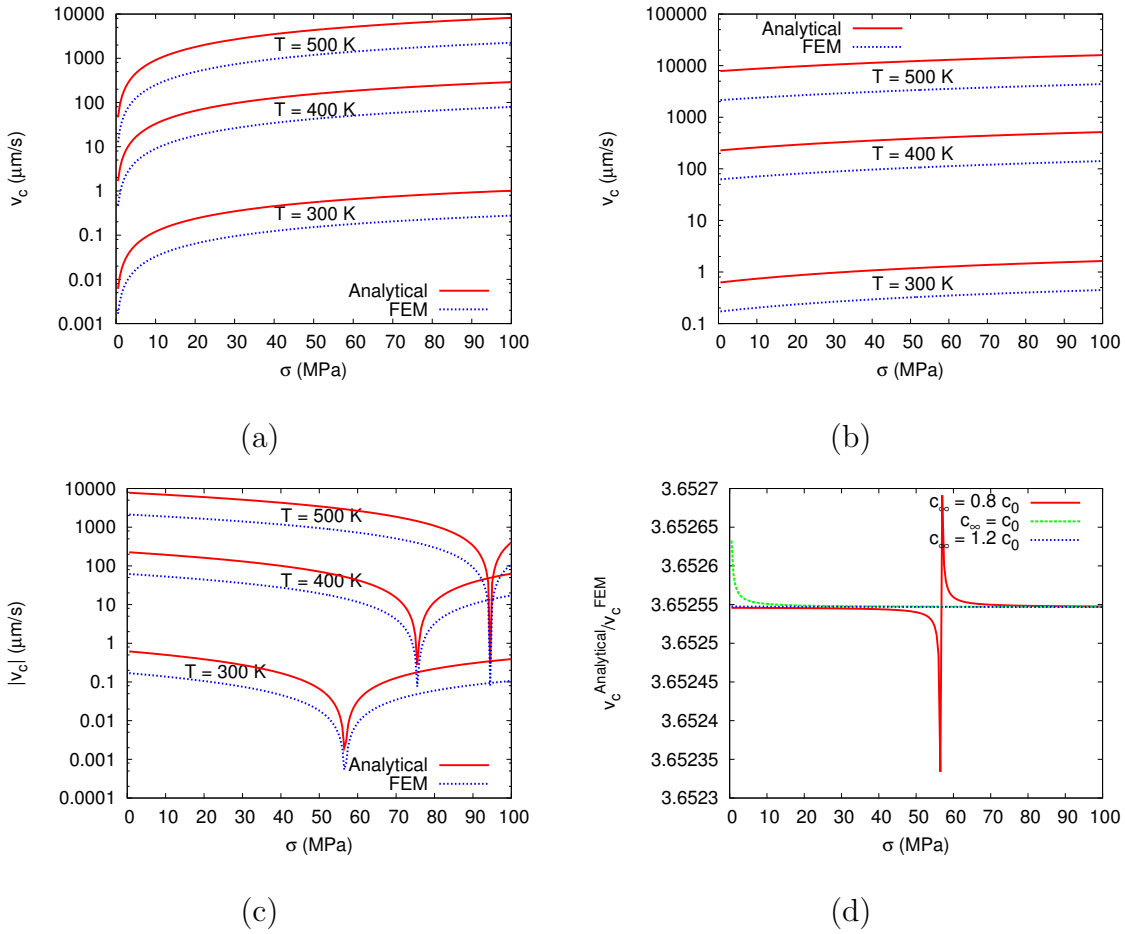

Fig. 90. Comparison of the dislocation climb velocity from the analytical and FEM solutions for cases of (a) remote vacancy equilibrium ($c_\infty = c_0$) (b) vacancy supersaturation ($c_\infty = 1.2c_0$) and (c) vacancy subsaturation ($c_\infty = 0.8c_0$). (d) Ratio of the two climb velocity estimates for the three cases in (a)–(c) at $T = 300$ K.

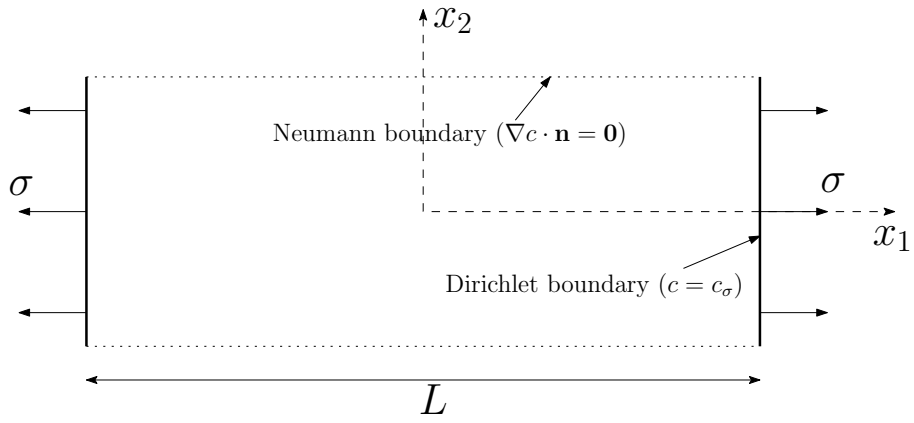

Fig. 91. Schematic of a test problem for one dimensional time dependent vacancy diffusion.

suddenly applied tractions, σ, at $t = 0$ at the two ends as illustrated in Fig. 91. The initial condition for c corresponds to $c = c_0$ (thermal equilibrium) everywhere except at the two ends where the initial values of c, denoted c_σ, is given by equation (8.39) with $\mathbf{t}^0 \cdot \mathbf{n} = \sigma$. This is a one-dimensional problem of transient vacancy diffusion governed by equation (8.38), where the last two terms vanish identically due to the absence of pressure gradients and dislocations in the sample. An analytical solution to (8.38) may be obtained in the form of an infinite series as

$$c(x_1, t) = c_\sigma + \frac{4c_\sigma}{\pi} \sum_{n=1}^{\infty} \frac{(-1)^n}{n} \sin \frac{n\pi}{2} \cos \frac{n\pi x_1}{L} \exp\left(-\frac{Dn^2\pi^2 t}{L^2}\right) \tag{8.43}$$

Fig. 92 compares equation (8.43) with the FEM solution for the vacancy field at different instants of time and at different locations along the x_1 axis. Typical values of the diffusion coefficient D and atomic volume Ω for Aluminum are used in computing the solutions and the temperature is assumed to be $T = 600$ K ($\sim 2/3T_{\mathrm{m}}$). The results of Fig. 92 indicate excellent agreement between the two solutions.

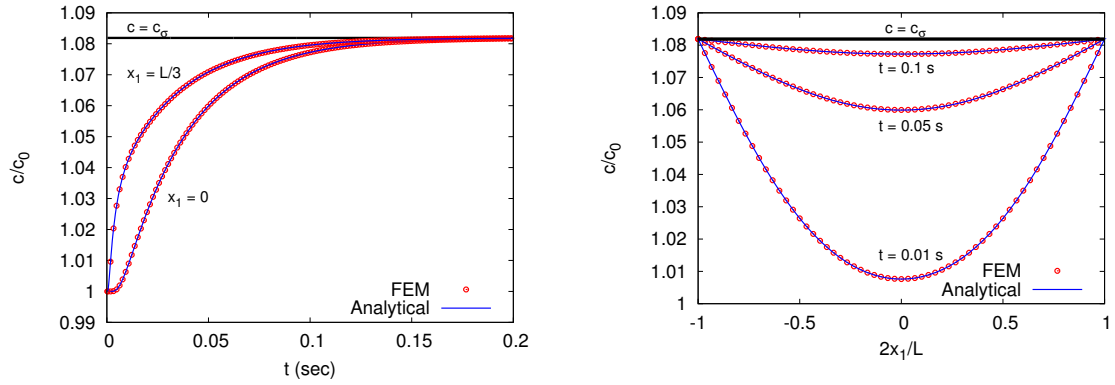

(a) (b)

Fig. 92. Comparison of the FEM solution for the transient diffusion problem of Fig. 91 with the analytical solution (8.43): (a) evolution of c as a function of time at two different locations along x_1 and (b) profile of c along x_1 at different instants of time.

D. Creep of Aluminum Single Crystals

As mentioned in the introduction, the primary motivation for development of the coupled DD and vacancy diffusion framework is the study of material properties at high temperatures using a bottom up modeling paradigm as opposed to the empirical approach that is followed currently. Moreover, a discrete description of the defects allows us to probe material properties at small scales where experimental results are scarce. As a first step towards this goal, we present in this section a simulation framework for creep in single crystals at elevated temperatures subjected to plane strain loading. Fig. 93 shows a sketch of a typical creep curve under uniaxial loading in a polycrystalline specimen. For an imposed creep stress σ at time $t = 0$, the evolution of the strain ϵ with time shows three distinct stages as illustrated in Fig. 93. The initial offset strain ϵ_0 is the instantaneous elastic strain due to the imposed stress. Stage I denotes the transient region where the creep strain rate $\dot{\epsilon}$ decreases with time due to strain hardening. The dominant part of the creep curve is the steady

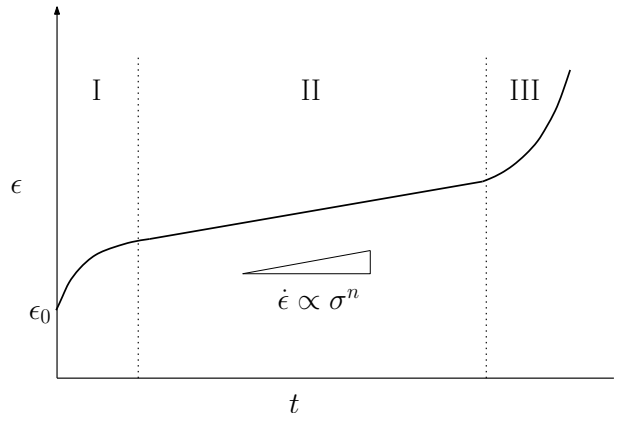

Fig. 93. Sketch of a typical creep curve for a polycrystalline specimen.

state stage II creep where the strain rate remains approximately constant with time as the result of a dynamic balance between strain hardening and thermal recovery processes. The final stage of accelerated deformation is due to damage processes such as cavitation and/or strain localization. The reported strain rates in the literature (eg. Fig. 85) are usually the steady state stage II creep rates which typically follow a power law of the form $\dot{\epsilon} \propto \sigma^n$. Values of the power law exponent from experiments on bulk polycrystals fall in the range 3–8 [153].

1. Problem Formulation

Using the coupled vacancy diffusion and DD formulation, we examine the creep behavior of a plane strain single crystalline specimens of the type sketched in Fig. 94. The sample is loaded in plane strain tension along the x_1 direction using uniformly distributed tractions σ on the two end faces while the lateral boundaries of the specimen are traction free. A symmetric double slip arrangement is assumed with the two slip systems oriented at $\pm 35.25^\circ$ with respect to the tensile direction. The arrangement considered may correspond to an FCC single crystal oriented such that the plane of analysis coincides with the (110) crystallographic plane and loaded along

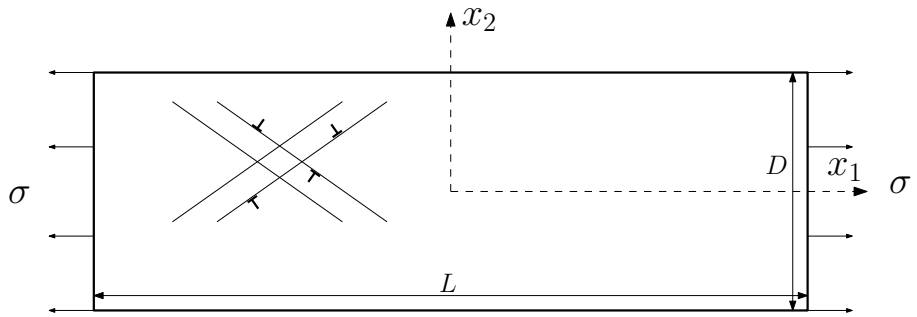

Fig. 94. Schematic sketch of the plane strain tension specimen used in the creep computations.

the $\langle 001 \rangle$ direction. The two slip systems considered correspond to the $\langle \bar{1}12 \rangle$ and $\langle 1\bar{1}2 \rangle$ slip directions with an included angle of approximately 109.5°. Rectangular specimens are considered with an aspect ratio $L/D = 3$ and sizes of the order of several microns. Initially, the crystal contains a distribution of dislocations and point sources with an average density of $150\mu\text{m}^{-2}$ and point obstacles with a density of $600\mu\text{m}^{-2}$. These are distributed at random on the two slip systems considered, with the slip planes distributed with a uniform spacing of $20b$. The random initial dislocation structure is assigned in such a way that the net Burgers vector in the specimen vanishes. The point sources represent Frank-Read sources whose nucleation strengths follow a normal distribution with an average resolved shear strength for dislocation nucleation, τ_{nuc}, and a standard deviation, τ_{sd}. The vacancy concentration field $c(\mathbf{x})$ is initialized such that it corresponds to the equilibrium (steady state) vacancy field in the sample of Fig. 94 subjected to the tensile tractions σ at $x_1 = \pm L/2$ and traction free conditions at $x_2 = \pm D/2$.

The dislocations in the sample can glide on their respective slip planes in accordance with the Peach-Koehler force and the associated glide mobility law described in section 3. The dislocations can also climb to a neighboring slip plane according to the climb mobility law established in section 2, equation (8.29). Thus, unlike the

glide process, dislocations climb between the slip planes in discrete steps set by the slip plane spacing. The climb distances of each dislocation, determined according to (8.29), are tracked at each time step. When the climb distance of a dislocation exceeds the slip plane spacing, the dislocation is moved from its original slip plane to the new slip plane. The production/consumption of vacancies as a result of the climb motion are used to calculate the vacancy source/sink term c_{src} that enters in the governing equation (8.38) for the evolution of the vacancy field. A positive climb step equal to the slip plane spacing of d_{slp} required the absorption of N_v vacancies into the dislocation core given by

$$N_v = \frac{d_{\text{slp}} b^2}{\Omega} \tag{8.44}$$

Negative climb, on the other hand, requires the nucleation of the same number of vacancies with the associates atoms being absorbed into the dislocation core. Thus, negative climb of a dislocation occurs only when the local stresses are high enough to nucleate vacancies according to the energy criterion [169]

$$\sigma^i b^3 = E_f \tag{8.45}$$

where σ^i is the normal stress along the Burgers vector direction (excluding the self stress) at the location of dislocation i.

As remarked previously, the main challenge in a coupled DD and vacancy diffusion simulation is the widely differing characteristic time scales associated with the dislocation glide and climb processes. In the context of the creep problem, we use an adaptive time stepping scheme where dislocation nucleation and glide processes are modeled using a fixed time step $t_{\text{gl}} = 0.5$ ns while the vacancy diffusion and dislocation climb processes are simulated using a much larger time step $t_{\text{cl}}(T)$, whose value depends strongly on the temperature. A conservative estimate of the climb time step

is made as $t_{\text{cl}} = 10^{-3} t_{\text{est}}$, where t_{est} is an estimated time taken for a dislocation to climb a distance equal to the slip plane spacing. For the latter, an estimate of the climb velocity is made using equation (8.29) assuming $c_\infty = c_0$ and c_d calculated from (8.26) with f_c taken as $100\sigma b$ to allow for local stress concentrations within the sample. Creep simulations performed using different values of t_{cl} indicate the results are insensitive to the choice of the time step as long as $t_{\text{cl}} \leq 10^{-2} t_{\text{est}}$. The iterative strategy used to perform the creep simulations is detailed below.

1. The time step, $\mathrm{d}t$, is initialized as the glide time step t_{gl} at the beginning of the simulations.

2. Uniform displacements $\pm U/2$ are applied on the two faces $x_1 = \pm L/2$ while the lateral faces $x_2 = \pm D/2$ are assumed to be traction free. The linear elastic boundary value problem, described in detail in Chapter V, is solved to obtain the stress and displacement fields in the sample. The average tensile stress and strain for the specimen are calculated as

$$\sigma = \frac{1}{D} \int_{-D/2}^{D/2} \sigma_{11}(\pm L/2, x_2)\, \mathrm{d}x_2, \qquad \epsilon = \frac{U}{L} \tag{8.46}$$

   An iterative procedure is used to update the value of U until the computed value of the average tensile stress equals the desired creep stress σ.

3. The Peach-Koehler forces on the dislocations are computed using equation (8.11). The dislocation positions are updated using the glide components of the Peach-Koehler force and the glide mobility law (5.9) from Chapter V. The constitutive rules for short range interactions between dislocations and obstacles described in Chapter V are used during the glide steps to determine the new positions of the dislocations. For simplicity, the 2.5D rules such as junction formation are not used in the creep simulations.

4. Steps 2–3 are repeated until the average axial strain ϵ attains a steady state value. This may correspond to the dislocations in the sample reaching local equilibrium positions, such as stuck at obstacles, so that the glide activity in the system ceases and the overall strain remains constant. In practice, dislocation activity never completely stops in a large dynamic system and an alternative criterion is needed to detect steady state conditions. In our simulations steady state conditions are considered to be attained when the average strain rate remains zero (within a specified tolerance) over a period of 100 glide increments.

5. When steady state is reached, the dislocations are frozen at their current positions and the time step $\mathrm{d}t$ is switched to the climb time step t_{gl}. The unsteady diffusion PDE, equation (8.38), is solved using the finite element method according to the formulation described previously. At the beginning of the simulation, the vacancy field is initialized using the equilibrium distribution consistent with the imposed boundary tractions and the temperature. The initial conditions for each subsequent step corresponds to the vacancy field at the end of the previous time step. The contribution to the total strain as a result of the diffusive flux of vacancies through the boundaries is calculated as

$$\epsilon_d = -\int_0^t \frac{\mathrm{d}t}{LD} \int_{-D/2}^{D/2} \mathbf{J}(x_1 = \pm L/2, x_2) \cdot \mathbf{n} \, \mathrm{d}x_2 \tag{8.47}$$

6. The climb distanced of the dislocations at the end of each increment are evaluated using equation (8.29). When the climb distance of any of the dislocations in the sample reaches the slip plane spacing, the dislocation is removed from its original slip plane to the new slip plane. Positive and negative climb are treated differently according to the energy based criterion for vacancy nucleation, equation (8.45). The total number of vacancies nucleated/annihilated as

a result of dislocation climb is estimated using equation (8.44) and the vacancy concentration fields within the element are updated.

7. The time step dt is switched back to the glide time step after the first climb event and the glide steps 2–3 are repeated until a new steady state value of the strain ϵ is reached.

Material properties for Aluminum are used in the simulations with Young's modulus $E = 70$ GPa and Poisson's ratio $\nu = 0.33$. The modulus of the Burger's vector $b = 0.25$ nm is assumed on all slip systems. The drag factor is assumed to scale linearly with the temperature as $B = 10^{-4}T/300$ Pa s, where $B = 10^{-4}$ Pa s is the drag factor at $T = 300$ K. A constant value of $\tau_{\text{obs}} = 150$ MPa is used for the athermal strength of the point obstacles. However, thermally activate bypass of obstacles at subcritical values of the Peach-Koehler force is modeled using the probabilistic criterion of equation (8.36). A normal distribution of initial source strengths τ_{src} is assumed with an average value of 50 MPa and a standard deviation of 10 MPa. A constant nucleation time of $t_{\text{nuc}} = 10$ ns is assigned for all sources. The material properties that enter into the constitutive rules for vacancy diffusion (based on data from the literature) are tabulated in Table. VII. Note that the formation volume for a vacancy in Al is very nearly equal to the atomic volume as determined from experiments [170] and atomistic calculations [171] so that the relaxation volume Ω_v is nearly zero. Thus, the pressure gradient term in equation (8.38) is taken to be zero in the following simulation results. Also, the temperature dependence of the elastic modulii are ignored in the simulation results presented here.

Table VII. Material properties for Al used in the creep simulations. From refs. [a] [104], [b] [170], [c] [171], [d] [172].

Property	Symbol	Value
Melting Temperature	T_m	933 K
[a]Atomic Volume	Ω	16.3 Å^3
[b,c]Vacancy Relaxation Volume	Ω_v	~ 0 Å^3
[d]Vacancy diffusion coefficient pre-exponential	D_0	1.51×10^{-5} m^2/s
[d]Vacancy formation energy	E_f	0.67 eV
[d]Vacancy migration energy	E_m	0.61 eV

2. Simulation Results

Creep simulations were performed for single crystalline specimens of the type shown in Fig. 94 at three different values of the temperature, $T = 400, 600$ and 800 K, and different values of the creep stress σ below the yield stress of the specimen in tension. Assuming material properties of Aluminum, the chosen range of the temperature corresponds to $0.43 - 0.86T_m (T_m = 933\,\text{K})$. As discussed in the introduction, dislocation creep is the expected deformation mode in the above range of the homologous temperature, enabled by the climb of dislocations due to bulk diffusion. Self-similar specimens with aspect ratio $L/D = 3$ are considered. The yield stress of the computational specimen is set by the chosen values of the average nucleation strength of the static Frank-Read sources that are distributed randomly within the specimen. We first look at the stress–strain response of a typical specimen under plane strain tension at a constant imposed deformation rate $\dot{\epsilon} = 10^4 \text{s}^{-1}$ to determine the yield strength and post-yield behavior of the material. Fig. 95 shows a representative stress–strain response of a specimen of size $D = 4\mu\text{m}$. The material exhibits an elastic-plastic behavior with a yield stress of approximately 80 MPa and no strain hardening due

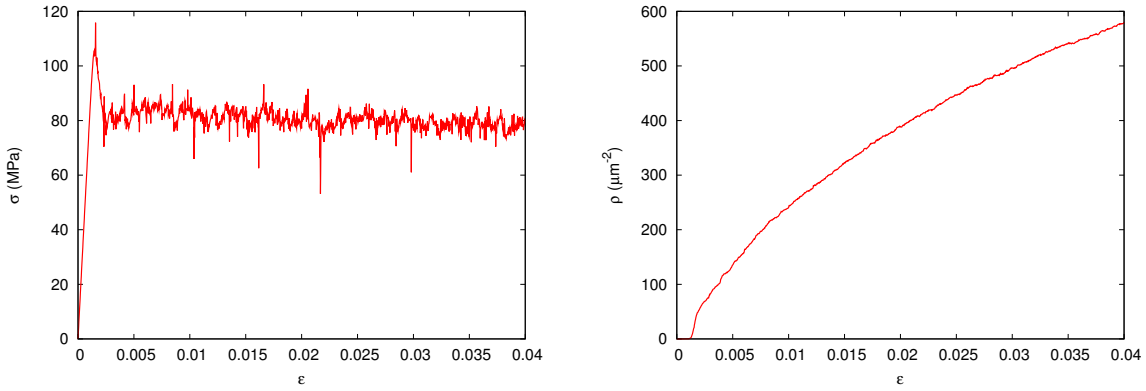

(a) (b)

Fig. 95. Evolution of the (a) flow stress σ and (b) dislocation density ρ for a computational specimen with $D = 4\mu$m subjected to a constant deformation rate $\dot{\epsilon} = 10^4 \text{s}^{-1}$.

to the absence of the 2.5D constitutive rules. It is observed that there is minimal scatter in the value of the flow stress for different realizations of the initial source and obstacle populations due to the rather high values of the source and obstacle densities chosen. Examination of similar results for different values of D shows that there is also no size dependence for the yield stress. The choice of high initial densities enable us to reduce the scatter in the simulation results and to isolate collective emergent behavior in a large dynamic system.

a. Dislocation Creep

Fig. 96 shows the creep response of the same computational specimen for different values of the creep stress σ in the range $10 - 60$ MPa. The temperature is assumed to be $T = 400$ K $\approx 0.43 T_{\text{m}}$. Fig. 96(a) shows the evolution of the axial strain ϵ as a function of time and Fig. 96(b) shows the evolution of the dislocation density with time. Note that, due to the rapid oscillation of the dislocation density about a well defined mean, the curves of ρ vs. time have been smoothed out using the plotting

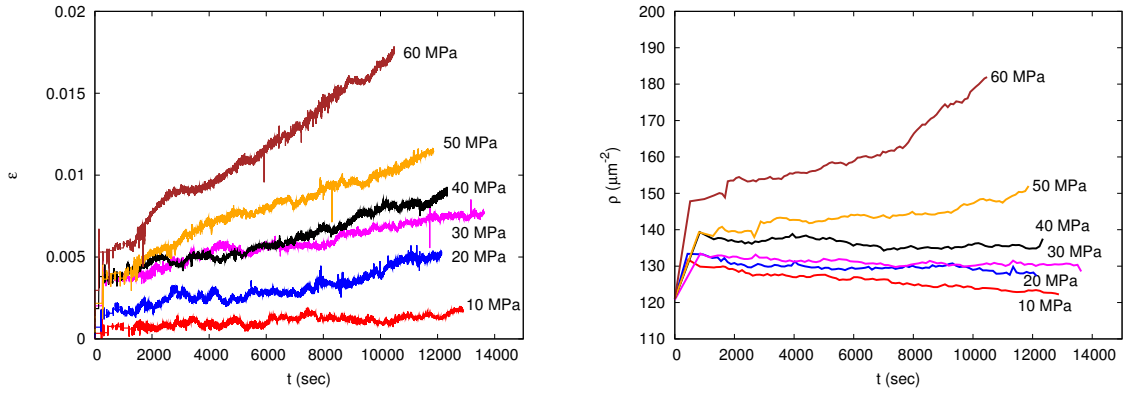

(a) (b)

Fig. 96. Creep response of specimens with $D = 4\mu$m at $T = 400$ K for different values of the creep stress σ below the macroscopic yield stress: (a) strain ϵ vs. time t and (b) dislocation density ρ vs. t. The curves are labeled by the value of the creep stress σ.

software so that the different curves are clearly distinguishable in the figure. It can be seen from Fig. 96 that after an initial transient region, the dislocation density does not vary significantly with strain except for very high values of the creep stress, unlike in the case of the tension simulation of Fig. 95. Steady state 'stage II' creep (see Fig. 93) is characterized by more or less constant values of the microstructural variables [153], which in the case of our single crystal simulations correspond to the dislocation density. Hence, we may consider the part of the creep curves after the transient in Fig. 96 to correspond to the steady state creep regime in Fig. 93. However, closer examination of the initial transient region in Fig. 96(a) shows a serrated curve with alternating regions of rapid straining followed by large plateau regions with no accumulation of strain unlike a smooth transient of the type shown in Fig. 93. This is probably an artifact of the specific initial conditions chosen for the system. For instance, sufficient time must elapse of the vacancy flow into the dislocation cores to cause dislocation climb, which means that the mean time between climb events is

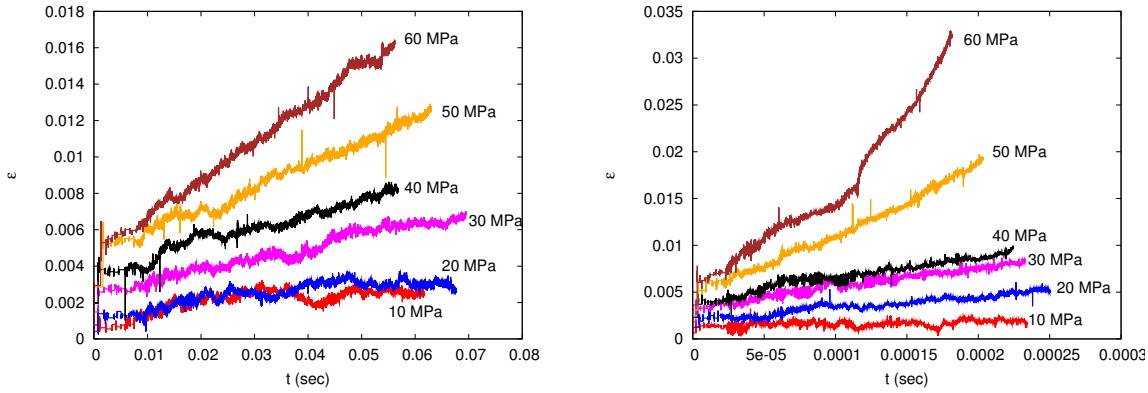

(a) (b)

Fig. 97. Creep curves for the $D = 4\mu$m specimen at (a) $T = 600$ K and (b) $T = 800$ K and different values of the creep stress.The curves are labeled by the value of the creep stress σ.

large initially, before a steady state is reached for the rate at which glide and climb events occur in the system. Finally, we also note that the final stage of accelerated deformation (stage III creep in Fig. 93) is a result of damage processes in the system such as cavitation or strain localization, which we do not attempt to model using the present small strain framework. Also limitations of computing time, especially at larger temperatures which necessitate the use of a much smaller climb time step $t_{\rm cl}$, restrict the usefulness of our approach to modeling the steady state creep regime.

Fig. 97(a) and (b) show similar creep curves for the $D = 4\mu$m specimen at higher values of the temperature $T = 600$ K and $T = 800$ K respectively. Notice that the simulation results are shown for much shorter durations of time compared to the simulations at $T = 400$ K. This is due to the fact that the climb time step $t_{\rm gl}$ is a rapidly decreasing function of the temperature, although even at $T = 800$ K, $t_{\rm cl}$ is at least three orders of magnitude larger than the glide time step $t_{\rm gl} = 0.5$ ns. Despite the different ranges of the time axis, the creep curves at the different temperatures are qualitatively similar with an extended steady state regime following

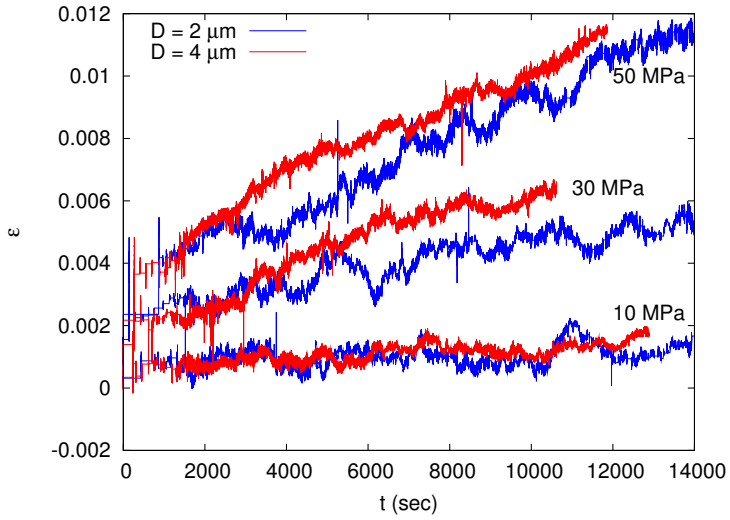

Fig. 98. Comparison of the creep curves for two different values of the specimen size D and several values of the creep stress at $T = 400$ K.

a short transient stage. The creep strain rates $\dot{\epsilon}$ are significantly higher at higher temperatures as expected. The evolution of the dislocation density associated with the results in Fig. 97 (not shown) are very similar to that in Fig. 96(b) with similar values for the steady state dislocation density.

While all the results presented so far have been for specimens with $D = 4\mu$m and different realizations of the initial configurations of sources and obstacles, similar calculations have been performed for self-similar specimens of different sizes. Fig. 98 compares the stress strain response at $T = 400$ K for two values of the specimen size D and three different values of the creep stress. Similar calculations performed for several values of the temperature T indicate that the creep response from the DD calculations is independent of the specimen size within the range of parameters considered in our simulations.

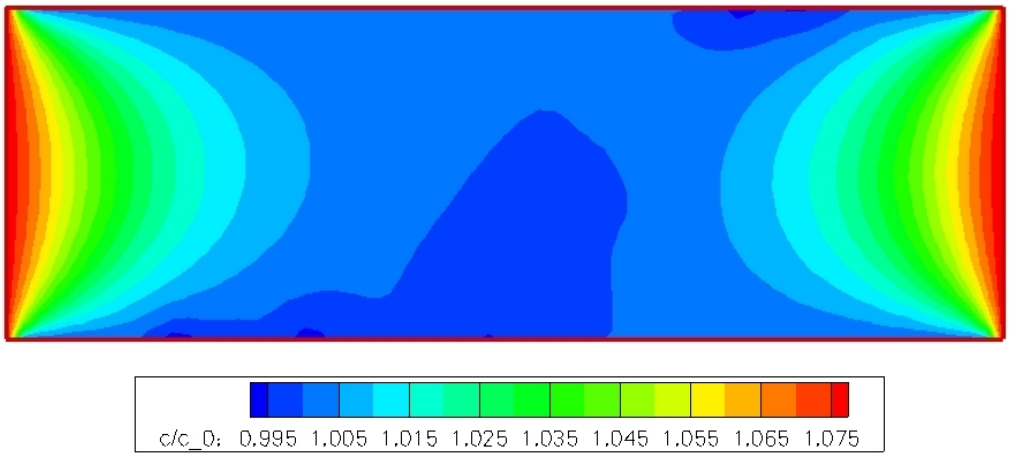

Fig. 99. Contours of vacancy concentration c normalized by the equilibrium vacancy concentration c_0 in the $D = 4\mu$m specimen at $T = 600$ K, $t = 0.05$ s and creep stress $\sigma = 40$ MPa.

b. Diffusional Creep

Apart from the strain $\epsilon = U/L$ shown in Figs. 96–98, which mainly results from dislocation glide on the slip systems, part of the total creep strain is due to the contribution from the flux of vacancies between the boundaries of the specimen. In the case of the tensile sample of Fig. 94, the boundaries at $x_1 = \pm L/2$ have a higher chemical potential for vacancies compared to the free boundaries at $x_2 = \pm D/2$, which leads to a continuous flux of vacancies from the former to the latter. Since the diffusive flux of mass is opposite to the flux of vacancies, this leads to inelastic extension of the bar called Nabarro-Herring creep. The total strain in the computational specimen due to diffusional creep ϵ_d is given by equation (8.47). Fig. 99 shows an example of the typical contours of vacancy concentration $c(\mathbf{x})$ in the specimen. The contours in Fig. 99 corresponds to the instantaneous profile of vacancies at $t = 0.05$ s in the $D = 4\mu$m specimen at $T = 600$ K and subjected to a creep stress $\sigma = 40$ MPa. One can clearly see from Fig. 99 that the gradients in c and hence the flux of vacancies

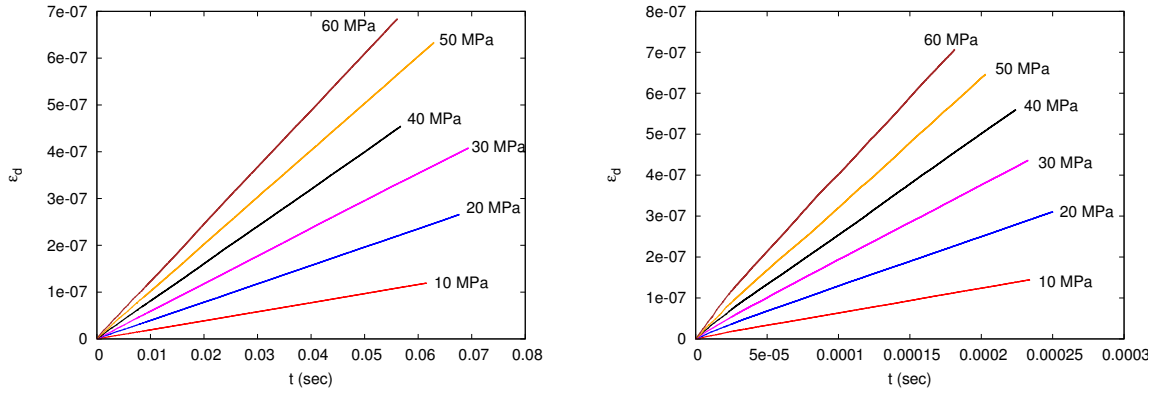

(a) (b)

Fig. 100. Diffusional creep strain ϵ_d for the $D = 4\mu$m specimen at (a) $T = 600$ K and (b) $T = 800$ K and different values of the creep stress.The curves are labeled by the value of the creep stress σ.

is directed away from the tensile boundaries on the right and left and towards the free boundaries at the top and bottom. Fig. 100(a) and (b) show the evolution of the Nabarro-Herring creep strain ϵ_d computed using equation (8.47) as a function of time. Notice that the magnitudes of ϵ_d are several orders of magnitude smaller than the strain ϵ due to dislocation creep, shown in Fig. 97, at all times. Thus the simulations show that dislocation creep is the dominant mode of deformation for the considered ranges of temperatures and creep stresses. However, one can see that when the creep stresses are sufficiently small that there is no dislocation activity in the sample, the only remaining contribution to the total strain rate will be due to diffusional creep shown in Fig. 100.

c. Stress Dependence of the Creep Rate

The creep strain rate is usually related to the stress through a power law relationship of the form $\dot{\epsilon} \propto \sigma^n$, where n denotes the dominant mode of creep. In polycrystals, values of n in the high stress dislocation creep regime are known to vary in the range

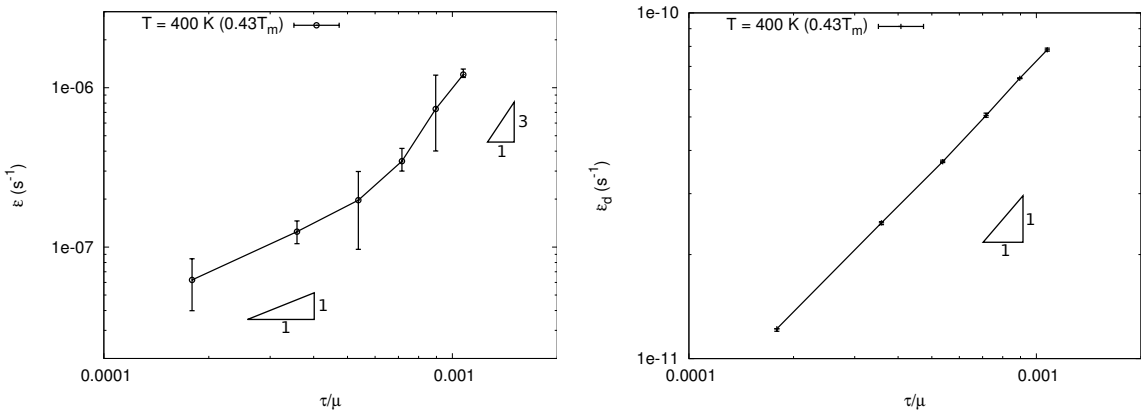

Fig. 101. Variation of the creep strain rate as a function of stress obtained from the DD simulations at $T = 400$ K. The error bars denote the scatter in the predicted creep rates obtained from at least three realizations of the initial configurations of dislocations, sources and obstacles.

$3-8$ [153]. Here, we examine the scaling of the creep strain rate as a function of the stress obtained from the simulations. Fig. 101 shows the variation of the creep strain rate as a function of the stress at $T = 400$ K, plotted on a log-log scale. The resolved shear stress on the slip systems $\tau = f_s\sigma$, normalized by the value of the shear modulus μ, are shown along the x-axis for ease of comparisons with experimental data. The Schmid factor, f_s, in the above equation is equal to 0.47 for both the slip systems in the case of the symmetric slip system configuration considered. Average strain rates obtained from simulations on multiple sample realizations are shown along with the scatter in the simulation results. A minimum of three realizations have been considered for each case. Values of the strain rates $\dot{\epsilon}$ and $\dot{\epsilon}_d$ are calculated using a linear least square fit in the steady state region of the creep curves. Notice that the scatter is much lower for the diffusional creep rates $\dot{\epsilon}_d$ compared to the dislocation creep rates $\dot{\epsilon}$, reflecting the fact that the latter rates are set by the collective behavior of the discrete dislocations, which introduces some stochasticity. Examination of

the deformation mechanism map for polycrystalline Al, Fig. 85 in the introduction, shows that at $T = 400$ K ($0.43T_m$) the experimental range of the creep strain rates is roughly $10^{-8} - 10^{-5}$ for resolved shear stresses in the range $2 \times 10^{-4} - 10^{-3}$. The creep rates obtained from the simulations fall completely within this range, which indicates that our simulations predict the correct order of magnitude for the strain rates. However, it is observed that the slope of the creep rate vs. stress plot on a log-log scale, which is equal to the stress exponent n in a power law, is not a constant, but varies continuously from a value of around 1 at $\tau \approx 10^{-4}\mu$ to around 3 for $\tau \approx 10^{-3}\mu$ close to the macroscopic yield stress of the specimen. Collected experimental data for creep in polycrystalline Al in [153], based on which the deformation mechanism map of Fig. 85 is constructed, invariably show a stress exponent $n \geq 3$ in the above range of stresses. The difference is likely due to the fact that our simulations consider single crystals where bulk diffusion is the only possible mode of mass transport, unlike in polycrystals where grain boundaries and dislocation cores serve as channels for rapid vacancy diffusion. Finally, we observe that the diffusional creep rates in Fig. 101(b) are much smaller than the creep due to dislocation glide and the scaling exponent for the stress is nearly equal to 1.

Figs. 102 and 103 show similar results for higher values of the temperature $T = 600$ K ($0.64T_m$) and $T = 800$ K ($0.86T_m$) respectively. The qualitative trends are similar as in the results at $T = 400$ K with $\dot{\epsilon}_d \ll \dot{\epsilon}$ and the exponent n generally increasing as a function of the stress. Also, the order of magnitude of the creep rates are in agreement with experimental values from Fig. 85. The values of the stress exponent n at $T = 600$ K are similar to those at $T = 400$ K in Fig. 101(a). However, at high temperature $T = 800$ K, higher values of the stress exponent are obtained with n varying in the range $2 - 4$ in the range of stresses considered. Note that the stress exponent for $\dot{\epsilon}_d$ is nearly equal to unity in all cases.

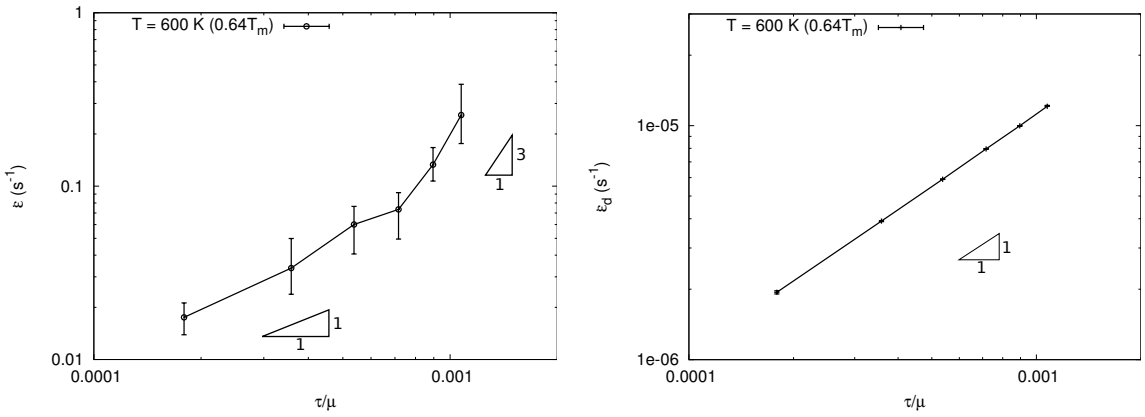

(a) (b)

Fig. 102. Variation of the creep strain rate as a function of stress obtained from the DD simulations at $T = 600$ K. The error bars denote the scatter in the predicted creep rates obtained from at least three realizations of the initial configurations of dislocations, sources and obstacles.

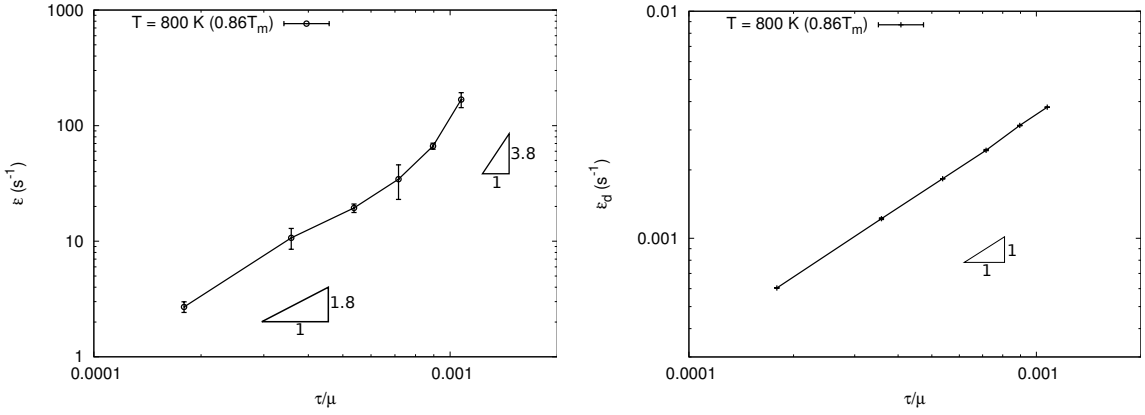

(a) (b)

Fig. 103. Variation of the creep strain rate as a function of stress obtained from the DD simulations at $T = 800$ K. The error bars denote the scatter in the predicted creep rates obtained from at least three realizations of the initial configurations of dislocations, sources and obstacles.

E. Discussion and Conclusions

A computational framework has been proposed for the modeling of creep and other temperature dependent phenomena in small volumes using a coupled dislocation glide and vacancy diffusion assisted climb formulation. The main difference in our approach vis-a-vis other recent efforts to incorporate dislocation climb into DD simulation frameworks [117, 118] is the simultaneous solution of the coupled DD and vacancy diffusion problems within a two dimensional approximation, which allows us to tackle realistic boundary value problems involving large number of dislocations and macroscopic gradients in the vacancy concentration field. Example results presented in the previous section for creep in micron sized single crystals showed a clear steady state regime with strain rates in reasonably good agreement with experimental data for polycrystals [153]. However, the simulations did not capture well the initial transient (stage I of Fig. 93) in the creep curve.

Unlike the case of bulk polycrystals, experimental data is not readily available for single crystal creep at small scales. However, recently Ng and Ngan [160] have performed creep experiments on micron sized single crystalline Al columns manufactured using focussed ion beam milling subjected to nominally homogeneous compression using a flat tip nanoindenter. Unlike other recent experiments that examined the effect of specimen size on the flow strength at small scales [5, 6], their experiments were performed under load control rather than displacement control and the investigation was focused on the creep behavior of the pillars at room temperature. Their main finding was that creep curves for these pillars at high stresses exhibited a staircase like aspect with regimes of steady state creep interspersed with intermittent strain bursts. Such strain bursts have not previously been observed in creep experiments in bulk polycrystals. A similar behavior has also been observed in some of our DD

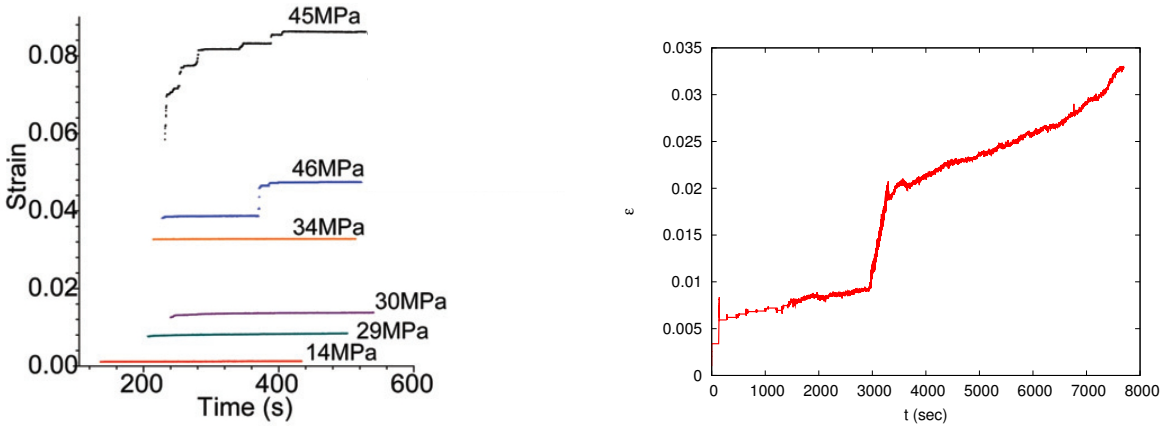

(a) (b)

Fig. 104. (a) Experimental data for creep of 6.3μm diameter Al single crystals, adapted from [160]. (b) Strain burst observed during a DD simulation of creep in a $D = 4\mu$m specimen subjected to tensile creep stress $\sigma = 50$ MPa.

simulations at high values of the creep stress below the yield stress of the specimens. Fig. 104 shows a qualitative comparison of the experimental creep data from [160] with an example creep curve from our simulations that exhibited a similar staircase aspect. The experimental data in in Fig. 104(a) correspond to cylindrical micropillars of diameter 6.3μm and an aspect ratio of 4 oriented along the $[3\bar{1}5]$ crystallographic direction and subjected to creep loading at various values of the stress for a duration of 300 seconds. The simulation data corresponds to a plane strain tension specimen with $D = 4\mu$m subjected to a creep stress $\sigma = 50$ MPa. Based on microscopic examination of the deformed specimens, Ng and Ngan [160] have concluded that the strain bursts are not the result of discrete nucleation events localized to a single slip plane and rather occur due to coordinated action of dislocation sources on multiple slip systems. Figs. 105(a) and (b) show the contours of total slip, Γ, in the computational specimen during two time intervals corresponding to $t = 2500 - 3000$ s and $t = 3000 - 3500$ s respectively. Note that the latter time interval encompasses the

(a)

(b)

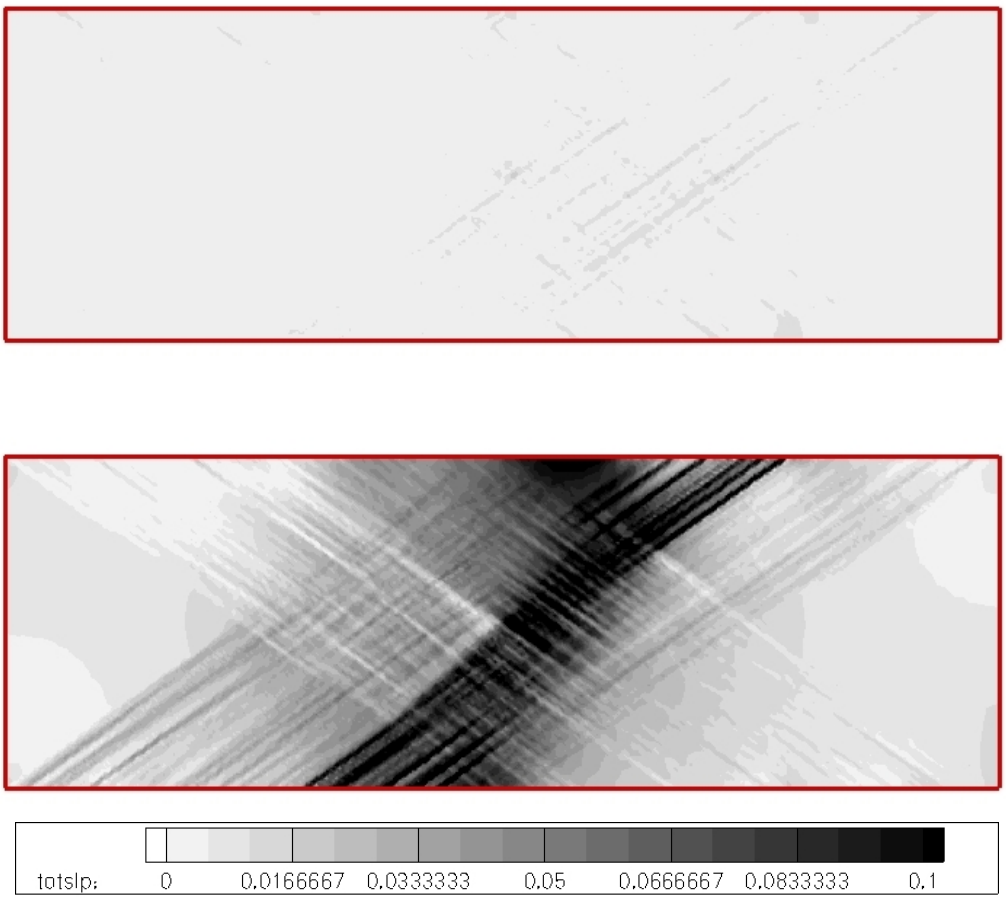

Fig. 105. Contours of total slip Γ in the specimen corresponding to the creep simulation of Fig. 104(b) in the time interval (a) $t = 2500 - 3000$ seconds and (b) $t = 3000 - 3500$ seconds.

duration of the strain burst in Fig. 104(b). Total slip Γ for the time interval $t_1 - t_2$ is defined as $\Gamma = \int_{t_1}^{t_2} \dot{\Gamma}\, \mathrm{d}t$, where $\dot{\Gamma}$ is a measure of the point-wise slip rate defined by $\dot{\Gamma} = \sum_\kappa |\dot{\gamma}^\kappa|$, with $\dot{\gamma}^\kappa = m_i^\kappa \dot{\epsilon}_{ij}^s n_j^\kappa$. Here, $\mathbf{m}$ and $\mathbf{n}$ denotes the slip direction and slip plane normal respectively for slip system κ and $\dot{\boldsymbol{\epsilon}}^s$ is a smooth strain rate field introduced in each finite element and computed by differentiating the total displacement rate field $\dot{\mathbf{u}}$ in that element using the finite element shape functions. The slip contours in Fig. 105 show significantly higher slip activity during the strain burst

compared to a similar time interval during the steady state creep regime. Further, it can be seen that slip activity during the strain burst is distributed over a band of slip planes in one of the two slip systems considered.

Any comparison between simulation results and experiments is currently restricted to qualitative aspects due to the fact that appropriate choices for several simulation parameters such as the initial source and obstacle densities are uncertain in small scale structures. Currently, rather high values have been chosen for these parameters in order to reduce the scatter in the simulation results. Also, the simulations currently ignore several aspects of the physics, such as pipe diffusion, which may play an important role in determining the creep rates depending on the temperature. Additional physics is also needed to model grain boundary creep in polycrystals. The simplest approach to model pipe diffusion, for example, is by using an effective diffusivity for the material that includes a contribution from the diffusivity through the dislocation cores [153]. Grain boundaries, on the other hand, need to be modeled explicitly using an appropriate model for grain boundary diffusion.

In conclusion, one can say that the proposed computational model for dislocation climb aided by vacancy diffusion provides physically reasonable results for the creep rates of single crystals and reproduces some qualitative aspects of creep deformation observed in creep experiments at small scales. However, additional work is needed to (i) extend the simulation methodology so that more general types of microstructures and boundary conditions can be considered and (ii) incorporate additional physics such as grain boundary and pipe diffusion so that thermally activated phenomena across a wider range of temperatures and stresses can be modeled.

CHAPTER IX

CONCLUSION AND RECOMMENDATIONS FOR FUTURE WORK

A. Summary

The research work presented in this dissertation addresses some fundamental issues in the modeling of plasticity and fracture in metals, namely the development of (i) enhanced continuum models of ductile fracture incorporating additional microstructural information and (ii) advancing the state of the art in mesoscale discrete dislocation mechanics methods for modeling plasticity and creep in metals. The former is relevant to a variety of technological applications such as metal forming and failure analysis where plastic anisotropy can significantly influence the limits of ductility of a material. The latter is relevant in applications where traditional continuum models break down due to the emergence of size dependent material response at small scales. Examples include metallic components used in MEMS/NEMS systems, flexible electronics, thin films, etc. From a broader perspective, incorporation of high temperature effects within the discrete dislocation dynamics framework has the potential to enable bottom up modeling of a more complete range of inelastic phenomena across different regimes of stress and temperature. Specific conclusions from the research presented in this dissertation are listed below.

Anisotropic Ductile Fracture

1. Computational cell model studies of anisotropic porous materials made of aligned spheroidal voids in a Hill orthotropic matrix evidenced strong effects of material anisotropy, heretofore not appreciated in the literature. In particular, the effect anisotropic material texture on ductility and damage growth rates was found to be strong irrespective of the imposed loading triaxiality. This is in contrast

with the effect of void shape evolution, which is found to be negligible at high triaxialities although of the same order as the effect of material texture under low triaxiality loading, consistent with previous studies in the literature.

2. The effects of the two types of microstrural anisotropy were found to be coupled in a non-trivial fashion, which can not be easily captured using empirical approaches used previously.

3. An approximate constitutive model of void growth accounting for material anisotropy and void shape effects was developed using a Hill-Mandel homogenization and limit analysis approach. Several simplifying assumptions and approximations were used to arrive at a close form yield function and evolution equations for the microstructural variables. The new model was shown to be consistent with existing void growth models in the literature in special cases and reduces to the Gurson model for an isotropic material.

4. The approximate analytical yield function was evaluated by comparison with a numerically determined upper bound yield locus for the special case of axisymmetric stress states. A numerical limit analysis method was developed to derive the latter by minimization of the plastic dissipation using a large number of trial velocity fields and without recourse to approximations inherent in the analytical model. A good comparison was demonstrated between the analytical and 'exact' yield loci.

5. The analytical model was integrated for specified axisymmetric radial loading paths to obtain the evolution of the flow stress and the microstructural variables. These were compared against (supposedly exact) finite element predictions for the same using the unit cell method. The model was shown to pick up some

important qualitative effects like the non-trivial coupling between void shape and material anisotropy evidenced in the finite element simulations. Also, reasonable quantitative agreement was obtained by using some additional heuristic parameters proposed in previous investigations.

Discrete Dislocation Dynamics

1. An existing two dimensional dislocation dynamics model of Van der Giessen and Needleman [25], extended by Benzerga at al. [26] for strain hardening (2.5D method), was enhanced in several important ways. Scalability to large dislocation systems was achieved by parallelizing the code and implementation of the fast multipole method for long range dislocation–dislocation interactions. The elastic boundary value problem formulation was extended to the general case of arbitrary non-convex and multiply connected domains using the approach of Romero et al. [109]. The boundary conditions were generalized to handle doubly periodic unit cells containing discrete dislocations. These enhancements were leveraged to study several problems of engineering interest.

2. The convergence of the strain hardening rates predicted by 2.5D DD to the limit case of a bulk material was studied by examining the mechanical response of finite rectangular crystals subjected to plane strain compression. The fast multipole method and the university supercomputing facilities were used to solve very large sample sizes containing millions of dislocations. The bulk limit was simulated by examining the response of periodic unit cells containing discrete dislocations. The athermal hardening rates predicted by 2.5D DD were shown to converge to the bulk range of values for large sample dimensions. In addition, the hardening rates obtained from the periodic cell simulations were shown to fall within the band of bulk hardening rates. Predictions for the evolution of the

flow stress and dislocation density from the 2.5D DD simulations were shown to be consistent with the Taylor hardening relation in the bulk limit. However, progressively larger deviations from Taylor hardening behavior were observed towards smaller sample sizes consistent with the previous results of Guruprasad et al. [129].

3. The effect of matrix hardening on the growth of micron and sub-micron sized voids periodically distributed in a single crystalline matrix was analyzed using 2.5D DD and doubly periodic boundary conditions. The investigations built on the previous study of Segurado et al. [131] by generalizing the boundary conditions and materials behaviors considered. Unlike in earlier investigations using a non-hardening matrix, void size effects were evidenced both under low triaxiality (shear) and high triaxiality (biaxial stretching) loadings. In general, strain hardening of the matrix was found to lead to an effective hardening of the void-matrix composite as well as slower void growth rates.

4. The 2D DD framework was extended to include dislocation climb at elevated homologous temperatures, by coupling the elastic boundary value problem for dislocation motion with an unsteady diffusion boundary value problem for a continuous vacancy field. An ad hoc simulation strategy was developed for creep of finite single crystalline specimens using the model of climb assisted dislocation creep. An adaptive time stepping scheme was used to resolve the widely differing time scales of the glide and climb events. Initial investigations using the method have predicted creep rates consistent with experimental data for Aluminum. Power law scaling exponents for the creep strain rates with stress obtained from the simulations were found to range from 1–4. Also, some qualitative features such as strain bursts observed in creep experiments at micron scales

were noticed in some simulations.

B. Recommendations for Future Work

Anisotropic Ductile Fracture

Continuum models of ductile fracture have been developed for a long time starting in the late 60's. Models such as the Gurson void growth model are widely used and supported in commercial softwares. Nevertheless, there are several areas where the Gurson model falls short such as low triaxiality shear fracture. Although phenomenological extensions of the Gurson model have been proposed to account for such effects, microstructure based models such as the one developed in this dissertation hold better promise of modeling these and other effects without recourse to additional heuristics. From this perspective, several possible avenues for future research building on the present work are outlined below.

1. The steps taken in Chapter IV towards validation of the model have revealed some areas where more work is needed. For example, it has been noticed that some heuristics adopted from previous proposals in the literature are needed to obtain reasonable quantitative agreement between the model predictions and finite-element results. It is clear from these results that additional calibration based on unit cell results for anisotropic materials is needed to improve the model's accuracy. This is an important area of future work for the usability of the new model.

2. While the focus of the research in this dissertation was restricted to the modeling of void growth in anisotropic materials, the effect of material anisotropy on void nucleation and void coalescence have not been subject to investigation.

In this context, our finite element results from Chapter II had evidenced some effects of material anisotropy on coalescence for which satisfactory models do not currently exist. In general, unlike the void growth models, models of void nucleation and coalescence are less mature. Moreover, practical application of the anisotropic void growth model in a finite-element study requires that void nucleation and coalescence be considered using some method. Thus, it is of interest to develop models incorporating the effect of material anisotropy on void nucleation and coalescence, possibly using a similar micromechanics approach.

3. The model developed here needs to be implemented in a finite element software such as Abaqus so that predictions from the model can be compared directly against experimental data, such as the results of Bao and Wierzbicki [87].

Discrete Dislocation Dynamics

Unlike continuum mechanics, the field of bottom up modeling of the mechanical properties of materials using *ab initio*, molecular dynamics and mesoscale methods such as DD is still in its infancy. The fast paced improvements in computing infrastructure has enabled the use of these methods to push the limits in understanding material properties at small scales. In contrast to molecular dynamics and similar resolution methods, mesoscale methods such as DD are far more scalable although more approximate. As such, these can be applied to larger systems currently beyond the reach of atomistic methods such as the problems examined in this dissertation. In particular, the developments to the 2.5D DD model undertaken in this dissertation can be used to examine a broader class of problems than was possible before, some of which are identified and listed below.

1. In the DD studies presented here, size dependent mechanical response has been observed under macroscopically homogeneous deformation (Chapter VI) and under macroscopic strain gradients (Chapter VII). Considering that currently the main utility of models such as DD is to inform higher level continuum models, one needs to use the detailed microscopic information provided by the DD models to come up with coarse grained variables that are experimentally measurable and can be used in continuum modeling. While Guruprasad et al. [129] had identified an 'effective' measure of the geometrically necessary dislocation density to characterize the size effects in micropillars, similar analysis needs to be performed under more general loading conditions to verify and validate their hypothesis.

2. The coupled dislocation climb and vacancy diffusion framework developed in Chapter VIII can be extended in various ways to enable investigations of high temperature deformation, heretofore not possible. While the theory is developed for the general case, the boundary value problem framework developed in Chapter VIII is restricted to the specific problem of creep. Additional work is needed to generalize the code for other types of high temperature deformation phenomena.

3. The high temperature DD framework is currently based on bulk diffusion of vacancies while the rapid pipe diffusion mechanism through the dislocation cores is neglected. At low temperatures ($T < 0.4T_m$), pipe diffusion plays an important role in creep and needs to be accounted for. Another important creep mechanism currently neglected in the so called Coble creep due to vacancy diffusion through grain boundaries, due to which the present framework is restricted to single crystals. Incorporating this mechanism requires consideration of the

diffusional properties of grain boundaries. Modeling of the whole range of creep phenomena and the transitions between them is only feasible after all known microscopic mechanisms are taken into account.

REFERENCES

[1] L. Freund and S. Suresh, *Thin Film Materials*, Cambridge University Press, Cambridge, UK, 2004.

[2] R. Modlinski, Microelectron. Reliab. 44 (2004) p.1733–1738.

[3] R. Modlinski, P. Ratchev, A. Witvrouw, R. Puers and I. De Wolf, J. Micromech. Microeng. 15 (2005) p.S165–S170.

[4] M. Abtew and G. Selvaduray, Mater. Sci. Eng.: R: Reports 27 (2000) p.95–141.

[5] M.D. Uchic, D.M. Dimiduk, J.N. Florando and W.D. Nix, Science 305 (2004) p.986–989.

[6] J.R. Greer, W.C. Oliver and W.D. Nix, Acta Mater. 53 (2005) p.1821–1830.

[7] C.P. Frick, B.G. Clark, S. Orso, A.S. Schneider and E. Arzt, Mater. Sci. Eng. 489 (2008) p.319–329.

[8] M.A. Meyers, A. Mishra and D.J. Benson, Prog. Mater. Sci. 51 (2006) p.427–556.

[9] V. Tvergaard and J. Hutchinson, J. Mech. Phys. Solids 40 (1992) p.1377–1397.

[10] A. Needleman, J. App. Mech. 54 (1987) p.525.

[11] J.R. Rice and D.M. Tracey, J. Mech. Phys. Solids 17 (1969) p.201–217.

[12] A.L. Gurson, J. Eng. Mat. Tech. 99 (1977) p.2–15.

[13] V. Tvergaard and A. Needleman, Acta Metall. 32 (1984) p.157–169.

[14] V. Tvergaard, Int. J. Frac. 17 (1981) p.389–407.

[15] A.A. Benzerga and J.B. Leblond, Adv. Appl. Mech. 44 (2010) p.169–305.

[16] J.B. Leblond *Mćanique de la Rupture Fragile et Ductile*, Hermes Science Publications, Lavoisier, 2003.

[17] A.S. Argon, J. Eng. Mat. Tech. 18 (1976) p.60–68.

[18] S.H. Goods and L.M. Brown, Acta Metall. 27 (1979) p.1.

[19] C. Chu and A. Needleman, J. Eng. Mat. Tech. 102 (1980) p.249–256.

[20] W.D. Nix, Mater. Sci. Eng. A 234 (1997) p.37–44.

[21] J.S. Stölken and A.G. Evans, Acta Mater. 46 (1998) p.5109–5115.

[22] J.G. Swadener, E.P. George and G.M. Pharr, J. Mech. Phys. Solids 50 (2002) p.681–694.

[23] N.A. Fleck, G.M. Muller, M.F. Ashby and J.W. Hutchinson, Acta Metall. Mater. 42 (1994) p.475–487.

[24] Y. Huang, H. Gao, W.D. Nix and J.W. Hutchinson, J. Mech. Phys. Solids 48 (2000) p.99–128.

[25] E. GiessenVan der and A. Needleman, Model. Simul. Mater. Sci. Eng. 3 (1995) p.689–735.

[26] A.A. Benzerga, Y. Bréchet, A. Needleman and E. GiessenVan der , Model. Simul. Mater. Sci. Eng. 12 (2004) p.159–196.

[27] A. Needleman, J. Mech. Phys. Solids 20 (1972) p.111–127.

[28] V. Tvergaard, Int. J. Frac. 18 (1982) p.237–252.

[29] J. Koplik and A. Needleman, Int. J. Solids Struct. 24 (1988) p.835–853.

[30] C.L. Hom and R.M. McMeeking, J. App. Mech. 56 (1989) p.309–317.

[31] M.J. Worswick and R.J. Pick, J. Mech. Phys. Solids 38 (1990) p.601–625.

[32] A.A. Benzerga and J. Besson, Eur. J. Mech. 20 (2001) p.397–434.

[33] K.S. Zhang, J.B. Bai and D. Francois, Int. J. Solids Struct. 38 (2001) p.5847–5856.

[34] J. Kim, X. Gao and T. Srivatsan, Eng. Frac. Mech. 71 (2004) p.379–400.

[35] X. Gao and J. Kim, Int. J. Solids Struct. 43 (2006) p.6277–6293.

[36] I. Barsoum and J. Faleskog, Int. J. Solids Struct. 44 (2007) p.5481–5498.

[37] M. Gologanu, J.B. Leblond and J. Devaux, J. Mech. Phys. Solids 41 (1993) p.1723–1754.

[38] M. Gologanu, J.B. Leblond, G. Perrin and J. Devaux, *Recent Extensions of Gurson's Model for Porous Ductile Metals. Part I: Gurson-like Models Incorporating the Influence of Void Shape*, in *Continuum Micromechanics*, P. Suquet ed., Springer–Verlag, 1995, pp. 61–97.

[39] V. Monchiet, O. Cazacu, E. Charkaluk and D. Kondo, Int. J. Plasticity 24 (2008) p.1158–1189.

[40] S.M. Keralavarma and A.A. Benzerga, C. R. Mecanique 336 (2008) p.685–692.

[41] S.M. Keralavarma and A.A. Benzerga, J. Mech. Phys. Solids 58 (2010) p.874–901.

[42] O. Sovik and C. Thaulow, Fatigue Fract. Engng. Mater. Struct. 20 (1997) p.1731–1744.

[43] T. Pardoen and J.W. Hutchinson, J. Mech. Phys. Solids 48 (2000) p.2467–2512.

[44] J. Besson and R. Foerch, Comput. Methods Appl. Mech. Engrg 142 (1997) p.165–187.

[45] P. Ladeveze, *Sur la Théorie de la Plasticité en Grandes Déformations*, 9, L.M.T. Ecole Normale Supérieure, Cachan, France, 1980.

[46] T. Hughes and J. Winget, Int. J. Numer. Meths. Engrg. 15 (1980) p.1862–1867.

[47] R. Hill, Proc. Roy. Soc. London A 193 (1948) p.281–297.

[48] J.C. Simo and R.L. Taylor, Comput. Methods Appl. Mech. Engrg 48 (1985) p.101–118.

[49] A.A. Benzerga, *Rupture Ductile des Tôles Anisotropes*, Ecole Nationale Supérieure des Mines de Paris, 2000.

[50] A. Pineau and P. Joly, *Local versus Global Approaches of Elastic-Plastic Fracture Mechanics. Application to Ferritic Steels and a Cast Duplex Stainless Steel*, J. Blauel and K. Schwalbe, eds., ESIS, European Group on Fracture Publication, 1991, pp. 381–414.

[51] S. Bugat, J. Besson, A.F. Gourgues and A. Pineau, Mater. Sci. Eng. 317 (2001) p.32–36.

[52] D. Lassance, F. Scheyvaerts and T. Pardoen, Eng. Frac. Mech. 73 (2006) p.1009–1034.

[53] A.A. Benzerga, J. Besson and A. Pineau, Acta Mater. 52 (2004) p.4623–4638.

[54] S. Yerra, C. Tekoglu, F. Scheyvaerts, L. Delannay, P.V. Houtte and T. Pardoen, Int. J. Solids Struct. 47 (2010) p.1016–1029.

[55] R. Lebensohn, C. Tomé and P. Maudlin, J. Mech. Phys. Solids 52 (2004) p.249–278.

[56] M. Gologanu, J.B. Leblond, G. Perrin and J. Devaux, Int. J. Solids Struct. 38 (2001) p.5581–5594.

[57] A.A. Benzerga, J. Mech. Phys. Solids 50 (2002) p.1331–1362.

[58] A.A. Benzerga, J. Besson and A. Pineau, Acta Mater. 52 (2004) p.4639–4650.

[59] A.A. Benzerga, J. Besson and A. Pineau, J. Eng. Mat. Tech. 121 (1999) p.221–229.

[60] A. Pineau and T. Pardoen, Comprehensive Structural Integrity 2 (2007) p.684–797.

[61] F.A. McClintock, J. App. Mech. 35 (1968) p.363–371.

[62] V. Tvergaard, Adv. Appl. Mech. 27 (1990) p.83–151.

[63] G. Perrin, *Contribution à l'étude Théorique et Numérique de la Rupture Ductile des Métaux*, Ecole Polytechnique, 1992.

[64] M. Gologanu, J.B. Leblond and J. Devaux, J. Eng. Mat. Tech. 116 (1994) p.290–297.

[65] M. Garajeu, J.C. Michel and P. Suquet, Comput. Methods Appl. Mech. Engrg 183 (2000) p.223–246.

[66] P. Ponte Castaneda, J. Mech. Phys. Solids 39 (1991) p.45–71.

[67] P. Ponte Castañeda and M. Zaidman, J. Mech. Phys. Solids 42 (1994) p.1459–1495.

[68] M. Kailasam and P. Ponte Castaneda, J. Mech. Phys. Solids 46 (1998) p.427–465.

[69] M. Gologanu, *Etude de Quelques Problèmes de Rupture Ductile des Métaux*, Université Paris 6, 1997.

[70] J.B. Leblond and G. Mottet, C. R. Mecanique 336 (2008) p.176–189.

[71] F. Scheyvaerts, T. Pardoen and P. Onck, Int. J. Damage Mech. 19 (2010) p.95.

[72] A. Pineau, Int. J. Frac. 138 (2006) p.139–166.

[73] A.A. Benzerga, J. Besson, R. Batisse and A. Pineau, Model. Simul. Mater. Sci. Eng. 10 (2002) p.73–102.

[74] E. Riks, Int. J. Solids Struct. 15 (1979) p.529–551.

[75] R. Hill, J. Mech. Phys. Solids 15 (1967) p.79–95.

[76] J. Mandel, *Contribution Théorique à l'étude de l'écrouissage et des Lois d'écoulement Plastique*, in 11$^{\text{th}}$ *International Congress on Applied Mechanics* Springer, Berlin, 1964, pp. 502–509.

[77] P. Suquet, *Plasticité et Homogénéisation*, Université Pierre et Marie Curie – Paris VI, 1982.

[78] K. Danas and P. Ponte Castañeda, Eur. J. Mech./A Solids 28 (2009) p.387–401.

[79] J. Leblond and M. Gologanu, C. R. Mecanique 336 (2008) p.813–819.

[80] B.J. Lee and M.E. Mear, J. Mech. Phys. Solids 40 (1992) p.1805–1836.

[81] I. Gradshteyn and I. Ryzhik *Table of Integrals, Series, and Products*, Academic Press, New York, 1980.

[82] S.M. Keralavarma, A Micromechanics based Ductile Damage Model for Anisotropic Titanium Alloys; Master's thesis, Texas A&M University, USA (2008), .

[83] J. Eshelby, Proc. Roy. Soc A241 (1957) p.357–396.

[84] B. Budiansky, J.W. Hutchinson and S. Slutsky, *Void Growth and Collapse in Viscous Solids*, H.G. Hopkins and M.J. Sowell, eds., Pergamon Press, New York, 1982, pp. 13–45.

[85] J. Besson, D. Steglich and W. Brocks, Int. J. Plasticity 19 (2003) p.1517–1541.

[86] J.B. Leblond, G. Perrin and J. Devaux, Eur. J. Mechs, A/Solids 14 (1995) p.499–527.

[87] Y. Bao and T. Wierzbicki, Int. J. of Mech. Sci. 46 (2004) p.81–98.

[88] P. Gill, W. Murray and M. Wright *Practical Optimization*, Academic Press, 1981.

[89] Y.C. Liu and L.K. Johnson, Met. Trans. A 16A (1985) p.1531–1535.

[90] O. Sovik, *The Effect of Non–Spherical Void–Shape on the Evolution of Ductile Damage*, in 11^{th} *European Conference on Fracture*, J. Petit ed., Chameleon Press, Poitiers, France, 1995, pp. 935–940.

[91] R. Foerch, J. Besson, G. Cailletaud and P. Pilvin, Comput. Methods Appl. Mech. Engrg 141 (1997) p.355–372.

[92] M. Ortiz and J. Simo, Int. J. Numer. Meths. Engrg. 23 (1986) p.353–366.

[93] J. Simo and T. Hughes *Computational Inelasticity*, Springer, 1998.

[94] M.D. Uchic, P.A. Shade and D.M. Dimiduk, Annual Review of Materials Research 39 (2009) p.361–386.

[95] V. Vitek, Prog. Mater. Sci. 36 (1992) p.1–27.

[96] J. Lepinoux and L.P. Kubin, Sripta Metall. 21 (1987) p.833–838.

[97] R.J. Amodeo and N.M. Ghoniem, Phys. Rev. B41 (1990) p.6958–6967.

[98] L.P. Kubin, G. Canova, M. Condat, B. Devincre, V. Pontikis and Y. Bréchet, *Dislocation Microstructures and Plastic Flow: A 3D Simulation*, in *Nonlinear Phenomena in Materials Science*, J. Martin and L.P. Kubin, eds., Sci-Tech, Vaduz, 1992, pp. 455–472.

[99] H.H.M. Cleveringa, E. GiessenVan der and A. Needleman, J. Mech. Phys. Solids 48 (2000) p.1133–1157.

[100] E. GiessenVan der , V. Deshpande, H. Cleveringa and A. Needleman, J. Mech. Phys. Solids 49 (2001) p.2133–2153.

[101] A. Widjaja, E. GiessenVan der and A. Needleman, Mater. Sci. Eng. A 400 (2005) p.456–459.

[102] P.J. Guruprasad and A.A. Benzerga, Phil. Mag. 88 (2008) p.3585–3601.

[103] M. Hussein, U. Borg, C. Niordson and V. Deshpande, J. Mech. Phys. Solids 56 (2008) p.114–131.

[104] J.P. Hirth and J. Lothe *Theory of Dislocations*, McGraw-Hill, New York, 1968.

[105] W. Cai, A. Arsenlis, C. Weinberger and V. Bulatov, J. Mech. Phys. Solids 54 (2006) p.561–587.

[106] D. Hull and D. Bacon *Introduction to Dislocations*, Butterworth-Heinemann, Oxford, 2001.

[107] D. Kiener, P.J. Guruprasad, S.M. Keralavarma, G. Dehm and A.A. Benzerga, Acta Mater. 59 (2011) p.3825–3840.

[108] J. Friedel *Les Dislocations*, Gauthier–Villars, Paris, 1956.

[109] I. Romero, J. Segurado and J. LLorca, Model. Simul. Mater. Sci. Eng. 16 (2008) p.35008.

[110] R. Chandra *Parallel Programming in OpenMP*, Morgan Kaufmann, Waltham, MA, 2001.

[111] L. Greengard and V. Rokhlin, J. Comput. Phys. 73 (1987) p.325–348.

[112] J. Carrier, L. Greengard and V. Rokhlin, SIAM J. Sci. Stat. Comp. 9 (1988) p.669.

[113] A.F. Bower *Applied Mechanics of Solids*, CRC Press, New York, 2009.

[114] S. Chakravarthy and W. Curtin, Model. Simul. Mater. Sci. Eng. 19 (2011) p.045009.

[115] J.C. Simo, J. Oliver and F. Armero, Comput. Mech. 12 (1993) p.277–296.

[116] V. Lubarda, M. Schneider, D. Kalantar, B. Remington and M. Meyers, Acta Mater. 52 (2004) p.1397–1408.

[117] D. Mordehai, E. Clouet, M. Fivel and M. Verdier, Phil. Mag. 88 (2008) p.899–926.

[118] Y. Gao, Z. Zhuang, Z. Liu, X. You, X. Zhao and Z. Zhang, Int. J. Plasticity 27 (2010) p.1055–1071.

[119] W.D. Nix and H. Gao, J. Mech. Phys. Solids 46 (1998) p.411–425.

[120] H. Gao, Y. Huang, W.D. Nix and J.W. Hutchinson, J. Mech. Phys. Solids 47 (1999) p.1239–1263.

[121] N.A. Fleck and J.W. Hutchinson, J. Mech. Phys. Solids 49 (2001) p.2245–2271.

[122] C.A. Volkert and E.T. Lilleodden, Phil. Mag. 86 (2006) p.5567–5579.

[123] D. Kiener, C. Motz and G. Dehm, J. Mater. Sci. 43 (2008) p.2503–2506.

[124] H. Espinosa, M. Panico, S. Berbenni and K. Schwarz, Int. J. Plasticity 22 (2006) p.2091–2117.

[125] H. Tang, K.W. Schwarz and H.D. Espinosa, Acta Mater. 55 (2007) p.1607–1616.

[126] J. Greer, C. Weinberger and W. Cai, Mater. Sci. Eng. A 493 (2008) p.21–25.

[127] A.A. Benzerga and N.F. Shaver, Scr. Mater. 54 (2006) p.1937–1941.

[128] V.S. Deshpande, A. Needleman and E. GiessenVan der , J. Mech. Phys. Solids 53 (2005) p.2661–2691.

[129] P.J. Guruprasad and A.A. Benzerga, J. Mech. Phys. Solids 56 (2008) p.132–156.

[130] R. Hill, J. Mech. Phys. Solids 35 (1987) p.23–33.

[131] J. Segurado and J. Llorca, Acta Mater. 57 (2009) p.1427–1436.

[132] J. Gil Sevillano, Flow Stress and Work Hardening, in *Materials Science and Technology*, R.W. Cahn, P. Haasen, E. Kramer and H. Mughrabi, eds., VCH, Weinheim, 1993, pp. 19–88.

[133] A.S. Argon *Strengthening Mechanisms in Crystal Plasticity*, Oxford University Press, USA, 2008.

[134] H. Mecking and U.F. Kocks, Acta Metall. 29 (1981) p.1865–1875.

[135] Y. Estrin and H. Mecking, Acta Metall. 32 (1984) p.57–70.

[136] A. Arsenlis and D. Parks, Acta Mater. 47 (1999) p.1597–1611.

[137] M. Gologanu, J.B. Leblond, G. Perrin and J. Devaux, *Recent Extensions of Gurson's Model for Porous Ductile Metals. Part II: A Gurson-like Model Including the Effect of Strong Gradients of Macroscopic Fields*, in *Continuum Micromechanics*, P. Suquet ed., Springer–Verlag, 1995, pp. 97–130.

[138] K. Enakoutsa, J. Leblond and G. Perrin, Comput. Method. Appl. M. 196 (2007) p.1946–1957.

[139] W.M. Garrison, A.L. Wojcieszynski and L.E. Iorio, *Effects of Inclusion Distributions on the Fracture Toughness of Structural Steels*, R.K. Mahidhara, A.B. Geltmacher, P. Matic and K. Sadananda, eds., February 10–13, Orlando, Florida, TMS, 1997, pp. 125–136.

[140] N.R. Abdel Al, An Experimental Study of Deformation and Fracture of a Nanostructured Metallic Material, Master's thesis, Texas A&M University, USA (2009).

[141] N.A. Fleck and J.W. Hutchinson, Adv. Appl. Mech. 33 (1997) p.295–361.

[142] V. Tvergaard and C.F. Niordson, Int. J. Plasticity 20 (2004) p.107–120.

[143] B. Liu, X. Qiu, Y. Huang, K. Hwang, M. Li and C. Liu, J. Mech. Phys. Solids 51 (2003) p.1171–1187.

[144] Z. Li and P. Steinmann, Int. J. Plasticity 22 (2006) p.1195–1216.

[145] U. Borg, C. Niordson and J. Kysar, Int. J. Plasticity 24 (2008) p.688–701.

[146] J. Kysar, Y. Gan and G. Mendez-Arzuza, Int. J. Plasticity 21 (2005) p.1481–1520.

[147] Y. Gan, J. Kysar and T. Morse, Int. J. Plasticity 22 (2006) p.39–72.

[148] W. Liu, X. Zhang, J. Tang and Y. Du, Comp. Mater. Sci. 40 (2007) p.130–139.

[149] G. Potirniche, M. Horstemeyer, G. Wagner and P. Gullett, Int. J. Plasticity 22 (2006) p.257–278.

[150] S. Traiviratana, E. Bringa, D. Benson and M. Meyers, Acta Mater. 56 (2008) p.3874–3886.

[151] J. Segurado and J. LLorca, Int. J. Plasticity 26 (2010) p.806–819.

[152] S.M. Keralavarma and A.A. Benzerga (2011) In preparation.

[153] H.J. Frost and M.F. Ashby *Deformation-Mechanism Maps: The Plasticity and Creep of Metals and Ceramics*, Pergamon Press, Oxford, 1982.

[154] D. Caillard and J. Martin *Thermally Activated Mechanisms in Crystal Plasticity*, Vol. 8, Elsevier Science, Amsterdam, 2003.

[155] C. Herring, J. App. Phys. 21 (1950) p.437–445.

[156] F.R.N. Nabarro, Z.S. Basinski and D.B. Holt, Adv. Phys. 13 (1964) p.193–323.

[157] R.L. Coble, J. App. Phys. 34 (1963) p.1679–1682.

[158] J. Weertman, J. App. Phys. 28 (1957) p.362–364.

[159] M. Ashby, Acta Metall. 20 (1972) p.887–897.

[160] K. Ng and A. Ngan, Phil. Mag. Letters 87 (2007) p.967–977.

[161] N.M. Ghoniem, S.H. Tong and L.Z. Sun, Phys. Rev. B 61 (2000) p.913–927.

[162] Y. Xiang, D.J. Srolovitz, L.T. Cheng and E. Weinan, Acta Mater. 52 (2004) p.1745–1760.

[163] A. Hartmaier, M.J. Buehler and H.J. Gao, Mater. Sci. Eng. A-Struct. 400 (2005) p.260–263.

[164] D. Mordehai, E. Clouet, M. Fivel and M. Verdier, Annealing of Dislocation Loops in Dislocation Dynamics Simulations, in *IOP Conference Series: Materials Science and Engineering* 3 (2009) p. 012001.

[165] A. Cocks, J. Mech. Phys. Solids 44 (1996) p.1429–1452.

[166] Y. Gao and A. Cocks, Acta Mech. Solida Sin. 22 (2009) p.426–435.

[167] A. Cottrell *An Introduction to Metallurgy*, Universities Press, Oxford, 1990.

[168] A. Hindmarsh, IMACS Trans. Sci. Comput. 1 (1983) p.55–64.

[169] D. Raabe, Phil. Mag. A 77 (1998) p.751–759.

[170] W. Schilling, J. Nucl. Mater. 69 (1978) p.465–489.

[171] E. Harrison and P. Wilkes, Acta Metall. 20 (1972) p.31–36.

[172] P. Freund and K. Heinloth *Numerical Data and Functional Relationships in Science and Technology: New Series*, Springer, New York, 2002.

VITA

Shyam Mohan Keralavarma obtained his Bachelor of Technology degree in Mechanical Engineering from College of Engineering Trivandrum, University of Kerala, India in May 2000. Before joining Texas A&M University in the fall of 2005, he has worked as a software engineer at leading technology companies in India, Infosys Technologies and Tata Consultancy Services. He obtained his M.S. and Ph.D. degrees in Aerospace Engineering from Texas A&M University in May 2008 and December 2011 respectively. His research interests are in the broad area of analytical and computational mechanics and materials science with focus on multi-scale modeling of inelasticity and fracture phenomena. Shyam will be working as a post-doctoral research associate at Brown University from fall 2011.

Contact Information:

Shyam M. Keralavarma
Department of Aerospace Engineering,
H.R. Bright Building, Rm. 701, Ross Street,
College Station, TX 77843-3141, USA
Phone: +1-979-635-4725
email: shyammk@gmail.com